Politecnico di Milano

SCHOOL OF INDUSTRIAL AND INFORMATION ENGINEERING
Master Degree in Engineering Physics

Novel experimental approaches in High-Harmonic Spectroscopy of atoms and molecules

Advisor: Prof. Salvatore Stagira
Supervisor: Prof.ssa Caterina Vozzi

Candidate: Gabriele Crippa
Matr.: 858924

Academic Year: 2016 - 2017

Abstract

When intense femtosecond laser pulses interact with atoms and molecules, high order harmonics of the fundamental frequency can be generated. This nonlinear process is well described by the so-called three step model, for which one electron is freed through tunnel ionization and is then accelerated by the external field, eventually recombining with its parent ion with the emission of an XUV photon. This radiation contains some information on the electronic structure of the generating system, thus allowing to perform spectroscopic studies.

The aim of this thesis is to analyse two new approaches for increasing the data that can be collected in such experiments. The first one addressed the restrictions linked to the necessity to spectrally disperse and spatially focus the radiation onto a detector of limited dimension. A motorized translation stage was previously developed by the group to move the detector along the spectral focal curve of the grating. In this way, the harmonics can be acquired over more spectral windows and such data can then be subsequently connected. For this purpose, a calibration procedure allowed to correct for the pixel dependent responsivity of the detection system, which deforms the spectral shape between different acquisitions. Such procedure was validated collecting the extended spectra of carbon dioxide and ethylene, which gave also the opportunity to explore the possibility to align complex molecular systems.

The second approach, instead, explored new ways for increasing the signal-to-noise ratio by the generation of XUV radiation over an extended medium inside microstructured channels fabricated with the femtosecond laser micromachining technique. In particular, two different waveguide configurations were analysed. In the first case a straight channel allowed to achieve a higher emission compared to the standard gas-jet geometry. However, both absorption and phase matching were found to reshape the spectrum as a function of the experimental conditions. In the second case a modulated waveguide was employed, which provided a less intense but much more robust signal. Indeed, absorption was found to be negligible even at very high pressures.

Sommario

Quando un impulso laser molto intenso interagisce con atomi e molecole, può avvenire la generazione di armoniche di ordine elevato della sua frequenza fondamentale. Questo processo nonlineare è ben descritto dal così detto modello a tre fasi, secondo cui un elettrone viene liberato per effetto tunnel ed è successivamente accelerato dal campo esterno, fino a ricombinare con il suo ione emettendo un fotone XUV. Tale radiazione contiene informazioni sulla struttura elettronica del sistema e può quindi essere sfruttata per studi spettroscopici.

Lo scopo di questa tesi è stato quello di analizzare due nuovi approcci volti ad aumentare il numero di informazioni che può essere estratto in questo tipo di esperimenti. Il primo ha affrontato le limitazioni connesse alla necessità di disperdere spettralmente e focalizzare spazialmente la radiazione su di un detector di dimensioni finite. Uno stage traslazionale precedentemente sviluppato dal gruppo permette di muovere il detector lungo la curva focale dello spettrometro. In questo modo, le armoniche possono essere acquisite in diverse finestre spettrali. Una procedura di calibrazione ha successivamente permesso di unire tali acquisizioni correggendo la dipendenza dalla responsività del detector, la quale deforma lo spettro tra differenti misure. Questa procedura è stata quindi validata tramite l'acquisizione degli spettri estesi dell'anidride carbonica e dell'etilene. In questo modo è stato anche possibile studiare l'allineamento di sistemi molecolari piuttosto complessi.

Il secondo approccio, invece, ha esplorato nuovi metodi per aumentare il rapporto segnale-rumore tramite la generazione di radiazione XUV in un mezzo esteso, grazie all'utilizzo di microcanali ottenuti con la tecnica di microfabbricazione laser a femtosecondi. In particolare, due diverse configurazioni di guida sono state analizzate. Nel primo caso l'utilizzo di un semplice canale rettilineo ha permesso di raggiungere una emissione più elevata rispetto alla tradizionale generazione in getto di gas. Tuttavia, lo spettro è risultato essere fortemente influenzato sia dall'assorbimento che dalle condizioni di phase matching. Nel secondo caso è stata invece utilizzata una guida modulata, la quale ha fornito una emissione meno intensa ma più robusta rispetto alle condizioni sperimentali. L'assorbimento della radiazione è infatti risultato essere trascurabile anche per pressioni molto elevate.

Contents

List of Figures

Introduction

Over the years laser sources have constantly improved both in terms of peak power and pulse duration. In particular, the developments of mode-locked oscillators and of the chirped pulse amplification technique allowed to reach peak intensities above $10^{14}\mathrm{W/cm^2}$. The interaction between such high intensity femtosecond laser pulses and matter is understood within the semiclassical three-step model. In this framework the atom subjected to the laser field is tunnel ionized and the freed electron is subsequently accelerated by the external field until it is eventually driven back to the parent ion during its motion. In this way it will have some probability to recombine with the emission of an XUV photon due to energy conservation. Owing to the peculiarities of such process the emitted radiation consists of odd harmonics of the fundamental laser frequency up to even very high orders. Moreover, as the harmonic emission is temporally restricted in a subcycle of the driving field, a train of attosecond pulses is generated. This radiation is coherent and can thus be used as a probe for time resolved studies of rapid electronic dynamics in matter on their characteristic time scale. This paved the way to the development of the field of attosecond physics. In a different approach the generation process itself can also be used as a probe of the generating system. Indeed the ionization and recombination steps can be thought of as respectively the pump and probe stages of a pump-probe experiment, with all the information encoded in the emitted spectrum. In this way it is possible to study the atomic and molecular dynamics with very high temporal and spatial resolution. This led to the development of the so-called self-probing scheme of high-harmonic spectroscopy experiments.

The theoretical principles of high-order harmonic generation in atomic targets will be covered in **Chapter 1**. Particular attention will be given to the building up of the XUV field in extended media, since the macroscopic signal is the one actually detected during the experiments. The generation of high-order harmonics in molecular targets is instead more complex due to the higher number of internal degrees of freedom. Therefore it will be treated separately in **Chapter 2** along with the theoretical aspects of the field-free alignment technique, which allows to control the relative orientation of the molecular system with respect to the driving field during experiments.

The handling of the XUV radiation is also experimentally challenging as this region of the electromagnetic spectrum is easily absorbed by almost every medium. For this reason the experimental setup must be maintained in high vacuum during the measurements and the spectrometer used for analysing the harmonic signal must employ optical elements at grazing incidence only. The description of the experimental apparatus used in this thesis is given in **Chapter 3**.

Finally in **Chapter 4** the experimental activity performed in the Ultras (center for ultraintense and ultrafast optical science) and UDynI (Ultrafast DYNamic Imaging) laboratories of the Physics Department in Poliecnico di Milano will be presented. The aim of this work was in particular to analyse two approaches for increasing the amount of information that can be retrieved in high-harmonic spectroscopy experiments. The first one relies on a motorized translation stage to move the detector along the focal curve of the spectrometer and acquire data in different spectral windows. These are then connected and the extended spectrum of the system under study is retrieved. On the other hand, the second one exploits the generation of XUV radiation over an extended medium in microchannels. In this way an enhancement of the signal-to-noise ratio is possible, along with the possibility to develop complex phase matching geometries for extending the cutoff frequency of the spectrum. Anyway, due to the high complexity of the generation process numerical simulations regarding the gas dynamics and the fields propagation in the microchannel are needed in order to better understand such results.

CHAPTER 1

High Harmonic Generation

Classically the interaction of atoms with light is treated in terms of the Lorentz oscillator model. In this frame the electrons are subjected to the radiation fields and to the internal restoring force of the nucleus, modelled with Hooke law. When the Newton equation is solved for such system, considering only the electric part of an incoming harmonic field in non relativistic approximation, an oscillatory response of the electron is obtained. Indeed, as the external field displaces the particle from its equilibrium position, the atomic restoring force opposes to the motion and an harmonic oscillation sets in, creating an electric dipole in the system. In a medium the number of such single dipoles per unit volume is called the polarization induced by the external field. In the limit of the Lorentz oscillator model, this response is linear in Fourier domain:

$$\mathbf{P}(\omega) = \varepsilon_0 \chi(\omega, \mathbf{r})\, \mathbf{E}(\omega)$$

where χ is the *linear optical susceptibility* of the medium. In general it is a tensor of rank two that depends both on the position and the frequency of the excitation to account for the non homogeneity of the medium and its non instantaneous response. Therefore in the case of the interaction of a perfectly harmonic field with an isotropic and homogeneous medium it will be a simple scalar. Unless otherwise specified, we will always assume this scalar case. The optical polarization acts then as a source term in the Maxwell wave equation:

$$\left(\nabla^2 - \frac{1}{c^2}\frac{\partial^2}{\partial t^2}\right)\mathbf{E}(\mathbf{r}, t) = \mu_0 \frac{\partial^2}{\partial t^2}\mathbf{P}(\mathbf{r}, t)$$

that describes the time and space distribution of the fields in the medium.

This linear description of the interaction seemed to be pretty accurate until the first ruby laser was realized by Maiman in 1960 [1]. Thanks to this invention, sources of higher intensity became available, allowing the study of light-matter interaction in new regimes. In particular, for large electric fields the polarization of the medium was discovered to be dependent on the light intensity. To describe the situation, without entering in the microscopic details of the interaction, we can consider a Taylor expansion for the medium polarization:

$$P(t) = \varepsilon_0\left(\chi^{(1)}E(t) + \chi^{(2)}E^2(t) + \chi^{(3)}E^3 + ...\right)$$

where we have considered the electric field to be linearly polarized in order to write a simpler scalar equation in the fields. The $\chi^{(N)}$ terms are called the *nonlinear optical susceptibility* of order N of the medium and in the general case are tensors of rank N+1. This approach allows to explain many phenomena in nonlinear optics, but relies on the assumption that the terms in the series become rapidly smaller with increasing order. In other words, it is based on a perturbative description of the interaction, for which the nonlinearities introduce only a small correction to the overall linear response of the system.

Over the years, however, laser sources have improved both in terms of minimum pulse duration and accessible peak intensities. Today mode-locking lasers allow to directly generate pulses of few femtoseconds duration and the*chirped pulse amplification* technique (CPA) [2] allows to amplify them up to 10^{22} W/cm^2 of focused peak intensities. Sources with peak intensities in the order of 10^{14} W/cm^2 were already present in some laboratories by the end of the '80s. Since the electric field of such pulses is comparable with the one experienced by the electrons in an atomic ground state, their interaction with matter cannot anymore be described by a perturbative approach. One of the first phenomena observed in this new regime was high-order harmonic generation (HHG hereinafter) by the gorup of A. McPherson at the University of Illinois, Chicago, in 1987 [3], which consists in the generation of high order odd harmonics of the driving laser frequency when an intense enough pulse is focused onto a gas-jet. It is important to underline that harmonics can be obtained also in the perturbative regime, but with different proprieties. Indeed in this case the intensity of the emission decreases rapidly with the harmonic order and the process is thus limited to relatively low frequencies. On the other hand, when the electric field becomes high enough, the harmonics in the intermediate frequency range form an intensity plateau. This extends into the XUV and soft X-ray part of the electromagnetic spectrum up until a cutoff frequency, from which an exponential decay is present.
Afterwards an empiric law for the cutoff frequency was derived by J. L. Krause *et al.* in the limit of the single atom response [4]:

$$\hbar\omega_{\text{cutoff}} \approx I_p + 3U_p$$

where I_p is the ionization potential of the considered atomic species and U_p the ponderomotive energy of the driving pulse, which is defined as the cycle averaged quiver energy of a free electron in its electric field. For linearly polarized radiation this is given by:

$$U_p = \frac{e^2 E_f^2}{4 m_e \omega_f^2}$$

with e the electron charge, m_e the electron mass, E_f the electric field amplitude and ω_f the driving laser frequency. Another important propriety of HHG is that the radiation emission is concentrated in a subcycle of the driving field, giving rise to a train of attosecond pulses [5]. More recently it was also demonstrated that isolated attosecond pulses can be extracted from this process [6], which can then be used to probe electron dynamics in atoms and molecules on their natural time scales [7, 8].

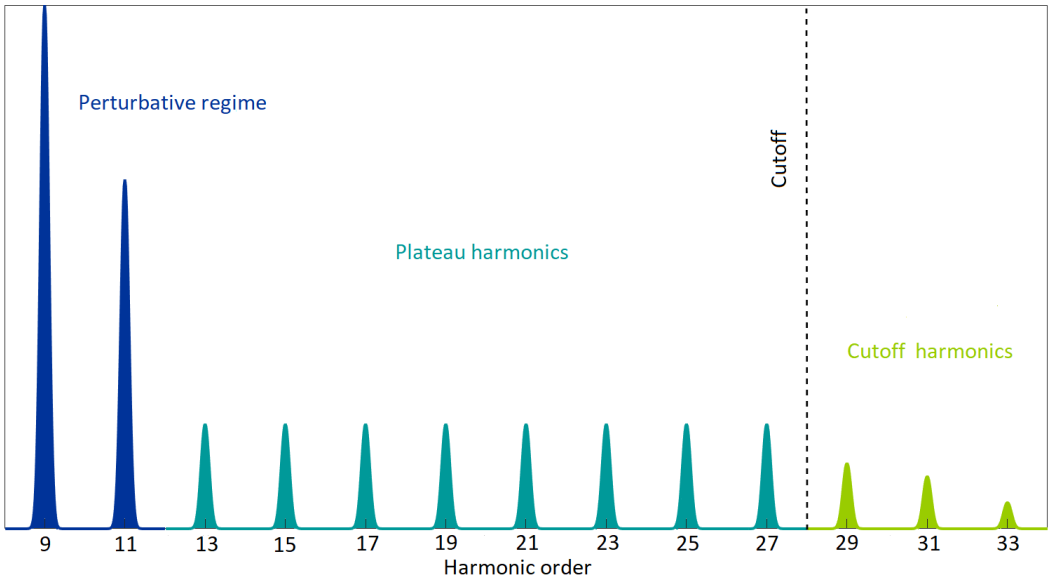

Figure 1.1: Sketch of a typical HHG spectrum.

Depending on the application, an extended cutoff or the selection of a single harmonic may generally be needed. However, one of the main limitations of HHG as a source in the XUV region of the electromagnetic spectrum is the conversion efficiency which is limited to yelds in the order of $10^{-6\div7}$. This is mainly due to the limited interaction region of the comonnly used gas-jet generation geometry and to the difference in phase velocity of the driving and the harmonic fields inside the nonlinear medium, which doesn't allow an efficient build up of the signal. This issue can be addressed switching to a hollow waveguide geometry, which both extends the interaction region and allows to better control the phase matching conditions, as proposed by A. Rundquist *et al.* [9]. An extension of the cutoff frequency, instead, can be achieved using atoms with higher ionization potential I_p or driving fields with longer wavelengths. Recently T. Popmintchev *et al.* demonstrated the possibility to produce radiation up to 1.5 keV employing a 4 µm driving field in a waveguide geometry [10]. This energies are far above the so-called water window, delimited by the K absorption edges of oxygen (530 eV) and carbon (280 eV), which is of great importance in the study of biological samples. Moreover, the employment of a guiding geometry allow to tune, within some limits, the frequency range for which the phase matching conditions are more favourable. For all these reasons the generation of high-order harmonics in hollow core waveguides has lately become a topic of fairly great importance.

In this first chapter we will present the theoretical basis of the HHG process, focusing on the case of simple atomic targets. In Section 1 the semiclassical theory of high intensity laser-atom interaction developed indipendenty by Corkum [11] and Kulander [12] will be covered. Since this model allows to derive in a rather straightforward way some of the main peculiarities of HHG, it will be treated quite

extensively. In Section 2 we will then give a brief presentation of the fully quantum theory developed by Lewenstein [13] in the framework of the so-called *strong field approximation* (SFA). Particular attention will be given to those aspects that cannot be accounted for by the more simple semiclassical model. Finally in Section 3 we will cover the building up of the harmonic fields in an extended medium, focusing on phase matching and absorption effects.

1.1 Semiclassical three-step model

The semiclassical model of high intensity laser-atom interaction accounts in a rather simple way for some of the main aspects of HHG. Arguments from both classical and quantum mechanics are used in this approach and the process of light generation is divided in three steps:

I. **Ionization:** In the first step the atom is ionized by the external field. The treatment is completely quantum and many regimes of photoionization are devised. In particular, the most important one in the case of HHG is tunnel ionization, in which an electron is detached from the valence shell of the atom via tunnelling through the potential barrier bent by the external field. Usually an assumption is made, considering only the most weakly bound electron of the atom and neglecting multiple photoionization events, which is referred to as *single active electron approximation* (SAEA).

II. **Propagation:** The freed electron is then considered as subjected to the action of the external field only, neglecting any contribution of the Coulomb potential of the parent ion. This assumption is called *strong field approximation* (SFA). Moreover, also the magnetic field of the driving pulse is neglected, as its intensity is usually not enough to trigger a relativistic motion of the electron. The treatment of this step is completely classical and the system dynamics is solved simply by means of Newton equations.

III. **Recombination:** In the last step the electron is driven back by the external field and interacts with its parent ion. This can result in scattering, both elastic or inelastic (in which case the ion is either excited or further ionized), or in the recombination of the electron, triggering the emission of a XUV photon due to energy conservation.

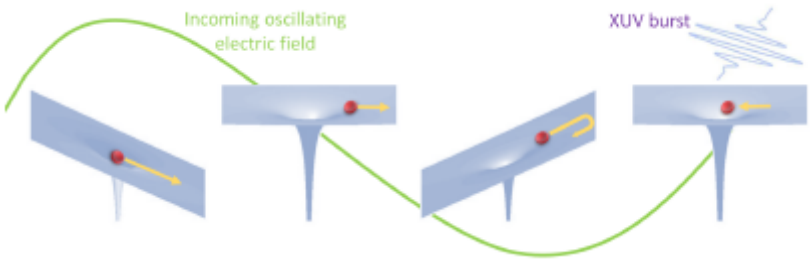

Figure 1.2: Schematics of the process giving rise to HHG. In the first step the atomic potential well is bent by the driving field and the electron can tunnel out. Then it is accelerated until it recollides with its parent ion. The accumulated kinetic energy is finally released in the form of an XUV burst.

In the following sections each one of these steps will be analysed more in details.

1.1.1 Ionization

Ionization of atoms under the influence of an external electric field is a rather vast and complex topic, with many aspects that are not fully understood even at these days. Therefore we will present here only few arguments, beneficial to the study of HHG, without claiming to be exhaustive and focusing in particular on the limits of validity of the various approximations employed. For a more complete review on the topic one can refere to [14].

One possible approach to the problem of evaluating the ionization of atoms in strong field phenomena is to numerically solve the Schrödinger equation for the system. Even though this is possible, it can be rather complex and surely doesn't give any physical insight on the process. Therefore over the years many analytical approaches have been proposed to avoid this full numerical computation. In 1965 L.V.Keldysh [15] proposed a theory for the photoionization of atoms in intense monochromatic laser fields treated in scalar approximation, when the photon energy is much less than the atomic ionization potential. This implies that an upper limit for the frequency of the incoming radiation $\omega_f < I_p/\hbar$ is assumed, which depends on the considered atom. For the noble gases usually employed in HHG experiments this gives a limit of $\omega_f < 10^{16}$ rad/s, which falls far into the ultraviolet region of the spectrum. Therefore this condition is generally achieved by the laser sources commonly used in laboratories.

Other limitations to the applicability of Keldysh theory are then imposed by the fact that the interaction Hamiltonian is treated in dipole approximation. This implies that the spatial variations of the fields must be small compared to the average radius of the atom:

$$\mathbf{k}\cdot\mathbf{r} \ll 1 \Rightarrow \omega_f << \frac{c}{r_{atm}} \approx 10^{18}\ \frac{\text{rad}}{\text{s}}$$

which gives another upper frequency limit. However, since this is higher that the previous one, it is generally not important. At the same time, for the dipole approximation to hold, also the displacement felt by the electron due to the magnetic field must be small when compared to the average atomic radius[16], otherwise higher orders in the multipole expansion of the interaction must be considered[1]. If we assume that the electric field is polarized along **z** and the magnetic field along **y**, the motion of a free electron is defined by the following set of equations:

$$m_e\frac{\mathrm{d}V_z}{\mathrm{d}t} = -eE_f\cos\left(\omega_f t\right) \rightarrow V_z\left(t\right) = -\frac{eE_f}{m_e\omega_f}\sin\left(\omega t\right)$$

$$m_e\frac{\mathrm{d}V_z}{\mathrm{d}t} = eV_xB_f cos\left(\omega_f t\right) \rightarrow x\left(t\right) = \frac{e^2I_f}{4m_e^2c^2\varepsilon_0\omega_f^3}\left[2\omega_f t + \sin\left(2\omega_f t\right)\right]$$

[1]This must not be confused with the non relativistic approximation, which is always assumed in this thesis. Indeed the relativistic effects scale as the Lorentz factor $\gamma_L \approx 1 + (v/c)^2 + ...$ while the effects given by the magnetic field to the particle motion scale as $B/E \approx (v/c)$ and may therefore play a role even in non-relativistic regime.

Note that the magnetic force acting on **z** due to the electron motion along **x** has been neglected in the first order solution, which is a good approximation when the magnetic field is small. Thus this sets a lower frequency limit to the dipole approximation, which is intensity dependent:

$$\omega_f^3 > \frac{I_f e^2}{4m_e^2 \epsilon_0 c^2 r_{atm}} \approx 1.1 \cdot 10^{26} \ \frac{\text{rad}^3\text{m}^2}{\text{s}^3\text{W}} \cdot I_f$$

where I_f is the intensity of the incoming field, ϵ_0 the vacuum permittivity, e and m_e the electron charge and mass respectively and c the speed of light in the vacuum. Considering the intensities usually employed in HHG experiments, which are on the order of 10^{14} W/cm^2, this would give a limit of around $4.7 \cdot 10^{14}$ rad/s, corresponding to a wavelength of almost 4 µm. Although this is far bigger than the ones employed in this thesis, such limit should be taken into account carefully when the driving wavelength is extended in the MIR region.

Within this limits, Keldysh proposed to describe the ionization of atoms using a perturbative approach as the transition rate between the electronic ground state Ψ_g and the final continuum state Ψ_c, computed using SFA:

$$W \propto \left| \langle \Psi_c | \mathbf{E}_f \cdot \mathbf{r} | \Psi_g \rangle \right|^2$$

By directly solving the Schrödinger equation such final states are found to be a continuum and so an integral over all the possible transitions should be in principle considered. The resulting expressions are rather complex and they will not be covered here in details.

Anyway one of the most important results of Keldysh theory is the introduction of a simple parameter:

$$\gamma = \sqrt{\frac{I_p}{2U_p}}$$

with I_p the atomic ionization potential and U_p the field ponderomotive energy. This allows to easily distinguish between two distinct regimes of photoionization. When $\gamma \ll 1$ Keldysh asserted that the process could be interpreted as the quasi-static tunnelling of the electron through the atomic potential barrier bent by the external field (*tunnelling ionization*, TI). On the other hand, when $\gamma \gg 1$ a better interpretation could be provided by a vertical transition triggered by the simultaneous absorption of multiple photons (*multiphoton ionization*, MPI). Indeed, the Keldysh parameter can be thought as the ratio between the tunnelling time of the electron and the period of the driving field. If the former is bigger, than the electron has not enough time to travel through the barrier before the external field reverses its sign and so the spatial directionality of the suppression, thus MPI is favourable. Instead, when the latter is bigger the particle experiences an almost static potential barrier and therefore TI can take place with high probability. Considering the intensities and frequencies used in HHG, which are respectively around 10^{14} W/cm^2 and the MIR region, it is easy to prove that $\gamma \leq 1$ and therefore it is usually assumed that the tunnelling description of the ionization process is the more accurate one. However

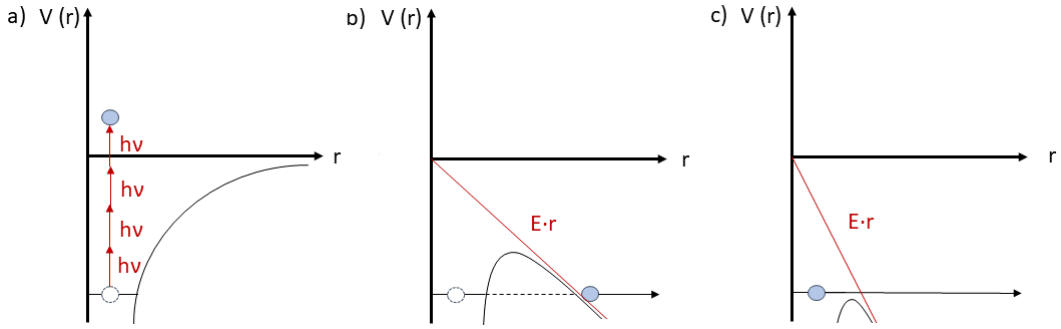

Figure 1.3: The three main mechanisms of strong field ionization of atoms are sketched. In a) MPI, in which a vertical transition is given by the absorption of multiple photons; in b) TI, in which the electron tunnels through the potential barrier bent by the external field; in c) OBI, in which it can classically escape the atom.

it is important to underline that these are only two physical pictures which may accurately describe atomic photoionization only when the Keldysh parameter is far from unity, while in principle both processes are always present during the interaction.

A third regime, which is called *over the barrier ionization* (OBI), is then reached when the effective atomic Coulomb potential felt by the electron falls below I_p due to the bending given by the external field. In this way the particle sees no barrier at all and can classically escape the atomic electric field. Such regime can be present at any frequency of the driving pulse and the only condition that applies in this case is regarding the external field strength. This can be easily derived setting the maximum of the overall potential felt by the electron equal to I_p:

$$E_{\mathrm{OBI}} = I_p^2 \frac{\pi \varepsilon_0}{Z_{\mathrm{res}} e^3} \rightarrow I_{\mathrm{OBI}} = I_p^4 \frac{c \pi^2 \epsilon_0^3}{2 Z_{\mathrm{res}}^2 e^6}$$

where Z_{res} is the residual charge left on the ion after the electron escapes. As an important example, for noble gases the intensities that trigger OBI are on the order of $10^{14 \div 15}$ W/cm^2. Therefore the limit for OBI may be reached in HHG experiments and this process generally coexist with TI. However, due to the induced high ionization, the areas where OBI takes place usually do not contribute to the final harmonic spectrum[2]. Anyway, in experiments it is difficult to achieve both conditions $\gamma << 1$ and $E_f << E_{\mathrm{OBI}}$ when fields in the visible or near IR are employed and this is one of the reason why sources in the MIR region of are generally preferred.

Another important caution in the use of the Keldysh parameter is then related to the tunnell ionization, as exposed in [17]. The limit of $\gamma \rightarrow 0$ is usually considered as

[2]This is due both to the rapid depletion of the single atom ground state and to the impossibility to reach good phase matching conditions in extended media.

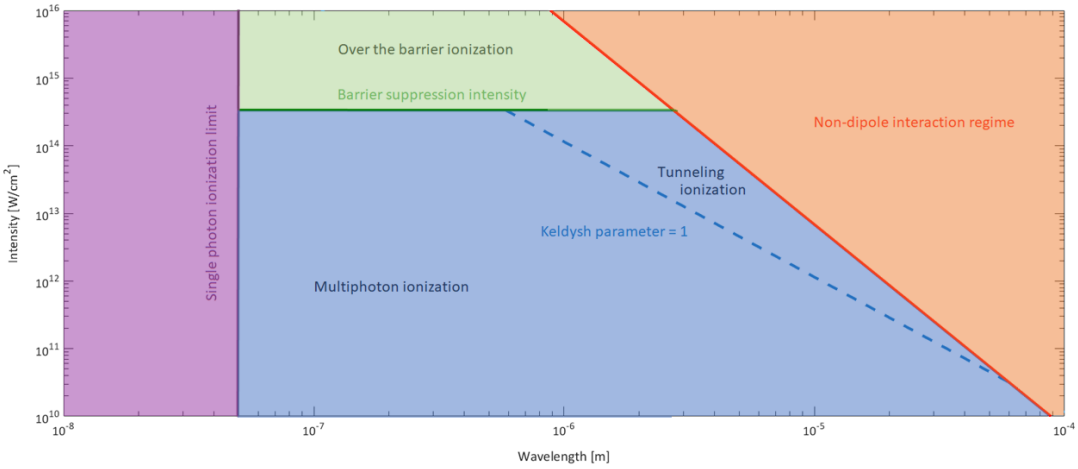

Figure 1.4: Regimes of the Keldysh theory in the case of Ar atoms ($I_p = 15.76$ eV). The blue shaded area gives the limits of validity of the theory, while the dotted line is $\gamma = 1$. The x-axis is given in wavelengths for the ease of the reader.

approaching more and more the TI regime. However as can be seen from Figure 1.4 this is not strictly true. Indeed when we move to lower values of γ, both increasing λ_f or I_f, we also start entering the non-dipole interaction regime, where the theories here presented don't strictly hold anymore. Therefore great attention must be used when handling the limit of very small values of γ.

Anyway, since the purpose of this thesis is the study of the HHG process, we will now on focus more deeply on the TI regime. Simplified theories are available in this limit, which treat the problem directly as a tunnelling process. These so called *tunnelling formulae* allow to greatly ease the computation of ionization rates and therefore are sometimes used also in regions where γ is not much lower than unity. The first attempt to describe TI with this approach was performed by L.D. Landau and E.M. Lifshitz [18] in 1981 for an hydrogen atom in a static electric field. Using parabolic coordinates to simplify the problem and WKB approximation they calculated a ionization rate of:

$$W_{\mathrm{LL}}(E) = \frac{8E_{\mathrm{H}}}{E}\left(\frac{I_p^{\mathrm{H}}}{\hbar}\right)\exp\left(-\frac{2E_{\mathrm{H}}}{3E}\right) \tag{1.1}$$

where E_{H} and I_p^{H} are respectively the atomic field felt by the electron and the ionization potential of hydrogen. This result holds in the quasi-classical approximation, for which $E \ll E_{\mathrm{H}}$ and the barrier penetration is rather small. The exponential factor in the rate is a typical feature of tunnelling processes and is common to all tunnel ionization formulae. The extension of this theory to time dependant fields was then done by A.M. Perelomov, V.S. Popov and M.V. Ter'entev [19, 20, 21], assuming a short-range potential for the generic atom and a long-range Coulomb interaction as first-order correction in the quasi classical action of the freed electron. The so called PPT theory gives actually a very general expression, which can be used also for values of the Keldysh parameter outside the limit of the tunnelling

regime, but we will here present only the case $\gamma \ll 1$. The result for the ionization rate of a Rydberg atom in a static electric field from an energy level described by the quantum numbers (n, l, m) can be written as:

$$W_{\text{stat}}(E) = \omega_p \left|C_{nl}\right|^2 A(l,m) \left(\frac{4\omega_p}{\omega_t}\right)^{2n-|m|-1} \exp\left(-\frac{4\omega_p}{3\omega t}\right) \tag{1.2}$$

where the coefficients are $\left|C_{nl}\right|^2 = 2^{2n}/n\Gamma(n+l+1)\Gamma(n-l)$ and $A(l,m) = [(2l+1)(l+|m|)!]/[2^{|m|}|m|!(l-|m|)!]$, the frequency linked to the ionization potential is $\omega_p = I_p^n/\hbar$ and the tunnelling frequency is $\omega_t = eE/\sqrt{2m_e I_p^n}$. In this formula $I_p^n = I_p^{\text{H}}(Z_{\text{res}}/n)^2$ is the effective ionization potential while $\Gamma(\cdot)$ is the Euler's gamma function. For the ground state of a more general atom we should then substitute the quantum numbers n and l with the effective ones $n^* = Z_{\text{res}}\sqrt{(I_p^{\text{H}}/I_p^n)}$ and $l^* = n^* - 1$, both in $\left|C_{nl}\right|$ and in the exponential, but not in $A(l,m)$. Then, for a time dependant field, the amplitude in Eq.(1.2) is substituted with its instantaneous value and an average over one optical cycle is computed:

$$W_{\text{PPT}}(E_f) = \sqrt{\frac{3E_f}{\pi E_{n^*}}} W_{\text{stat}}(E_f) \tag{1.3}$$

where E_f is the amplitude of the oscillating field and $E_n = E_{\text{H}}(Z_{\text{res}}/n)^3$ is the effective binding field felt by the electron in its ground state.

A further simplification of this expression was then given by M.V. Ammosov, N.B. Delone and V.P. Krainov considering the limit for which $n^* \gg 1$ and the Stirling approximation for the Euler's gamma function:

$$C_{n^*l^*,\text{ADK}} = \left(\frac{4\text{e}^2}{n^{*2}-l^{*2}}\right)^{n^*} \left(\frac{n^*+l^*}{n^*-l^*}\right)^{l^*+1/2} \left(\frac{1}{2\pi n^*}\right) \tag{1.4}$$

with e the Euler constant. Inserting Eq.(1.4) in Eq. (1.3) we obtain the ADK expression for the tunnel ionization of atoms in intense laser fields, which is probably the most used formula due to its relative simplicity. However, owing to the many approximation we had to assume in its derivation, many authors doubt the accuracy of this result. In particular F.A. Ilkov asserted that the use of the ADK rate should be limited to values of $\gamma < 1/2$ [22].

It is important to underline the fact that the presented tunnelling formulae were obtained by means of an optical cycle averaging in a perfectly monochromatic field. Therefore in the case of short pulses they don't give a correct evaluation of the ionization rate, since the electric field varies heavily under the envelope. A more correct approach would be in this case to use the so called adiabatic approximation and consider the static expression of Eq.(1.2) point by point in time. We should also underline the fact that in the case of few cycle pulses the Keldysh parameter is a function of time $\gamma(t)$ and therefore it is no more simple to distinguish between the various ionization regimes.

1.1.2 Propagation

After ionization, the freed electron according to SFA is subjected to the external electric field only. Its motion can thus be treated classically with the Newton equation for a point charge in a linearly polarized monochromatic plane wave. The choice of this kind of polarization is consistent with the experimental practice and will be justified better in Section 1.1.3:

$$m_e \ddot{z}(t) = -eE_f \cos(\omega_f t)$$

where **z** is assumed to be the polarization direction of the driving field. This equation can be solved easily once the initial conditions at the ionization time t' are known. Since we are considering the TI limit, the electron kinetic energy after leaving the atom may be approximated to be almost null and therefore we can set:

$$z(t') = 0 \qquad\qquad v_z(t') = 0$$

assuming for simplicity the atom initially in the origin of the axis. This allows to retrieve the expressions for the electron velocity and displacement in the continuum:

$$z(t) = \frac{eE_f}{m_e \omega_f^2}\left[\cos(\omega_f t) - \cos(\omega_f t') + \sin(\omega_f t')(t - t')\omega_f\right] \tag{1.5}$$

$$v_z(t) = -\frac{eE_f}{m_e \omega_f}\left[\sin(\omega_f t) - \sin(\omega_f t')\right] \tag{1.6}$$

The electrons will therefore follow different trajectories depending on the ionization phase $\phi' = \omega_f t'$ at which the atom undergoes ionization. As an example, in Figure 1.5 some of the possible electron trajectories are represented during the two optical cycles of the driving field after ionization as a function of ϕ'. In particular, for intensities around 10^{14} W/cm^2 and a driving wavelength of 800 nm, which are the usual conditions of HHG experiments, the maximum excursion of the electron is in the order of tens of nanometers. This a posteriori justifies the SFA assumption of neglecting the atomic potential to describe its motion. Moreover, as can be seen from the figure, electrons freed at two ionization phases separated by π experience exactly the same trajectory in space, but with opposite directions with respect to the polarization axis of the driving field.

Regarding the electron energy in the continuum, it can be easily derived from Eq.(1.6) as in the framework of the SFA it consists of only its kinetic contribution:

$$\mathcal{E}_k(t) = \frac{e^2 E_f^2}{2m_e^2 \omega_f^2}\left[\sin(\omega_f t) - \sin(\omega_f t')\right]^2 = 2U_p\left[\sin(\omega_f t) - \sin(\omega_f t')\right]^2 \tag{1.7}$$

Therefore also the kinetic energy is the same for electrons released at ionization phases separated by π, as they have the same velocity up to the sign. In Figure 1.6 the energy of the released electrons is plotted in the two optical cycles after ionization, normalized to the ponderomotive energy of the driving field. From the figure it is possible to observe that every electron posses zero energy at the end of each optical cycle after ionization and that the maximum energy which can be attained in the continuum is $8U_p$, for a ionization phase of $\phi' \approx 0.061$ and after an accumulated phase of π in the external field.

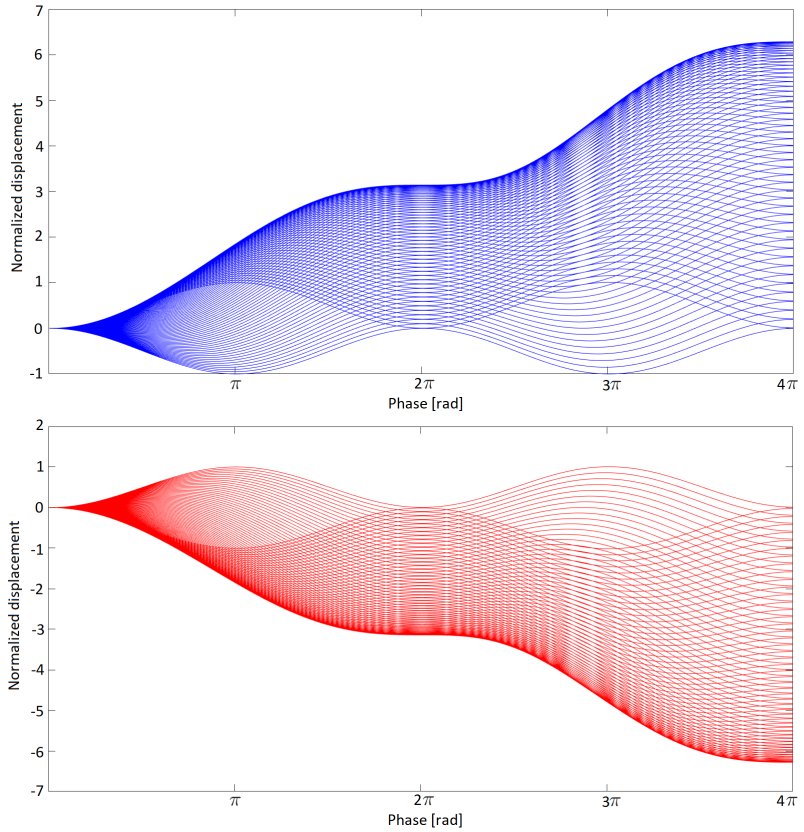

Figure 1.5: Classical trajectories of the electron for various ionization phases as calculated from Eq.(1.5). The blue ones correspond to a ionization phase in the range $\phi' \in \{0, \pi\}$ while the red ones correspond to a ionization phase in the range $\phi' \in \{\pi, 2\pi\}$. One hundred trajectories were computed for each range.

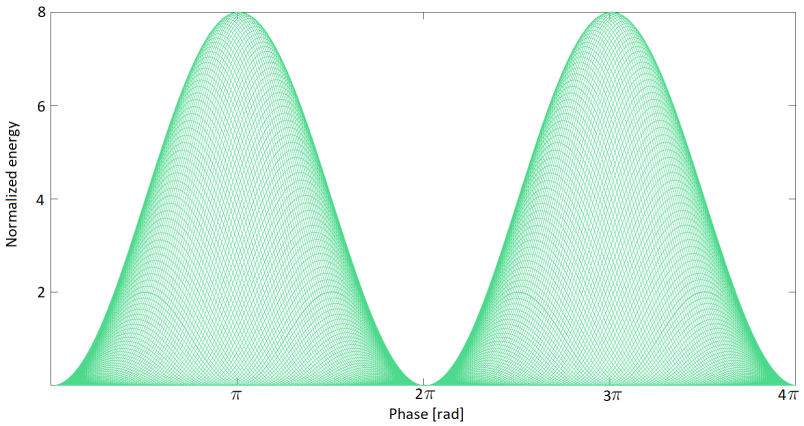

Figure 1.6: Energies of the electron for various ionization phases as calculated from Eq.(1.7), with ionization phases in the range $\phi' \in \{0, \pi\}$. One hundred trajectories were computed.

1.1.3 Recombination

During their motion some of the electrons may be driven back to their parent ions. In this case they have some probability to recombine to the state from which they were ionized, releasing in the process a photon of energy

$$\omega = \frac{1}{\hbar}\Big(I_p + \mathcal{E}_k\left(t\right)\Big)$$

where t is the recombination time at which the emission is evaluated. This can be found from Eq.(1.5) by setting the particle displacement to zero:

$$\cos\left(\omega_f t\right) - \cos\left(\omega_f t'\right) + \sin\left(\omega_f t'\right)\left(t - t'\right)\omega_f = 0 \tag{1.8}$$

Therefore solving Eq.(1.8) the trajectories $(t';t)$ which contribute to the emission of radiation can be studied. Generally three possible behaviours are identified depending on the ionization phase: none, only one or multiple recollisions with the parent ion. Usually the assumption is made that only the electrons recombining within the first optical cycle after ionization contribute to the emission of radiation and in the case of multiple recombination times only the first one is considered. This is due to the fact that the particles which undergo longer trajectories in the continuum have lower probability to recombine with their parent ion. However only the quantum treatment of Section 1.2 can rigorously justify this assumption, since its explanation involves the spreading in space of the electron wavefunction.

Anyway Eq.(1.8), being transcendental, doesn't have a simple closed-form solution. One possibility is to solve it numerically and to try to fit the result with some analytical function. This has the advantage to give a simple expression for the recombination phase ϕ of the electron, which can be used to further study the process [23]:

$$\omega_f t \equiv \phi \approx \frac{\pi}{2} - 3\sin^{-1}\Big(\frac{2}{\pi}\phi' - 1\Big)$$

Since it is possible to show that the only electrons which can recombine with their parent ion within one optical cycle are the ones with ionization phase in the ranges $\phi' \in \{0, \pi/2\}$ and $\phi' \in \{\pi, 3\pi/2\}$, we will from now on concentrate on these values of ϕ'. The result for the first of such ranges is shown in Figure 1.7.

The recombination of the electron is therefore concentrated in a time range that is approximately $\Delta t = 1.5\pi/\omega_f$, giving a rule of thumb for the possible duration of the subsequent XUV burst. In particular, considering a 800 nm driving field this gives an emission time of around 2 fs, which correspond to a pulse duration of some hundreds of as. This is however only a rough estimation and should not be taken as an exact value, since many other parameters may actually influence it. Another important information that can be taken from the figure is that the electrons escaping from the atom earlier are the ones that recombine lately in the following optical cycle, experiencing a longer time in the continuum. Therefore, due to the spreading of the electronic wavefunction they are expected to have a lower probability to recombine with the parent ion.

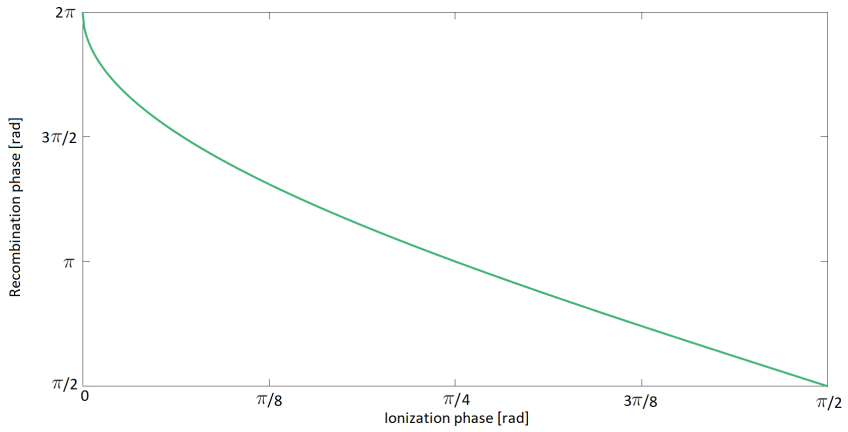

Figure 1.7: Fitting of the numerical solution of Eq. (1.8).

The numerical solution of Eq.(1.8) allows also to compute by substitution in Eq. (1.7) the energy of the electron upon recollision:

$$\mathcal{E}_k(t) = 2U_p\left[\sin(\omega_f t) - \sin(\omega_f t')\right]^2 \approx 2U_p\left[\cos\left(3\sin^{-1}\left(\frac{2}{\pi}\omega_f t' - 1\right)\right) - \sin(\omega_f t')\right]^2 \tag{1.9}$$

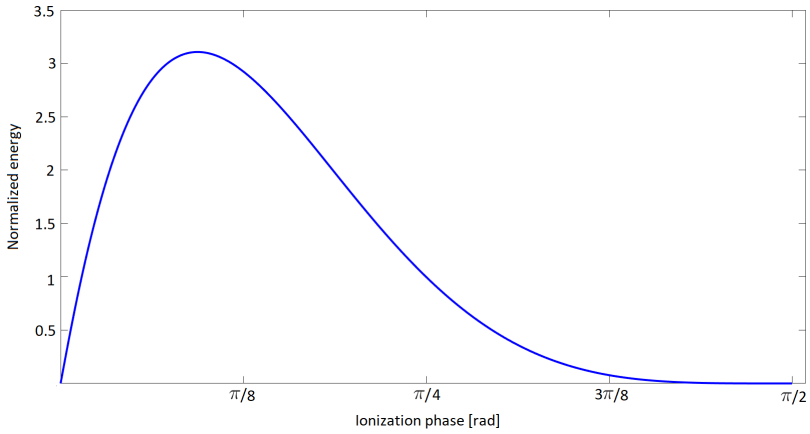

Figure 1.8: Recombination kinetic energy of the electron, as calculated from Eq.(1.9). The electron energy is normalized to the ponderomotive energy of the driving field.

The maximum emitted photon energy is thus given by the maximum of the recombining electron kinetic energy which is $E_{k,\max} \approx 3.17U_p$ for a ionization phase of $\phi' \approx 0.1\pi$ and a recombination phase of $\phi \approx 1.4\pi$. This allows to formulate the famous cutoff law for the single atom spectrum, which is one of the main success of the semiclassical model:

$$\hbar\omega_{\text{cutoff}} = I_p + 3.17U_p \tag{1.10}$$

Moreover the maximum in recollision energy of Eq.(1.19) marks a separation

between two classes of trajectories. Indeed for every given photon energy there are always two of them contributing to the emission, one with $\phi' \in \{0, 0.1\pi\}$ and the other one with $\phi' \in \{0.1\pi, \pi/2\}$. Since electrons with lower ionization phases experience a higher propagation in the continuum, these are called respectively long and short trajectories. Their contributions always coexist and converge near the cutoff, giving interfering contributions to the overall spectrum.

In many cases a higher cutoff frequency is desirable for extending the emitted spectrum to the near X-ray region. The expression of Eq.(1.10) suggests that this is possible both using atoms with higher ionization potentials or fields with higher ponderomotive energy. Due to the scaling of $U_p \propto I_f \lambda_f^2$ the latter can be achieved with higher-intensities or lower-frequencies driving pulses. However as exposed in Section 1.1.1 both this approaches have limitations linked to the presence of a higher ionization fraction and the magnetic field contribution. The latter in particular reduces the recombination probability due to the displacement of the electron in the direction perpendicular to the polarization axis of the driving field. Moreover, the scaling to longer wavelengths is not so favourable as the HHG yield is approximately proportional to $\lambda^{-5\div6}$ [24]. Out of it, a factor λ^{-2} is given by the redistribution of the harmonics over an extended cutoff for a fixed incoming energy, while the remaining λ^{-3} contribution is due to the higher spreading of the electron wavefunction in the continuum. For all these reasons MIR sources are frequently used in HHG experiments, since they represent a good compromise between an extended cutoff and a high yield. It is important to underline that this treatment strictly holds only for linearly polarized electric fields. Indeed the electron is driven back to its parent ion with lower efficiency for driving pulses of higher ellipticity and this ultimately justify the use of linearly polarized fields in HHG experiments.

The process described thus far takes place every half cycle of the driving field. In particular, since the ionization probability is highly dependent on the driving field intensity, being maximum on its peaks and zero on its nodes, the process results in the emission of a train of XUV pulses separated by the half of its period $T_f = 2\pi/\omega_f$. Moreover, due to the fact that the driving field changes sign every half cycle, subsequent bursts experience a π phase shift. In time the emitted field can thus be written as:

$$E_{xuv} = e_{xuv}(t) * \sum_{\mathrm{n}=-\infty}^{+\infty} \delta\Big(t - \frac{n\pi}{\omega_F}\Big) e^{in\pi}$$

where $e_{xuv}(t)$ represents the envelope in time of the single burst. The frequency spectrum of the emission will then be given by the Fourier transform of this expression:

$$\mathcal{F}\{E_{xuv}\}(\nu) = \nu_f \mathcal{F}\{e_{xuv}(t)\}\Big[\sum_{\mathrm{m}=-\infty}^{+\infty} \delta(\nu - m\nu_f) - \sum_{m=-\infty}^{+\infty} (-1)^m \delta(\nu - m\nu_f)\Big]$$

where $\nu_f = \omega_f/2\pi$ is the driving field frequency. Therefore for even values of m the terms of the two combs simplify while for odd values they sum up. This implies that in centrosymmetric targets, as the case of single atoms, only odd harmonics of

the fundamental frequency interfere constructively, while even ones are suppressed:

$$\mathcal{F}\{E_{xuv}\}(\nu) = 2\nu_f \mathcal{F}\{e_{xuv}(t)\} \sum_{\text{m=odd}} \delta(\nu - m\nu_f)$$

In order to obtain a more quantitative result for the emitted spectrum, one should then know the exact expression of $\mathcal{F}\{e_{xuv}(t)\}$, which cannot be found in the framework of the semiclassical model here presented. However this qualitative description is one of the main result of such simple theory.

Moreover, it is also possible to predict the presence of a chirp in the generated XUV pulses. From Figure 1.6 and Figure 1.7 it is indeed clear that the frequency of the emitted radiation varies with the recombination phase. In particulr, for the short trajectories photons of higher energies are emitted later in time and they thus show a positive chirp, while longer trajectories show a negative chirp. This so-called *attochirp* can be compensated, once only one of the two classes of trajectories is selected, in order to obtain pulses with duration down to tens of attoseconds [25].

1.2 Lewenstein model

In 1994 Lewenstein proposed the first fully quantum description of HHG from driving fields of arbitrary polarization [13]. Even though it is still in many ways an approximated treatment, this theory can overcome some of the main limitations of the semiclassical model, which are linked to the impossibility to get quantitative results for the emitted spectrum.

In principle, for studying the evolution of the harmonic fields one must know the atomic polarization that acts as the source term in Maxwell equations. This is proportional to the dipole moment induced on the single atom by the driving field:

$$\mathbf{P}(t) \propto \boldsymbol{\mu}(t) = -e\mathbf{r}(t)$$

where $\mathbf{r}$ gives the displacement of the negative charge from the positive nucleus, directed towards the former, and e is the modulus of the electronic charge. From a quantum point of view this must be evaluated as the expectation value of the relative operator over the state $|\Psi\rangle$ of the electron system:

$$\langle \mathbf{r}(t) \rangle = \langle \Psi | \mathbf{r}(t) | \Psi \rangle$$

Therefore to obtain the properties of the emitted radiation, we need to find the solutions of the corresponding time dependent Schrödinger equation (TDSE):

$$i\hbar \frac{\partial}{\partial t} |\Psi\rangle = \hat{H} |\Psi\rangle$$

where the Hamiltonian can be decomposed as $\hat{H} = \hat{H}_0 + \hat{H}_{\text{em}}$, with $\hat{H}_0$ the unperturbed atomic one and $\hat{H}_{\text{em}}$ the contribution given by the interaction with the external electromagnetic field. Although it might be possible to find numerically the solutions for such TDSE, in practice this is not trivial at all since the unperturbed Hamiltonian of a general atom can be quite complicated. Instead, the Lewenstein model allows to solve the equation analytically exploiting two main approximations: the SAEA and the SFA. Moreover an even simpler expression for the dipole moment can be retrieved under the so called *saddle point approximation* (SPA).

1.2.1 Single active electron and strong field approximations

The first source of complications in the TDSE is the unperturbed atomic Hamiltonian, which for multi electron atoms couples the motion of all the particle in the system. Indeed, for an N-electrons atom it is rigorously given by:

$$\hat{H}_0 = \sum_{\mathrm{i}=1}^{\mathrm{N}} \Big[-\frac{\hbar^2}{2m_i} \nabla_{r_i}^2 + V_{\text{nucl}}(r_i) + \sum_{\mathrm{i} \neq \mathrm{j}} V_{ij}(r_{ij}) \Big]$$

where the first and second term are respectively the kinetic and the Coulomb energy of each single electron in the field of the nucleus, while the last term represents the coupling between all electrons. For simplifying this expression the SAEA is assumed, for which only the most weakly bound electron is considered to take part

in the interaction with the external field. Moreover the field experienced by the single active electron in the atom is modelled with an effective Coulomb potential which eliminates the coupling between the multiple coordinates:

$$\hat{H}_0 = \left[-\frac{\hbar^2}{2m_e}\nabla_r^2 + V_{\text{eff}}(r_i) \right]$$

where $V_{\text{eff}}(r)$ is chosen to reproduce as accurately as possible the characteristics of the atom and in particular its ionization potential I_p. The discrete eigenstates of this Hamiltonian will define the energy levels allowed for the single electron inside the atom. A further simplification is then assumed, considering only the ground state of the electron to play a role in its interaction with the external field. This means that no resonance with excited atomic levels occurs in the process, which is a good approximation for $U_p \gg I_p$. Indeed only recently the role of excited states in high-order harmonic generation has started to be investigated [26]. Anyway, the resulting eigenstates of the unperturbed atomic Hamiltonian can be written as:

$$|\Psi_0\rangle = \exp\left\{ \frac{-iE_g}{\hbar}t \right\} |0\rangle = \exp\left\{ \frac{iI_p}{\hbar}t \right\} |0\rangle$$

with $|0\rangle$ the solution of the time independent Schrödinger equation for the electron system.

Regarding the interaction Hamiltonian $\hat{H}_{\text{em}}$ we can instead assume a description in terms of a pure dipole interaction, remembering however the limits that this assumption brings (see Section 1.1.1):

$$\hat{H}_{\text{em}} = e\mathbf{E}_f(t) \cdot \mathbf{r}(t)$$

In the framework of SFA the freed electron experiences only the external field and so the eigenstates in the continuum are the same of the pure interaction Hamiltonian. For simplicity these can be written as the superposition of plane-wave states of wave vector $\mathbf{k}$. Exploiting the δ-Dirac normalization, we can thus write:

$$|\mathbf{k}\rangle = \frac{1}{\sqrt{(2\pi)^3}} \exp\{i(\mathbf{k}\cdot\mathbf{r} - \omega_e t)\}$$

$$\mathbf{k} = \frac{m_e \mathbf{v}_e}{\hbar} \qquad \omega_e = \frac{m_e v_e^2}{2\hbar}$$

This model works well for harmonic orders near the cutoff, where the electrons have higher kinetic energies and therefore the plane wave description is more accurate, while it is not expected to describe efficiently the lower orders of harmonics. Under these assumptions the generic wavefunction can be written as:

$$|\Psi\rangle = e^{i\frac{I_p t}{\hbar}} \left[a(t)\ |0\rangle + \int b(\mathbf{k}, t)\ |\mathbf{k}\rangle\, d\mathbf{k} \right] \tag{1.11}$$

It is important to underline that his is however a rather huge approximation, since there is no rigorous proof that these states form a basis for the electron system.

In this frame work the expectation value of the displacement induced by the external field can therefore be divided in four parts:

$$\langle \mathbf{r}(t) \rangle = a^2(t)\ \langle 0|\,\mathbf{r}\,|0\rangle + \int a^*(t)\, b(\mathbf{k},t)\ \langle 0|\mathbf{r}|\mathbf{k}\rangle\, d\mathbf{k} + \int a(t)\, b^*(\mathbf{k},t)\ \langle \mathbf{k}|\mathbf{r}|0\rangle\, d\mathbf{k} + \\ + \int\int b(\mathbf{k},t)\, b^*(\mathbf{k'},t)\, \langle \mathbf{k'}|\,\mathbf{r}\,|\mathbf{k}\rangle\, d\mathbf{k} d\mathbf{k'}$$

where the last term represents the coupling between states in the continuum, while the first term is zero owing to the defined symmetry of the atomic ground state. The two in the middle, on the other hand, reflect the coupling between the continuum and the atomic ground state, which is the origin of the harmonic emission. Therefore the formers can be neglected and the expectation value of the electron dipole can finally be written as:

$$\langle \boldsymbol{\mu}(t) \rangle = 2e\,\mathrm{Re}\left\{ \int a^*(t)\, b(\mathbf{k},t)\ \langle 0|\mathbf{r}|\mathbf{k}\rangle\, d\mathbf{k} \right\} \tag{1.12}$$

From this expression it is possible to notice that the HHG signal is expected to be quenched when the atomic ground state is depleted and $a(t) \to 0$, which is not a priori visible in the semiclassical model. This shows that the oscillating dipole that generates the harmonics rises from the interference between the electronic ground state and the continuum wave packet, which is recombining to the atom. Since the value of $a(t)$, which represents the ground state population of the atom, may be in principle calculated using the ionization rates exposed in Section 1.1.1, the only unknown variable in the expression is $b(\mathbf{k},t)$, that describes the evolution of the electron wavepacket in the external field.

1.2.2 Saddle point approximation

In order to find the expression for $b(\mathbf{k},t)$ we should substitute Eq.(1.11) inside the TDSE. The derivation is rather complex and will be left in Appendix A. The final result is given as a function of the electron canonical momentum in the external field $\mathbf{p} = \hbar\mathbf{k} - e\mathbf{A}(t)$:

$$b(\mathbf{p},t) = -i\frac{e}{\hbar}\int_{-\infty}^{t} a(t')\mathbf{d}[\mathbf{p} + e\mathbf{A}_f(t')]\cdot\mathbf{E}_f(t')e^{-\frac{i}{\hbar}S(\mathbf{p},t,t')}dt' \tag{1.13}$$

where we have defined the dipole transition matrix element $\mathbf{d}(\mathbf{k}) = \langle \mathbf{k}|\,\mathbf{r}\,|0\rangle$, while in the exponential is present the quasi-classical action of the electron in the external field from the ionization time t' to the emission time t:

$$S(\mathbf{p},t,t') = \int_{t'}^{t}\left(I_p + \frac{[\mathbf{p} + e\mathbf{A}_f(t'')]^2}{2m_e}\right)dt''$$

which is defined as quasi-classical due to the presence of the additional term proportional to the atomic ionization potential. Therefore for obtaining the electric dipole we need to simply substitute this expression into Eq.(1.12):

$$\langle \boldsymbol{\mu}(t) \rangle = -i\frac{2e}{\hbar^4}\,\mathrm{Re}\left\{ \int d\mathbf{p}\int_{-\infty}^{t} dt' a^*(t)\mathbf{d}^*[\mathbf{p} + e\mathbf{A}_f(t)]a(t')\mathbf{d}[\mathbf{p} + e\mathbf{A}_f(t')]\cdot\mathbf{E}_f(t')e^{-\frac{i}{\hbar}S(\mathbf{p},t,t')} \right\} \tag{1.14}$$

where the dependence on the atomic Coulomb energy $V_{\text{eff}}(r)$ is no more present explicitly, but it is only implicit in the expression for $|0\rangle$. From this equation it is simple to recall the three steps of the semiclassical model:

I. $a(t')\mathbf{d}[\mathbf{p} + e\mathbf{A}_f(t')] \cdot \mathbf{E}_f(t')$ gives the probability of ionization at time t', linked to the dipole transition matrix from $|0\rangle$ to $|\mathbf{k}\rangle$ due to the interaction with the external field.

II. $exp\{-iS(\mathbf{p}, t, t')/\hbar)\}$ represents the phase accumulated by the electron owing to the propagation in the continuum between the ionization time t' and the emission time t. During its motion the electron changes its state from the initial one identified by $\mathbf{k} \propto \mathbf{p} - e\mathbf{A}(t')$ to the one identified by $\mathbf{k'} \propto \mathbf{p} - e\mathbf{A}(t)$, while maintaining constant its canonical momentum.

III. $a^*(t)\mathbf{d}^*[\mathbf{p} + e\mathbf{A}_f(t)]$ gives the probability of recombination at time t, linked to the dipole transition matrix from $|\mathbf{k}'\rangle$ to $|0\rangle$.

The main difference between this quantum model and the semiclassical one is that to determine the dipole at time t the contribution from all electron freed at times $t' \leq t$ is considered due to interference.

The direct integration of Eq.(1.14) is however still analytically impossible and thus the so-called *saddle point approximation* (SPA) is usually employed to further simply it. Indeed the exponential term of the quasi-classical action can be demonstrated to oscillate with respect to $\mathbf{p}$ much faster than the dipole transition matrix elements. In this way the integration over the canonical momentum of the electron can be considered to yield approximately zero apart from the regions where $S(\mathbf{p}, t, t')$ is stationary. These so-called saddle points are defined by the condition:

$$\boldsymbol{\nabla}_p S(\mathbf{p}, t, t')\Big|_{\mathbf{p}_{\text{sd}}} = \int_{t'}^{t} \frac{\mathbf{p}_{\text{sd}} + e\mathbf{A}_f(t'')}{m_e} dt'' = 0$$

where $\mathbf{p}_{\text{sd}}$, being a constant of motion of the electron, can be taken out from the integral:

$$\mathbf{p}_{\text{sd}}(t, t') = \frac{1}{(t - t')} \int_{t'}^{t} e\mathbf{A}_f(t'')dt''$$

This expression have the physical interpretation to require that the displacement of the electron between the ionization time t' and the recombination time t is zero. Being a definite integral, only one possible saddle point exists for every couple of ionization and recombination times $(t'; t)$. Therefore in Eq.(1.14) the dipole transition matrices can be evaluated at the saddle points and so they can be taken out from the integral in the momentum space:

$$\int d\mathbf{p} \int_{-\infty}^{t} dt' a^*(t)\mathbf{d}^*[\mathbf{p} + e\mathbf{A}_f(t)]a(t')\mathbf{d}[\mathbf{p} + e\mathbf{A}_f(t')] \cdot \mathbf{E}_f(t')e^{-\frac{i}{\hbar}S(\mathbf{p},t,t')} \approx$$

$$\int_{-\infty}^{t} dt' a^*(t)\mathbf{d}^*[\mathbf{p}_{\text{sd}} + e\mathbf{A}_f(t)]a(t')\mathbf{d}[\mathbf{p}_{\text{sd}} + e\mathbf{A}_f(t')] \cdot \mathbf{E}_f(t') \int d\mathbf{p} e^{-\frac{i}{\hbar}S(\mathbf{p},t,t')}$$

The quasi-classical action can then be approximated with a Taylor series around these saddle points:

$$S(\mathbf{p},t,t') \approx S(\mathbf{p}_{\mathrm{sd}},t,t') + \frac{1}{2}(\mathbf{p}-\mathbf{p}_{\mathrm{sd}})\cdot\mathcal{H}(\mathbf{p}_{\mathrm{sd}},t,t')\cdot(\mathbf{p}-\mathbf{p}_{\mathrm{sd}})$$

where $\mathcal{H}(\mathbf{p}_{\mathrm{sd}},t,t')$ is the relative Hessian matrix. In this way, the integral in the momentum space can be further reduced, as it can be demonstrated that:

$$\int d\mathbf{p} e^{-\frac{i}{\hbar}S(\mathbf{p},t,t')} \approx e^{-\frac{i}{\hbar}S(\mathbf{p}_{\mathrm{sd}},t,t')}\int d\mathbf{p} e^{-\frac{i}{2\hbar}(\mathbf{p}-\mathbf{p}_{\mathrm{sd}})\cdot\mathcal{H}\cdot(\mathbf{p}-\mathbf{p}_{\mathrm{sd}})} = \Big(\frac{\pi\hbar m_e}{i(t-t')/2}\Big)^{3/2} e^{-\frac{i}{\hbar}S(\mathbf{p}_{\mathrm{sp}},t,t')}$$

The denominator is proportional to the time spent by the electron in the continuum $(t-t')$ and thus the longer the particle moves in the external field the lower is its contribution to the final dipole due to quantum diffusion. This is one of the aspects that the semiclassical model was not able to describe, while it is obtained naturally in this quantum treatment. Moreover, since for $t = t'$ this expression would diverge, which is unphysical, a small empiric regularization constant α is added in the denominator for avoiding it. It is important to underline that the presence of such singularity means that the SPA cannot accurately describe trajectories for which $t \to t'$.

By substitution in Eq.(1.14) we finally retrieve the equation for the electron dipole moment in the framework of SPA for the canonical momentum:

$$\langle\boldsymbol{\mu}(t)\rangle = -i\frac{2e}{\hbar^4}\,\mathrm{Re}\Big\{\int_{-\infty}^{t} dt' a^*(t)\mathbf{d}^*_{\mathrm{PR}}a(t')\Big(\frac{\pi\hbar m_e}{\alpha+i(t-t')/2}\Big)^{3/2}\mathbf{d}_{\mathrm{PI}}\cdot\mathbf{E}_f(t')e^{-\frac{i}{\hbar}S(\mathbf{p}_{\mathrm{sd}},t,t')}\Big\} \tag{1.15}$$

where for simplicity in the notation we have called $\mathbf{d}^*_{\mathrm{PR}} = \mathbf{d}^*[\mathbf{p}_{\mathrm{sd}} + e\mathbf{A}_f(t)]$ the dipole matrix element representing photo recombination and $\mathbf{d}_{\mathrm{PI}} = \mathbf{d}[\mathbf{p}_{\mathrm{sd}} + e\mathbf{A}_f(t')]$ the one describing photoionization. The response of the single atom to the external field can thus be computed once the quasi-classical action and the dipole transition matrix elements are known.

1.2.3 High harmonic spectrum

The Lewenstein model in the framework of the SPA for the canonical momentum allowed to retrieve Eq.(1.15), which is a very general expression for the dipole moment of an atom in a high-intensity laser field. Once this is known the emitted radiation can be described in time using Larmor formula:

$$P(t) = \frac{|\langle\ddot{\boldsymbol{\mu}}(t)\rangle|^2}{6\pi\epsilon_0 c^3}$$

where the classical dipole acceleration is formally replaced by its expectation value. The power spectrum of the XUV field can instead be calculated through a simple Fourier transform:

$$P(\omega) \propto \omega^4\mathcal{F}\{|\langle\boldsymbol{\mu}\rangle|\}^2$$

where:

$$\mathcal{F}\{|\langle\boldsymbol{\mu}\rangle|\} = \int_{-\infty}^{+\infty} dt|\langle\boldsymbol{\mu}(t)\rangle|e^{i\omega t}$$

In order to solve the integration in t and t' it is then possible expand the procedure of SPA also to these coordinates. This will not be covered extensively here, but only the most important results of such approach are presented. In particular, the new saddle point conditions have nice physical interpretations:

I. After ionization the kinetic energy of the electron is equal to $-I_p$. This is a consequence of the quantum nature of the tunnel ionization process:

$$\left.\frac{\partial S}{\partial t'}\right|_{t'_{\mathrm{sd}}} = 0 \rightarrow \frac{[\mathbf{p}_{\mathrm{s}} + e\mathbf{A}_f(t'_{\mathrm{sd}})]^2}{2m_e} + I_p = 0$$

Since $I_p > 0$ this equation can be satisfied only by complex values for the velocity and ionization time. In particular, the higher is the ionization potential the higher is the imaginary part of t'_{sd} and the lower is the ionization probability of the atom.

II. Energy is conserved upon recombination:

$$\left.\frac{\partial S}{\partial t}\right|_{t_{\mathrm{sp}}} = 0 \rightarrow \frac{[\mathbf{p}_s + e\mathbf{A}_f(t_{\mathrm{sd}})]^2}{2m_e} + I_p = \hbar\omega_q$$

where $\hbar\omega_q$ is the energy of the emitted XUV photon. This condition selects the trajectories that can contribute to the spectrum.

Within this approach it can also be demonstrated that the saddle point solutions found for each frequency of the high harmonic spectrum are related to the semiclassical long and short trajectories. These two contributions have similar strength in the plateau region, while approaching the cutoff from lower energies the long trajectories become more relevant. The most important difference between the quantum result and the semiclassical one is that in this case the trajectories whose coherent superposition gives the harmonic spectrum are intrinsically complex. Moreover, if only the semiclassical quantum paths are considered, the spectral amplitude of the q^{th} harmonic can be written as [28, 29]:

$$\mu_q = \sum_{\mathrm{n}} A_{\mathrm{n}}(q, I) e^{i\Phi_{\mathrm{n}}(q,I)} \tag{1.16}$$

where the sum over n identifies short and long trajectories. The dipole amplitude A_{n} in the plateau region is only weakly dependant on the harmonic order, while the phase Φ_{n} can change highly with respect to it. From the Lewenstein model we can also directly write out the expression for the latter:

$$\Phi_{\mathrm{n}}(q, I) = q\omega_f t - \frac{1}{\hbar} S(\mathbf{p}, t, t')$$

with the first term that depends simply on the semiclassical recombination time and the second that describes the phase acquired from the electron propagation in the continuum. This last contribution is particularly interesting since its dependence on the driving intensity is an effect that is not present in lower order nonlinear

optics. In the particular case of a linearly polarized driving field, it is possible to demonstrate that:

$$\Phi_{\mathrm{n}}(q, I) \approx \alpha_0(q, \mathrm{n}) + \alpha(q, \mathrm{n}) I_f \tag{1.17}$$

with both constants depending on the considered harmonic order and trajectory. More precisely α is always negative and its modulus is usually one order of magnitude bigger for the long trajectories with respect to the short ones. This is a fundamental difference that plays a big role in defining the characteristics of the harmonic radiation [30].

Moreover, when dealing with monochromatic driving field, also an expression for the cutoff energy can be found by solving the saddle point equations:

$$\hbar\omega_{\mathrm{cutoff}} = f(\frac{I_p}{U_p}) I_p + 3.17 U_p \tag{1.18}$$

which is equal to the semiclassical result up to a slight correction due to the contribution of quantum diffusion and quantum interference. Indeed $f(I_p/U_p) \approx 1.32$ for $I_p \ll U_p$ and it decreases with increasing ionization potentials, approaching the semiclassical limit $f(I_p/U_p) \approx 1$. However, differently from the semiclassical case, this does not imply a sharp cutoff but an exponential decrease in the power spectrum. Anyway, such expression holds only as long as we do not have any depletion of the atomic ground state. Indeed, when the driving laser intensity becomes higher than the so called saturation intensity I_s for which $a(t) \approx 0$, the HHG process is suppressed. This is due to the fact that the dipole moment of Eq.(1.15) is quenched and XUV emission from ions is not favourable as ionization defocusing of the driving pulse is too high [31]. In this case the spectral extension is limited by I_s and the cutoff law becomes independent on the driving intensity [33]:

$$\hbar\omega_{\mathrm{cutoff}} \approx I_p + 3.17 U_p(I_s)$$

For an efficient generation of XUV radiation it is thus important to avoid saturation even when high driving intensities are employed. To do so it is possible to use atoms of high ionization potentials, since it can be demonstrated that $I_s \propto I_p^3$, or driving pulses with very short duration, since it can also be demonstrated that $I_s \propto \ln(\Delta t_f)^{-1}$ [32]. For a fixed cutoff frequency, instead, the use of longer wavelengths allows to employ driving fields of lower intensity, as the ponderomotive energy increases.

1.3 Macroscopic effects

In the previous sections the theory of HHG from a single atom was treated. However in experiments we deal with extended media, in which both the driving and the harmonic fields propagate. The contributions of every single emitter need therefore to be summed up for getting the final macroscopic signal. In the case of a linearly polarized driving field interacting with a homogeneous and isotropic medium, the propagation of the fields can be studied with Helmholtz scalar equation:

$$\nabla_r^2 E(t,\mathbf{r}) - \frac{1}{c^2}\frac{\mathrm{d}^2}{\mathrm{d}t^2}E(t,\mathbf{r}) = \mu_0 \frac{\mathrm{d}^2}{\mathrm{d}t^2}P(t,\mathbf{r})$$

where the polarization of the medium can be written as a Taylor series of the electric field to account for its non linearities:

$$P(t,\mathbf{r}) = \epsilon_0[\chi^{(1)}E(t,\mathbf{r}) + \chi^{(2)}E^2(t,\mathbf{r}) + \chi^{(3)}E^3(t,\mathbf{r}) + ...]$$

Note that for very high-intensity fields this sum cannot be in principle truncated as the terms of the power series does not become negligible with increasing order. Moreover the electric field that needs to be consider in the propagation equation is given by both the fundamental and the harmonic radiation:

$$E(t,\mathbf{r}) = E_f(t,\mathbf{r}) + \sum_{\mathrm{q}}^{\mathrm{cutoff}} E_q(t,\mathbf{r})$$

where q is the harmonic order. For simplicity it is possible to rewrite Helmholtz equation in Fourier domain for getting rid of the temporal derivatives:

$$\nabla_r^2 E(\omega,\mathbf{r}) + \frac{\omega^2}{c^2}E(\omega,\mathbf{r}) = -\frac{\omega^2}{c^2}[\chi^{(1)}E(\omega,\mathbf{r}) + \chi^{(2)}E^2(\omega,\mathbf{r}) + \chi^{(3)}E^3(\omega,\mathbf{r}) + ...]$$

Since the nonlinear terms depend on the total electric field in the medium, this expression in principle defines a set of coupled differential equation for the individual harmonics. However it can be reduced considering that the efficiency of the HHG process is quite low, so that only the fundamental radiation is actually able to trigger a nonlinear response in the material, and assuming that the harmonic fields do not spectrally overlap, so that their interaction is negligible [34]. In this way the equations become decoupled for each field contribution:

$$\nabla_r^2 E_f(\omega,\mathbf{r}) + \frac{\omega^2}{c^2}n_f^2 E_f(\omega,\mathbf{r}) = -\mu_0\omega^2 P_f^{\mathrm{NL}}(E_f(\omega,\mathbf{r})) \tag{1.19}$$

$$\nabla_r^2 E_q(\omega,\mathbf{r}) + \frac{\omega^2}{c^2}n_q^2 E_q(\omega,\mathbf{r}) = -\mu_0\omega^2 P_q^{\mathrm{NL}}(E_f(\omega,\mathbf{r})) \tag{1.20}$$

where we have introduced the refractive index of the medium $n = \sqrt{1+\chi^{(1)}}$ and a term P^{NL} that resumes the nonlinear polarization induced by the driving field. The latter describes in the first equation the classical low order nonlinearities present during the propagation of the driving field, while in the second one it is linked

to the density of the atomic dipoles giving rise to the high harmonic fields in the material. Therefore in this framework the fundamental field propagates in the medium without any influence from the harmonics, while each harmonic is treated as a perturbation to the initial field. The solutions can thus be found by firstly computing the propagation of the unperturbed driving beam and then substituting it in the source term of the second equation. For this reason the solutions of such equations are highly dependent on the geometry of the system, which defines the propagation of the fundamental field. In the following sections we will present a simplified approach to this problem, renouncing to obtain the exact expression of the fields and focusing mainly on two features: the phase matching of the harmonic radiation and its absorption from the medium.

1.3.1 Plane wave geometry

Since the solution of the wave equation for the driving field depends on the geometry of the interaction, the simplest possible case we can consider is the one of perfectly plane waves. Even though strictly speaking this isn't a feasible condition in actual experiments, it can anyway give important insight on the problem and may be used as an approximation when dealing with more complex geometries. As it is known in nonlinear optics, the wave vector of P_q^{NL} acting as the source term for the q^{th} harmonic field will be equal to the one of the fundamental multiplied by q. Perfect phase matching is then achieved when this matches the one of the harmonic field E_q, satisfying in this way the momentum conservation for the photons. The emission from different single atoms in the material can thus efficiently sum up without getting out of phase, as sketched in Figure 1.9.

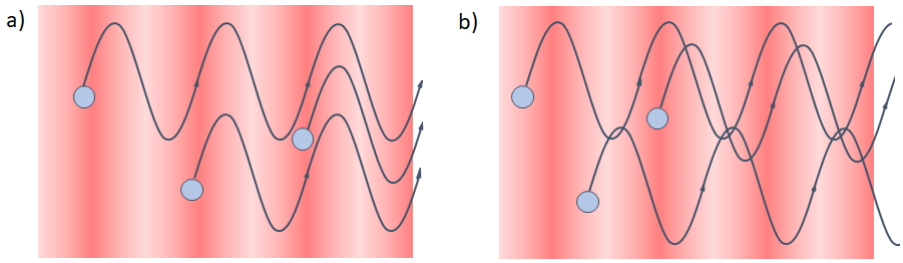

Figure 1.9: Sketch of the phase matching mechanism for plane waves. In a) the perfect phase matching case is represented, in which the emission of the single emitters adds up constructively. In b), instead, some phase mismatch is present and the fields interfere along the medium length.

For plane waves two contributions to the phase mismatch can be identified for each harmonic order [35]:

$$\Delta k_q = q k_f - k_q = \Delta k_{\mathrm{neutrals},q} + \Delta k_{\mathrm{plasma},q} \tag{1.21}$$

where the wave vectors are considered as scalar quantities along the optical axis **x** of the system. The first term is simply given by the different refractive indexes seen

by the waves due to the medium dispersion:

$$\Delta k_{\text{neutrals},q} = q n_f \frac{2\pi}{\lambda_f} - n_q \frac{2\pi}{\lambda_q} = q \frac{2\pi}{\lambda_f}(n_f - n_q)$$

Since the driving field is usually in the IR while the harmonics are in the XUV range, the refractive index needs to be evaluated in very different regions of the electromagnetic spectrum. In the first case it is usually possible to derive the refractive index theoretically, once the static atomic polarizability α_{atom} of the gas is known [36]:

$$n_{\text{IR}}(\lambda) = \sqrt{1+\chi^{(1)}(\lambda)} \approx 1 + \frac{1}{2}\chi^{(1)}(\lambda) = 1 + N_{\text{neutrals}} \frac{\alpha_{\text{atom}}}{2\varepsilon_0} = 1 + (1-\eta)N(\mathbf{r}) \frac{\alpha_{\text{atom}}}{2\varepsilon_0}$$

where η and $N(\mathbf{r})$ are respectively the ionization fraction and the atomic density of the medium. Note that the low order nonlinearities induced by the high-intensity driving field, such as Kerr effect, are not considered in this expression for the index of refraction. Indeed, as a matter of fact the direct contribution of such terms to phase matching is always very low for HHG in gases and this is usually a good approximation. However, it is important to underline that they may contribute to it indirectly, as they may alter the propagation of the fundamental beam and thus influence some of the parameters relevant to phase matching (e.g. the shape of the phase front of the driving pulse, its intensity, ...). On the other hand, in the XUV range of the spectrum the problem of evaluating the refractive index of atoms was undertaken by Henke *et al.* [37]. In this framework it is written as a function of the so-called atomic scattering factor $f = f_1 + i f_2$:

$$n_{\text{UV}}(\lambda) \approx 1 - \frac{r_e}{2\pi}\lambda^2 N_{\text{neutrals}} f_1 = 1 - \frac{r_e}{2\pi}\lambda^2 (1-\eta) N(\mathbf{r}) f_1$$

where $r_e = e^2/(4\pi\varepsilon_0 m_e c^2)$ is the classical electron radius and only the real part of f is considered, being the one linked to the medium dispersion. For the usual conditions explored in HHG experiments we have that $f_1 > 0$ and thus $n_{\text{UV}}(\lambda) < 1$. Therefore the contribution $\Delta k_{\text{neutrals}}$ of the neutral atoms to the phase mismatch is generally positive. This can be finally written making explicit the dependence on the neutrals density in the material:

$$\Delta k_{\text{neutrals},q} = q \frac{2\pi}{\lambda_f}(1-\eta) N(\mathbf{r}, P) \delta n_q \tag{1.22}$$

where $N(\mathbf{r}, P) = N_{\text{atm}} P / P_{\text{atm}}$ is the atomic density at pressure P and $\delta n_q = \alpha_{\text{atom}}/2\varepsilon_0 + r_e \lambda_q^2 f_1 / 2\pi$ is the difference in refractive index per unit atomic density between the fundamental and the q^{th} harmonic. The ionization fraction η can be calculated using one of the methods presented in Section 1.1.1, while the pressure is usually setted by the experimental conditions and can in principle be a function of the position in the system.

The second term in Eq.(1.21) is instead linked to the presence of free electrons in

the medium, owing to the unavoidable ionization linked to the HHG process. The index of refraction in a cold plasma is a well known quantity [39]:

$$n_{\text{plasma}}(\lambda) = \sqrt{1 - \left(\frac{\lambda}{\lambda_p}\right)^2}$$

$$\lambda_p = 2\pi c \sqrt{\frac{m_e \epsilon_0}{N_e e^2}}$$

with λ_p the so-called plasma wavelength, which is a function of the electron density in the material $N_e = \eta N(\mathbf{r}, P)$ in the approximation of only single-ionized atoms. The underdense plasma condition $\lambda_p << \lambda$ must be satisfied for light to travel efficiently in the medium. For noble gases and the usual parameters of high-order harmonic generation experiments this is always the case and so the expression can be simplified taking a Taylor expansion of the radical:

$$n_{\text{plasma}}(\lambda) \approx 1 - \frac{1}{2}\left(\frac{\lambda}{\lambda_p}\right)^2$$

Also in this case the dependence on the atomic density can then be made explicit for simplicity:

$$\Delta k_{\text{plasma}} = q r_e \lambda_f \eta N(\mathbf{r}, P)\left(\frac{1}{q^2} - 1\right) \tag{1.23}$$

Considering that $q > 0$, this contribution is always negative and thus opposes to the phase mismatch due to the neutrals.

Substituting Eq.(1.23) and Eq.(1.22) inside Eq.(1.21) the final expression for the phase mismatch in the plane wave interaction geometry is then obtained:

$$\Delta k_q = q\frac{2\pi}{\lambda_f} N(\mathbf{r}, P)\left[(1-\eta)\delta n_q + \frac{r_e}{2\pi}\lambda_f^2 \eta\left(\frac{1}{q^2} - 1\right)\right] \tag{1.24}$$

from which we can see that for every harmonic order q it is always present a ionization fraction allowing perfect phase matching, which is independent on the medium pressure:

$$\eta_q^{\text{PM}} = \frac{1}{1 - \frac{r_e \lambda_f^2}{2\pi\delta n_q}\left(\frac{1}{q^2} - 1\right)} \approx \frac{1}{1 + \frac{r_e \lambda_f^2}{2\pi\delta n_q}}$$

where $1/q^2$ can be approximated to zero for high orders of harmonics. This so-called critical ionization fraction is determined only by difference in the refractive index of the medium between the fundamental field and the considered q^{th} order. Since it depends on a single parameter, the phase matching window is thus usually very narrow. Moreover, as the refractive index in the XUV region is usually increasing with the wavelength, the critical ionization fraction is lower for higher harmonics, as can be seen from Figure 1.10.
For a fundamental field of wavelength $\lambda_f = 800$ nm the values of η_q^{PM} in noble gases are always lower than 10% . Since the higher order of harmonics are generated at

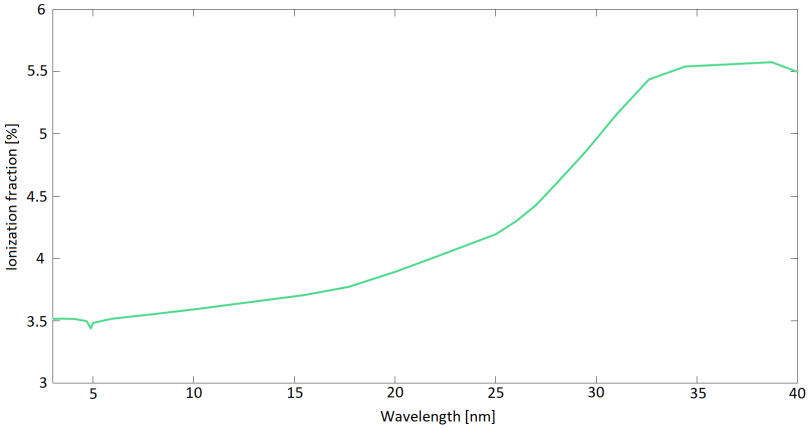

Figure 1.10: Ionization fraction allowing perfect phase matching in Ar for $\lambda_f = 800$ nm.

higher intensities, this means that for efficiently phase matching them the ionization fraction needs to be limited even at the peaks of the driving field. This issue is similar to the saturation of the single atom emission analysed in Section 1.2.3 and the parameters used to overcome it are quite alike, but it is important to underline that they are two different physical phenomena. In particular, phase matching issues are macroscopic effects that arise generally at lower ionization fractions with respect to the saturation of the single emitter.

For the plane wave interaction geometry we can also directly solve Eq.(1.20) quite easily, starting from the approximation of lossless medium. Setting the optical axis as **x**, the equation for the q^{th} harmonic field reads:

$$\frac{\partial^2}{\partial x^2} E_q + \frac{\omega_q^2}{c^2} n_q^2 E_q = -\mu_0 \omega_q^2 P_q^{\mathrm{NL}}(E_f)$$

which can be reduced inserting a plane wave behaviour as ansatz[3]:

$$E_q = \widetilde{E}_q(x) e^{-ik_q x} \qquad P_q^{\mathrm{NL}} = \widetilde{P}_q^{NL}(\widetilde{E}_f) e^{-iqk_f x}$$

Considering *paraxial approximation*, the small $\partial^2 \tilde{E}_q / \partial x^2$ term can be neglected and the final expression for the harmonic field equation is obtained:

$$\frac{\partial}{\partial x} \widetilde{E}_q(x) = -i \frac{\mu_0 \omega_q^2}{2k_q} \widetilde{P}_q^{\mathrm{NL}}(\widetilde{E}_f) e^{-i\Delta k_q x}$$

which depends explicitly on the phase mismatch. In the important case of Δk_q independent from **x** this can be solved quite simply[4] for a medium of length L. Indeed, as the driving field is approximately not depleted during propagation, the

[3]The solution of Eq.(1.19) is implicit in the plane wave assumption, when the nonlinear polarization of the medium at the fundamental frequency is neglected.

[4]For plane waves this essentially requires that the medium density is not changing along its length.

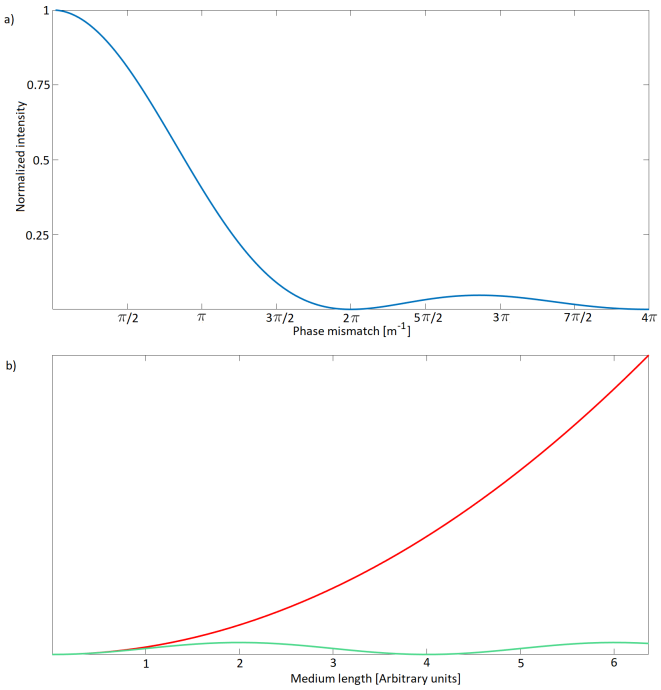

Figure 1.11: a) Intensity of the harmonic field after a medium of length $L = 1m$ as a function of the phase mismatch, normalized to its maximum. b) Intensity of the emitted harmonic as a function of the medium length. The red curve is drawn for $\Delta k_q = 0$ while the green one for $\Delta k_q \neq 0$.

amplitude of the non linear term can be considered as constant and the equation is integrated in a straightforward way:

$$\widetilde{E}_q = -i\frac{\mu_0\omega_q^2}{2k_q}\widetilde{P}_q^{\mathrm{NL}}\int_0^L e^{-i\Delta k_q x}dx = \frac{\mu_0\omega_q^2}{2k_q}\widetilde{P}_q^{\mathrm{NL}}\left(\frac{e^{-i\Delta k_q L}-1}{\Delta k_q}\right)$$

The corresponding intensity, replacing the non linear polarization amplitude with the number of dipole moments emitting the q^{th} harmonic per unit volume, reads:

$$I_q = \frac{1}{2}c\varepsilon_0\left(\frac{\mu_0\omega_q^2}{2k_q}\right)^2 \mid \boldsymbol{\mu}_q \mid^2 (1-\eta)^2(NL)^2\,\mathrm{sinc}^2\left(\frac{\Delta k_q L}{2}\right) \tag{1.25}$$

where we have used the definition $\mathrm{sinc}(x) = \sin(x)/x$ for the cardinal sine function. Therefore the harmonic intensity depends on the product between the medium length and the density of the emitters. This is a fingerprint of the coherence of the generation process, since we need to firstly add the single dipole amplitudes and then square them to obtain the intensity of the harmonic radiation, instead of directly summing their squared values [34]. One important quantity that can be defined for describing the macroscopic propagation of the harmonics is the so called coherence length:

$$L_{\mathrm{coh},q} = \frac{\pi}{\Delta k_q} \tag{1.26}$$

that is the length over which the q^{th} harmonic and the fundamental field acquire a phase difference of π and the intensity of the relative XUV field reaches a local maximum. Therefore it is a measurement of the quality of phase matching and as a rule of thumb the medium should not be longer that the coherence length for the frequency of interest, otherwise the build-up of the signal wouldn't be efficient due to the interference between radiation generated in different positions. In particular, for perfect phase matching $\Delta k_q = 0$ the coherence length diverges to infinity and the harmonic radiation adds up constructively over the whole medium, with an intensity that increases quadratically with its length.

In actual media, however, the absorption of the harmonics by the atoms cannot be neglected and so the contribution of such losses should be added explicitly. Indeed this is the main reason why HHG experiments are performed in vacuum, as the XUV absorption along propagation should be minimized. The equation for the harmonic fields in this case reads:

$$\frac{\partial}{\partial x}\widetilde{E}_q(x) = -i\frac{\mu_0\omega_q^2}{2k_q}\widetilde{P}_q^{\mathrm{NL}}(\widetilde{E}_f)e^{-i\Delta k_q x}e^{-\alpha_q x}$$

where the absorption coefficient is linked to the imaginary part of the index of refraction at the harmonic frequency $\alpha_q = k_q \,\mathrm{Im}\{n(\lambda_q)\}$ and thus to the atomic scattering factor f_2. Neglecting also in this case the depletion of the fundamental wave, the equation can be integrated to obtain the expression for the XUV field after a medium of length L:

$$\widetilde{E}_q = -i\frac{\mu_0\omega_q^2}{2k_q}\widetilde{P}_q^{\mathrm{NL}}\int_0^L e^{-i\Delta k_q x}e^{-\alpha_q x}dx = i\frac{\mu_0\omega_q^2}{2k_q}\widetilde{P}_q^{\mathrm{NL}}\Big(\frac{e^{-L(\alpha_q+i\Delta k_q)}-1}{\alpha_q+i\Delta k_q}\Big)$$

and therefore the harmonic intensity reads:

$$I_q = \frac{1}{2}c\epsilon_0\Big(\frac{\mu_0\omega_q^2}{2k_q}\Big)^2 \mid \boldsymbol{\mu}_q \mid^2 (1-\eta)^2N^2\Big(\frac{1+e^{-2\alpha_q L}-2e^{-\alpha_q L}cos(\Delta k_q L)}{\alpha_q^2+\Delta k_q^2}\Big) \tag{1.27}$$

When absorption is included, it is no more possible to establish a simple dependence on the material density-length product and the optimization of the photon flux with respect to the various parameters is not straightforward. Anyway, its ultimate effect is to set an asymptotic value for the harmonic intensity that cannot be exceeded. Therefore, it is possible to define another important parameter to characterize the macroscopic emission, which is the absorption length for the q^{th} harmonic:

$$L_{\mathrm{abs},q} = \frac{1}{2\alpha_q} \tag{1.28}$$

This is the distance over which the intensity of the harmonic radiation decreases of a factor e due to absorption when perfect phase matching is present. It is important to underline that its value depends only on the considered atom and harmonic order. A rule of thumb for maximizing the emission for a given harmonic in a lossy medium could be to have $L \approx L_{\mathrm{coh},q}$ and $L_{\mathrm{coh},q} >> L_{\mathrm{abs},q}$, while a more precise treatment of this issue was given in [40] where the conditions to reach at least half of the highest possible radiation output are setted:

$$L > 3L_{\mathrm{abs},q} \qquad L_{\mathrm{coh},q} > 5L_{\mathrm{abs},q} \tag{1.29}$$

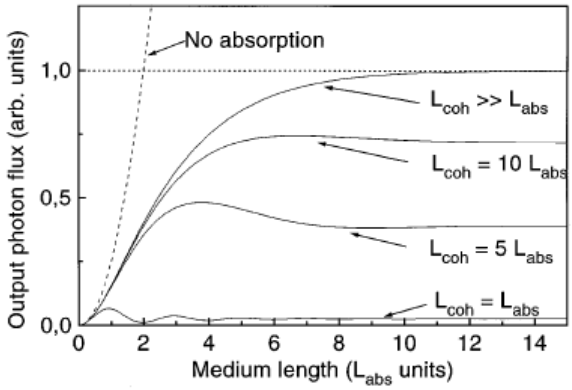

Figure 1.12: Behaviour of the harmonic signal in the presence of absorption as given in [40].

1.3.2 Tight focusing geometry

In actual experiments the driving field is generally focused in a small region in order to reach higher intensities and therefore higher orders of harmonics. In this case the gas is injected using a valve and freely diffuses in a vacuum chamber, thus ensuring the interaction to be spatially confined. The driving field in paraxial approximation and without the contribution of lower order nonlinearities can be well approximated with a fundamental TEM_{00} Gaussian beam. Exploiting the cylindrical symmetry of the problem, the coordinate r is defined as the distance from the optical axis $\mathbf{x}$, whose zero is setted at the focal position:

$$\mathbf{E}_f(t,r,x) = \widetilde{E}U(t)\frac{w_0}{w(x)}exp\Big\{-\frac{r^2}{w(x)} + \frac{kr^2}{2R(x)} - i\xi_g(x)\Big\}e^{i(\omega_f t - kx)}\mathbf{e}_z$$

where $w(x)$ and $R(x)$ are respectively the spot radius and the radius of curvature of the wave front at position x, while w_0 is the beam waist and ξ_g the so-called Gouy phase. All these quantities depend on a parameter x_R named Rayleigh length, which is defined as the distance from the focus at which the spot size of the beam increases by a factor $\sqrt{2}$:

$$x_R = \frac{\pi w_0^2}{\lambda_f}$$

Indeed, once this is known, the other quantities read:

$$w(x) = w_0\sqrt{1+\Big(\frac{x}{x_R}\Big)^2} \qquad R(x) = x + \frac{x_R^2}{x} \qquad \xi_g(x) = -\tan^{-1}\Big(\frac{x}{x_R}\Big)$$

Differently from the case of a plane wave, the electric field of a Gaussian beam varies strongly both radially and axially, thus giving ultimately more complicated conditions for phase matching. Indeed, the phase mismatch has four contributions:

$$\Delta\mathbf{k}_q = q\mathbf{k}_f - \mathbf{k}_q = \Delta\mathbf{k}_{\text{neutrals}} + \Delta\mathbf{k}_{\text{plasma}} + \Delta\mathbf{k}_{\text{geometrical}} + \Delta\mathbf{k}_{\text{dipole}} \tag{1.30}$$

which are simple scalars when only the dependence on the **x** coordinate is considered, focusing on the forward emission along the optical axis.

The first two terms in Eq. (1.30) are exactly the same of Eq.(1.22) and Eq.(1.23) with the only difference that now the ionization fraction is in principle a function of both the temporal and the spatial coordinates $\eta(t, \mathbf{r})$. Indeed at a fixed time the medium won't experience the same ionization at two different positions, as it was in the case of perfectly plane wave geometry. The third term arises instead from the Gouy phase:

$$k_{\text{geometrical}} = \frac{\partial \xi_g}{\partial x} = -\frac{x_R}{x^2 + x_R^2}$$

This is a rapidly varying wave vector, which is always negative and attains its minimum in the focal position. Assuming also the harmonic field to be well described by a Gaussian beam, due to the power scaling of nonlinear effects $E_q \propto E_f^q$ we have that $w_{0,q}^2 = w_{0,f}^2/q$. The final expression for the geometrical phase mismatch can thus be found:

$$\Delta k_{\text{geometrical}} = (1-q)\frac{x_R}{x^2 + x_R^2} \tag{1.31}$$

as the Rayleigh parameters of the two beams are equal $x_{R,f} = x_{R,q} \equiv x_R$. This contribution to the phase mismatch is therefore negative and linearly decreases with the harmonic order.

The last term in Eq.(1.30) is instead linked to the intrinsic dipole of the emitted harmonics, which depends linearly on the intensity of the driving field (see Eq.(1.17)). This will therefore give a contribution to the phase mismatch for the forward emission along the optical axis that reads:

$$k_{\text{dipole}} = -\frac{\partial \Phi_n(q, I)}{\partial x} \rightarrow \Delta k_{\text{dipole}} = \alpha(q, n)\frac{\partial I}{\partial x} \tag{1.32}$$

where it is important to remember that the constant α is negative and depends on both the harmonic order q and the quantum trajectory n of the electron, being higher in modulus for the long trajectories. The exact analytical expression of this phase contribution is difficult to compute. However, due to the focusing geometry, its value is always negative before the focus and positive after it.

Since the first two terms of Eq.(1.30) are proportional to the gas density while the last two are independent from it, if the pressure is enough low only the geometrical and dipole mismatch play a role [42]:

$$\Delta k_q \approx (1-q)\frac{x_R}{x^2 + x_R^2} + \alpha(q, n)\frac{\partial I}{\partial z} \tag{1.33}$$

Therefore, perfect phase matching on axis can be achieved only after the focal position, since the two terms should compensate, as can be seen in Figure 1.13. Moreover, for a given harmonic order the phase mismatch is a function of both the focusing condition and the considered trajectory. In particular, short trajectories would require a higher derivative of the intensity to compensate the geometrical mismatch and are therefore phase matched nearer the focus, thus suffering more

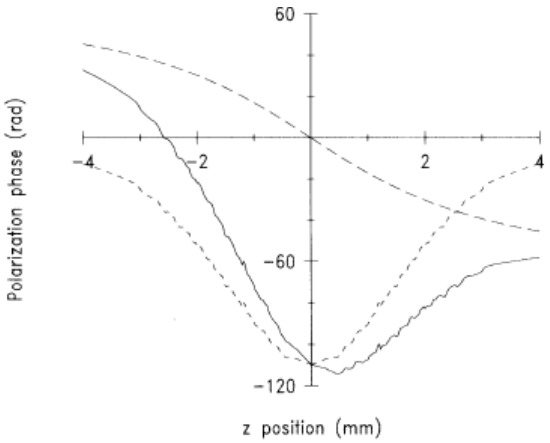

Figure 1.13: Behaviour of the dipole and gemetrical phase on axis around the focus for a peak intensity of 6×10^{14} W/cm^2 and a low density medium. An almost stationary phase is achievable only after the focus, for $x > 0$. Figure taken from [42].

from ionization effects such as depletion of the ground state.

At higher densities, instead, the pressure of the gas becomes an important tuning parameter to achieve phase matching [41]. The first two terms in Eq.(1.30) indeed depends linearly on the pressure and their contribution can be therefore increased or reduced until it compensate for the geometrical and dipole mismatch:

$$P^{PM}\Big[\frac{\partial}{\partial P}\Delta k_{\text{neutrals}} + \frac{\partial}{\partial P}\Delta k_{\text{plasma}}\Big] + \Delta k_{\text{geometrical}} + \Delta k_{\text{dipole}} = 0 \tag{1.34}$$

where P^{PM} is called phase matching pressure. Before the focus this equation can be satisfied only if $|\Delta k_{\text{neutrals}}| > |\Delta k_{\text{plasma}}|$, since the last two terms are both negative. Therefore the ionization of the medium must be less than the critical value η_q^{PM} found in the case of the plane wave geometry for the considered harmonic to allow phase matching. Owing to the fact that generally the focusing conditions of the beam are fixed in the experiment, Eq.(1.34) establishes a relation between the pressure and the ionization fraction to have perfect phase matching of a given harmonic. In particular at low ionization levels P^{PM} varies weakly with the considered harmonic order and thus we have a broad intensity interval over which the generation is efficient. On the other hand, at higher η a good phase matching is supported for narrower intensity intervals in the pulse, as the ionization rate scales exponentially with the driving field. Therefore an increasing of the gas pressure does not give a straightforward quadratic scale of the harmonic intensity as in the case of plane waves, since the phase matching region shifts at higher intensity and shrinks both in space and time.

Considering now the generation far from the optical axis, the geometrical and

dipole terms will show also a phase mismatch contribution in the radial direction:

$$k_{\text{geometrical}}\Big|_{r\neq 0} = \frac{kr}{R(x)} \qquad k_{\text{dipole}}\Big|_{r\neq 0} = \alpha(q,n)\frac{\partial I}{\partial r}$$

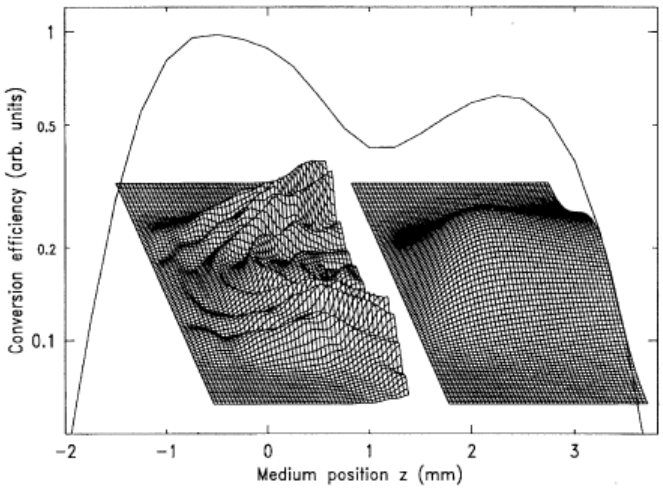

Figure 1.14: Conversion efficiency of th 45^{th} harmonic as a function of position with respect to the focus ($x = 0$). Also the radial distribution of radiation is plotted. For $x > 0$ collinear phase matching is possible, with high spatial coherence, while for $x < 0$ annular emission due to non collinear phase maching is present. The figure was taken directly from [42].

The first one, being linear with respect to k, goes to zero when taking the wave vector difference in Eq.(1.30), while the second gives always a positive contribution. Therefore it may compensate for a negative phase mismatch, allowing the non collinear phase matching of the harmonics. This is, for instance, the typical case for harmonics generated before the focus in a low density medium. Due to the cylindrical symmetry of the system, this gives rise to ring like emission of the radiation which spoils to some extent the spatial coherence of light [42]. Moreover the study of the harmonics' phase along the radial coordinate allows to determine their divergence[43]. In this case the dipole term tends always to make harmonics diverging more. In particular, owing to the different values of α, long trajectories happens to have higher divergence than short trajectories, providing a way to spatially select their contributions in the far field.

The treatment here presented is however a very approximated one and to study correctly the phase matching of harmonics in a tight focusing geometry a full 3D model including lower order non linearities and the pressure profile of the gas jet should be in principle considered. We have also neglected any temporal profile of the laser beam, which would make the phase mismatch dependent on time. Perfect phase matching is indeed a transient condition that is achieved for a given harmonic order at different times in different regions of the pulse. Anyway, due to

the complexity of such evaluation, in experimental practice the optimization of the harmonic signal is performed with an iterative approach in which all the parameters (e.g. the gas jet position, the pressure ...) are tuned until a good working condition is achieved. For instance the employment of an iris on the optical path of the fundamental beam allows to easily modify both its intensity and phase behaviour in the focal region. Since in the tight-focusing geometry many factors influence the phase mismatch, differently from the plane wave case, it is indeed possible to achieve a good macroscopic signal for a wide range of parameters. However from a practical point of view the main disadvantages of this geometry are the presence of the Gouy phase, which is rapidly varying near the focus where the maximum of the generation is expected, and of the radial dipole term, that doesn't allow to achieve a perfect phase matching for all the interaction spot.

1.3.3 Waveguide geometry

In order to overcome many of the limitations of the tight focusing geometry with respect to phase matching, waveguiding of the fundamental field can be exploited. In this case the solution of Eq.(1.19) was studied by Marcatili and Schmeltzer [44]. A brief presentation of its derivation is left in Appendix B, while only its most important consequences are presented here. In particular, the coupling of a laser beam to a hollow waveguide can be studied by describing the input field as a superposition of waveguide modes:

$$\mathbf{E}_{wg}(r,\theta,x,t) = \sum_{\mathrm{s,m}} \mathbf{E}_{sm} = \sum_{\mathrm{s,m}} c_{sm}(t)\mathbf{A}_{sm}(r,\theta,\omega)e^{i(\omega t-\gamma_{sm}x)} \tag{1.35}$$

The complex propagation constant γ_{sm} of each elemental mode is a function of the modulus of the wave vector in vacuum $\mathbf{k}$, the index of refraction of the cladding n_e, the radius of the waveguide a and u_{sm}, which is the m^{th} zero of the Bessel function of the first kind J_s:

$$\gamma_{sm} \approx k\Big[1-\frac{1}{2}\Big(\frac{u_{sm}}{ka}\Big)^2\Big(1-i\frac{(n_e^2+1)}{\sqrt{n_e^2-1}}\frac{1}{ka}\Big)\Big] = \beta_{sm}+i\alpha_{sm} \tag{1.36}$$

where the real part describes the wave propagation along the direction $\mathbf{x}$, while the imaginary part is linked to the propagation losses induced by the guiding mechanism. Generally for longer wavelengths the former decreases while the latter increases, leading to higher losses. The same happens when higher order modes are considered, as u_{nm} increases in this case. Anyway the wave vector of the field in the propagation direction is always lower in the waveguide with respect to the free space case.

Each incoming field will then be identified by the specific coefficients c_{sm}, which give the relative contribution of the correspondent waveguide modes. Their initial value is defined by the spatial overlap integral between the field and the each mode at the entrance surface of the channel:

$$c_{sm}(t) = \int \mathbf{E}_f^*(r,\theta,t)\cdot\mathbf{A}_{sm}(r,\theta,\omega)dS \tag{1.37}$$

where the normalization of $\mathbf{A}_{sm}$ is assumed. It is important to underline that such waveguide modes have been derived for a monochromatic wave and therefore in the case of an incoming pulsed laser every spectral component should in principle be decomposed over the correspondent modes. However, when the laser pulse is not too short, the *slowly varying envelope approximation* (SVEA) can be considered and the waveguide modes can be computed at the central frequency ω_f of the spectrum only. Moreover, if the temporal behaviour of the wave is separable with respect to its transverse coordinates, it can be taken out from the overlap integral in Eq.(1.37) and will thus be directly transmitted to the waveguide modes:

$$\mathbf{E}_f(r,\theta,x,t) = U(t)\mathbf{E}_0(r,\theta,x)e^{i(\omega_f t - k_f x)} \rightarrow c_{sm}(t) = U(t)\int \mathbf{E}_0^*(r,\theta)\cdot\mathbf{A}_{sm}(r,\theta,\omega_f)dS$$

In this way the envelope of the fundamental beam modulates in time the amplitude of the modes in the waveguide, but doesn't affect their distribution. If we further assume that during propagation no coupling is present between the modes, this distribution will then persist along all the waveguide[5]. In the particular case of an incoming linearly polarized Gaussian beam, only linearly polarized EH_{1m} modes can be excited and the overlap integral depends directly on the ratio between the spot size of the beam at the channel entrance and the radius of the waveguide core w/a. It is possible to demonstrate that for a wide range of parameters $0.3 < w/a < 0.7$ only the first three lower order EH_{1m} modes are excited, while for $w/a = 0.64$ a maximum overlap with the fundamental EH_{11} of 98% is achieved. Therefore sometimes, in order to further simplify the problem, the description of the field propagation is restricted only to this mode.

The phase mismatch in the waveguide has four contributions, as in the tight focusing geometry. Also in this case we consider only collinear phase matching for obtaining more simple scalar equations. The geometrical contribution for a mode EH_{sm} is determined by the real part of its complex propagation constant γ_{sm}:

$$k_{\text{geometrical}} = \beta_{sm} - k = -\frac{1}{2k}\left(\frac{u_{1m}}{a}\right)^2 = -\frac{u_{1m}^2\lambda}{4\pi a^2}$$

Therefore the geometrical phase mismatch term depends on the harmonic order, the channel radius and the considered mode:

$$\Delta k_{\text{geometrical}} = -q\frac{\lambda_f}{4\pi a^2}\left[u_{1m,f}^2 - \frac{u_{1m,q}^2}{q^2}\right]$$

where the guiding term of the XUV field can usually be neglected for high order harmonics. Indeed the difference between the free space wavevector and the one in the waveguide is in this case very small and thus the behaviour of the XUV field can be well approximated with a plane wave. If we further assume that only the fundamental EH_{11} mode is excited, a rather simple expression for the geometrical

[5]This approximation holds as long as the variation of the modes' electric field in the transversal direction (e.g. due to the modulation of the index of refraction given by the plasma) is lower than the one in the axial direction.

phase mismatch is obtained:

$$\Delta k_{\text{geometrical}} \approx -q\frac{u_{11}^2\lambda_0}{4\pi a^2} \tag{1.38}$$

where $u_{11} = 2,4048$. Such term is negative as in the tight focusing geometry but it does not depend on the coordinate along the optical axis, thus giving a much more controllable phase mismatch along extended media. Moreover, the dependence on the waveguide radius gives a further parameter that can be tuned to obtain good phase matching conditions. The dipole phase term behaves instead very differently with respect to the tight focusing geometry. Indeed, owing to the guiding mechanism, the intensity doesn't change with respect to $\mathbf{x}$, provided that the coupling between the modes and the variation of the channel radius are negligible. Such term will therefore give only a positive radial contribution allowing for non collinear phase matching, but doesn't affect the building up of radiation in the forward direction:

$$\Delta k_{\text{dipole}} = \alpha(q,n)\frac{\partial I}{\partial r}$$

All the conclusions derived in the case of tight focusing geometry (e.g. lower spatial coherence of the radiation) hold also here. It is however important to underline that in principle the divergence of the harmonic beam caused by the dipole term prevents the treatment of the XUV radiation as a perfectly plane wave, contradicting our previous discussion. This would give rise to a much more complex dynamics, where also the field of each harmonic should be decomposed in waveguide modes. Anyway in this thesis we will stick to the simpler plane wave approximation for the XUV radiation, expecting some deviation from this description in particular when rather long channels are employed.

The expression for the phase mismatch in the waveguide thus reads:

$$\Delta k_q = q\frac{2\pi}{\lambda_f}N(\mathbf{r},P)\Big[(1-\eta(t))\delta n_q + \frac{r_e}{2\pi}\lambda_f^2\eta(t)\Big(\frac{1}{q^2}-1\Big)\Big] - q\frac{u_{11}^2\lambda_f}{4\pi a^2} \tag{1.39}$$

The most important control knobs to achieve phase matching are therefore the pressure and the driving laser intensity, being generally fixed the capillary radius and the atomic dispersion. At low intensities, in particular, the ionization of the medium is rather low and phase matching appears as the equilibrium between the neutrals' term and the waveguide contribution [9]. The more dispersive is the medium, the lower is the pressure necessary to achieve perfect phase matching for a given harmonic order. On the other hand, as the intensity of the incoming beam increases, the plasma contribution starts to become more and more important and therefore also the pressure required to compensate for the geometrical phase mismatch increases. This is true until the ionization fraction reaches the critical value for the phase matching of plane waves at the given harmonic order. Then, for values equal or bigger than this, phase matching is no more possible and the signal will be quenched. This is the most important factor limiting the extension of the harmonic spectrum in the waveguide geometry. Indeed, even if it is possible as exposed in Section 2.3 to limit the medium ionization at high driving intensities

using shorter pulses, this method is limited by the lowering of the output emission [47].

The situation presented until now is however oversimplified. In actual experiments the gas is injected in the channel trough some inlets and thus the pressure varies considerably in space[6], while the ionization of the medium varies both in space and time due to the dynamics of the driving field.

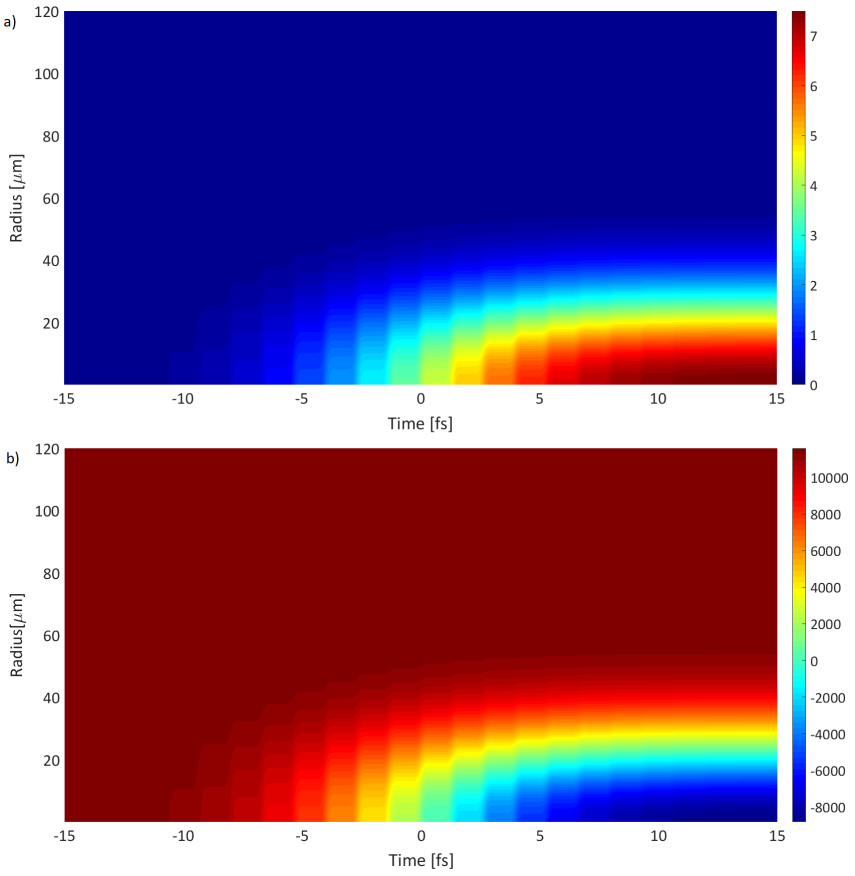

Figure 1.15: Spatial and temporal effect of phase matching in Ar for the 29^{th} harmonic. In a) the ionization rate is calculated using the ADK model, while in b) the phase mismatch is evaluated. As can be seen perfect phase matching starts on axis for lower times and then moves radially as ionization increases. Data: capillary radius $a = 120$ µm, pulse duration 40 fs FWHM, driving intensity $2 \cdot 10^{14}$ W/cm^2 and pressure 150 mbar. The code was inspired by [46].

The perfect phase matching condition is therefore highly transient and for obtaining quantitative results a full model of both gas and field propagation in the waveguide should be considered. In particular, for a fixed harmonic and pressure level perfect phase matching starts on axis and then move at larger radial positions in time, as

[6] A temporal variation of the pressure could also be in principle present, if the inlet doesn't give a continuous flux of gas but works impulsively.

intensity increases [46], following a given ionization level. On the other hand, for a fixed harmonic and intensity profile of the driving field, phase matching is possible at higher pressures near the peak of the pulse and at lower pressures along its tails. Indeed when the medium density increases, also the ionization level needed to perfectly compensate the geometrical contribution of the waveguide increases and vice versa.

Regarding the intensity of the harmonic radiation along the capillary, the same Eq.(1.25) and Eq.(1.27) of the plane wave geometry can be used, if the behaviour of the XUV field is approximated in this way. It is important to notice that in the case of waveguides the absorption of the harmonic radiation is of much higher importance with respect to the tight focusing geometry, since it interacts with an extended medium. In particular, as the gas density usually decreases towards the end of the channel, the emission of those harmonics which are highly absorbed by the gas may be possible only in these regions. The radiation that is not so much absorbed by the medium, instead, is emitted mostly in the central part of the waveguide where the pressure is more constant and the field can thus efficiently build up for longer distances. In any case, the interplay of absorption and phase matching ultimately defines the shape of the harmonic spectrum, which can be very different from the classical plateau of the single atom emitter [9].

1.3.4 Quasi phase matching

The waveguiding geometry has many advantages when compared to the tight focusing one, since the interaction length is longer and the collinear phase mismatch is much more controllable. This allows to obtain a higher XUV intensity, which is ultimately limited only by absorption. However the extension of the spectrum is still bounded by the ionization of the medium. Indeed typical ionization levels from which the phase matching becomes impossible are on the order of 5% in Ar, 1% in Ne and 0.5% in He, which are easily achieved at the intensities necessary to generate radiation above 100 eV. Due to the high phase mismatch, in the soft x-ray region of the spectrum the signal will thus oscillate along the waveguide length, without efficiently building up[7]. Anyway to overcome this limitation it is possible to use a *quasi phase matching* (QPM) technique, similarly to what is done in classical non linear optics. The idea is to introduce some periodic modulation of one of the parameters which influence the phase mismatch in order to allow an efficient generation of XUV radiation only in those sections of the waveguide for which it can add up coherently and to quench it in those regions where destructive interference takes place. In this way the signal can build up over long distances even when it is not possible to achieve perfect phase matching. In this section we will try to give a brief presentation of the most important QPM techniques, without in any way claiming to be exhaustive.

[7] In this region of the electromagnetic spectrum the absorption of the media used for HHG is generally very low, giving a good scalability to lower wavelengths. The signal is therefore limited only by phase matching conditions and in particular by the free electron density.

Corrugated waveguides

One of the possible approaches in QPM is to employ waveguides with a periodically modulated diameter $a = a(x)$ [48]. If such variation is enough slow, so that it doesn't affect the distribution of the waveguide modes, it is possible to describe its effect as a simple modulation of the nonlinear polarization induced by the driving field in the medium. Since this will be a periodic function itself, we can write it by means of a Fourier series. Using the same notation of the simple model developed for plane waves in Section 3.1 it will thus read:

$$\widetilde{P}_q^{NL} = \sum_{\mathrm{n}=-\infty}^{+\infty} P_{n,q} e^{iK_n x}$$

$$K_n = n\frac{2\pi}{\Lambda}$$

where Λ is the period of the diameter modulation and n an integer index. Then the building up of the harmonic field along the waveguide can be computed as:

$$\widetilde{E}_q = -i\frac{\mu_0 \omega_q^2}{2k_q} \int_0^L \sum_{n=-\infty}^{+\infty} P_{n,q} e^{iK_n x} e^{-i\Delta k_q x} dx \tag{1.40}$$

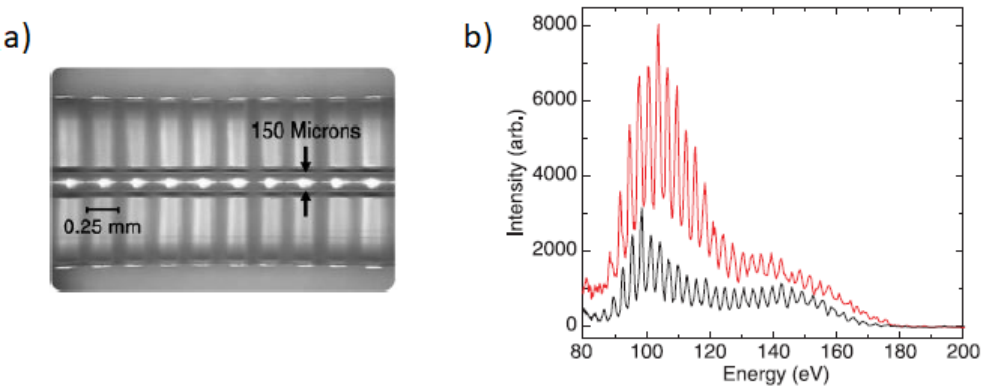

Figure 1.16: Corrugated waveguide used in [48]. In a) the optical microscope image of the capillary, showing the dimensions of the modulation produced with glassblowing technique. In b) effects of the enhancement due to QPM in Ar at 7 torr with driving intensity of $9 \cdot 10^{14}$ W/cm^2. The black line is the spectrum measured in a straight waveguide while the red line in the modulated capillary of a). The images are taken directly from [48].

Therefore, when perfect phase matching isn't present, it is possible to enhance the harmonic signal if $K_n = \Delta k_q$ for some value of n. This intensification will be greater for first order QPM ($|n| = 1$) and lower for higher orders QPM ($|n| > 1$), as in this case the signal will rise and fall n-1 times across the channel. Still the enhancement remain significant with respect to the straight waveguide case even for pretty high values of n. Moreover, since the phase mismatch for a given frequency varies

strongly both in space and time, a rather wide window of harmonic order can be intensified.

Due to the fact that the harmonics near the cutoff are generated near the peak of the pulse, they will generally suffer from the highest phase mismatch. To compensate it with high efficiency ($|n| = 1$) it is thus necessary to employ waveguides with very small modulation periods, which is one of the main practical limitation of this approach. Another drawback of this QPM method is that the driving field during its propagation is inevitably perturbed by the modulation. This leads to the necessity of rearranging the parameters along the waveguide length if one wants to grant the same phase matching conditions, which is not feasible in bulk structures as these. Finally the maximum phase mismatch that can be compensated with this mechanism is ultimately limited by the waveguide diameter, since it is possible to demonstrate that for QPM to be efficient the modulation should be much smaller than a.

Multiple sources

Another possible QPM technique is the use of multiple sources, which offers the possibility to rearrange the parameters along the propagation direction of the driving laser in a more flexible way. The idea is here to divide the interaction length L in M different parts and to separate them in space in order for controlling their phase matching conditions individually. Indeed a trade off is generally present between the harmonic yield and the coherence length, as higher pressures increase both the output intensity of the XUV radiation and its phase mismatch. In the case of multiple sources instead the distance between them can be experimentally arranged in such a way that the radiation emitted from the last part of one section and from the first part of the following has a phase difference of π. In this way the generated light can efficiently build up along all the medium length and the gas pressure inside each single section can be increased to obtain an higher output yield. For example, in [49] an enhancement of the pressure inside the single source up to the number of sections M was possible. The dependence of the optimal distance between the sources with respect to the harmonic order has been proved to be quite low for the lower harmonic orders, while it is bigger for higher ones. This is mainly due to the fact that the former are generated in different times and regions of the medium and thus experience a wider range of phase mismatches that may be compensated with QPM. The latter, instead, are generated mainly near the peak of the driving pulse in narrow temporal window and have therefore more sharply defined phase matching conditions.
The signal that can be obtained from M sources with this approach can be computed using the simple plane wave approximation:

$$I_q \propto \frac{1-(-1)^M \cos\left(L\Delta k_q\right)}{1+\cos\left(\frac{L\Delta k_q}{M}\right)} \sin^2\left(\frac{L\Delta k_q}{2M}\right) \tag{1.41}$$

The main technical difficulties of this method derive from the fact that usually free space propagation of the driving field is employed to allow for the flexibility given

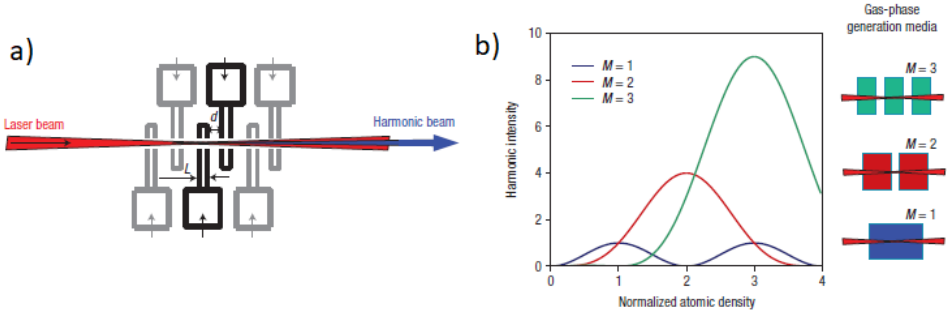

Figure 1.17: a) Schematics of the system, in which multiple sources are pumped collinearly by the same laser. Their density and distance can be independently arranged. b) Saturation of the output harmonic intensity with pressure for a fixed medium dimension due to the lowering of the coherence length. As the medium is divided in multiple sources the optimal pressure increases, leading to an higher yield. The images are taken directly from [49].

by the sources' motion. Therefore the beam divergence and plasma defocusing effects limit the practical scalability to bigger numbers of separated sources.

Counterpropagating waves

Another possibility to quench the harmonic emission in out-of-phase regions is the use of weak counterpropagating fields at the same frequency of the driving beam. In the approximation of perfectly plane waves the total field can be described assuming that the behaviour of the more intense forward wave prevails and the net effect of the counterpropagating one is a modulation in the longitudinal direction of both the amplitude and the phase:

$$E_f e^{i(kx-\omega_f t)} + E_c e^{i(-kx-\omega_f t)} \approx E_{\text{tot}}(x) e^{i(kx-\omega_f t+\phi(x))}$$

where it can be demonstrated that [50]:

$$E_{\text{tot}}(x) = E_f \sqrt{1 + \left(\frac{E_f}{E_c}\right)^2 + 2\left(\frac{E_f}{E_c}\right)\cos(2kx)}$$

$$\phi(x) = -\tan^{-1}\left(\frac{\frac{E_c}{E_f}\sin(2kx)}{1+\frac{E_c}{E_f}\cos(2kx)}\right)$$

This modulation takes thus place on a scale of half the fundamental wavelength. Using a power law model for the medium response, it is then possible to characterize the microscopic emission from such small area. The harmonic field at the exit of this region will be proportional to:

$$E_q \propto \int_0^{\lambda_f/2} E_{tot}^q e^{iq(\phi(x)-\omega_f t)} dx$$

where the comoving frame $(x, t + \frac{x}{c})$ is employed. On the other hand, if only the driving pulse were present, the harmonic field would be proportional to:

$$E_q \propto \int_0^{\lambda_f/2} E_f^q e^{-i\omega_f t} dx = \frac{\lambda_f E_f^q}{2} e^{-i\omega_f t}$$

It is therefore possible to define a microscopic phase-mismatch factor of the counter-propagating wave as the ratio between these two values.

$$\xi = \frac{2}{\lambda_f E_f^q} \int_0^{\lambda_f/2} E_{\text{tot}}^q e^{iq\phi(x)} dx \tag{1.42}$$

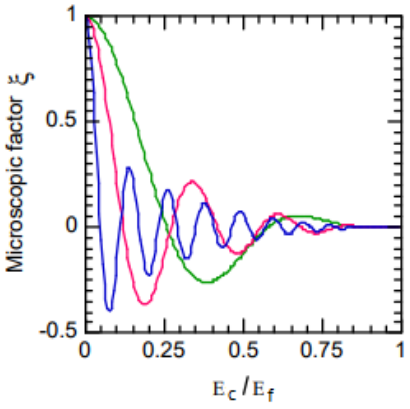

Figure 1.18: Behaviour of the microscopic phase-mismatch factor as a function of the ration between the two field amplitudes. The green curve refers to $q = 11$, the red one to $q = 21$ and the blue one to $q = 51$. The image is adapted from [50].

This parameter describes how the response of the atoms is disrupted by the presence of the second field. In particular, the radiation emission results to be quenched for even low values of E_c. Moreover, as can be seen from Figure 1.18, the higher is the considered harmonic order, the lower is the intensity of the second wave that is necessary to obtain a complete suppression of the emission. Also ratios for which ξ is negative are present, meaning that the emission is out of phase with respect to the one driven by a single pulse, providing another possible degree of freedom to compensate the phase mismatch of the harmonics. However, in actual experiments focused and pulsed lasers are employed instead of perfectly plane waves. The microscopic phase mismatch factor will thus be a function of both position and time $\xi = \xi(\mathbf{r}, t)$. Therefore QPM will be possible only if the second field is able to selectively quench the radiation emission from a considerable part of the regions which would give an out of phase contribution.

The same technique was demonstrated to be feasible in the waveguide geometry by Zhang *et al.* [51]. In this case a train of counterpropagating pulses is employed to quench the harmonic generation in the sections of the channel where the phase mismatch is larger than π. Therefore the pulses in the counterpropagating train

need to be accurately designed to overlap with the fundamental field in precise positions along the optical axis and to cover the whole out-of-phase regions, which is not trivial. In particular, to achieve the maximum enhancement the such pulses should be separated by $4L_{\mathrm{coh},q}$ and have a duration of around $L_{\mathrm{coh},q}/c$. Therefore the optimal parameters of the counterpropagating pulse train depend on the particular harmonic order for which QPM is designed, thus limiting the frequency window of the enhancement.

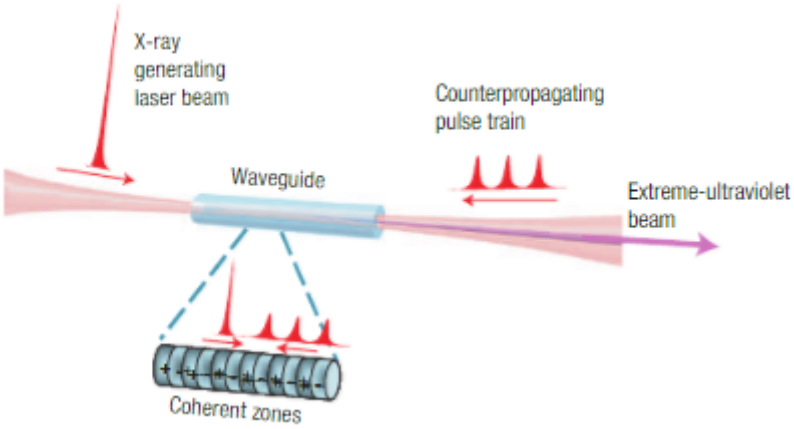

Figure 1.19: Geometry of the QPM in waevguide using counterpropagating waves. The image is taken directly from [51].

This all optical QPM method has the main advantage of being easily extendible to even very high orders of harmonics and of compensating also for the phase mismatch in the transverse direction if suitable pulse shaping techniques are employed. Moreover it doesn't disturb the medium, apart from the collision regions between the two beams. However it still suffers from the narrow quasi phase matching window, owing to the frequency dependence of the radiation coherence length. Moreover, in order to allow the passage of the emitted XUV radiation, the optics used to send the counterpropagating pulses in the waveguide should present a hole, which may then perturb the IR field.

Multi-mode propagation

In Section 1.3.3 light propagation inside a waveguide was described in terms of modes, among which only the EH_{1m} were considered due to the linearly polarization of the driving field. Afterwards an approximation was taken, considering only the fundamental EH_{11} to be active, since usually its coupling efficiency can be easily maximized designing the beam spot size at the entrance of the channel. When this is not the case, however, the excitation of multiple modes is possible, each one of which is described by its own propagation constant β_{1m}. As a consequence the total field intensity in the longitudinal direction is modulated by their interference [52]. In the limiting case of only two excited modes, this leads to a beating length that

can be derived directly from Eq.(1.36):

$$L_{\text{beating}} = \frac{2\pi}{\beta_{1m} - \beta_{1m'}} = \frac{8\pi^2 a^2}{\lambda_f (u_{1m}^2 - u_{1m'}^2)}$$

Even when this modulation is rather small, it can be used to selectively quench the harmonic generation in some areas of the waveguide and to achieve QPM. In particular it is possible to compensate for a phase mismatch of [53]:

$$\Delta k_{\text{beating}} = \frac{2\pi n}{L_{\text{beating}}} = n \frac{\lambda_f (u_{1m}^2 - u_{1m'}^2)}{8\pi a^2} \tag{1.43}$$

where $n = 1, 2, ...$ is an integer number defining the order of the QPM process. To compensate for bigger phase mismatches it is thus necessary to excite higher order modes of the capillary, which is one of the main limitations of this approach, as the guiding losses become rapidly quite important. Moreover, in actual experiments it is difficult to achieve the ideal condition of only two excited modes and thus the mathematical description becomes quite complex. However in case of multimodal propagation the field intensity follows empirically the beating frequency between the lower and the higher mode among the ones that are excited, with some peaks that are missing due to the perturbation given by the others. These deviations are more evident for longer medium and thus limit the effective length over which QPM can be achieved with this method.

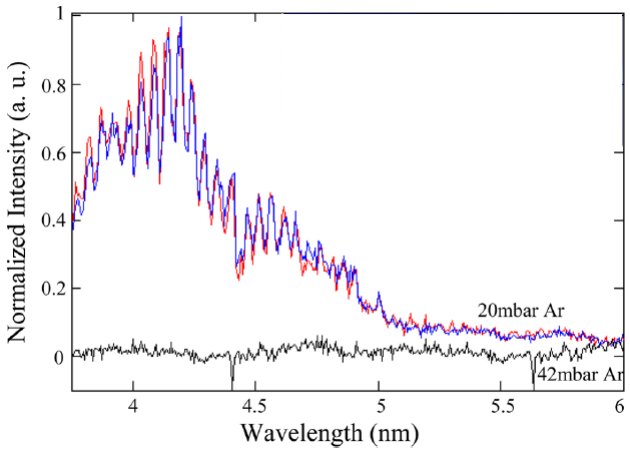

Figure 1.20: Example of QPM with multi-mode propagation in Ar. In red and blue are shown the signals due to quasi-phase matching while in black is represented the emission from single mode propagation in the waveguide. The image is adapted from [53].

One advantage of this approach is instead the lower average ionization fraction that is reached in the channel with respect to the single mode propagation, due to the intensity fluctuations. This reduces the effective phase mismatch, allowing for an easier compensation. Indeed with this approach the feasibility of achieving QPM also for ionic species has been demonstrated [53].

CHAPTER 2

HHG in Molecules

One of the main results of Chapter 1 is that the high harmonic signal radiated by a single emitter in the SFA limit of the Lewenstein model can be considered as the sum of three contributions, related to the semiclassical steps of ionization, electron propagation in the continuum and recombination. In particular, the latter is proportional to the transition dipole matrix element between the continuum and the ground state of the system and it thus depends only on the species of the emitter and the considered harmonic order, due to the fact that the wave vector of the recollinding electron is fixed by the energy conservation law. The first two terms depend also on the structure of the driving field and they are usually refferd to as the continuum electron wave packet (EWP) [54]. This factorization is at the basis of *high-harmonic spectroscopy* (HHS), which is a powerful tool to self-probe atoms and molecules [55]. Indeed the EWP can be thought of as a probe of the static and dynamical structure of the emitter, which is encoded in the recombination part of the dipole with high temporal and spatial resolutions. The first one is guaranteed by the HHG process itself, which takes place on a subcycle of the driving field. Moreover the attochirp of the short trajectories allows also to encode the temporal evolution of the system in the harmonic order [58], when the contribution of long trajectories is efficiently filtered out [28]. The high spatial resolution is assured by the small De Broglie wavelength of the recombining electron. Therefore the cutoff frequency in a spectroscopic experiment defines in some way the amount of information that can be extracted and the resolution that can be achieved. Some examples of the successes of this technique are the tomographic reconstruction of molecular orbitals with sub-Åmströng resolution [57, 117], the probing of structural rearrangements in molecules [58], the mesurement of the electronic structure of atoms [59] and the monitoring of molecular vibrations [60].

High-harmonic spectroscopy suffers, however, from one important limitation. Indeed the presence of the high-intensity driving pulse cannot be neglected and thus the information that is retrieved is in principle referred to the system "dressed" by the strong-field and not to its unperturbed state [63]. Besides this issue it is also important to underline that such information is encoded in the recombination term, which can be easily factored out and described with a simple dipole expression only within the SFA framework, whose validity is not undoubted for generic systems. Moreover, in order to obtain useful data it is also necessary to recover the single-emitter spectrum from the measurement of the macroscopic signal, which is not

always trivial.

Apart from these limitations, HHS is indeed a promising tool for retrieving important static and dynamic pieces of information about the emitting system. Owing to their rich structure, molecules are naturally interesting targets for such studies. However the use of molecular media implies a more complex theoretical and experimental treatment of the generation process with respect to simple atoms. In Section 1 we will therefore briefly sketch the main aspects that are unique to HHG in molecular samples. Afterwards in Section 2 we will present the theory of impulsive alignment of molecules, which is a technique used to control important parameters in these experiments. A brief treatment of the quantum mechanical structure of molecules, which is useful for the topics of this chapter, is reported in Appendix C.

Throughout all the chapter, two different frames of reference are used, depending on the situation: the molecular one and the laboratory fixed one. These two can be related through three angular coordinates named Euler angles $\mathbf{Q} = (\theta, \phi, \chi)$. In particular θ is the angle between the molecular axis **a** and the laboratory axis **z**, ϕ the angle of rotation of **a** around **z** and χ the angle of rotation of the molecular frame around **a**. Moreover, following the convention of the previous chapter, the laboratory axis **z** is always considered parallel to the polarization of the driving pulse, which is propagating along **x**.

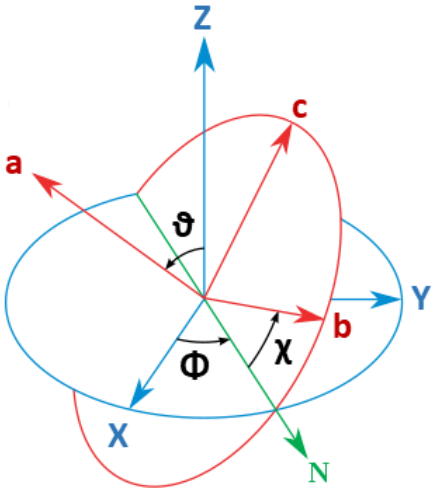

Figure 2.1: Representation of the three Euler angles (θ, ϕ, χ). The blue coordinates are relative to the laboratory frame, while the red ones are relative to the molecular frame. The image was adapted from [64]

Sometimes also the set of three angles $\boldsymbol{\beta} = (\beta_a, \beta_b, \beta_c)$ is employed, which represents the position of the molecular frame axis with respect to **z**. These angles are linked to the Euler angles through the relations:

$$\cos\beta_a = \cos\theta \qquad \cos\beta_b = \sin\theta\cos\chi \qquad \cos\beta_c = \sin\theta\sin\chi$$

2.1 The three-Step model for molecules

In this section we will consider the adjustments that should be done to the Lewenstein model as presented in Section 1.2 in order to account for the peculiarities of molecules with respect to simple atoms within the SFA framework. This will be carried out without seeking for a complete treatment of the problem and avoiding the derivation of a general analytical expression for the dipole moment as Eq.(1.15). Eeach one of the three semiclassical steps linked to HHG will be considered separately. The main purpose of this treatment is indeed to justify the necessity to use molecular alignment techniques for studying such systems. A deeper analysis of the topics of this section can be found in [65].

2.1.1 Molecular ionization

The problem of molecular ionization can be faced in two ways, as was already the case in Section 1.1.1 regarding atoms: the numerical solution of the time dependent Schrödinger equation or the use of approximated tunnelling formulae. In this section we will focus only on the latter, remembering the assumptions and limits of validity of such approach. In particular we will briefly present the results of the so-called *molecular ADK* rate (MO-ADK), which is an extension of the ADK equation used for atoms [66].

The much richer structure of molecules gives rise to a more complex ionization dynamics with respect to the atomic case, that in principle can be influenced by the internal vibrational and rotational degrees of freedom of the system. Moreover, due to the lack of spherical symmetry of the electron wavefunction, the ionization rate is expected to depend also on the relative direction between the linearly polarized driving field and the molecular axis. If multi-electron effects are neglected and the internal degrees of freedom of the molecule are considered frozen during the process, the MO-ADK rate in a static field reads:

$$W_{\text{stat}}^{\text{MO}}(E,\mathbf{Q}) = \sum_{\text{m}'} \omega_p \frac{B^2(m',\mathbf{Q})}{2^{|m'|}|m'|!}\Big(\frac{4\omega_p}{\omega_t}\Big)^{2n^*-|m'|-1} exp\Big(-\frac{4\omega_p}{3\omega_t}\Big) \tag{2.1}$$

where the same notation of Section 1.1.1 is used for ω_p and ω_t, while m' is the quantum number representing the projection of the electron orbital momentum along the polarization direction of the external field. This equation is composed of two parts: the exponential term, that is a function of the ionization potential only and is the same of the atomic case, and the prefactor, which depends on the molecular structure. In the case of linear molecules the quantum number m, which identifies the projection of the orbital angular momentum along the molecular axis, is a good quantum number and so the prefactor will be given by:

$$B(m',\mathbf{Q}) = \sum_{\text{l}} (-1)^{m'} C_{lm} D^{l}_{m',m}(\mathbf{Q}) \sqrt{\frac{(2l+1)(l+\mid m' \mid)!}{(l-\mid m' \mid)!}}$$

where C_{lm} are the coefficient of the spherical harmonics expansion of the electron wavefunction, that can be computed numerically or can be found tabulated [66, 67],

and $D^l_{m',m}(\mathbf{Q})$ are the so-called Wigner rotation matrices [1]. The latter are defined as [69]:

$$D^j_{m',m}(\mathbf{Q}) = e^{im'\phi} d^j_{m',m}(\theta) e^{-im\chi}$$

$$d^j_{m',m}(\theta) = \sum_s P(j,m,m',s) \cos^{2j+m'+m-2s}\left(\frac{\theta}{2}\right) \sin^{m'-m+2s}\left(\frac{\theta}{2}\right)$$

$$P(j,m,m',s) = (-1)^s \frac{\sqrt{(j+m')!(j-m')!(j+m)!(j-m!)}}{s!(j+m+s)!(m'+m+s)!(j-m'-s)!}$$

where the sum over s in $d^j_{m',m}(\theta)$ runs over all the values for which the factorials in the expression are positive. On the other hand, for a nonlinear molecule m is no more a good quantum number and therefore this expression must be slightly modified:

$$B(m') = \sum_{l,m} (-1)^{(m+|m'|)/2} C_{lm} D^l_{m',m}(\mathbf{Q}) \sqrt{\frac{(2l+1)(l+\mid m' \mid)!}{2(l-\mid m' \mid)!}}$$

where $m = -l, -l+1, ..., l-1, l$. Note that if (l, m, m') were all good quantum numbers, the expression would go back to the simpler atomic ADK rate and the dependence on $\mathbf{Q}$ would cancel out.

Even if the MO-ADK theory is a highly approximated approach to the study of strong-field ionization in molecules, it allows to predict in a rather simple way the dependence upon the orientation of the system. In particular the rate will be maximum when the electron cloud of the molecule is aligned with respect to the external field and will be minimum when one of the orbital nodes lies along its polarization direction. One example of such behaviour is the different ionization rate for aligned N_2 and O_2 molecules, as can be seen in Figure 2.2. For this reason when an ensemble of molecules is considered, the macroscopic ionization signal should be computed as a weighted sum:

$$S_{ion} \propto \int \rho(\mathbf{Q}) d\mathbf{Q} \int (1 - e^{-\int W_{stat}(E(t),\mathbf{Q})dt}) 2\pi r dr dz$$

where $\rho(\mathbf{Q})$ is the weighting function of the possible molecular orientations and both the cylindrical symmetry of the system and the adiabatic approximation for ionization driven by pulsed lasers are exploited. The modulation effect given by the molecular alignment to the external field is thus purely geometrical and will reflect on the HHG yield as a scaling factor.

Until now the focus of the discussion has been on the prefactor of Eq.(2.1), which is the main difference with respect to the atomic case and is directly influenced by the structure of the electron wavefunction. However, also the exponential factor, that is a common feature to all tunnelling formulae, contains a peculiar behaviour of molecules with respect to atoms. Indeed molecular orbitals are much less separated in energy with respect to atomic ones, with a difference of ionization potentials

[1] Wigner rotation matrices are used to represent spherical harmonics, which are the usual basis set for quantum rotators, in rotated frames of reference.

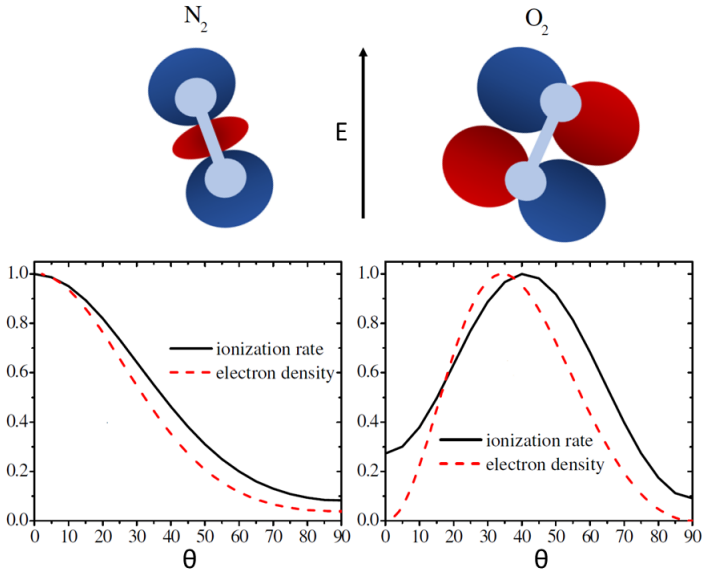

Figure 2.2: Example of different behaviours for the ionization of the HOMO as a function of θ. For N_2, being the HOMO a σ orbital, the rate is enhanced for maximum alignment ($\theta = 0$) while for O_2 is quenched owing to its geometry. The image was adapted from [68].

that shrinks as the system becomes more and more complex. Therefore it is not possible to neglect a priori the possibility to ionize also inner molecular orbitals. This effect will be more important when ionization of the HOMO is quenched by the geometrical effects presented before. More recently it was also demonstrated that electron correlation can excite the ionic system during tunnelling, leading to ionization of inner orbitals which is not subjected to the exponential suppression typical of the TI regime [70]. Therefore molecular ionization is strictly a multi-body process in which all the electrons play a role and the single active electron approximation of the Lewenstein model starts to become no more applicable. Moreover the external strong field may be also able to polarize the ground state of both the neutral molecule and its ionic state, influencing strongly the ionization process [71]. In this case, also the SFA is no more a suitable description of ionization. For all these reasons the MO-ADK theory here presented is not able to outline all the rich phenomena that may be linked to molecular ionization.

2.1.2 Molecular relaxation

In the semiclassical picture presented in Section 1.1.2 the motion of the freed electron is determined by the external field only. However, for a generic molecular system the SFA is not always an adequate approximation. Indeed the ionic Coulomb field can play an important role and thus the simple plane wave description for the returning electron begins to fail. This effect is sometimes treated as an acceleration of the returning electron with respect to the asymptotic value of its momentum up

to a factor I_p [72]:

$$\mathcal{E}_{\mathrm{k}} = \frac{\hbar^2 k^2}{2m_e} + (1-\epsilon) I_p = \hbar\omega_q \tag{2.2}$$

This is however only an heuristic formula, where the correction factor $0 < \epsilon < 1$ is fitted for reproducing the experimental results in the more accurate way possible. Moreover in the description of the continuum wave packet it is important to consider the influence of the ionization mechanism on the distribution of the electrons' momenta. Indeed energy conservation fixes the absolute value of the momenta while the SPA defines their average orientation along the driving field polarization. However, when a molecule is ionized along a nodal plane of its orbital, the continuum wavepacket is expected to maintain such node and thus it will not include states propagating along this direction. In this way, the returning electron cannot be described as a simple plane wave during the reombination step. Therefore the shape of the continuum wavepacket in momentum space is influenced by the orbital symmetry and orientation, expecially when the driving field is parallel to one of the molecular nodal planes [73].

Apart from the continuum wave packet, also the description of the ionic system should be improved to account for both its internal relaxation and its interaction with the external strong field during the motion of the released electron. The first example of such effects is the vibration relaxation of the nuclei in the cation. Indeed molecular ionization can be viewed as a vertical transition from the ground state of the neutral molecular energy potential surface to the ground state of the ionic energy potential surface, similarly to the Franck-Condon principle in vibrational spectroscopy. Therefore the cation may found itself in an excited vibrational state and will start to relax. The returning electron will probe a modified nuclear arrangement in the molecule and this will directily reflect on the emitted spectrum. Using BO approximation in the standard SFA framework of Lewenstein model, it can be demonstrated that the HHG yield is modulated by the vibrational autocorrelation function [74]:

$$C(\tau) = \int \chi_n(\mathbf{R}) \chi_c(\mathbf{R}, \tau) d\mathbf{R} \tag{2.3}$$

where χ_n and χ_c are the vibrational part of the wavefunction respectively in the ground state of the neutral molecule and the cation, τ is the electron excursion time in the continuum and $\mathbf{R}$ the coordinates of the nuclei. This means essentially that, as the electron must return to its initial state in order to give rise to a coherent emission of harmonics, radiative recombination will be more likely if the vibrational wavepacket hasn't changed too much during its motion in the continuum. Since the vibrational period of the nuclei is approximately proportional to their masses, they can generally be assumed fixed in the small period of time between ionization and recombination ($\tau \approx 1 \div 2$ fs for $\lambda = 800$ nm). However, when small nuclei such as hydrogen are considered or the electron excursion time in the continuum is increased using longer wavelengths, the effect of the vibrational relaxation of the system cannot in principle be neglected.

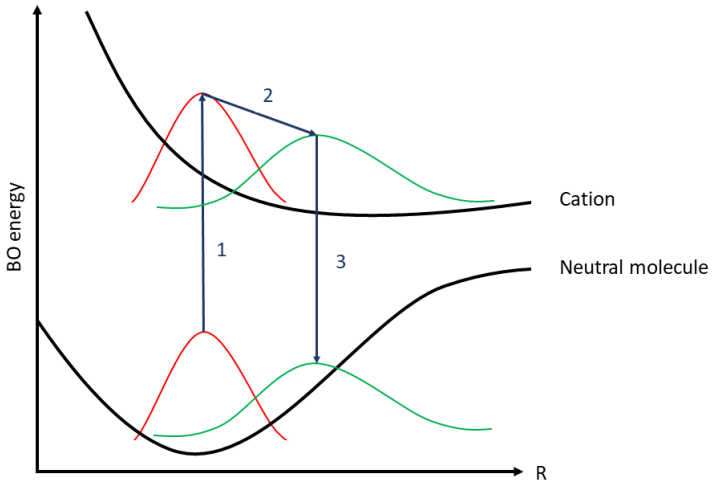

Figure 2.3: Mechanism of nuclear relaxation influencing HHG spectra. (1) Ionization launches a vibrational wave packet from the ground state of the neutral molecule to the ground state of the cation. (2) The wave packet evolves in time during the electron excursion time τ. (3) During recombination the system must return to the initial ground state of the neutral molecule. The efficiency of such transition is given by the overlap integral between the initial and the final vibration wave packets, represented in figure in red and green respectively.

Another possible relaxation effect during the continuum propagation is linked to the electron correlation in the system. The rigorous treatment of multi-electron contributions in HHG is far from simple. We will therefore focus only on the description of the multi-channel contribution given by the possibility to ionize multiple molecular orbitals, as exposed in Section 2.1.1. Such channels are named after the excited states of the ionic system (X, A, B, ...) which in the Hartree-Fock framework are represented as a hole in inner shell orbitals. When multiple channels are present, the wavefunction of the ionic system can therefore be written as:

$$|\Psi_{\text{ion}}\rangle = \sum_{\text{c=X,A,B ...}} \alpha_c(t)\, |\psi_c^+\rangle\ |\mathbf{k}_c\rangle$$

where $|\psi_c^+\rangle$ represents the ionic state[2] linked to channel c, which is antisymmetrized to account for the electron indistinguishability, $|\mathbf{k}_c\rangle$ is the continuum state of the relative freed electron and $\alpha_c(t)$ is the weighting coefficient of the different channels, whose initial value is set by the ionization mechanism. The temporal dependence of such expression is given both by the free evolution of the ionic and continuum states and by the possible coupling with the external field. In order to write the matrix element describing the recombination to the neutral molecular state $|\Psi_0\rangle$ the N-electron dipole should then be considered as the sum over the single dipoles

[2]Note that in principle the single-particle wavefunctions used to obtain the ionic ground state in the Hartree-Fock framework may be different from the ones used for the ground state of the neutral molecule.

of the system:

$$\mathbf{d}_{\text{rec}}(t) = \langle \Psi_0 | \sum_{\text{i=1}}^{\text{N}} \mathbf{d}_i \, | \Psi_{\text{ion}} \rangle = \langle \Psi_0 | \, \mathbf{d}_{\text{N}} \, | \Psi_{\text{ion}} \rangle$$

Using the previous ansatz for the ionic wavefunction and exploiting the symmetry of both the multi-electron dipole and the ionic state it is possible to rewrite such expression as [75]:

$$\mathbf{d}_{\text{rec}}(t) = \sum_{\text{c}} \Big(\alpha_c \, \langle \Psi_c^d | \, \mathbf{d}_{\text{N}} \, | \mathbf{k}_c \rangle + \mathbf{d}_c^{\text{ex}} \Big) \tag{2.4}$$

where $|\Psi_c^d\rangle = \langle \Psi_0 | \psi_c^+ \rangle$ is the Dyson orbital linked to the channel c, which represents a hole in the molecule, and $\mathbf{d}_c^{\text{ex}}$ is a term representing the exchange correlation between the electrons. In particular, the latter is negligible whenever the actual ionic states are not very different from the unrelaxed ones and it is thus dependent on the degree of orbital relaxation upon ionization. In this way the contributions of the various channels adds up coherently and the multi-electron contribution to HHG can be thought of in terms of their interferometric superposition. In particular, during propagation in the continuum each channel will acquire two phase terms. The first one is due to the oscillation of the plane wave state, which for a given harmonic order is determined only by the external strong field and the considered semiclassical trajectory, as was already pointed out in Section 1.2. The second is linked to the ionic state and, if laser-induced dynamics can be neglected, is simply given by the beating of the free evolution of the Dyson orbital with frequency $\mathcal{E}_c/\hbar$ which describes a time-dependent hole in the molecule [75]. It is important to underline however that, strictly speaking, the hole and the free electron are entangled and a more precise description of multi-channel HHG should account for that [73].

2.1.3 Recombination interference

Since the recombination of the electron can be though of as the reverse process of ionization[3], we can expect also in this step an angular dependence on the molecular alignment with respect to the driving field. Indeed the returning particle probes different electronic distributions depending on the alignment of the molecule, thus the emitted radiation will encode such structural data. The first theoretical identification of this effect was performed by Lein *et. al* [76] by numerically solving the TDSE for an ensemble of H_2^+ molecules, where the alignment degree was found out to modulate the harmonic spectrum. Surprisingly a rather simple *two-centre interference model* could explain the results. If an homonuclear diatomic molecule is considered and only its HOMO is contributing to the spectrum, the molecular orbital in LCAO theory can be written as (see Appendix C):

$$\psi_{el} = \phi_{\text{at}}\Big(\mathbf{r} - \frac{\mathbf{R}}{2}\Big) \pm \phi_{\text{at}}\Big(\mathbf{r} + \frac{\mathbf{R}}{2}\Big)$$

[3]This is not strictly true since in this case recombination is a single-photon process while tunnelling ionization is intrinsically a multiphoton process. However the argument still stands from a qualitatively point of view.

where $\mathbf{R}$ is the interatomic distance and ϕ_{at} the atomic orbitals which are combined to form the molecular one, while the sign $\pm$ defines the symmetry of the wavefunction. In this way, if the plane-wave approximation for the returning electron holds, the recombination dipole can be directly computed:

$$\mathbf{d}_{\text{rec}}(t) = \langle \psi_{el} | \, \mathbf{d} \, | e^{i\mathbf{k}\cdot\mathbf{r}} \rangle$$

In the case of a symmetric orbital ($+$ sign) this gives:

$$\mathbf{d}_{\text{rec}}(t) = 2\mathbf{k} \cos\Big(\frac{\mathbf{k}\cdot\mathbf{R}}{2}\Big) \langle \phi_{\text{at}} | e^{i\mathbf{k}\cdot\mathbf{r}} \rangle \tag{2.5}$$

while for an antisymmetric orbital ($-$ sign) we have:

$$\mathbf{d}_{\text{rec}}(t) = i2\mathbf{k} \sin\Big(\frac{\mathbf{k}\cdot\mathbf{R}}{2}\Big) \langle \phi_{\text{at}} | e^{i\mathbf{k}\cdot\mathbf{r}} \rangle \tag{2.6}$$

By studying the prefactors of these expressions it is thus possible to obtain conditions for constructive or destructive interference between the harmonics emitted by the two electronic centres. Generally however constructive effects do not give a modulation in the spectrum as clear as the destructive ones, and so the model is mostly used to predict only such interference minima. For a symmetric orbital these are given by:

$$R\cos(\theta) = \Big(n - \frac{1}{2}\Big)\lambda_{el}$$

and for antisymmetric orbitals by:

$$R\cos(\theta) = n\lambda_{el}$$

Therefore their position in the spectrum depends on the distance between the two centres, the alignment angle and the orbital symmetry, encoding in this way important structural information about the system. Moreover, the solution of the TDSE predicts also the presence of a π phase-shift in the emission in correspondence of such minima. Afterwards the same model, even if rather approximated, was able to describe the spectra of more complex molecules, such as CO_2 [77]. In this case $\mathbf{R}$ is the distance between two centres of the electronic distribution in the orbital and is thus a purely electronic property. Indeed the fact that in diatomic molecules this is equal to the internuclear distance is only due to the natural LCAO description of such systems. However, for more complex systems the two-centre interference model cannot describe all the spectral structures that may be present, since both the static single-channel assumption and the plane wave approximation for the returning electron are expected to fail.

For instance, in bigger molecules the possibility to ionize multiple orbitals can give rise to multi-channel contributions in the spectrum. Indeed these channels are expected to gain a relative phase between ionization and recombination and will therefore provide another degree of freedom to produce interference patterns. The phase accumulated by the electron in a given channel can be decomposed in three parts [73]:

$$\Phi^c = \phi^c_{\text{ionization}} + \phi^c_{\text{continuum}} + \phi^c_{\text{recombination}}$$

The first term is linked to the relative phase that may be present upon ionization due to non-adiabatic effects and electron coupling. The second contribution is instead provided by the electron propagation and is composed by both the phase linked to the semiclassical action in the continuum and the one determined by the evolution of the hole in the cation. Therefore it is a function of the driving laser parameters such as its intensity and wavelength. Finally, the last term is given by the phase of the dipole matrix element upon recombination. As already treated, if only short trajectories contribute to the final spectrum, it is possible to establish a relation between the excursion time of the electron and the harmonic order due to the intrinsic atto-chirp of the emission. The interference between these channels will thus be visible as a minimum in the spectrum at a given photon energy. Since the continuum phase can be modified by both the intensity and the wavelength of the driving field, the position of the actual minimum will be altered by such parameters and for this reason this effect is usually named dynamical interference. One requirement for such interference to give an appreciable effect is that the contribution of the various channels to the high-harmonic signal should be comparable. Moreover, being intensity-dependent, it requires a quasi-adiabatic generation condition [57]. Indeed if short pulses are used, the interference effect will be washed out by the averaging over the pulse cycles.

The first experimental observation of such effect was given by Bucksbaum *et al.* [78], while the interplay of structural and dynamical interferences was analyzed in [73]. In particular, near a structural minimum both the relative contributions and the recombination phases of the channels vary heavily, obscuring the dynamical interference effect. Moreover, it has been demonstrated the possibility for the same molecule to show a structural or dynamical minimum depending on the driving wavelength that is chosen [79]. Indeed at lower wavelengths the minimum is located closer to the cutoff, where the contributions of the different channels may be comparable, giving the possibility for the dynamical interference to appear. Using longer wavelengths, instead, the cutoff region shrinks and the minimum shifts towards the plateau region, where the contribution of the HOMO is predominant and thus only a structural minimum can be observed.

2.2 Molecular alignment

As it was presented in the previous section, HHG from molecules is strongly dependent on their alignment with respect to the driving field and therefore this important parameter needs to be controlled in experiments. Many different approaches have been developed over the years in physics and chemistry for aligning molecules in the laboratory frame, one of which is the use of non-resonant strong field lasers. In this case the first experimental proof of molecular alignment prior to ionization was given by Normand *et al.* in 1992 [80]. The origin of such effect was found in the interaction between the non-resonant laser field and the dipole induced in the molecule due to the anisotropy of its polarizability.

Two main techniques of molecular alignment with strong field lasers have been developed. In adiabatic alignment long pulses are used, whose duration is much longer than the characteristic rotational period of the target molecule $\Delta t >> T_{\text{rot}}$ [81, 82]. In this way the molecule starts to align at the rising edge of the pulse and reaches maximum alignment at its peak. When the field is off, then, also the alignment effect is no more present. However the major disadvantage of such approach is that it is not possible to perform any field-free measurement on the molecular ensemble. In HHG experiments this creates a lot of problems, since the presence of another high-intensity field can lead to fast ionization and saturation of the medium. Therefore impulsive alignment is usually chosen, in which the aligning pulse has a duration much lower that the characteristic rotational period of the target molecule $\Delta t << T_{\text{rot}}$ [83]. In this way a coherent superposition of rotational states is excited by the laser, leading to a revival structure in time due to their periodic rephasing.
In this section we will briefly present the technique of impulsive alignment with linearly polarized fields, starting from the case of simple linear molecules and then moving to more complex ones. With this approach 1D alignment can be achieved, for which only one axis of the molecular system is aligned in the laboratory frame. More complex experimental setups can be used to achieve also 3D impulsive alignment of molecules [84, 85], but they will not be covered in this thesis.

2.2.1 1D alignment of linear molecules

From a classical point of view, laser-induced molecular alignment can be understood in terms of the torque imposed by the electric filed on the molecular dipole:

$$\boldsymbol{\tau} = \boldsymbol{\mu} \times \mathbf{E}$$

where the latter can be expanded in a Taylor series with respect to the external field:

$$\boldsymbol{\mu} = \boldsymbol{\mu}_0 + \alpha \cdot \mathbf{E} + ...$$

When the molecule has no permanent electric dipole $\boldsymbol{\mu}_0$, the interaction is thus governed by the molecular polarizability α. This is generally a tensorial quantity, which can however be diagonalized along the three principal axis of the molecule.

In the molecular frame for the simple case of a linear rotor it can be written as[4]:

$$\alpha = \begin{pmatrix} \alpha_\perp & 0 & 0 \\ 0 & \alpha_\perp & 0 \\ 0 & 0 & \alpha_{//} \end{pmatrix}$$

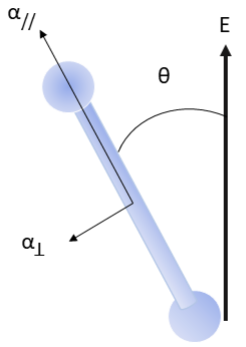

Figure 2.4: Representation of the geometry of the system. The angle θ describes the relative orientation between the molecular axis and the polarization direction of the driving field.

However, in order to evaluate the torque imposed in the laboratory frame it is necessary to determine the polarizability along the direction of the aligning field. If the latter is assumed to lie at an angle θ with respect to the molecular axis, the expression of the tensor in the laboratory frame will be:

$$\alpha = \begin{pmatrix} \alpha_{//} - \Delta\alpha\cos^2(\theta) & 0 & \Delta\alpha\sin(2\theta) \\ 0 & \alpha_\perp & 0 \\ \Delta\alpha\sin(2\theta) & 0 & \alpha_\perp + \Delta\alpha\cos^2(\theta) \end{pmatrix}$$

where $\Delta\alpha = \alpha_{//} - \alpha_\perp$. This allows to directly retrieve an expression for the torque induced by the external field, which can then be substituted in the equation for the evolution of the alignment angle $\theta(t)$:

$$I\frac{\partial^2\theta}{\partial t^2} = -E^2(t)\Delta\alpha\sin(2\theta)$$

From this expression it is clear that the induced molecular alignment is directly proportional to the external field amplitude and to the molecular anisotropy. For an impulsive electric field $E(t) = E_0\delta(t)$ and an initial position θ_0 the evolution of the alignment angle reads:

$$\theta(t) = \theta_0 - \Big(\frac{E_0^2\Delta\alpha}{I}\sin(2\theta_0)\Big)t$$

[4]Note that in principle the polarizability of the molecule an its moment of inertia could have different axis of diagonalization. However for small molecules these generally coincide and we will always assume such case in this thesis.

Thus for $\theta_0 \in [0, \pi/2]$ the torque tends to decrease this angle in time, until alignment is achieved[5]. In a molecular ensemble the alignment is then ensured by the fact that the rate of the induced angular motion is proportional to $-\sin(2\theta_0)$. In this way, molecules starting at higher angles will experience a faster rotation and they will be able to catch up with the ones starting from lower values of θ_0. However, this classical treatment allows to predict only the fast alignment induced right after the impulsive field, which is called prompt alignment, but cannot describe the revival structure that is experimentally measured.

For this reason a more precise quantum treatment is necessary [83]. In this framework the Hamiltonian of the system can be divided in two terms. The first one describes the field-free molecular system and the second one represents the interaction [86]:

$$\hat{H} = \hat{H}_{\text{mol}} + \hat{H}_{\text{int}}$$

Since we are considering the situation in which the IR field is far from resonances, the molecular Hamiltonian can be approximated with its purely rotational part (see Appendix C). Moreover, the second term can be written in dipole approximation as a function of the molecular polarizability for a molecule with no permanent dipole:

$$\hat{H}_{\text{int}} = -\sum_{\text{pp}'} E_p \alpha_{pp'} E^*_{p'}$$

If a linearly polarized sinusoidal field is considered, the cycle averaged interaction should be taken into account and the full Hamiltonian of the system for a linear molecule reads:

$$\hat{H} = B\hat{J}^2 + D_J\hat{J}^4 - \frac{E_0^2(t)}{4}(\Delta\alpha\cos^2\theta - \alpha_\perp) \tag{2.7}$$

The general rotational state of the molecule can be written as a superposition of spherical harmonics.

$$\Psi(t) = \sum_{\text{J}} c_J(t)\,|JM\rangle$$

$$|JM\rangle = (-1)^M\Big[\frac{(2J+1)(J-M)!}{4\pi(J+M)!}\Big]^{1/2}P_J^M(\cos\theta)e^{iM\phi}$$

where P_J^M are the associated Legendre polynomials. This expression can then be directly substituted in the TDSE in order to obtain a set of coupled differential equations for the $c_J(t)$ coefficients:

$$i\hbar\frac{\partial}{\partial t}c_J(t) = (BJ(J+1) + D_J J^2(J+1)^2 - \frac{E_0^2}{4}\alpha_\perp)c_J(t) - \frac{E_0^2}{4}\Delta\alpha\sum_{\text{J}',\text{M}'} c_{J'}(t)\,\langle JM|\cos^2\theta\,|J'M'\rangle$$

where the quantum operator for the angular momentum has been substituted with the correspondent expectation value. In order to simplify these equations, it is possible to exploit the properties of spherical harmonics:

$$\cos^2\theta\,|JM\rangle = a_0(J,M)\,|JM\rangle + a_2(J,M)\,|J+2,M\rangle + a_{-2}(J,M)\,|J-2,M\rangle$$

[5]Since molecular alignment and not orientation is considered, this is the angular range of interest. Indeed with linearly polarized fields it is not possible to control the orientation of the molecular axis.

$$a_0(J,M) = \frac{2(J^2 - M^2 + J) - 1}{(2J-1)(2J+3)}$$

$$a_2(J,M) = \sqrt{\frac{(J-M+1)(J+M+1)(J-M+2)(J+M+2)}{(2J+1)(2J+5)(2J+3)^2}}$$

$$a_{-2}(J,M) = \sqrt{\frac{(J-M)(J+M)(J-M-1)(J+M-1)}{(2J+1)(2J-3)(2J-1)^2}}$$

The term depending on $\cos^2\theta$ is thus responsible for the coupling of states with different J and the creation of a rotational wave packet. In particular, since it links only states with $\Delta J = \pm 2$ and $\Delta M = 0$, this is present between states with odd and even values of J separately. Substituting this result in the set of differential equations we get:

$$\begin{aligned} i\hbar\frac{\partial}{\partial t}c_J(t) = \Big[BJ(J+1) + D_J J^2(J+1)^2 - \frac{E_0^2}{4}(\Delta\alpha a_0(J,M) + \alpha_\perp)\Big]c_J(t) + \\ -\frac{E_0^2}{4}\Delta\alpha\Big[a_2(J-2,M)c_{J-2}(t) + a_{-2}(J+2,M)c_{J+2}(t)\Big] \end{aligned} \tag{2.8}$$

The coupling directly depends on both the anisotropy of the molecular polarizability and the electric field strength, similarly to the alignment effect found in the classical treatment. Therefore, once the initial occupation of the molecular rotational states is known, from Eq.(2.8) it is possible to numerically compute the wave packet induced by the aligning field.

After the pulse, the molecule is thus left in a state that can be written as the field-free evolution of such wave packet. If the centrifugal distortion is neglect this can be written as:

$$\Psi(t) = \sum_{\mathrm{J}} c_J(\tilde{t})e^{-i\mathcal{E}_J t/\hbar}\,|JM\rangle = \sum_{\mathrm{J}} c_J(\tilde{t})e^{-iBJ(J+1)t/\hbar}\,|JM\rangle \tag{2.9}$$

where the $c_J(\tilde{t})$ coefficients describe the final population induced by the aligning pulse. During the field-free evolution, at times multiples of $t_{\mathrm{rev}} = \pi\hbar/B$ the phase factor of each one of the $|JM\rangle$ states will be an integer multiple of 2π. In this way the wave packet will reproduce the state of the system at the start of the field-free evolution, which is the prompt alignment induced by the laser. This time period at which alignment is observed is called *rotational revival*. A lower degree of coherence may also be re-established at times that are fractions of t_{rev}, which are called *fractional revivals*, when only a smaller subset of spherical harmonics gets in phase. In particular, at times $t = t_{\mathrm{rev}}/4, 3t_{\mathrm{rev}}/4, 5t_{\mathrm{rev}}/4, ...$ states with odd and even values of J show an opposite revival dynamics, while at times $t = t_{\mathrm{rev}}/2, 3t_{\mathrm{rev}}/2, 5t_{\mathrm{rev}}/2, ...$ they have the same rotational behaviour. If the centrifugal distortion cannot be neglected, the energy levels of the rotational states have an additional term that prevents the perfect rephasing at times t_{rev}. This effect is more pronounced when field of higher intensities are used, since they populate also states characterized by large values of J, or for longer period of times during the rotational dynamics.

The theory developed so far explains the impulsive alignment of a single molecule, but generally in experiments we deal with a macroscopic medium. In this case a more precise description needs to account for the classical probability for each molecule to initially occupy a given rotational state. This can be done using the so-called density matrix formalism for mixed states. The density matrix operator for the system is defined as:

$$\hat{\rho} = \sum_{\mathrm{J,M}} p_{J,M} \left|JM\right\rangle \left\langle JM\right|$$

where the sum is extended to all possible spherical harmonics and the $p(J, M)$ coefficients are the classical statistical weights of each state. The evolution in time of such operator is described by the so-called Liouville equation:

$$i\hbar \frac{\partial \hat{\rho}}{\partial t} = [\hat{H}, \hat{\rho}]$$

and the expectation value for a generic operator $\hat{A}$ in the system can be computed as:

$$\left\langle \hat{A} \right\rangle = \mathrm{Tr}\left(\hat{\rho}\hat{A}\right) = \sum_{\mathrm{J,M}} p_{J,M} \left\langle JM\right| \hat{A} \left|JM\right\rangle$$

Before the interaction with the aligning pulse, the molecular gas can be treated as a canonical ensemble of particles, characterized by a certain rotational temperature T_{K} in Kelvin. In this way the initial statistical weights of the rotational states are described by the Boltzmann distribution:

$$p_{J,M}(0) = \frac{1}{Z} g_J e^{-\mathcal{E}_J / K_{\mathrm{B}} T_{\mathrm{K}}}$$

where K_{B} is the Boltzmann constant and Z the partition function for the system:

$$Z = \sum_{\mathrm{J,M}} e^{-\mathcal{E}_J / K_{\mathrm{B}} T_{\mathrm{K}}}$$

The statistical weights depend only on the quantum number J and therefore states that are different only for the quantum number M will have the same initial occupation probability. The prefactor g_J is linked to the symmetry properties of the considered molecule. Indeed the total molecular wavefunction Ψ_{mol} should commute with respect to all the symmetry operations of its group that permute identical nuclei without breaking or twisting any existing bond. Since the vibrational and electronic ground states of molecules are always symmetric with respect to all the group operations, the combination of nuclear and rotational wavefunctions needs to be symmetric with respect to permutations of an even number of fermions' pairs or any number of bosons and to be antisymmetric with respect to permutations of an odd number of fermions' pairs. It is known that rotational states are symmetric for even values of J and antisymmetric for odd values of J. Therefore, once the distribution of the nuclear spins of the atoms in the molecule is know, this sets a symmetry requirement for the rotational part of the wavefunction. In this way the population ratio between odd and even J states is defined, which is accounted for

by g_J [87]. For linear rotors this quantity will then be preserved by the interaction with the aligning field since $\Delta J = \pm 2$ from the selection rules. In this way such ratio will reflect on the presence and the strength of the fractional rotational revivals, during which states with odd and even values of J show a different behaviour, as we discussed above. For this reason fractional revival can be used as an indirect probe of the molecular structure.

Once the initial statistical weights for the rotational states in the gas are known, the evolution of the system due to the alignment dynamics induced by the external field can be found using Liouville equation. The alignment degree in the ensemble after the laser pulse can then be evaluated through the so-called *alignment parameter* $\langle \cos^2\theta \rangle$. Exploiting the density matrix formalism, this can be computed as:

$$\langle \cos^2\theta \rangle = \sum_{\mathrm{J,M}} p_{J,M}(\tilde{t}) \, \langle JM | \cos^2\theta \, | JM \rangle$$

where $p_{J,M}(\tilde{t})$ are the statistical weights describing the final population induced by the aligning pulse. For a random ensemble of molecules, such as the one present at $t = 0$, we have $\langle \cos^2\theta \rangle = 1/3$, while if $\langle \cos^2\theta \rangle = 1$ we have perfect alignment and if $\langle \cos^2\theta \rangle = 0$ perfect anti-alignment. In the former case the distribution of the molecular axis is peaked along the aligning field polarization direction, while in the latter the distribution is peaked on a plane perpendicular to it. During a rotational revival the alignment parameter spans between the limits of alignment and anti-alignment, without reaching a perfect condition for any of them. Outside the revival structure a baseline alignment is always present as $\langle \cos^2\theta \rangle > 1/3$ for any t. The origin of this effect can be understood with the simple semiclassical vector model for the angular momentum. Indeed, since during the interaction the quantum number M is conserved, the molecules that are excited to rotational states characterized by higher values of J will preferentially occupy the energy levels with $M \ll J$. Therefore they will on average rotate in a plane that is a little bit shifted towards the polarization direction of the aligning field.

Many factors can then influence the degree of alignment in experiments. Higher intensities, for example, allow to populate rotational states with higher J, giving rise to sharper and narrower peaks in the alignment parameter. Moreover an enanchement of the alignment is expected also when the initial rotational temperature of the molecular ensemble is lower. In this case, indeed, the states that are populated by the excitation are not initially occupied by the thermal motion and this allows to maintain an higher degree of coherence in the wave packet.

Anyway, it is important to underline that $\langle \cos^2\theta \rangle$ is only a phenomenological parameter, which cannot fully describe the alignment dynamics of the ensemble. Indeed only lower-order fractional revivals up to $1/4$ are described by such expectation value, while HHG is a physical process which is very sensitive to the rotational state of the target molecules and allows to record even higher-order fractional revivals [88]. Therefore a more complete description of the alignment dynamics of the system can be given once the full rotational wave packet $\Psi(\theta, \phi, t)$ is known, as a probability density function:

$$P(\theta, \phi, t) = \mid \Psi(\theta, \phi, t) \mid^2 d\Omega \tag{2.10}$$

which represents the probability to find the molecular axis lying within an infinitesimal solid angle $d\Omega$. The HHG intensity as a function of the probed time during the revival dynamics can then be expressed as:

$$I(t) = \left| \int H(\theta) P(\theta, \phi, t) d\Omega \right|^2$$

where $H(\theta)$ is the HHG signal from a single emitter perfectly oriented along the direction θ, which can be evaluated for example with the Lewenstein theory or the more simple two-center interference model[6]. Therefore to describe higher-order fractional revivals one could refer to this whole probability density function. Another more simple approach would be instead to consider the so-called cosine moments $\langle \cos^N \theta \rangle$. In particular the higher is the considered N, the higher is the order of fractional revivals that can be described by such expectation value [89].

2.2.2 1D alignment of complex molecules

Up to now we have considered the 1D alignment of linear rotors. However only few molecules belong to this class and as the complexity of the molecular system increases symmetric or asymmetric tops are much more common. Therefore it is essential to briefly sketch the alignment dynamics induced by an intense non-resonant linearly polarized field also for these classes of molecules. The case of symmetric top molecules is rather straightforward, but can also give an insight into the case of asymmetric rotors for which the Ray parameter is very near the prolate or oblate limit [90]. The interaction Hamiltonian is indeed the same of the simple linear case:

$$\hat{H}_{\text{int}} = -\frac{E_0^2(t)}{4} (\Delta\alpha \cos^2 \theta - \alpha_\perp)$$

which is independent from the Euler angle χ. For this reason also in this case the quantum number K, representing the projection of the angular momentum along the molecular axis, is conserved during the interaction with the external field. The main difference with respect to linear molecules is given by the field-free Hamiltonian which for prolate rotors reads:

$$\hat{H}_{\text{rot}} = B\hat{J}^2 + (A - B)\hat{J}_a^2 - \hat{H}_{\text{CD}}(\hat{J}, \hat{J}_a)$$

where $\hat{H}_{\text{CD}}(\hat{J}, \hat{J}_a)$ resumes the contribution given by the centrifugal distortions. As discussed in the previous section, this term starts to play a role for higher excitation intensities, higher initial temperatures or longer times in the revival and has the effect of deteriorating the regular rephasing of the rotational wave packet. In order to obtain the alignment dynamics of the molecule it is then necessary to solve the TDSE for the system. The generic rotational wavefunction of the system can be written as:

$$\Psi(t) = \sum_J c_J |JKM\rangle$$

[6] We are assuming in this case that the polarization of the field driving HHG is parallel to the one aligning the molecules. This is not always true, but corresponds to the experimental setup used in this thesis.

where $|JKM\rangle$ are eigenstates of the field-free Hamiltonian for symmetric rotors. Substituting this ansatz in the Schrödinger equation, a set of coupled differential equations is obtained:

$$i\hbar\frac{\partial}{\partial t}c_J(t) = \sum_{J'}[\langle JKM|\,\hat{H}_{\text{rot}}\,|JKM\rangle + \langle JKM|\,\hat{H}_{\text{int}}\,|J'KM\rangle]c_{J'}(t)$$

$$= \mathcal{E}_{\text{JK}}c_J(t) + \sum_{J'}\langle JKM|\,\hat{H}_{\text{int}}\,|J'KM\rangle\,c_{J'}(t)$$

where $\mathcal{E}_{\text{JK}}$ is the field-free rotational energy associated with the eigenstate $|JKM\rangle$ neglecting the centrifugal distortion term. To compute the matrix elements of the interaction Hamiltonian it is convenient to rewrite it as a function of Wigner rotation matrices:

$$\hat{H}_{\text{int}} = -\frac{E_0^2}{6}\Delta\alpha D_{00}^2(\mathbf{Q})$$

In this way it is possible to exploit their properties with respect to the symmetric rotor eigenstates:

$$\langle JKM|\,D_{\text{qs}}^2(\mathbf{Q})\,|J'K'M'\rangle = (-1)^{K'+M'}\sqrt{(2J+1)(2J'+1)}\begin{pmatrix} J & 2 & J' \\ M & q & -M' \end{pmatrix}\begin{pmatrix} J & 2 & J' \\ K & s & -K' \end{pmatrix}$$

where the Wigner 3-j symbol is used:

$$\begin{pmatrix} J_1 & J_2 & J_3 \\ M_1 & M_2 & M_3 \end{pmatrix} = \frac{(-1)^{J_1-J_2-M_3}}{\sqrt{2J_3+1}}\langle J_1M_1; J_2M_2|J_3(-M_3)\rangle$$

with $\langle J1M1; J2M2|J_3(-M_3)\rangle$ the Clebsh-Gordan coefficient for the composition of the angular moments (J_1, M_1) and (J_2, M_2) to form $(J_3, -M_3)$. Substituting these results it is possible to numerically solve the set of coupled equations and to retrieve the rotational dynamics of the excited wave packet. In particular, the selection rules for the excitation are $\Delta J = \pm 1, \pm 2$, $\Delta M = 0$ and $\Delta K = 0$. Therefore, differently from the linear rotor case, a coupling effect is also present between states characterized by a different parity of J. The resulting rotational wavefunction can be written as:

$$\Psi(t) = \sum_{\text{J}} c_J(\tilde{t})e^{-i\mathcal{E}_{\text{JK}}t/\hbar}\,|JKM\rangle$$

where $c_J(\tilde{t})$ are the population values of the rotational states after the aligning pulse is gone. The expression for the rotational revival time is the same of linear molecules $t_{rev} = \pi/cB$. Anyway only 1D alignment is achievable with this technique and for symmetric top molecules the aligned axis is always the one of higher polarizability, which is usually also the rotationally special one.

Then, when an ensemble of molecules is considered, the same density matrix formalism of Section 2.2.1 should be exploited. In the case of symmetric rotors the thermal agitation will initially occupy states with different J and K values. As the excitation conserves the K value while populating states of different J, at the revival time t_{rev} the coherence will thus be re-established only within states having the

same K, while states with different K will maintain a small phase difference. This reflects on the alignment parameter as a fine structure during the revival, which is a function of the ratio between the two distinct moment of inertia of the molecule $R = I_{cc}/I_{aa}$. In particular such structure is more visible when the molecule is near the perfect oblate or prolate case $R \to 1/2, 2$ and less when $R \to 1$, as it can be seen from Figure 2.5. Moreover, for perfectly spherical top molecules the revivals are completely washed out. This is due to the fact that in this case the molecular polarizability is completely isotropic and therefore no alignment is possible.

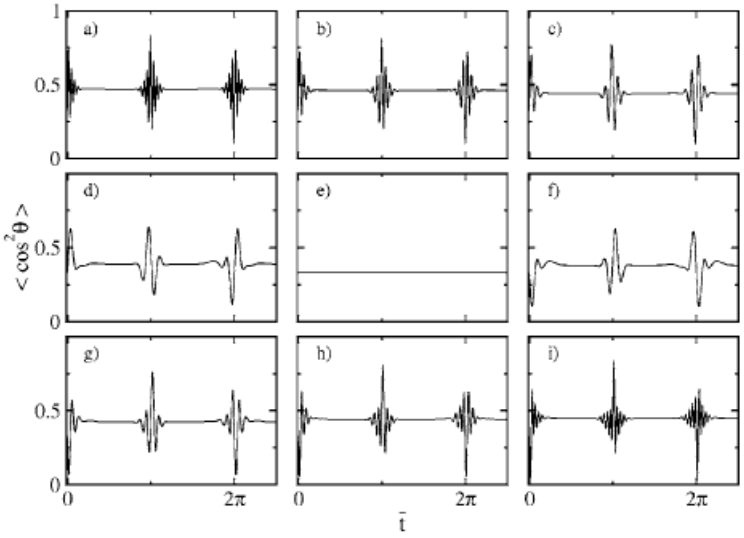

Figure 2.5: Variation of the revival fine structure with respect to the ratio between the two distinct moment of inertia of the molecule. Each image is taken at different values of R. a) 0.5; b) 0.625; c) 0.75; d) 0.875; e) 1; f) 1.14; g) 1.33; h) 1.6; i) 2. Image taken directly from [90].

An even richer rotational dynamics is expected from asymmetric top molecules [91]. In this case indeed both the moment of inertia and the molecular polarizability are different along all the three axis. The field-free Hamiltonian thus reads:

$$\hat{H}_{\text{rot}} = \frac{\hat{J}_a^2}{2I_{aa}} + \frac{\hat{J}_b^2}{2I_{bb}} + \frac{\hat{J}_c^2}{2I_{cc}}$$

where I_{ii} are the diagonal elements of the matrix of the molecular moment of inertia. Moreover, the energy levels are a function of both the quantum number J and the pseudo-magnetic quantum number τ (see Appendix C), while K is no more conserved. Also the interaction Hamiltonian is much more complex with respect to the symmetric top case:

$$\hat{H}_{\text{int}} = -\frac{E_0^2(t)}{4}(\Delta\alpha_{bc}\sin^2\theta\cos^2\chi + \Delta\alpha_{ac}\cos^2\theta) = -\frac{E_0^2(t)}{4}(\Delta\alpha_{bc}\cos^2\beta_b + \Delta\alpha_{ac}\cos^2\beta_a)$$

where we have defined $\Delta\alpha_{ij} = \alpha_i - \alpha_j$ the anisotropy of the polarizability along the molecular axis i and j. In any case, an asymmetric molecule can be aligned by the

external field only along its axis of highest polarizability. For instance, in the case of near-prolate rotors the interaction Hamiltonian shows a minimum for $\beta_a = 0, \pi$, a maximum for $\beta_c = 0, \pi$ and a saddle-point for $\beta_b = 0, \pi$ and so only the **a** axis can be efficiently aligned along the direction of the external field. To compute the alignment dynamics it is then necessary to solve the TDSE for the system. The most important difference with respect to symmetric top molecules is the fact that for asymmetric ones K is no more conserved and thus the generic wave packet reads:

$$\Psi(t) = \sum_{\mathrm{J,K}} c_{J,K}(t) \, |JKM\rangle$$

Substituting this ansatz in the equation, it is possible to obtain a set of coupled differential equations formally equal to the symmetric case:

$$i\hbar \frac{\partial}{\partial t} c_{J,K}(t) = \sum_{J',K'} c_{J',K'}(t) \Big[\langle JKM| \, \hat{H}_{\mathrm{rot}} \, |J'K'M\rangle + \langle JKM| \, \hat{H}_{\mathrm{int}} \, |J'K'M\rangle \Big]$$

where the matrix elements of the interaction Hamiltonian can be easily found once they are rewritten as a function of Wigner rotation matrices:

$$\hat{H}_{\mathrm{int}} = -\frac{E_0^2}{4} \Big[\frac{\alpha_{ac} + \alpha_{ab}}{3} D^2_{00}(\mathbf{Q}) - \frac{\alpha_{cb}}{\sqrt{6}} [D^2_{02}(\mathbf{Q}) + D^2_{0-2}(\mathbf{Q})] \Big]$$

while the matrix elements of the field-free Hamiltonian for the considered molecule can be calculated numerically. The selection rules for the excitation are $\Delta J = 0, \pm 1, \pm 2$, $\Delta K = 0, \pm 2$ and $\Delta M = 0$. Since K is not conserved in the process and the rotational levels of asymmetric molecules lack of any regularity, the rotational wave packet will show more frequency beats in its dynamics. The revival structure is therefore a lot more complex with respect to linear or symmetric top systems and doesn't show a simple periodic behaviour.

CHAPTER 3

Experimental setup

In this chapter the experimental setup used in this thesis work will be briefly presented. In particular, the experiments have been carried out in the Ultras (center for ultraintense and ultrafast optical science) and UDynI (Ultrafast DYnamic Imaging) laboratories of the Physics Department in Politecnico di Milano. Each one of these laboratories will be covered in a separate section, highlighting similarities and differences when necessary. In a third section we will present the technique used to obtain the microstructured structures that were used to confine the medium in some experiments.

3.1 Ultras laboratory

3.1.1 Laser system

The driving beam in Ultras is delivered by a two-stages optical parametric amplifier (OPA) pumped by a CPA Ti:Sapphire laser system and tunable in the MIR range between 1400 nm and 1800 nm with a few-cycle duration at a repetition rate of 10 Hz. The choice of MIR driving wavelengths is done to reach a good compromise between cutoff extension and signal in HHG experiments. The laser system starts with a commercial Kerr Lens Mode-Locked Ti:Sapphire oscillator (central frequency $\lambda_f \approx 800$ nm) that delivers 45 fs pulses at a rate of 76 MHz and with an energy content of 5nJ. The pulses are then stretched to 200 ps using a dispersion grating and are selected by a Pockels cell at a rate of 1 kHz in order to enter the amplification section, which is composed of two stages. The first one is a regenerative amplifier, that allows to reach an energy of 3 mJ. Only one pulse every hundred is then selected to enter the second stage, which is a multi-pass amplifier employing a water-cooled crystal. In this way it is possible to reach very high intensities, delivering pulses at a repetition rate of 10 Hz and with an energy content between 2 mJ and 120 mJ, tunable through the pump of the second stage. In particular, for HHG experiments the amplification section is usually setted to a low-energy content of around 15 mJ. The beam is then coupled to a small hollow core fiber where rough vacuum is made. In this way the waveguide acts as a filter that cleans the spatial beam shape, through propagation in the HE_{11} fundamental mode of the fiber. After compression, the linearly p-polarized pulses have a duration of 60 fs and an energy content of almost 12 mJ .

The beam is then divided into four lines by a cascade of three beam-splitters. The first three beams (a,b and c in Figure 3.1) are then used for producing the final driving field in the OPA system, while the fourth (d in Figure 3.1) is used to perform molecular alignment.

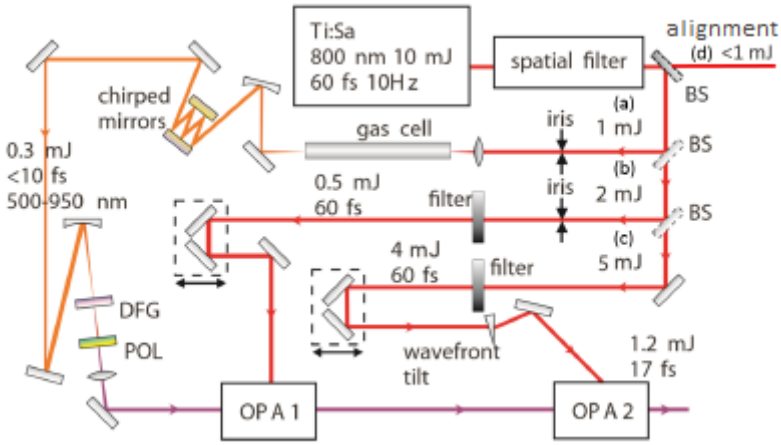

Figure 3.1: Sketch of the optical setup of the OPA system in Ultras. Image adapted from [92].

In particular, beam (a), with an energy content of around 1 mJ, is focused inside a gas cell filled with Kr gas, where optical filamentation takes place. This is a physical effect for which the laser can travel collimated for high distances in a ionized gas due to the equilibrium between plasma defocusing and self-focusing induced by the Kerr-effect in the neutrals. The radiation is in this way spectrally broadened, generally between $\lambda = 500$ nm and $\lambda = 950$ nm, exploiting the self-phase modulation (SPM) taking place in the plasma so that it can be subsequently recompressed. This is achieved with the use of chirped mirrors, which allow to reach a final pulse duration of almost 10 fs with an energy content of around 0.3 mJ. Moreover, the filamentation process has also been proved to further clean the spatial shape of the beam [94].

The pulses are then focused into a 400 µm thick β-BBO crystal where difference frequency generation (DFG) takes place between the spectral tails of the same pulse. In this way a broad MIR spectrum between $\lambda = 1400$ nm and $\lambda = 1800$ nm is generated. Since the nonlinear process takes place within the same pulse, only type II phase-matching can be achieved and the MIR signal is thus polarized perpendicularly with respect to the fundamental field (s-polarized). In this way it can be easily selected by a following polarizer. Moreover the DFG process allows also to obtain pulses with a stable carrier envelope phase (CEP), which is essential to generate isolated attosecond pulses. Anyway, the DFG radiation is used as the seed for the two OPA stages. Beam (b), with an energy content of around 2 mJ, is

used as the pump in the first one of these, composed by a 2 mm thick β-BBO crystal, after being temporally overlapped with the seed through a delay stage. Beam (c), with an energy content of almost 5 mJ, is instead used in the second OPA stage, composed by a 3 mm thick β-BBO crystal, after being also in this case synchronized with the seed by means of a delay stage. Moreover a prism is used on its path to tilt the wavefront of the pulses for further increasing the spatio-temporal overlap between the pump and the seed, enanches the efficiency of the second OPA stage. Both crystals operate at very narrow angles ($\sim 2^\circ$) between pump and seed, in order to easily select the output signal through an iris. The employment of type II phase-matching allows also to obtain a wide range of wavelength tunability of the system by tilting the crystals. The optimum output at $\lambda = 1450$ nm has an energy content of 1.2 mJ and a pulse duration of 17 fs, which is only slightly longer than the transform limited duration of 16 fs for its bandwidth. This OPA system was completely developed by the group of Proff. S. Stagira and C. Vozzi [92, 93].

Beam (d), with an energy content < 1 mJ, is instead exploited to perform molecular alignment. In order to improve its spatial shape and to broaden its spectrum, it is focused in an Ar-filled gas chamber where it undertakes filamentation. In this way, using a glass-plate its temporal duration can be further increased quite easily until around 100 fs, exploiting the more efficient dispersion in the broaden bandwidth. Then, a high- precision delay stage (± 0.28 fs) allows to control remotely from a computer the temporal distance between the aligning and generating pulses in the experiment. Moreover a $\lambda/2$ plate is placed on the line of the aligning field at 45° in order to make the polarization of the two beams parallel, which is the experimental condition chosen for all the experiments presented in this thesis work. Finally, a dichroic mirror is used to recombine the aligning and the driving beams in a collinear configuration during the experiments.

3.1.2 Generation and detection chambers

Since the XUV radiation is highly absorbed by air, both the generation and detection chambers are maintained in high vacuum ($\approx 10^{-6 \div 7}$ mbar) using turbomolecular pumps. The beams enter the first chamber through an iris, which can be used for tuning the focusing conditions during the experiments, and a small window. Here they are focused by a $f = 12.5$ cm mirror onto the gas jet. This is provided by a pulsed electromagnetic valve with a nozzle diameter of around 500 µm, an opening time of 300 µs and a repetition rate of 10 Hz in order to be synchronized with the driving beam. The gas expansion in vacuum induces also the cooling of the sample, which eases its alignment and avoids collisions between the particles. The position of the valve can be finely tuned with respect to the focus of the driving beam using a computer assisted translation stage in all three cartesian directions. In particular, its maximum excursion is 5 cm along the optical axis and 12.5 mm in the two orthogonal directions.

After generation, the light is collected through a 1 mm aperture placed at 20 cm from the interaction region, which allows to spatially filter out the non-collinear contribution to the harmonics. From here the beam enters the second chamber

where an XUV spectrometer allows to disperse the radiation, which is then analysed by means of a MCP-intensified CCD. This system was developed in collaboration with the group of Dr. L. Poletto from CNR-IFN Padova and consists of a toroidal mirror and a spherical varied line spacing (SVLS) grating, both at grazing incidence to minimize light absorption [95, 96]. The toroidal mirror focuses the harmonic radiation in both the tangential and sagittal plane, even if in two different positions. In particular, for the latter the focus lies before the grating while for the former it is exactly at the detector surface. The grating, on the other hand, focuses the radiation only in the tangential plane at a different position $q(\lambda)$ for each wavelength, thus ensuring the spatial separation of the frequency components on the detector surface. The groove density d of the SVLS grating is not constant but follows a polynomial law with respect to the coordinate y on its surface, with the origin placed in the center of the grating [96]:

$$d(y) = d_0 + d_1 y + d_2 y^2 + d_3 y^3$$

For this reason it can be demonstrated that the spectral focal surface of the spectrometer is described by the equation:

$$\frac{\cos^2\alpha}{p} + \frac{\cos^2\beta}{q} - \frac{\cos\alpha + \cos\beta}{R} + m\lambda d_1 = 0$$

where p and q are respectively the incoming and exit arm of the spectrometer, α and β the incidence and diffracted angle and m the considered diffraction order. The two angles depend further on the considered wavelength through the well-known grating equation:

$$\sin\alpha - \sin\beta = m\lambda d_0$$

Many of the grating parameters are fixed by the scientific requirements on the spectral resolution and the efficiency throughout the bandiwidth, while R and d_1 can be chosen to minimize the deviation between the spectral focal surface $q(\lambda)$ and the detector surface for the frequency range of interest. Higher-order aberrations on the focal plane, such as coma and spherical aberrations, can then be also minimized by an appropriate choice of the parameters d_2 and d_3. The SVLS grating used in Ultras is a golden coated one manufactured by Hitachi, whose parameters are shown in Figure 3.2. The two foci of the toroidal mirror can then be decided independently. In particular, the one on the tangential plane is chosen to maximize the incoming flux on the grating and to work at unity magnification on the detector plane. In this way high-order aberrations on this plane are minimized. The focus on the sagittal plane is instead positioned to compensate the grating astigmatism. Point sources can in this way be acquired as points at the detector plane. The toroidal mirror is platinum-coated and also its working parameters are given in Figure 3.2. Finally, the detector is a single-stage MCP-intensified CCD with magnesium fluoride (MgF_2) photo-cathode. The MCP is manufactured by Photeck and has an outside diameter of 40 mm with a pore size of 10 µm and a pitch of 12 µm. The photoelectrons are accelerated insider the micro-channels by a voltage drop of 900 V and then by a voltage of 4.5 kV onto the phosphor screen where light is released upon impact.

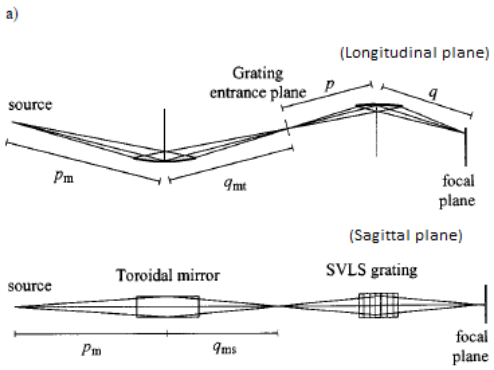

b) Toroidal mirror	
Tangential radius	6500 mm
Sagittal radius	14.7 mm
Incidence angle	86°
Entrance arm	453 mm
Tangential focus	453 mm
Sagittal focus	137 mm
Size—tangential×sagittal	60 mm×20 mm
c) SVLS grating	
Incidence angle	87°
Central groove density	1200 lines/mm
Radius	5649 mm
Blazed wavelength	10 nm
Entrance arm	237 mm
Size—tangential×sagittal	50 mm×30 mm
Ruling parameters	$d_1 = -8.497\ \text{mm}^{-2}$ $d_2 = 5.142\times10^{-2}\ \text{mm}^{-3}$ $d_3 = 3.153\times10^{-4}\ \text{mm}^{-4}$

Figure 3.2: a) Sketch of the instrument view along both the longitudinal and sagittal plane. b) Parameters of the toroidal mirror. c) Parameters of the SVLS grating. The images are adapted from [96].

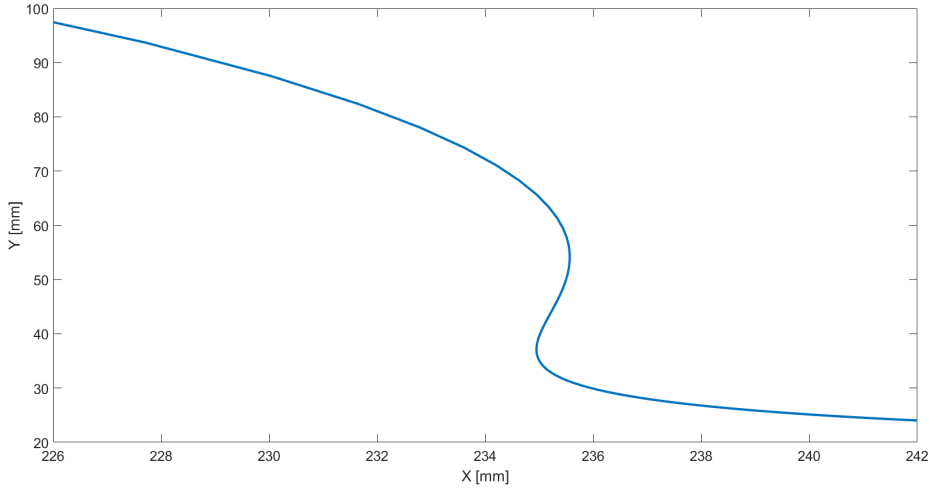

Figure 3.3: Sketch of the spectral focal surface of the grating.

The signal is analysed by a low-noise CCD camera manufactured by Hamamatsu with $1280x1024$ pixels of $6.7x6.7$ μm^2 size. The limited extension of the MCP and the camera thus limit the spectral window over which harmonics can be measured. For this reason, all the detector system is mounted on a motorized translation stage, which can be moved along the spectral focal surface of the grating in a circular motion. This allows to collect radiation from a wider wavelength range, even if the higher efficiency region is limited between 5 and 80 nm.

3.2 UDynI laboratory

3.2.1 Laser system

The oscillator in UDynI is a Ti:Sapphire laser system (Femtolaser Synergy), with central frequency $\lambda = 800$ nm, pumped by a intracavity frequency doubled Nd:YLF CW laser (Laser Quantum) and delivering 40 fs pulses with an energy of 6 nJ and a repetition rate of almost 75.28 MHz. The laser system as a whole was instead developed by Amplitude Technologies. Initially the beam is temporally stretched with a diffraction grating to enter three cascade CPA amplification stages. Before them, an acousto-optic modulator (Dazzler, Fastlite) acts as a grating allowing to introduce high-order dispersion terms in the pulses in order to facilitate their amplification and to reduce their temporal duration by pre-compensating the dispersion. Moreover the repetition rate is lowered to 1 kHz through a pulse selection device. The first amplification stage is a regenerative amplifier with a cooled Ti:Sapphire medium pumped by a frequency doubled Q-switched Nd:YLF laser (Evolution, Coherent). In the cavity an acousto-optic device (Mazzler, Fastlite) introduces frequency-selective losses and thus allows to maintain the spectral shape of the pulse and to compensate for the gain-narrowing of the medium. This effect is optimized using a procedure in which the beam after the regenerative cavity is analysed with a spectrometer and a feedback loop is established in order to make its spectral shape as similar as possible with respect to a reference one (Mazzler loop). After this stage the pulse energy is up to 0.5 mJ and the spatial shape of the beam is cleaned by the regenerative cavity. The second stage is instead composed by a standard multi-pass amplifier allowing to reach few mJ of pulse energy. Here a beam-splitter divide the output in two beams: a high-energy line ($\sim$ 15 mJ), which passes in the third amplification stage and is used for strong field experiments, and a low-energy line ($\sim$ 2 mJ), which enters in a independent compressor and is used for terahertz and ultrafast spectroscopy experiments. The third amplification stage is a multi-pass system where the amplifying medium is cooled to -135°C with a closed-circuit helium cryostat. This allows to limit thermal effects while amplifying high intensity pulses up to 17 mJ. To avoid condensation, the system operates in a small vacuum chamber with the employment of a ionic pump. After the amplification section a pair of facing cooled diffraction gratings are used to compress the duration of the pulses down to almost 25 fs.

3.2.2 Generation and detection chambers

Afterwards the beam enters through an iris, used to tune the focusing condition in the experiments, and a small window into the generation and detection chambers, where high vacuum ($\approx 10^{-6 \div 7}$ mbar) is maintained by means of turbomolecular pumps. Here a mounting is used to hold the chip used for the experiments of high-order harmonic generation in microchannels. Three motorized slits (Micronix) allow to remotely move it along all three Cartesian axis from a computer even when the chamber is sealed to maintain the vacuum. Onto the chip mounting a

swage-lock jack is positioned with UV-glue and Teflon tape to allow the gas supply in the channel. The flow is controlled from outside the chamber by a leak valve and a pressure gauge. When needed the chip can be removed to make space for a pulsed electromagnetic valve (Parker Corporations, series 9). This has a nozzle diameter of around 500 µm, operates at a repetition rate of 20 Hz and can be used for comparison tests between the tight focusing and the guided geometry or to perform other kinds of experiments.

The emitted radiation is then collected through a small iris to filter out the non-collinear light into the detection chamber. Differently from the Ultras laboratory, the spectrometer is here composed by two toroidal mirror and a final SVLS grating at grazing incidence. This allows to have an intermediate focus between the first two mirrors, which is useful when a target is needed, for instance to perform pump-probe experiments with attosecond pulses. Moreover the second toroidal mirror is placed on a translational stage that hosts also a spherical mirror. Such spherical

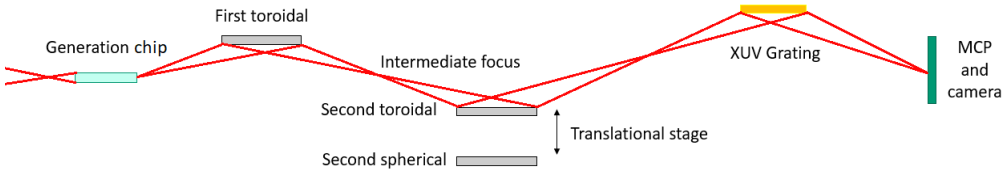

Figure 3.4: View in the longitudinal plane of the setup in the generation and detection chambers of the UDynI laboratory.

mirror, differently from the toroidal one, doesn't focus the beam in the sagittal plane and thus allows to characterize the divergence of the XUV radiation along this direction. The final part of the spectrometer, composed by the SVLS grating operates, instead, exactly in the same way as described in Section 3.1.2.

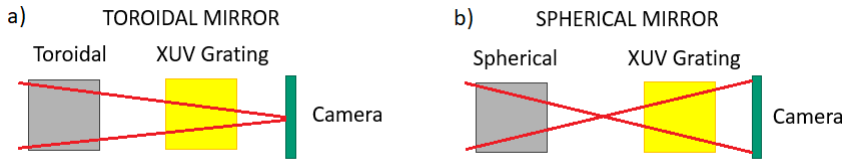

Figure 3.5: Sagittal view of the second mirror and the SVLS grating. a) Toroidal mirror configuration: the beam is focused directly on the detector plane. b) Spherical mirror configuration: a focus is present before the SVLS grating and the radiation maintain a certain angle on the detector plane in this direction, which can be used for evaluating the beam divergence.

Moreover, as in Ultras, the detector is a single-stage MCP-intensified CCD with magnesium fluoride (MgF_2) photo-cathode, an outside diameter of 40 mm, a pore size of 10 µm and a pitch of 12 µm manufactured by Photek. In this case

photoelectrons are accelerated inside the micro-channels by a voltage drop of 800 V and then by a voltage of 4.5 kV onto the phosphor screen. The CCD is instead a low-noise level camera manufactured by Apogee with a sensor size of $1920x1080$ pixels, which is cooled down to $35°C$ below room temperature in order to further limit the contribution of thermal noise.

3.3 Femtosecond laser micromachining

Femtosecond laser micromachining (FLM) is a technique which allows to induce permanent modifications in a transparent medium due to its nonlinear interaction with a ultrashort laser pulse. In this way, it is possible to inscribe waveguides or dig channels in the bulk of the material, with a control on the spatial parameters down to the micron scale. The main advantage of such technique with respect to the more traditional ones is the possibility to obtain arbitrary complex monolithic chips. Indeed FLM is a truly 3D fabrication technique, differently from standard planar technology in which the final device is obtained by subsequent layers. Moreover the fabrication is performed only by the relative motion of the material with respect to the laser focus and thus it doesn't need the employment of complex masks.

In this section we will briefly present the FLM technique, with special attention to the realization of the hollow structures exploited in this thesis, and the experimental setup used to perform such fabrication. In particular, in Section 3.3.1 the theoretical aspects of the interaction between short laser pulses and transparent materials will be covered, while in Section 3.3.2 the working parameters important for the fabrication process will be analysed. Finally, in Section 3.3.3 the laser system exploited for the realization of the devices used in this thesis will be presented. The experimental activity concerning FLM was performed by the group of Proff. R. Osellame and R. M. Vázquez from CNR-IFN Milano.

3.3.1 Interaction of short pulses with transparent materials

When a laser in the NIR region of the spectrum interacts with a glass the direct linear absorption of light is generally forbidden by the bandgap of the medium. If ultrashort pulses are employed, however, the intensity in the focal region can easily reach values above $I = 10^{11}$ W/cm^2, which is enough to trigger a nonlinear response in the material. Under certain circumstances this can lead to the absorption of the incoming radiation and a subsequent permanent modification of the medium that is highly confined in space due to the nonlinear nature of such interaction. The physical picture behind this process is not yet clear, but generally the dynamics can be divided in three steps:

I. The laser locally ionizes the material, leading to the formation of free electron plasma. In this way a lot of energy is deposited by the radiation in the focal spot.

II. The system relaxes and the energy is released to the bulk.

III. Permanent modifications of the medium appear as the accumulated energy is dissipated.

Strong field ionization has been already covered in Section 1.1.1. For the fabrication parameters commonly used in FLM the value of the Keldysh parameter in glasses is $\gamma \approx 1$ so an equal contribution of MPI and TI is expected. However if this were the case, the threshold intensity for optical breakdown would highly scale

with the material bandgap, which is not observed in experiments [97]. Therefore a third mechanism is actually responsible for plasma formation, that is avalanche photoionization. This process starts with the liner absorption of the incoming radiation by free carriers present in the conduction band of the medium, which are thus subsequently accelerated. When these have enough energy, they may then impact ionize other bound electrons. The process can then repeat itself continuously, releasing more and more particles and increasing the free carrier percentage rapidly, until plasma is formed. Note that this mechanism is not present in single atoms or molecules but only in solids, since it requires the initial presence of free electrons in order to seed the avalanche process. Generally these can be provided both by the thermal excitation of defect states in the medium gap or by MPI and TI. Employing femtosecond pulses with high peak intensity it is possible to trigger preferentially the latter, allowing thus for a more precise and spatially selective machining. Indeed this leads to a more deterministic optical breakdown with respect to avalanche ionization seeded by defect states, which is instead highly dependent on the distribution of impurities in the material.

After plasma is formed, the system releases the accumulated energy to the lattice on a time scale of tens of picoseconds. For very short femtosecond pulses the absorption and ionization processes are therefore efficiently decoupled from the heat diffusion in the material, increasing the precision and confinement of the induced modification. Depending on the working parameters, a different regime can be triggered by the relaxation process [98]:

I. At low energies, just above the threshold to induce permanent modifications ($I \approx 10^{11}$ W/cm^2), a smooth refractive index change is obtained, due to the local densification of the melted medium and the formation of color centers [99, 100]. The material quality and transparency are maintained and thus this regime is generally employed to write waveguides [101].

II. At intermediate intensities ($I \approx 10^{12}$ W/cm^2) the formation of nanogratings and cracks is observed, leading to a birefringent refractive index change [113]. This is the produced by an inhomogeneous dielectric breakdown and by the growth of nanoplanes from the blending of different nanoplasmas. In this way a selective etching of the material is possible, with the consequent creation of buried channels in the bulk [103].

III. At higher intensities ($I > 10^{14}$ W/cm^2) the relaxation creates empty voids surrounded by a higher refractive index cladding. This is due to the absorption of a lot of energy by the plasma in a small time window, which induces microexplosions and shock waves [104].

Owing to the purpose of this thesis we will now on concentrate mainly on the second regime. In this case the formation of plasma in the focal volume of the laser induces a local reduction of the material effective energy gap. The region thus becomes a preferential absorbing site for the radiation and a positive feedback sets in, leading to the initial formation of spherical-shaped nanoplasmas [108]. The electric

field of the laser beam then enhances the energy deposit in a preferential direction, perpendicularly to its polarization, breaking the symmetry of the nanoplasmas and generating nanoplanes [109]. Afterwards, when the increasing electron density in the material reaches the critical value for which the plasma frequency is equal to the one of the incoming laser, the planes become effectively metallic and start to influence the light propagation in the glass. In this way, the initially randomly spaced nanoplanes turn into a parallel configuration with a separation of $d = \lambda/2n$, where λ is the laser wavelength and n the material refractive index. For all these reasons the interaction dynamics depends highly on the polarization of the incoming field and it is a cumulative process rather then the effect of a single pulse.

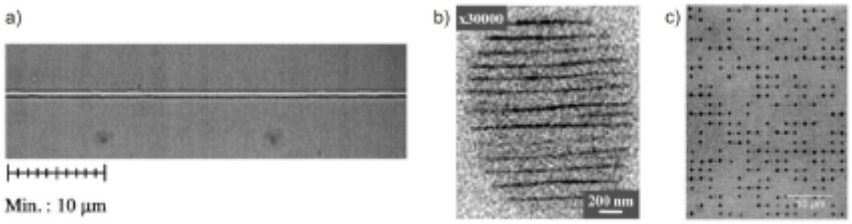

Figure 3.6: Three different regimes of modifications induced by a femtosecond laser in a transparent material. a) Smooth refractive index change. Image taken from [105]. b) Birefringent refractive index change due to nanogratings formation. Image taken from [106]. c) Empty voids in the material. Image taken from [107].

After the material is modified, hollow structures can be manufactured by means of a technique called femtosecond laser irradiation followed by chemical etching (FLICE) [97]. Indeed, silicon oxide is known to undergo a chemical reaction when it interacts with hydrofluoric acid:

$$SiO_2 + 4\,HF \longrightarrow SiF_4 + 2\,H_2O$$

The nanoplanes created by the laser act as a stimulant for this reaction, since they help the diffusion of the acid, and thus a selective etching of the material can be achieved. Moreover, also an higher reactivity is expected from the irradiated regions owing to the reduction of the length in the $Si - O - Si$ bridge, which deforms the oxigen valence electrons. For increasing the efficiency in the fabrication of the hollow structures the temperature of the acid solution should then be optimized and the material should be immersed in an ultrasonic bath allowing the fast removal of the etched material from the capillary hole [110].

3.3.2 Working parameters

Many working parameters can influence the micromachining process and its final result. One of the most important of them is the repetition rate of the laser source, which needs to be compared with the characteristic time of heat transfer in the medium. For fused silica such value is $t_{\text{heat}} \approx 1$ µs and thus three main different situations are possible:

I. For $f_{\text{rep}} \approx 1\text{kHz} - 200\text{kHz} \ll f_{\text{heat}}$ we are in the single pulse interaction regime, as the region is heated and cooled many times when exposed to successive pulses. The modification of the medium is therefore strongly affected by the focal volume, resulting in an elongation along the propagation direction of the beam. The writing speed is in this case low (≈ 10 µm/s) but the pulse energy is big enough to allow only a mild focusing. Regenerative amplified Ti:Sapphire systems are usually employed in this case.

II. For $f_{\text{rep}} \approx 200\text{kHz} - 4\text{MHz} \approx f_{\text{heat}}$ an intermediate regime is present, in which both a discrete translational speed and a mild focusing can be achieved. Yb-based lasers can thus be used, which deliver pulses with an energy content of hundreds of nJ.

III. For $f_{\text{rep}} > 4\text{MHz} \gg f_{\text{heat}}$ we are in the multiple pulses interaction regime, as the energy of different laser shots builds up in the region without the possibility for heat to diffuse in the time interval between them. The accumulated heat thus melts the material in a cylindrical symmetric region which extends much over the focal volume and washes out the main dependences on the laser spatial parameters. These repetition rates are achieved using long cavity Ti:Sapphire lasers with low energy output in the nJ range. Therefore focusing systems with a high numerical aperture must be used in order to obtain a high enough intensity in the interaction spot. However fast writing speeds in the range of some cm/s can be achieved.

Depending on the energy content of the pulses delivered by the laser source different focusing conditions are thus necessary. Once the numerical aperture (NA) of the focusing system is known, the waist radius and the Rayleigh length of the beam in the material can be computed:

$$w = \frac{M^2\lambda}{\pi NA} \qquad\qquad x_R = \frac{M^2 n\lambda}{\pi NA}$$

where M is the quality factor of the Gaussian beam. This is an empiric parameter that evaluates the degree to which the beam can be focused for a given divergence angle. These two parameters define the focal spot volume of the beam and thus the material region that is modified by the incoming radiation. Deviations from such values are mainly due to aberrations of the optical system, which are more pronounced for high NA, and to the nonlinearities of the medium influencing the focusing dynamics, such as Kerr effect and plasma defocusing. As a result, there is a strong dependence of the micromachining process with respect to the considered depth in the material [111, 112].

Moreover the fabrication can be influenced also by the velocity and the geometry of the laser writing system. In particular the effective number of pulses provided by the source can be computed as:

$$\#_{\text{pulses}} = \frac{2w}{v_{\text{translation}}} f_{\text{rep}}$$

which thus defines the effective energy deposited in the medium. Two main writing geometries are present. When the movement of the sample is parallel to the beam, the cross section of the modified region is regular and cylindrical symmetric due to the Gaussian profile of the laser. However the maximum possible length of the structure is limited by aberrations. For instance, in the case of a typical focusing system with $NA = 0.4$ this limit is $l \approx 5$ mm. When the movement of the sample is perpendicular to the beam, the cross section is instead irregular and suffers from a spatial asymmetry that may be evaluated as:

$$\frac{z}{w} = \frac{n}{NA}$$

This value for fused silica is in the range of $\approx 1.8 - 6$. However the maximum length of the structure is no more limited.

In the particular case of the formation of nanogratings for FLICE purposes, also the relative direction between the translation of the material and the polarization of the laser is then important. Indeed, if they are parallel the nanoplanes will be perpendicular to both and the diffusion of the acid will thus be obstructed by the cracks, reducing the effective digging rate. On the other hand, if they are perpendicular, the nanoplanes will be parallel to the sample writing and therefore the etching rate will be enhanced.

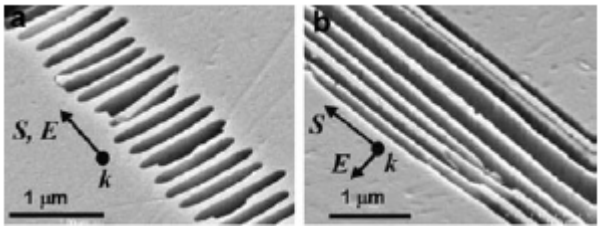

Figure 3.7: Scanning electron microscope images of nanoplanes formed at a depth of 65 µm. a) is for polarization direction perpendicular to the translation and b) for an electric field of the laser parallel to the sample movement. The images are adapted from [113].

Moreover the translation of the material can be in this case exploited to compensate the tapering of the channel that is induced by the exhaustion of the acid. Indeed the chemical reaction will be more efficient at the entrance of the hole with respect to the bulk of the material due to the different acid concentration. The resulting conic structure will thus show an apex angle that depends on the ratio between the etching rate of the non-irradiated medium and the diffusion efficiency of the acid in the nanoplanes. This angle is usually on the order of few degrees and can be evaluated once the radius at the entrance hole R_c and the length of the channel L_c are known:

$$\alpha = \tan^{-1}\left(\frac{R_c}{L_c}\right)$$

for compensating it, the irradiation can thus be performed in a conical spiral with a radius that increases with the material depth, as is shown in Figure 3.8. Sometimes

to enhance the final effect also the spiral axis is irradiated. In this way the etching is compensated by the inverse structure of the writing pattern. Moreover, if the electric field is maintained perpendicular to the translational stage, then the nanoplanes are parallel for different helices of the spiral and the acid can thus efficiently diffuse between them.

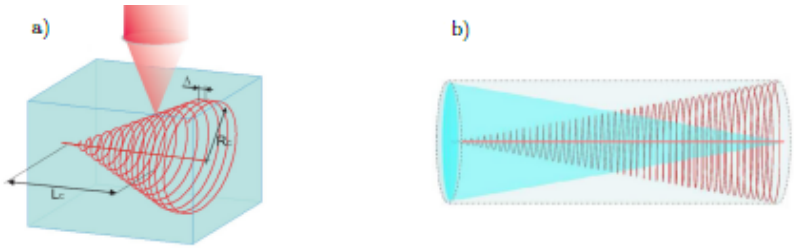

Figure 3.8: Technique used to compensate for the conical shape of the hollow channel. a) Schematic diagram of a conical spiral inscribed into the substrate. b) In light blue representation of an uncompensated conical microchannel and in red the compensating conical spiral. In dashed gray it is represented the expected final compensated cylindrical capillary. Image taken directly form [114].

3.3.3 Fabrication apparatus

The fabrication of the nanostructures used in this thesis for the experiments of high-order harmonic generation in hollow waveguides was performed in the FIRE (Fabrication by Infrared laser Radiation Exposure) laboratory of the Physics Department in Politecnico di Milano. The laser source in this laboratory is a commercial Yb:KYW (Potassium, Yttrium and Tungsten garnet) system manufactured by HighQLaser (FemtoREGEN) with a central wavelength of $\lambda \approx 1040$ nm and a tunable repetition rate up to ≈ 1 MHz. The oscillator is followed by a regenerative amplifier that produces pulses with an energy content up to 23 µJ. In particular, the maximum average power of the system is fixed at 8 W while three different output configurations can be selected: 23 µJ for $f_{\text{rep}} = 350$ kHz, 16 µJ for $f_{\text{rep}} = 500$ kHz and 8.3 µJ for $f_{\text{rep}} = 960$ kHz. After the amplification stage an electro-optic device acts as a pulse picker, enabling the selection down to one pulse every 255. In this way the final effective repetition rate can be tuned almost independently from the energy content of the pulses, increasing thus the flexibility of the source. At the end of such system pulses characterized by a duration of about 400 fs and a spatial profile with FWHM of 3 mm are achieved.

After the femtosecond source a rotating half-waveplate followed by a fixed polarizer acts as a power control unit, allowing to reduce the output energy for matching the desired one in the fabrication process. Then a mirror placed on a flip mounting allows to select between two paths. In one of them a LBO (Lithium triborate) nonlinear crystal is used to produce the second harmonic through type II phase matching [116]. An external temperature control unit is also employed

for better tuning the phase matching conditions in the crystal. The second arm is instead used to propagate the fundamental radiation in free space until a second flip mirror where the two beams are made collinear. In particular, for the devices used in this thesis only the second-harmonic beam was employed in the fabrication process.

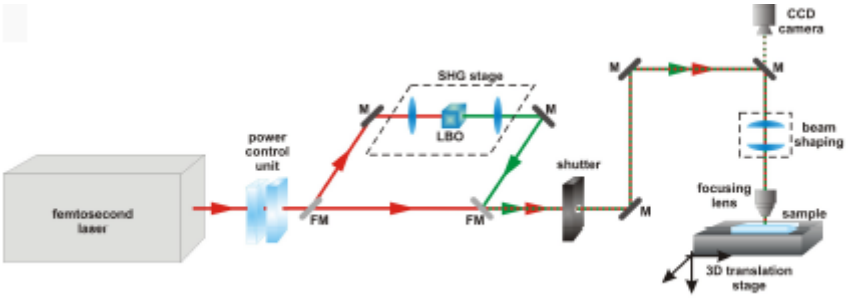

Figure 3.9: Sketch of the fabrication line in the FIRE labortory. Image taken directly from [115].

Following this stage an electro-mechanical shutter controlled from computer is used to synchronize the translation of the sample with the laser exposure time. The beam is then steered by a sequence of high-reflectance mirrors on the top of a 3D translation stage, where the sample is fixed on an horizontal plate that can be precisely moved in all three directions. The laser can thus inscribe the glass from above after going through a beam shaping stage and a focusing objective (NA=0.85). For diagnostic purposes a CCD camera is placed on top of the whole system to image the radiation that is back-reflected from the sample. This allows to align the writing beam with respect to the chip edges and surfaces with very high precision and reproducibility. The translation stage of the horizontal plate is placed on air bearings with electric brushless motors, allowing low friction even at high writing speeds. Its three axis can be moved up to $15x10x5$ cm in x, y and z respectively with a maximum speed of 15 cm/s.

The etching process is instead performed in a dedicated fume hood for the handling of HF acid, which ensures the quick removal of toxic fumes. The acid is diluted in deionized water for reaching the wanted concentration and the chip is then immersed in it using a polymer-protected beaker. An ultrasonic bath is also employed to facilitate the removal of the exhausted acid from the sample's hole and to enhance the chemical process along with a temperature control system. For monitoring the etching process in real time an optical microscope is present in the laboratory. Finally the sample is rinsed for several minutes in another ultrasonic bath with deionized water and isopropyl alcohol to clean it from the acid solution before being used.

CHAPTER 4

Results and discussion

4.1 Molecular alignment

In this section we will present the results of the molecular alignment experiments performed in Ultras, starting from a simple linear rotor such as CO_2 and moving to more complex systems such as ethylene, which is an asymmetric top molecule. The alignment was performed using a 800 nm pulse, while harmonics were generated by a 1450 nm beam, employing the setup discussed in Section 3.1. The synchronization between the two pulses was obtained both by measuring the generation of XUV continuum due to the temporal coincidence of the two fields and by checking their overlap in the far field. The valve backing pressure and position were instead optimized each time in order to maximize the harmonics' signal and the cutoff, while avoiding the clusterization of the molecules. For each molecule some scans were acquired as a function of the time delay between the aligning and the driving pulses using two motorized slits controlled through a Labview program developed by the group. When needed, the detector was also moved along the focal surface of the SVLS grating using a translation stage in order to cover multiple spectral regions.

In Section 4.1.1 we will present the procedure employed to calibrate such measurements both in frequency and in intensity, focusing in particular on the problems arising when connecting spectra taken at different detector positions. Each one of the studied molecules will then be covered in a separate section in order to outline the main results that were achieved with the data analysis.

4.1.1 Measurement calibration

The energy axis of the measurements was calibrated acquiring spectra in all the bandwidth of interest with Ne as generating medium and looking at the recurrence between the first and second order of the spectrometer. In particular, the fitting between the experimental results and the grating equation was performed with a Matlab code developed by Dr. D. Faccialà for obtaining the conversion relation between camera pixels and photon energies. The signal was also corrected by the Jacobian $J = d\text{pixels}/d\mathcal{E}$ in order to maintain constant the integral value of the harmonic intensity after the transformation of the axis.

When an extended bandwidth was acquired, acquisitions at different CCD

position had then to be connected. However, it is not possible to do this directly, even after the energy axis has been calibrated in all the regions. Indeed, the responsivity of the detector may depend on the considered pixel, thus deforming the shape of the harmonic spectrum between different acquisitions. In order to overcome this issue, we decided to exploit the small steps allowed by the motorized translational stage of the CCD. When the harmonic signal $S(\omega)$ is sampled in two very close detector positions, the spectrum is shifted on the camera by a small quantity Δx, measured in pixels, along the horizontal axis. The detected intensity $D(x, \omega)$ at the two positions can thus be written as:

$$D_1(x, \omega) = S(\omega)A(x)R(\omega)$$

$$D_2(x, \omega) = S(\omega)A(x + \Delta x)R(\omega)$$

where $A(x)$ and $R(\omega)$ are two functions accounting for the responsivity of the detector as a function of respectively the considered pixel position and the incoming radiation frequency. Performing easy mathematical steps, it is thus possible to construct an incremental ratio for $A(x)$, which can be approximated to a derivative for very small Δx:

$$\frac{D_2(x, \omega) - D_1(x, \omega)}{D_1(x, \omega)\Delta x} = \frac{A(x + \Delta x) - A(x)}{A(x)\Delta x} \approx \frac{1}{A(x)} \frac{\mathrm{d}A}{\mathrm{d}x}$$

This differential equation can be easily solved to obtain an analytical expression for the detector responsivity with respect to the pixel position:

$$\ln[A(x)] = \int \frac{D_2(x) - D_1(x)}{D_1(x)\Delta x} dx \rightarrow A(x) = exp\Big\{ \int \frac{D_2(x) - D_1(x)}{D_1(x)\Delta x} dx \Big\} \qquad (4.1)$$

where the constant term has been dropped since it represents only an overall scaling factor. This procedure allows thus to recover the responsivity function $A(x)$ and to calibrate the harmonic intensity in different spectral windows taking just two acquisitions at very close detector positions. However, it is important to underline that this method includes a lot of assumptions that may compromise its reliability. Fist of all, the definition of the incremental ratio is possible only as long as the detector responsivity can be factored out in the simple product of $A(x)$ and $R(\omega)$, so that the latter can be simplified. Physically this means that every pixel of the detector should have exactly the same spectral responsivity. This is usually not the case since, even if it is mainly determined by the physical design of its sensitive elements, some variability is always present in the manufacturing process. However, as a first approximation, this assumption may be considered true and its validity can then be checked a posteriori by the good outcome of the calibration procedure. Secondly, in order to limit the error in the approximation of the incremental ratio with a derivative, the translational step Δx should be small enough. For this reason the experimental setup must be able to deliver very tiny and precise movements of the detector, as in our case. Moreover, owing to this approximation the final result may also happen to depend somehow on the particular choice of Δx, even if we can expect this effect to be limited as long as the step is not too big. The last problem

arises then from the fact that the procedure is actually performed only on one of the dimensions of the detector. Indeed the radiation is focused in both the tangential and longitudinal plane onto the detector and the signal is then integrated along the vertical axis within a restricted region of interest (ROI) where the spectrum is concentrated. This is done to correct from the possible residual divergence of the harmonics. In this way, the final responsivity function is accounting only for the horizontal pixel position at a fixed detector line. In various acquisitions, however, the signal may lie along a different pixel row due to the changing of the experimental conditions. Therefore, strictly speaking, the found $A(x)$ is not a universal responsivity function and it may be necessary to apply this procedure before every scan in order to get precise results. Moreover, the slits of the translation stage are expected to have some roughness and for this reasons the two spectra used to derive $A(x)$ may move along directions that are quite different from the perfectly horizontal one. Owing to the fact that the integration is not performed in two dimensions, this information is thus inevitably lost during the analysis, introducing some further error in the final expression of the responsivity function. It is possible to speculate that this problem may be reduced by the initial integration taken along the vertical direction of the ROI, which somehow averages the behaviour of the pixels. Anyway we still expect this to be one of the limiting factor of the procedure.

During our first attempts to apply this method the second issue was the predominant one. Indeed the final result was found to be quite sensible not only on the particular choice of Δx but also on the absolute positions of the detector in the two considered acquisitions. Some improvements were made considering a set of discrete data given by the integration of each harmonic in a window $[\hbar\omega_f(q-1); \hbar\omega_f(q+1)]$ around their peak instead of the whole spectrum and substituting $D_1(x)$ with the average value $[D_2(x) + D_1(x)]/2$ in the denominator of the incremental ratio. The latter was done as for $\Delta x \to 0$ the denominator is expected to be independent on the particular choice between $D_1(x)$ and $D_2(x)$ since $A(x) \approx A(x + \Delta x)$. The integration around the peak of each harmonic was instead done to reduce the influence of the signal basement and to correct for the different focusing of the radiation at the two detector positions. Indeed the spectral focal curve of the grating has a complex shape while the MCP is moved along an almost perfectly circular trajectory, as exposed in Section 3.1.2. For this reason, the same harmonic is focused in a different way for every detector position and thus its intensity distribution shows a different width on the camera. However, even after these corrections, some important discrepancies were still present in the shape of spectra taken in different frequency windows after being calibrated using $A(x)$.

Therefore another procedure was followed for further improving the results of the calibration, in which a larger number of acquisitions at different detector positions was considered. In this way, following the motion of the spectrum on the CCD, a 2D map representing the detected intensity as a function of harmonic energy (vertical axis) and pixel position (horizontal axis) was built (see Figure 4.1). For an ideal detector, the values along each line of such matrix would be constant, while this is not the case for real ones, as their responsivity will change with the considered pixel. In this optics if a given harmonic covered all the detector width

during the movement of the translation stage, the responsivity function would be directly obtained from its intensity modulation. Anyway, due to the limits in the cutoff extension and in the excursion of the slits, such matrix is generally not completely covered during the measurements.

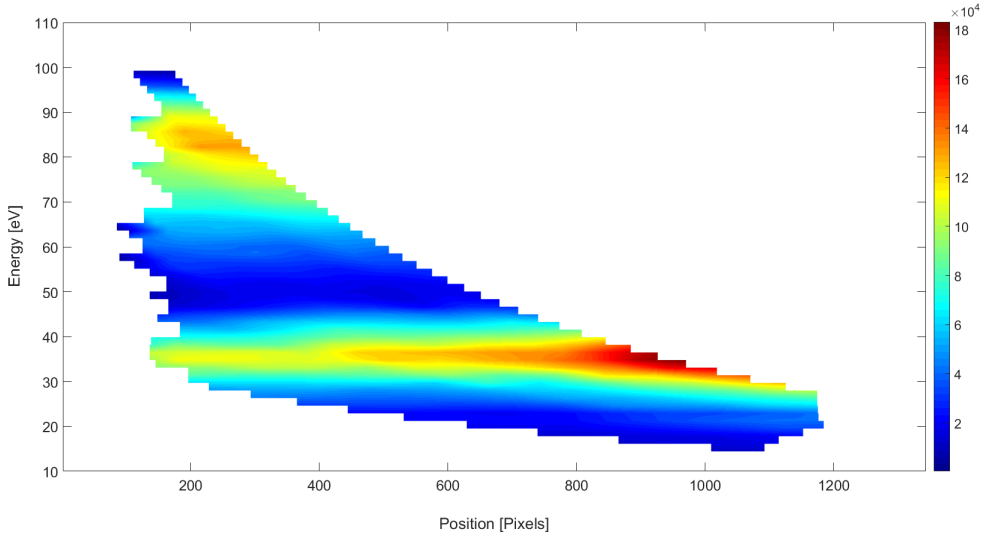

Figure 4.1: 2D map of the detected intensity as a function of harmonic energy and considered pixel. The values are given in arbitrary units.

The incremental ratio $[A(x+\Delta x) - A(x)]/[A(x)\Delta x]$ as a function of the harmonic order was obtained subtracting every two neighbouring columns of the matrix and dividing the result for their mean value. In this way the minimum possible value for Δx is used in the computation, which is one pixel, in order to limit the main issue affecting the previous attempts. The result was then used as the term in the exponent of Eq.(4.1) to retrieve another matrix, which represents for each row the value of $A(x)$ sampled by the correspondent harmonic. Finally, the responsivity function was obtained by averaging along the vertical axis all these values, which showed a similar functional behaviour up to a constant factor. The result is thus dependent only on the considered pixel and is expected to be rather robust. Indeed in the framework of this approach every harmonic can be thought of as a probe of the underlying pixel responsivity, with each row of the matrix representing an independent measurement of such function, even if in a restricted region of the CCD. In this way by averaging them the possible noises in the expression of $A(x)$ are reduced.

The result found analysing the harmonic emission from Ar atoms with a driving field of wavelength $\lambda_f = 1450$ nm is shown in Figure 4.2. As can be seen, the responsivity of the detector is stronger for higher pixel positions, which correspond to the low-energy part of the spectrum, probably due to wear. Therefore, for a fixed harmonic order the signal decreases when the detector is moved towards regions of lower energies, as was already quite visible in Figure 4.1. A small correction

was also performed on $A(x)$ for low pixel positions ($x \in [0, 242]$ in Figure 4.2), substituting the converging to zero behaviour with a constant plateau. Indeed this region of the computed responsivity is not reliable, since it is the starting point of the numerical integration and the signal is here randomly cut by the detector edge. This is due to the fact that in the experimental practice when the detector was moved we always checked that the lower-order harmonic was completely inside the screen before acquiring the data. In this way the higher-order one was always randomly placed with respect to the detector edge. For the same reason a plateau-like behaviour is present also in the high-pixel region of the detector ($x \in [1200, 1343]$ in Figure 4.2), as in this case it is linked to the absence of sampled signal in this region of the camera.

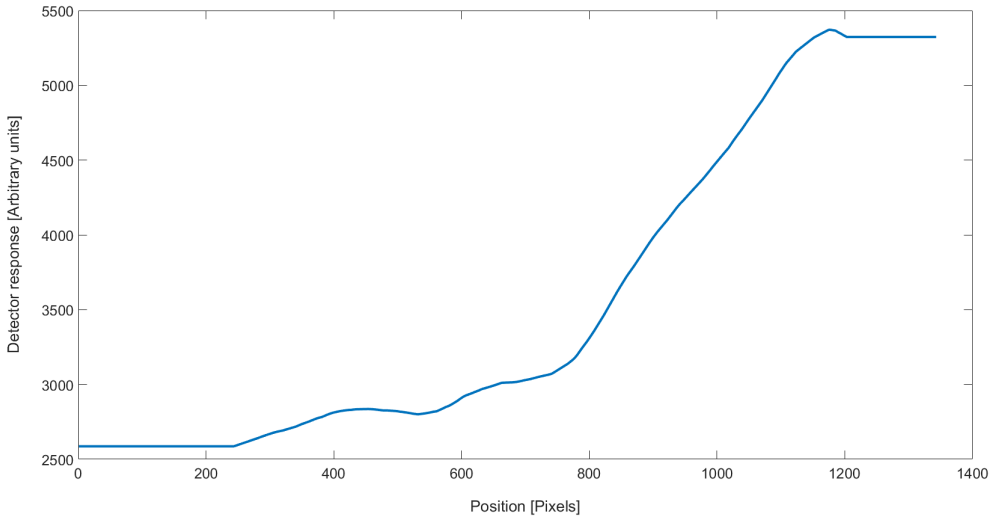

Figure 4.2: Functional behaviour of $A(x)$ found analysing with the described method a series of acquisitions at different detector positions of high order harmonics from Ar atoms generated by $\lambda_f = 1450$ nm.

However it is important to underline that the calibration procedure here proposed still suffers from two of the three issues underlined before. Indeed the necessity to suppose its responsivity as a product of a pixel-dependent and a frequency-dependent function is the unavoidable starting point of such approach, even if it is not always an adequate description of the system. We have also implicitly assumed that spectra acquired at very different positions of the detector would lie along the same row of the camera or at least that there is a negligible dependence of $A(x)$ on the vertical axis of the MCP, which is also not reasonable. Moreover, it doesn't allow to retrieve absolute intensity values for the spectra, as the function $A(x)$ is defined up to a multiplying constant due to the integral step in its derivation. Anyway, the results obtained in this thesis are quite encouraging regarding the applicability of this procedure. As an example, the calibration performed for three acquisitions in Ar with a driving field of $\lambda_f = 800$ nm is shown in Figure 4.3. Improvements are

rather clear, with corrected spectra that fit much better than the raw ones, even if discrepancies are still present for some harmonic orders.

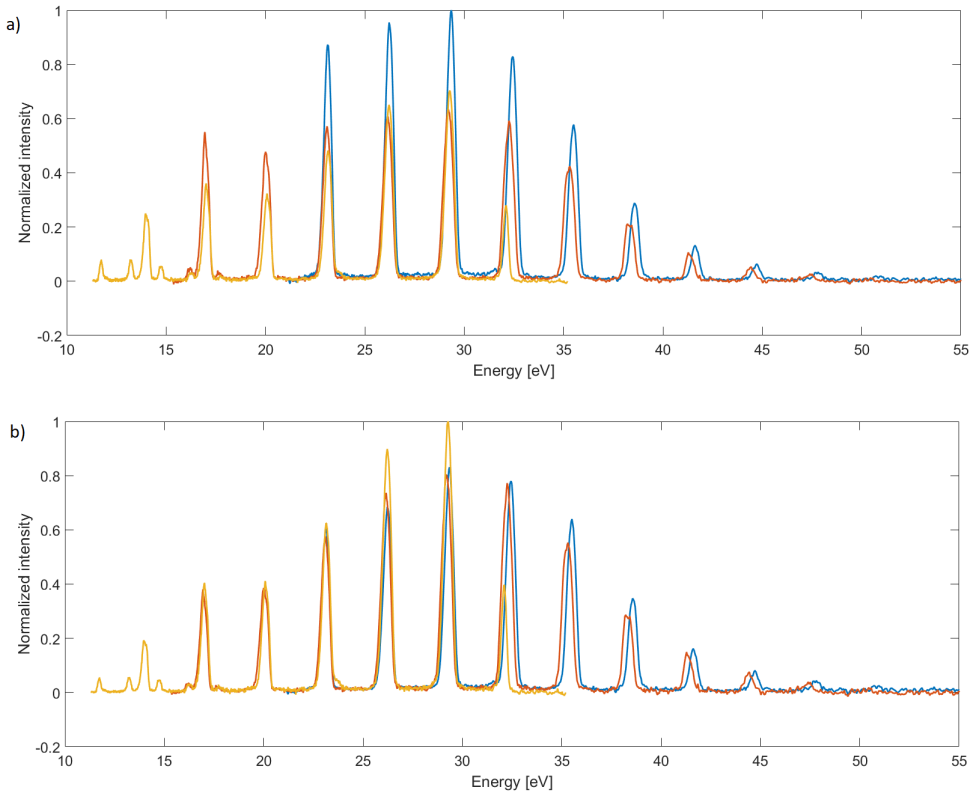

Figure 4.3: Normalized harmonic spectra acquired in Ar with $\lambda_f = 800$ nm at three different detector positions. a) Raw data where only the spectral axis is calibrated. b) Spectra corrected also for the pixel-dependent response of the detector.

Until now we have only considered the calibration of the measurements with respect to the pixel position on the detector. However this is usually not enough when performing HHS studies, as the spectrum should also be as close as possible to the real emission in the interaction region. For this purpose we need to retrieve the spectral responsivity of the whole spectrometer, which can be divided in three main parts: the toroidal mirror, the SVLS grating and the MCP. A characterization of them was previously performed by the group but only in the high-energy region of the spectrum [95] and the extension of such analysis also to lower frequencies is not trivial. Indeed both the toroidal mirror and the SVLS grating are designed to reach very high performances only in the range of $\lambda_q \approx 5 - 40$ nm and therefore the manufacturers don't provide any characterization of their behaviour outside this spectral window. Regarding the MCP, instead, the spectral responsivity data provided by Photek range in a pretty broad region of experimental error to account for the high manufacturing variability. Since it was not possible to perform an accurate experimental characterization of the detection system, an heuristic approach was

thus employed for obtaining a spectral calibration. In particular, the responsivity of the grating and the toroidal mirror were assumed to be flat in the low-frequency region, extending the last point available from the previous data. This is expected to be a better approximation for the latter, as its previous characterization shows a plateau-like behaviour below $\lambda_q = 30$ nm, while the responsivity for the grating is almost linearly increasing in all the available spectral region. On the other hand, for the MCP an average behaviour was extrapolated from the manufacturer data, which was then joined to its characterization at higher energies. A linear interpolation between data points was preferred over more complex ones, such as cubic or spline, in order to avoid problems related with the function crossing the zero axis. The spectral responsivity of the whole spectrometer retrieved in this way is presented in Figure 4.4.

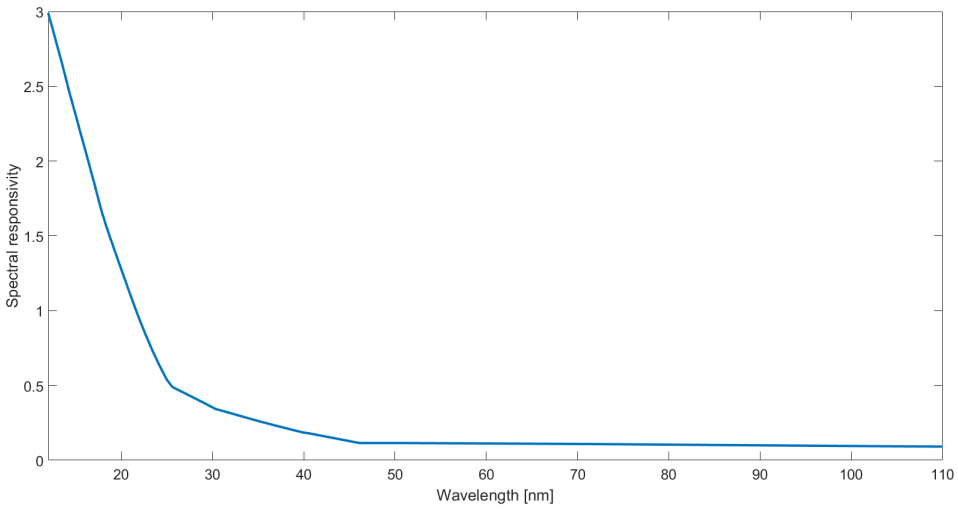

Figure 4.4: Spectral responsivity of the whole detection system. Below 40 nm the data are given by the already available characterization while above this value they are obtained heuristically from the assumptions presented above.

The overall efficiency of the detection system is lower at higher wavelengths, as it is reasonable from the initial purpose of its design. The validity of such heuristic approach and of the assumptions we had to made in order to retrieve this spectral responsivity are clearly objectionable. However the extended behaviour fits quite well the previously available one and the results obtained in this thesis seem reasonable. Further studies will then allow in the future to obtain a more precise and reliable characterization of the detection system.

4.1.2 Carbon dioxide

Carbon dioxide is a simple linear molecule, whose harmonic emission as a function of its alignment with respect to the driving field has been extensively studied in

the last decade. In particular, it is characterized by a polarizability anisotropy of $\Delta\alpha \approx 2.3 \cdot 10^{-40}\mathrm{F/m^2}$ ($\alpha_{\parallel} \approx 4.3 \cdot 10^{-40}\mathrm{F/m^2}$ and $\alpha_{\perp} = 2 \cdot 10^{-40}\mathrm{F/m^2}$) and a rotational constant of $B \approx 48$ μeV, thus showing a revival period of $t_{\mathrm{rev}} = 42.8$ ps. Moreover, due to the fact that the Oxygen atoms show a fixed nuclear spin $S = 0$, the aligning pulse can only excite rotational states with an even value of J and in this way both half and quarter revivals are visible in the dynamics of its $\langle \cos^2\theta \rangle$. However in our measurements we focused only on the temporal region around its first half revival, as our main interest was to collect its extended spectrum for performing a tomographic reconstruction of its HOMO orbital.

The possibility to perform molecular tomography from the emitted high-order harmonic radiation relies on the description of HHG given within the Lewenstein model. In this framework the intensity spectrum is proportional to the modulus squared of the Fourier transform of the recombination dipole matrix element between the bound molecular orbital $|\Psi_0\rangle$ and the countinuum wave-packet, described as a superposition of plane waves (see Section 1.2):

$$I_{\mathrm{XUV}}(\omega) \propto \omega^4 \left| \mathcal{F}\{ \langle \Psi_0 | \, \mathbf{d} \, | \Psi_c \rangle \} \right|^2 = \frac{\omega^4}{(2\pi)^3} \left| \int dt e^{i\omega t} \int dk \, \langle \Psi_0 | \, \mathbf{d} \, | e^{i(kz - \omega_e t)} \rangle \, e^{-iI_p t/\hbar} b(k) \right|^2$$

where $\mathbf{z}$ is assumed as the polarization direction of the driving field, following the convention of the previous chapters, and the recombining plane wave is approximated as being perfectly parallel to it. The integration in the temporal domain can be solved quite easily, as it fixes only the energy conservation upon recombination:

$$I_{\mathrm{XUV}}(\omega) \propto \frac{\omega^4}{(2\pi)^3} \left| \int dk \, \langle \Psi_0 | \, \mathbf{d} \, | e^{ikz} \rangle \, b(k) \delta(\omega - \omega_e - I_p/\hbar) \right|^2$$

The wave vector of the recombining electron is then linked to ω_e through its dispersion relation:

$$\omega_e = \frac{\hbar k^2}{2m_e}$$

For this reason, exploiting the delta function it is possible to compute also the integration in the wave vector space:

$$I_{\mathrm{XUV}}(\omega) \propto \frac{\omega^4}{(2\pi)^3} \left| b(k) \, \langle \Psi_0 | \, \mathbf{d} \, | e^{ikz} \rangle \right|^2 \qquad \text{with} \, \hbar\omega = \frac{\hbar^2 k^2}{2m_e} + I_p$$

The emitted spectrum can thus be considered as a spatial Fourier transform of the molecular orbital multiplied by the electric dipole up to the continuum wave packet amplitude, which includes both the steps of tunnel-ionization and electron propagation in the continuum. Provided that $b(k)$ can be evaluated in some independent way, the measurement of the high harmonic radiation can therefore be used to retrieve the 1D projection of Ψ_0 in a direction parallel to the returning electron, exploiting Fourier slicing theorem. Therefore, if the relative orientation between the driving field and the molecular axis is controlled, the whole 2D projection of the molecular ground state wavefunction can be reconstructed. The first experimental demonstration of this technique was performed by J. Itatani *et al.* in 2004 [117], with

the tomography of the N_2 HOMO (see Figure 4.5). In this work the amplitude of the continuum wave packet was determined using as a reference the emission of a noble gas with ionization potential similar to the one of the molecule, namely Ar. Indeed the electron wave packet is expected to be essentially the same in the two cases up to possible alignment effects (see Section 2.1.1), as it is mainly determined by the external field and the ionization potential of the system.

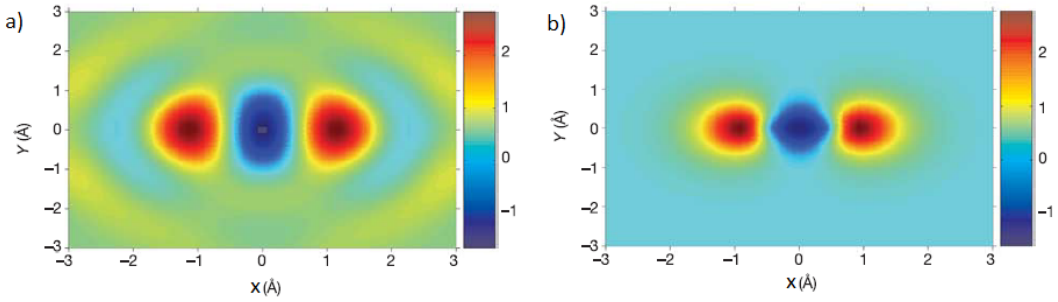

Figure 4.5: Molecular orbital of N_2. a) Reconstructed wavefunction using harmonic spectra from 19 different alignment angles. b) Orbital shape computed from ab initio calculations. The color scale is the same for both graphs. The image is adapted from [117].

Other two assumptions were then made by Itatani *et al.* in the development of such tomographic method. In order for the reconstruction to be possible, some information about the phase of the emitted field needed to be known. Since the measurements detected only the intensity of the radiation, a relative phase was introduced from first principles, exploiting the π shift expected from the two-center interference present at the 25^{th} harmonic. Moreover it was also necessary to assume that only the HOMO contributed to the emission and that the macroscopic spectrum could be directly related to the one of the single emitter. The first hypotesis was supported by the exponentially decrease of the ionization rate with I_p, while the second issue was overcome by artificially assuming that all the molecules were perfectly aligned in a fixed direction, neglecting in this way any angular distribution in the ensemble.

This approach is however limited only to small molecules by many factors. First of all, as we already discussed in Section 2.1, for bigger systems the Coulomb field of the parent ion greatly affects the recombining electron wave packet, which can no more be treated using the simple plane-wave approximation. Moreover, multi-electron effects start to play an important role and this procedure is not able to disentangle their contributions in the detected spectrum. In principle also the angular distribution of the molecules in the ensemble cannot be neglected. Finally, the necessity of an independent phase measurement may be a non trivial task. In order to overcome these limitations, in 2011 C. Vozzi *et al.* proposed a different method for the reconstruction of the HOMO in complex molecules [57]. A detailed analysis of such procedure is beyond the scope of this thesis and therefore it will be presented only briefly, while for a more detailed treatment one could refer to

[118]. In particular, the most important difference with respect to the tomographic approach proposed by Itatani is that the macroscopic XUV spectrum is considered as a function of the whole angular distribution in the molecular ensemble:

$$I(\omega,\tau) = \left| \int_0^{\pi/2} H(\theta,\omega) P(\theta,\tau) d\theta \right|^2 \tag{4.2}$$

where $H(\theta,\omega)$ is the high harmonic field emitted by a single molecule perfectly aligned at an angle θ, $P(\theta,\tau)$ is the angular distribution of the molecular axis at time τ during the revival and the integration is performed to account for the coherence of the generation process. This equation only assumes that macroscopic effects give a negligible contribution to the detected spectrum, which can be generally reasonable for a gas jet geometry, and that the angular distribution of the molecules is uniform with respect to the transversal direction of the beam. Since the temporal evolution of $P(\theta,\tau)$ is known from numerical simulations of the alignment dynamics, if enough data are available at different τ it is then possible to extract the single emitter response from the detected spectrum. This is done employing a retrieval algorithm developed by the group, which is based on Kaczmarz method. However, this approach is able to determine the phase of the emitted radiation only as a function of θ for a fixed photon energy. Therefore, for a complete reconstruction the single emmitter spectrum, the harmonic phase as a function of ω needs to be know at least for a given time τ. This can be done both by theoretical predictions on the system or experimentally by standard techniques such as the reconstruction of attosecond beating by interference of two-photon transitions (RABBIT) [119]. The retrieved single emitter spectrum can then be used to perform molecular tomography as proposed by Itatani, after the plane-wave term is corrected with a first-order perturbation theory in order to account for the Coulomb field of the parent ion [120]:

$$|k_\theta\rangle \approx e^{ikz}\left[1 - \frac{i}{k}\int dz V_{\mathrm{Cou}}(\mathbf{r},\theta)\right] \tag{4.3}$$

where V_{Cou} is the electrostatic potential of the molecular cation. Finally, in order to filter out the contribution of multi-electron effects, few-cycle mid-IR pulses can be employed ($\lambda_f = 1450$ nm, $\Delta t \approx 20$ fs), as already discussed in Section 2.1.3. For instance, this procedure was applied in the reconstruction of the carbon dioxide HOMO, which is presented in Figure 4.6. Even if the retrieved orbital agrees pretty well with the numerical calculations, some artifacts are present in the image. These are due to the high-pass Fourier spatial filtering of the wavefunction caused by the limited range of harmonics that were measured, as only the region of the spectrum above 35 eV was acquired. Therefore one of the main goal for improving such result was the extension of the analysis to lower energies.

For this reason we took two acquisitions of the spectrum at different detector positions, exploiting then the calibration procedure exposed in the previous section to connect the data. The measurements were performed around the first half revival from $\tau = 19.4$ ps to $\tau = 22.52$ ps with a step of $\Delta\tau = 40$ fs for studying the whole alignment dynamics of the molecule. For each one of these steps an integration over 400 laser pulses was performed. The backing pressure of the gas jet was set to

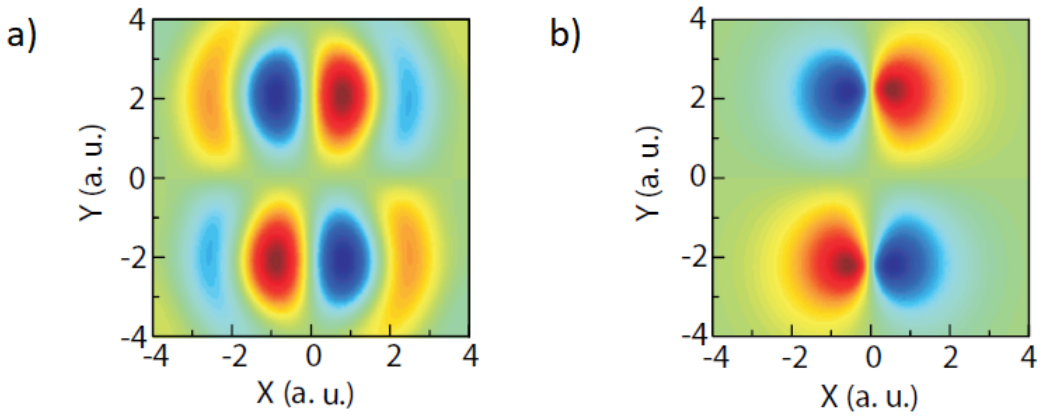

Figure 4.6: Representation of one of the two denegerate molecular orbitals of CO_2. a) Reconstructed wavefunction using the presented tomographic approach. b) Shape of the HOMO of CO_2 as computed from ab initio calculations with a quantum chemistry program. The color scale is the same for both graphs. The image is adapted from [57].

4 bar for maximizing the harmonic signal and the cutoff extension, while avoiding the clusterization of the molecules. The results of the procedure are presented in Figure 4.7 for a fixed time $\tau = 21.6$ ps in the revival dynamics. The calibration with respect to the pixel-dependent responsivity of the detector $A(x)$ already allows to correct pretty well the shape of the spectrum (b in Figure 4.7). In particular, the region just above 30 eV, which in the raw data showed a different behaviour in the two measurements, became much more similar after the calibration. Some discrepancies instead are still present in the absolute values of the harmonic peaks, probably due to the issues already exposed in Section 4.1.1. Anyway these are quite small if compared to the raw data. The spectra were joined at 24.6 eV, which is a minimum between two harmonics, and were calibrated for the spectral responsivity of the whole detection system to get the extended spectrum of CO_2 (c in Figure 4.7). Finally, a smoothing of the data over 10 points was performed below 20 eV for reducing the fast noise caused by the limited sensitivity of the system at these energies.

Spectra from different τ were then collected in a matrix in order to show the whole revival structure as a function of the harmonic energy (x axis) and the delay between the aligning and the generating pulses (y axis). Each harmonic was also integrated around its peak for increasing the signal to noise ratio before presenting the results. In particular, the integration was performed in an energy window of ± 0.14 eV, which is narrower than the distance between each peak and the neighbouring minimum $\hbar\omega_f \approx 0.855$ eV. This choice was done for filtering out the contribution of the second order of the spectrometer, which is visible below 20 eV. The obtained scan is showed in logarithmic units in Figure 4.8. The first thing that can be observed from it is that the harmonic cutoff is not constant along

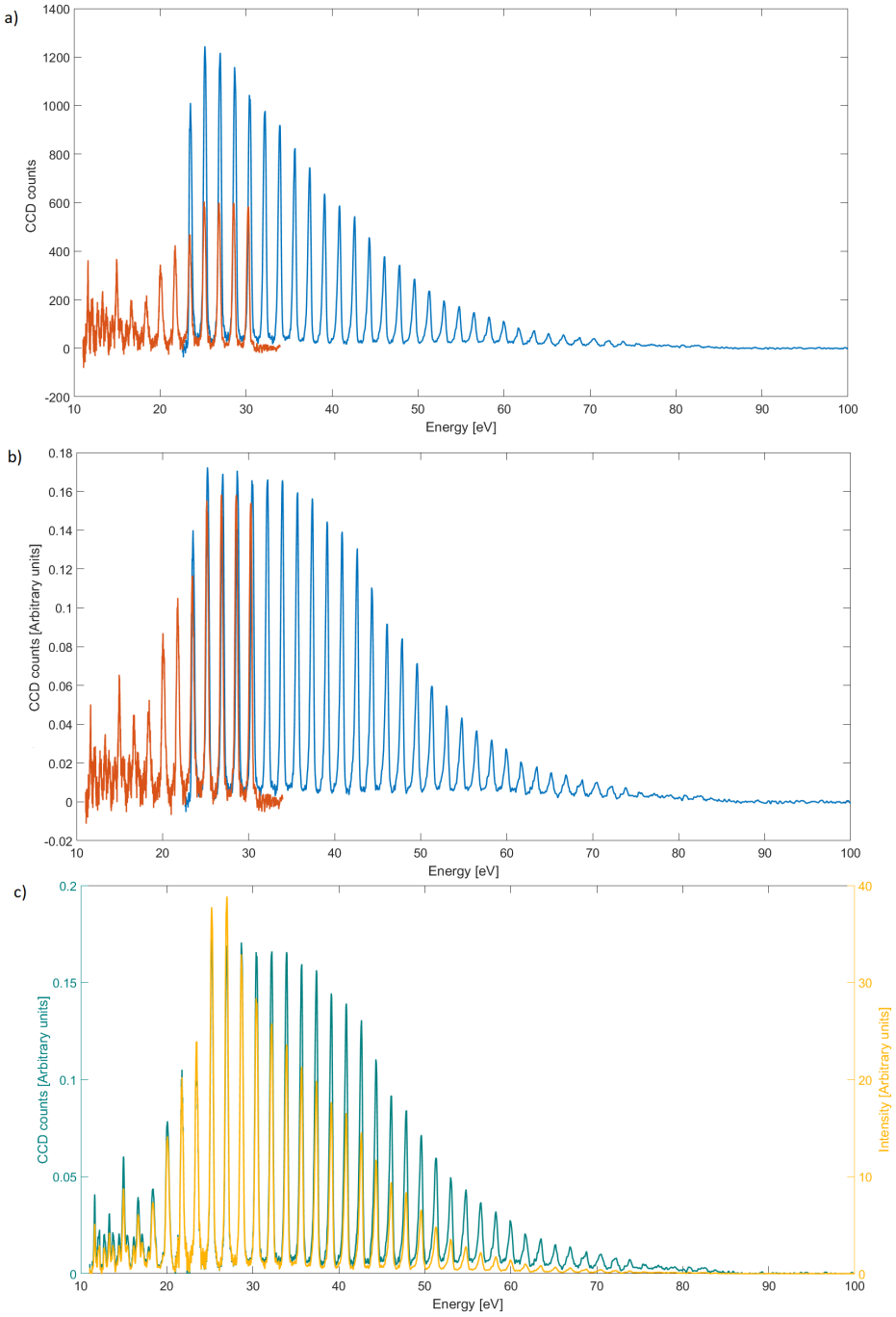

Figure 4.7: Calibration of the measurements taken in CO_2 for a time $\tau = 21.6$ ps in its revival dynamics. a) Raw intensity data collected in the two spectral regions. b) Same spectra calibrated for the pixel-dependent responsivity $A(x)$ of the detector. c) Comparison between the extended spectrum calibrated only for the pixel-dependent responsivity of the MCP (teal) and the one calibrated also for the spectral responsivity of the whole detection system (yellow). The spectra are normalized to the number of driving pulses.

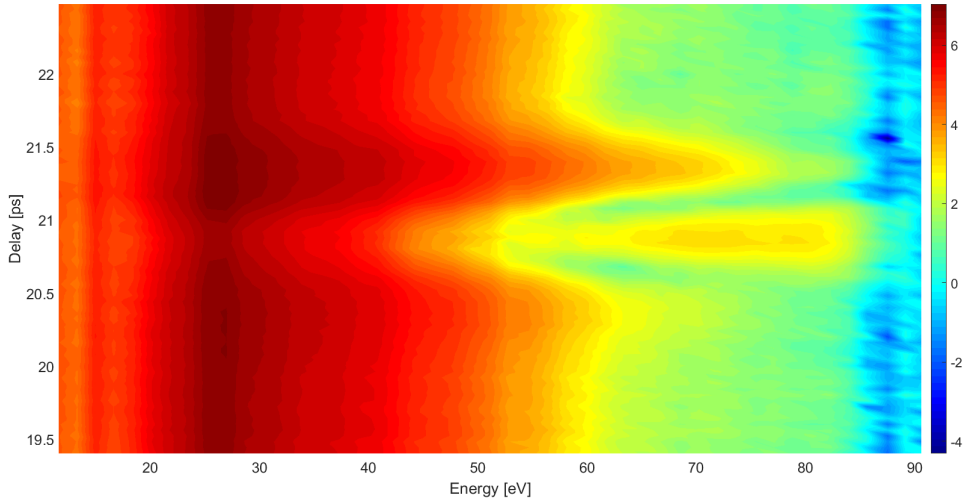

Figure 4.8: Intensity map of high-order harmonics generated around the first half revival in CO_2 with a driving wavelength of $\lambda_f = 1450$ nm normalized to the number of driving pulses. Logarithmic units have been used.

the rotational dynamics. In particular it is lower ($\approx$ 60 eV) far from the revival structure and is higher ($\approx$ 85 eV) during both alignment and antialignment. It is important to underline that this effect cannot be simply explained as a dependence of the harmonic amplitude with respect to the molecular orientation, since this usually implies only an intensity scaling factor. For instance, this is the case for the overall intensity quenching during alignment with respect to antialignment[1], due to the presence of the HOMO nodal axis along the polarization direction of the driving field [121]. A more reasonable description for the cuoff recession has been previously given in terms of the coherent build up of the XUV field in the target. Indeed in CO_2 a phase shift of $\approx \pi$ is present in the emitted radiation between molecules aligned at low ($\theta < 40°$) and high angles ($\theta > 40°$) with respect to the driving field [122]. For this reason, far from the rotational revival such contributions will interfere destructively, resulting in an lower cutoff.

Another visible feature in the scan is the sharp minimum, whose position is modulated by the revival structure and which has been previously attributed to a two center interference effect [77]. Indeed, the π_g HOMO of CO_2 is formed exclusively from the 2p orbitals of its oxygen atoms and therefore these can be treated as natural centres for the radiation emission. Following the treatment developed in Section 2.1.3 and exploiting the principle of energy conservation upon recombination, an expression for the structural minimum as a function of the alignment angle can be retrieved:

$$\hbar\omega_{\min} = \frac{2\pi^2\hbar^2}{m_e R^2 \langle cos^2\theta \rangle} + I_p$$

[1]It is important to underline that this cannot be linked only to the alignment dependence of the ionization step. Indeed in the case of carbon dioxide this is maximized for $\theta \approx 45°$.

where $R = 0.232$ nm is the distance between the two oxygen atoms in the molecule.

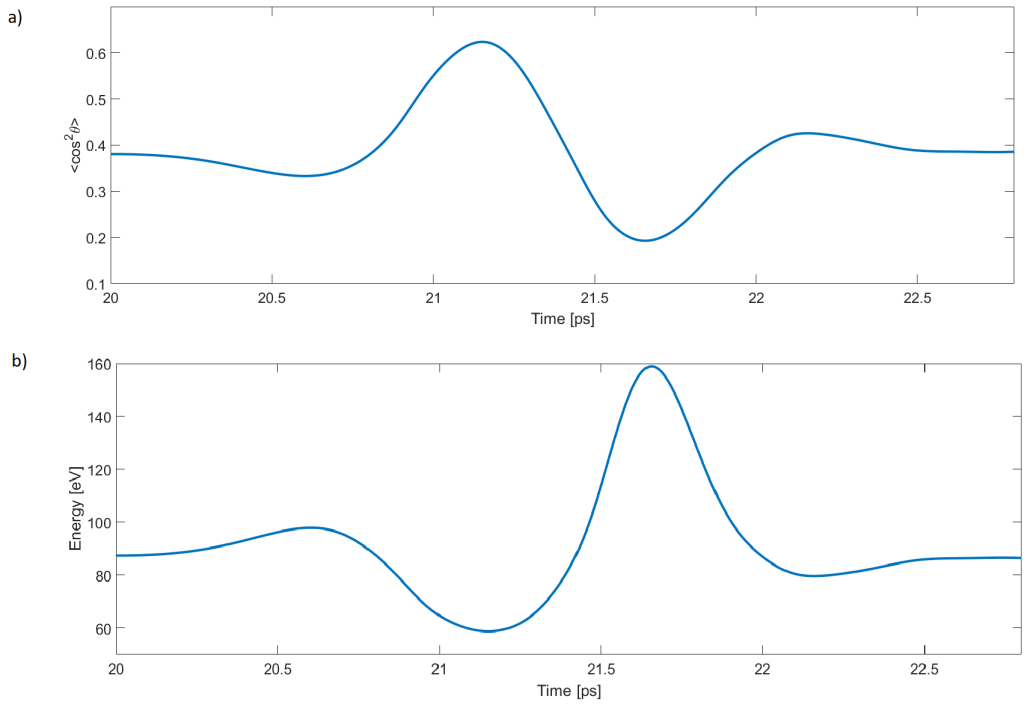

Figure 4.9: a)Evolution of the alignment parameter $\langle cos^2\theta \rangle$ during the first half rotational revival. The computation was performed for an aligning pulse with parameters $\lambda_f = 800$ nm, $\Delta t = 100$ fs, $I = 4 \cdot 10^{13}$ W/cm^2 and a rotational temperature $T_K = 75K$. The numerical simulation is taken from [57]. b) Theoretical position of the structural minimum as a function of the delay between the aligning and driving pulses.

In this expression a formal substitution $cos^2\theta \rightarrow \langle cos^2\theta \rangle$ has been made to account for the whole angular distribution of the molecules in the ensemble. The values of the alignment parameter and the minimum position computed in our usual experimental conditions are represented in Figure 4.9. From the graphs it is possible to observe that the position of the minimum shows an inverse behaviour with respect to the alignment parameter, as the De Broglie wavelength of the recombining electron needs to fit the projection of the molecular axis along the polarization direction of the external field. In the scan of Figure 4.8 the structural interference is well predicted by this equation during alignment, while we are not able to see its full dynamics during antialignment as the cutoff is too low. Indeed, using the semiclassical equation we obtain a theoretical cutoff of $\hbar\omega_{\text{cutoff}} \approx 85$ eV for a driving wavelength of $\lambda_f = 1450$ nm and a peak pulse intensity of around $I_f \approx 1 \div 1.2 \cdot 10^{14}$ W/cm^2, which is in good agreement with the OPA system in our experimental conditions.

Another feature of the scan is the existence of a clear intensity peak around

27 eV (31^{th} harmonic). This shape was present also in other acquisitions, even if its exact position was found to slightly change from day to day. Therefore, it is reasonable to suppose that this is an effect of the phase matching conditions in the interaction region. In our acquisitions the gas pressure, the focusing conditions and the position of the valve are fixed. In this way, for every harmonic order there exists a given ionization fraction that allows to minimize the phase mismatch Δk_q. Since higher harmonics are generated only near the peak of the driving field, they experience a faster change of the medium ionization and so the temporal window over which phase matching is favourable becomes narrower. This could explain why the peak in the spectrum is always found near rather low energies. However, a more precise evaluation of macroscopic effects would require the exact knowledge of all the experimental parameters in the interaction region, which was not available during our measurements.

A final interesting feature is the presence of two minima in the spectrum at around 13.34 eV and 16.7 eV, which seem not to be modulated by the revival structure. Moreover, they could be observed at only slightly different positions in every acquisitions, with a maximum drift of ≈ 1.7 eV. We are not able to provide a reasonable and exhaustive physical interpretation for this observation, as the lower-energy region of the spectrum is not well studied in literature and the mechanism behind the harmonic generation in this spectral window is not well understood. Indeed these minima lie approximately in correspondence of the ionization potentials of the molecular HOMO (≈ 13.66 eV) and HOMO-1 (≈ 17.5 eV), which are the limits of the strong field interaction when considering the emission from these orbitals. For this reason, the harmonics generated here are expected to show also a contribution from the perturbative regime. If a pure SFA picture were employed to predict the response of the system, a quenching of the signal would be expected in correspondence of I_p due to energy conservation upon recombination. Indeed as $\hbar\omega \approx I_p$ we have that $k \to 0$ and thus the returning electron cannot be described by any propagating plane-wave. However, as we previously discussed, the SFA picture cannot be a reliable description for HHG in this spectral region, as the influence of the ionic field breaks the fundamental assumptions of such approach. A more precise theory of harmonic emission at these low energies should therefore be able to explicitly account for both the Coulomb potential of the cation and for the deformation of the molecular energy levels induced by the presence of the strong field. Indeed, other possible explanations may also involve some polarization effects induced by the external field, some intermediate resonances or the excitation of Rydberg states in the molecule. Further studies are thus needed in order to understand the physical picture in this spectral region.

4.1.3 Allene

1-2 propadiene (hereinafter named simply allene) is a symmetric top molecule, whose structure is represented in Figure 4.10. From a nuclear point of view it is a prolate rotor with the three rotational constants which are $A = 596.4$ μeV and $B = C = 36.7$ μeV, thus showing a revival period of $t_{\text{rot}} \approx 55.6$ ps. From an elec-

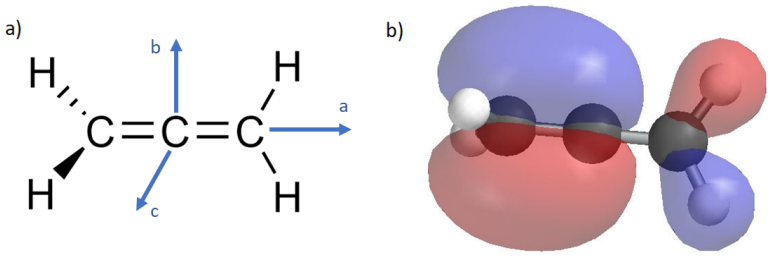

Figure 4.10: Molecular structure of allene. a) Nuclear arrangement of the molecule. The three principal rotational axis are represented in blue. b) Structure of one of its two degenerate HOMO.

tronic point of view, instead, its doubly degenerate HOMO shows π_u symmetry and is characterized by a rather low ionization potential $I_p = 9.692$ eV. Regarding the possibility to align well the molecule with respect to its **a** axis, it is ensured by the pretty high anisotropy of its polarizability $\Delta\alpha \approx 4.9 \cdot 10^{-40}$ F/m^2. The nuclear spin for each hydrogen atom is $S = 1/2$ while for the carbon atoms is $S = 0$. Sixteen possible nuclear spin states are thus allowed in the molecule, of which seven are even and nine are odd. Since each allowed symmetry operation involves the exchange of one couple of fermionic hydrogens, the product of the nuclear and the rotational wavefunctions needs to be antisymmetric. For this reason the initial ratio between rotational states with even and odd values of J is set to $9/7$. However it is important to remember that this ratio won't be conserved by the interaction with the aligning field, as in the case of symmetric rotors the selection rule $\Delta J = \pm 1, \pm 2$ allows to couple rotational states with different parity [90]. Therefore a full description of the alignment dynamics, such as the presence of partial revivals and their relative strength, would require a complete numerical analysis of the interaction.

Anyway, since our measurements had essentially an exploratory aim, we focused only on the first half revival, scanning the whole rotational dynamics from $\tau = 26.5$ ps to $\tau = 30.25$ ps with a step of $\Delta\tau = 50$ fs. Each spectrum was acquired integrating over 400 laser pulses, while the gas pressure in the gas jet was maintained at 0.6 bar. Differently from the case of carbon dioxide, however, only one spectral window was studied. The final result, calibrated for both the spectral and the pixel-dependent responsivity, is presented in Figure 4.11. The only main difference in the calibration procedure with respect to the one used for the analysis of CO_2 is that in this case the integration around each harmonic peak was performed in a wider region ± 0.4 eV, as there were no issues linked to the presence of the second order of the spectrometer.

The effect of the cutoff recession seems to be far smaller with respect to the case of carbon dioxide. The cause of this difference could be a lower alignment efficiency in the allene ensemble, but this is not reasonable as the anisotropy of its polarizability is greater than the one of CO_2. Thereore a better explanation could probably be found in a lower dependence of the harmonic phase on the molecular orientation. However, this speculation should be supported by further

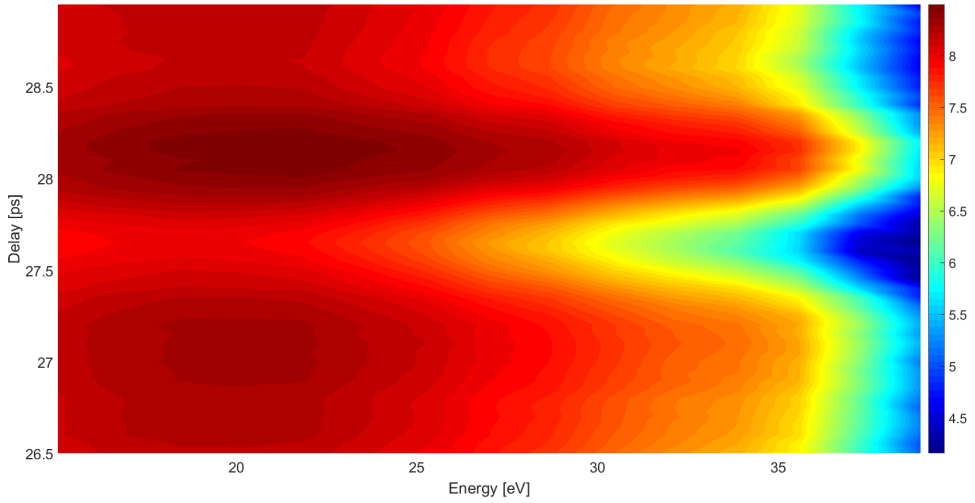

Figure 4.11: Intensity map of high harmonics generated around half revival in allene, with a driving wavelength of $\lambda_f = 1450$ nm normalized to the number of driving pulses. Logarithmic units have been used.

studies. It is also possible to notice that the overall emitted intensity is quenched during alignment $\tau \approx 27.7$ ps and it is enhanced during antialignment $\tau \approx 28.2$ ps quite alike CO_2. The nature of such scaling factor is indeed similar, with the harmonic generation that is suppressed when the orbital nodal axis lies along the polarization of the external field, as can be expected from the π_g symmetry of its HOMO [124]. In other studies it was also demonstrated that the position of the harmonic enhancement in allene is shifted towards lower alignment angles ($\theta < 90°$) with respect to what it would be expected by these simple considerations. This was justified with the presence of an additional electron density around the out of plane hydrogens, which creates another nodal plane perpendicularly to the molecular axis [125].

Another difference with respect to carbon dioxide is present if we compare the maximum relative intensity quenching $[I_{\text{antial}} - I_{\text{al}}]/I_{\text{antial}}$ at a fixed harmonic order. Indeed in the case of CO_2 this is approximately 0.3 while for allene it is around 0.7. This could be justified with an higher degree of alignment in the allene ensemble, which as we already said is supported by the higher anisotropy of its polarizability. However, another possible explanation could also be found in the different geometry of their HOMO. Indeed in the case of carbon dioxide this is perfectly antysimmetric with respect to the inversion of coordinates. Therefore during antialignment the returning electron will probe a charge distribution quite similar to the alignment case and this could lead to a lower difference in the harmonic yield between these two situations. Instead in the case of allene when the molecule is antialigned the HOMO lacks perfect antisymmetry with respect to the wave vector of the returning electron and for this reason the effect of the quenching is probably much more visible.

Moreover the cutoff energy seems to be pretty low as compared to the one of carbon dioxide. If we make use of the semiclassical equation with the previously estimated laser intensity of $I_f \approx 1 \div 1.2 \cdot 10^{14}$ W/cm^2, the cutoff is predicted to lie around 70 eV in allene, well beyond the measured one. However it is important to consider that complex molecules are characterized by pretty low saturation intensities. In particular, in the case of allene this is empirically known to be in the range of $I_{\text{sat}} \approx 2 \div 5 \cdot 10^{13}$ W/cm^2 [126]. Repeating the semiclassical calculation with these values we obtain a cutoff energy of $22 \div 40$ eV, which is more in agreement with our experiment. Another possible explanation for the reduced cutoff can als be found in the expected quenching of the emission at high energies caused by the nuclear motion. Indeed allene is known to undergo a structural rearrangement upon ionization, shifting to a completely planar structure due to the $\pi/2$ rotation of the out of plane hydrogen atoms. Since in our experiment we are collecting only the collinear radiation through a small aperture (see Section 3.1.2), we may suppose that we are filtering out the contribution of long-trajectories owing to phase matching conditions. The structural rearrangement would then be visible in the harmonic yield as a scaling factor proportional to the vibrational autocorrelation function, as exposed in Section 2.1.2. In particular, the signal would be quenched at higher frequencies due to the intrinsic time-energy mapping of short trajectories. In the framework of SFA the relation between the time τ spent by the electron in the continuum and the harmonic frequency ω_q for short trajectories is approximately given by [63]:

$$\tau = \frac{1}{\omega_f}\left\{0.786\left[f\left(\frac{\hbar\omega_q}{U_p}\right)\right]^{1.207} + 3.304\left[f\left(\frac{\hbar\omega_q}{U_p}\right)\right]^{0.492}\right\}$$

$$f(x) = \frac{\cos^{-1}(1 - \frac{x}{1.5866})}{\pi}$$

the behaviour of which, calculated for our experimental conditions, is presented in Figure 4.12.

The covered temporal window is therefore not so narrow, thanks to the use of a mid-IR driving field. To the best of our knowledge there isn't any estimation for the characteristic time of such structural rearrangement in allene and therefore it is not possible to affirm with certainty if it plays a role in our measurement. However similar experiments showed that the structural rearrangement upon ionization in CH_4 gives a visible effect on the HHG yield even for an electron excursion time of only $1 \div 2$ fs [58]. Anyway, to prove or dismiss this speculation it would be necessary to perform a HHG measurement with deuterated allene molecules in order to have a reference spectrum over which the signal quenching effect can be evaluated, which is not so trivial.

A further visible feature in the scan is the presence of a minimum around $\tau \approx 27.7$ ps during molecular alignment. This could be interpreted as the effect of two center interference between the part of the orbital that lies in the planar region of the molecule and the electron density around the out of plane hydrogens. Indeed a similar effect has been demonstrated in N_2O, that possess a very similar HOMO

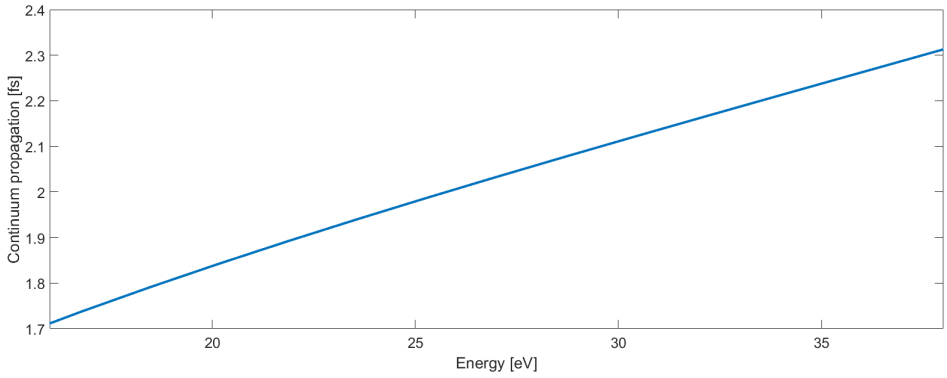

Figure 4.12: Time-energy mapping of short trajectories for a pulse of intensity $I_f = 10^{14}$ W/cm^2 and central wavelength $\lambda_f = 1450$ nm in the spectral window of Figure 4.11.

structure [127]. However, since at the moment we lack a precise simulation for the alignment factor $\langle cos^2\theta \rangle$ of allene, we cannot prove this speculation. Anyway, assuming from Figure 4.11 that the minimum position is around $\hbar\omega_{min} \approx 34$ eV and considering the distance between the first carbon and the out of plane hydrogens[2] of $R \approx 0.355$ nm, the resulting expectation value for the alignment factor would be $\langle cos^2\theta \rangle \approx 0.62$. This value could be reasonable, as it is almost the same attained in carbon dioxide. However, if this were the case, it would mean that the higher anisotropy of the polarizability in allene, which is almost double with respect to the one of CO_2, doesn't have such a huge effect on the final value of $\langle cos^2\theta \rangle$. Anyway, it is also important to underline that, due to its lower I_p, in our experimental conditions allene experiences a non negligible ionization from the aligning pulse. This can be estimated with the ADK rate, without taking into consideration any angular dependence on the molecular orbital structure, as $\eta \approx 24\%$, while the same calculation in CO_2 gives a negligible value of $\eta \approx 0.007\%$. Therefore the effective degree of alignment in allene may be spoiled by its fast ionization. Further studies need however to be performed in order to confirm or dismiss the possibility to observe a structural minimum, when a full characterization of its revival dynamics will be available.

Another important thing to underline is the absence of any fine structure in the revival, differently to what was derived in Section 2.1.2 for symmetric rotors. This can probably be explained by the low rotational temperature of the gas, which is estimated to be around 70 K. In such conditions, the energy linked to the thermal motion of the molecules is approximately 6 meV, while their rotational energy can be evaluated as:

$$\mathcal{E}_{\text{rot}} = BJ(J+1) + (A-B)K^2 = 36.7\ \mu\text{eV}\ J(J+1) + 559.7\ \mu\text{eV}\ K^2$$

Therefore initially only states with relatively low values of $K < 4$ are substantially occupied in the ensemble. Since this quantum number is conserved during the

[2]This choice of the emitting centres is done for similarity with the case of N_2O

alignment dynamics, we may then expect the fine structure to be not so visible in the final spectrum.The phase contributions of the second terms at the center of the first half revival $\tau \approx 27.75$ ps happen then to be very near integer multiples of 2π ($\phi_{K=1} \approx 3.7 \cdot 2\pi$, $\phi_{K=2} \approx 13.8 \cdot 2\pi$, $\phi_{K=3} \approx 33.8 \cdot 2\pi$, $\phi_{K=4} \approx 60.1 \cdot 2\pi$), thus contributing to further wash out any modulation. Moreover, we should also consider that the transversal profile of the beam doesn't allow to reach an homogeneous rotational dynamics of the gas in this direction. Therefore, the detected spectrum is an average over all these contributions, which may deteriorate well defined fine structure in the HHG signal.

4.1.4 Ethylene

Ethylene is a complex asymmetric molecule, whose structure is represented in Figure 4.13.

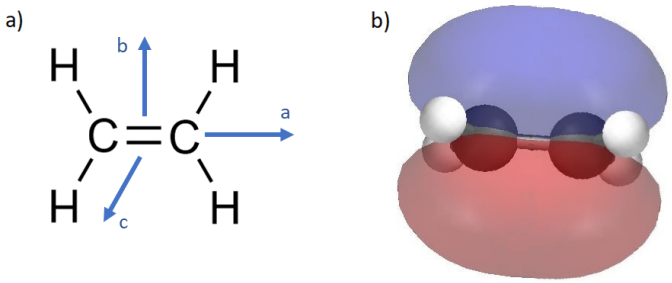

Figure 4.13: Molecular structure of ethylene. a) Nuclear arrangement of the molecule. The three principal rotational axis are represented in blue. b) Structure of the molecular HOMO.

From a rotational point of view it will thus show different constants along all three rotational axis, namely $A \approx 603$ µeV, $B \approx 124$ µeV and $C \approx 102.7$ µeV. In this way, its Ray parameter can be evaluated as $\kappa = (2A - B - C)/(A - C) \approx -0.915$, which classifies ethylene as an almost symmetric rotor, near the prolate limit $\kappa = -1$.

Since it is an asymmetric molecule, its interaction with an external aligning pulse can be written as (see Section 2.2.2):

$$H_{\text{int}} = -\frac{E_0^2}{4}[\Delta\alpha_{bc}\sin^2(\theta)\cos^2(\chi) + \Delta\alpha_{ac}\cos^2(\theta)]$$

The potential surface obtained from the interaction Hamiltonian substituting the values of the molecular polarizability along its three principal axis ($\alpha_a = 5.6 \cdot 10^{-40}$ HHG/m^2, $\alpha_b = 4.1 \cdot 10^{-40}$ F/m^2 and $\alpha_c = 3.6 \cdot 10^{-40}$ F/m^2) and the typical field amplitude in our experimental conditions ($E_0 \approx 1.74 \cdot 10^{10}$ V/m) is presented in Figure 4.14. It is possible to notice that a minimum is present for $\theta = 0$ almost independently on χ and therefore ethylene is preferentially prompt aligned along the electric field with its **a** axis. However, due to its asymmetric nature, the rotational dynamics of the molecule after the interaction is far more rich and complex. Indeed,

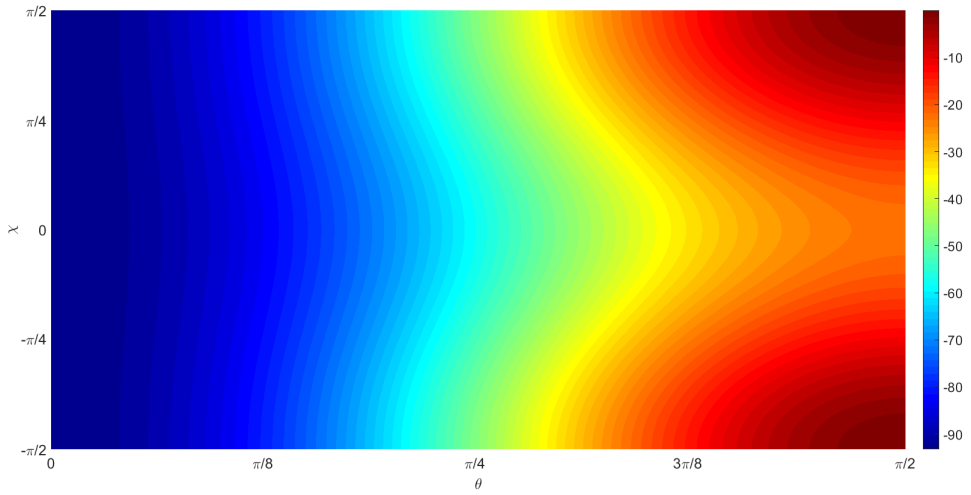

Figure 4.14: Potential surface of the interaction between ethylene and the external field in our experimental conditions. The parameters vary in the range $\theta \in [0, \pi/2]$ and $\chi \in [-\pi/2, \pi/2]$ to account for alignment but not orientation. Values are given in meV.

during its field-free evolution also **b** and **c** are alternatively aligned with respect to **z**, even if not as strongly as **a** owing to their lower molecular polarizability. Such effect can be characterized bt the expectation values of the cosine along the angles β_b and β_c respectively. To understand its origin, we should consider that, as it was already developed in Section 2.2.2, the selection rules for asymmetric top molecules are given by $\Delta J = 0, \pm 1, \pm 2$, $\Delta K = 0, \pm 2$ and $\Delta M = 0$. Precisely the irregular structure of the energy levels and the fact that the projection of the angular momentum on the principal molecular axis K is not conserved are the main causes of its complex rotational dynamics. Indeed, if we take into consideration the alignment prameters of the three molecular axis in the basis of the symmetric rotors' eigenfunctions, it can be demonstrated that $\langle cos^2\beta_a \rangle \equiv \langle cos^2\theta \rangle$ involves only rotational states having the same value of K, while both $\langle cos^2\beta_b \rangle$ and $\langle cos^2\beta_c \rangle$ includes also states linked by $\Delta K = \pm 2$ [128]. From a semiclassical point of view the impulsive interaction with the aligning field can therefore be thought of as a rotation induced both in $\theta \equiv \beta_a$ (excitation in J with $\Delta K = 0$) and in χ (excitation in K). For this reason, the difference between the alignment parameters along the three axis could generally be used as a good measure of the degree of asymmetry showed by a molecule in its rotational dynamics.

From a nuclear point of view the behaviour of ethylene is determine by the fact that every allowed symmetry operation involves the exchange of two couples of fermionic hydrogen nuclei with $S = 1/2$ and one couple of bosonic carbon nuclei with $S = 0$. Threfore the product of its nucler and rotational wavefunctions needs to be symmetric and the initial ratio betweem states with even and odd values of J is set to 7/9. In particular, each rotational state of ethylene J_{K_{-1},K_1} can be assigned to

a particular spin isomer and the statistical weights in the initial canonical ensemble will be $g_J = 7$ if both K_{-1} and K_1 are even and $g_J = 3$ otherwise. A more complete analysis of the topic, as well as an interesting theory about spin-selective alignment in ethylene, can be found in [129].

For all these reasons, the revival dynamics of the molecule is not trivial. An example of the evolution of its alignment parameter $\langle cos^2\theta \rangle$ computed for an aligning pulse of $I_0 = 4 \cdot 10^{12}$ W/cm^2 and an ensemble temperature of 9 K is presented in Figure 4.15.

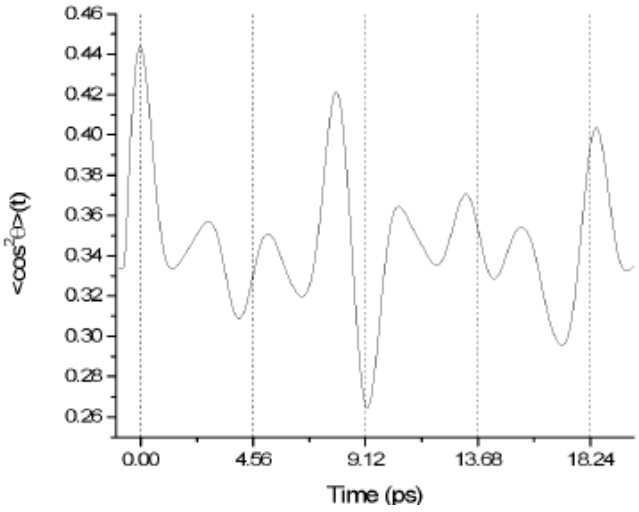

Figure 4.15: Evolution in time of $\langle cos^2\theta \rangle \equiv \langle cos^2\beta_a \rangle$ for an aligning pulse of peak intensity $I_0 = 4 \cdot 10^{12}$ W/cm^2 and a molecular gas at a rotational temperature of 9 K. The image is directly taken from [130].

Differently from the case of linear and symmetric rotors, no perfectly periodic revivals are present, due to the irregular rotational levels of the molecule. However, it is always possible to define subsets of energy levels that can be approximated as multiples of some combinations of rotational constants. Their partial rephasing will thus give rise to a nearly periodic structure in the alignment parameter, even though only for a relatively short period of time in the field-free evolution of the molecule. The most important recurrences for almost-prolate rotors such as ethylene are the so called J-type revivals $t_J = 2\pi\hbar/(B + C) \approx 18.24$ ps (see Figure 4.15), which are given by states with $\Delta J = \pm 2$ and $\tau \approx J$. Indeed, as the molecule approaches the prolate limit we would have $B \to C$ and so $t_J \to \pi\hbar/B$, which is the only revival period present for symmetric top rotors. From a semiclassical point of view during these revivals the molecule can be thought of being restricted in a precession motion of its **a** axis around the polarization direction of the aligning field **z**. As in the case of symmetric rotors, also fractional revivals may then be present, due to the rephasing of only a subset of these states.

Anyway, a more precise analysis of the rotational dynamics during J-type revivals should involve the whole angular distribution of the molecular axis $P(\theta, \chi, \tau)$.

A representation of such evolution around the first half J-revival in ethylene for an aligning pulse of $I_0 = 3 \cdot 10^{13}$ W/cm^2 and an ensemble temperature of 5 K is given in Figure 4.16.

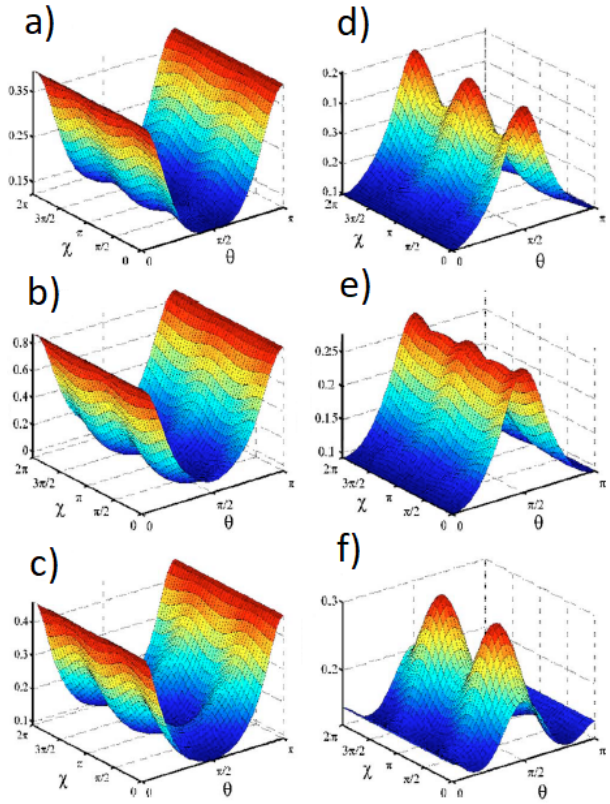

Figure 4.16: Angular distribution of the molecular axis $P(\theta, \chi, \tau)$ as a function of the two angles θ and χ at fixed times during the first half J-revival. a) $\tau = 7.84$ ps. b) $\tau = 8.34$ ps. c) $\tau = 8.84ps$ d) $\tau = 9.84$ ps. e) $\tau = 10$ ps. f) $\tau = 10.34$ ps. Image adapted from [128].

During the maximum alignment of the **a** axis (a, b and c in Figure 4.16) the angular distribution is completely delocalized in χ. However this is strictly true only as long as $\theta \to 0, \pi$ while, for imperfectly aligned molecules, there are always some values of χ that are more probable. During the antialignment of **a**, instead, the **b** and **c** axis are successively aligned with respect to the polarization direction of the field. In particular during the represented temporal range, firstly the **b** axis is aligned as $\chi = 0$ (d in Figure 4.16) and then, after a transition in which both are delocalized (e in Figure 4.16), the **c** axis is aligned as $\chi = \pi/2$ (f in Figure 4.16). Anyway, the importance of J-type revivals is linked to the fact that they represent the predominant dynamics for near-symmetric rotors in the weak alignment regime, when relatively low fields are employed.

Other recurrences may then be present in the revival structure of asymmetric molecules. For instance, the so-called C-revivals are produced by states linked by

$\Delta J = \Delta K_1 = \pm 2$ and lying in the lowest part of the rotational spectrum $\tau \approx -J$. They are characterized by a period $t_C = \pi\hbar/2C \approx 10.04$ ps and from a semiclassical point of view they can be thought of as rotations in the molecular plane around the **c** axis. These revivals have been demonstrated to be favoured when high intensity fields are used to align the molecular ensemble [128]. Indeed the interaction transfer the population towards higher J states preferentially through the lower part of the spectrum, for which $\tau \approx -J$. Moreover, also semiclassical rotations of the molecules around the **a** axis are allowed, which characterize the so-called A-revivals with $t_A = \pi\hbar/2A \approx 1.713$ ps. These are given by states lying in the upper part of the rotational spectrum $\tau \approx J$ which are linked by $\Delta J = \Delta K_{-1} = 2$. Since such energy levels are not much populated in ethylene below room temperature, these recurrences are usually negligible if compared to C and J-revivals. Finally, no recurrences are linked to the semiclassical rotation of the molecule around the *b* axis. Therefore the field-free rotational dynamics of an ethylene ensemble is rather complex, as it is defined by the interplay between the partial rephasing of all these subsets of states. Anyway, the principal aim of our measurements was to explore the feasibility to obtain a good alignment of asymmetric top molecules with our setup, as this is a preliminary requisite for their study.

In particular we focused on the first half J-revival around 9.1 ps. This choice was done to avoid the fast quenching in efficiency and regularity of the alignment due to the asymmetric nature of the molecule, which is estimated to happen on a temporal scale of ≈ 40 ps for J-revivals. The first scan was performed between $\tau = 8$ ps and $\tau = 11$ ps with a step of $\Delta\tau = 15$ fs at two different detector positions. Each spectrum was integrated over 120 laser pulses and the backing pressure of the gas jet was set to 1.6 bar for maximizing both the signal and the cutoff extension, while limiting clusterization effects. In order to connect the data obtained in the two different spectral windows we employed the calibration procedure discussed in Section 4.1.1. A resume of such results are presented in Figure 4.17. The relative intensity of the harmonic peaks is corrected pretty well by the calibration for the pixel-dependent sensitivity of the MCP (b in Figure 4.17), while the spectral responsivity of the detection system mainly modifies the overall shape of the spectrum (c in Figure 4.17). Even if discrepancies are still present after the first step of this procedure, the agreement between the two scans is far better than in the raw data. The spectra were then joined at 18.9 eV, which is a minimum between two harmonics.

Data acquired at different delays were then collected in a matrix for representing the whole rotational dynamics of the molecules during the first half J-revival. The signal was then integrated around the peak of each harmonic in a energy window between -0.4 eV and $+0.14$ eV. The choice of such range is done to account for the asymmetric width of the harmonics on the screen. We decided also to exclude the harmonic around 11 eV from the analysis, as it was cut by the detector edge and so its value was not reliable. Such scan, given in logarithmic units, is represented in Figure 4.18. As it can be easily seen from the graph, the cutoff is rather low if compared to its semiclassical estimation for ethylene in our experimental conditions $\hbar\omega_{\text{cutoff}} \approx 72eV$. However, considering that it is quite similar to the one

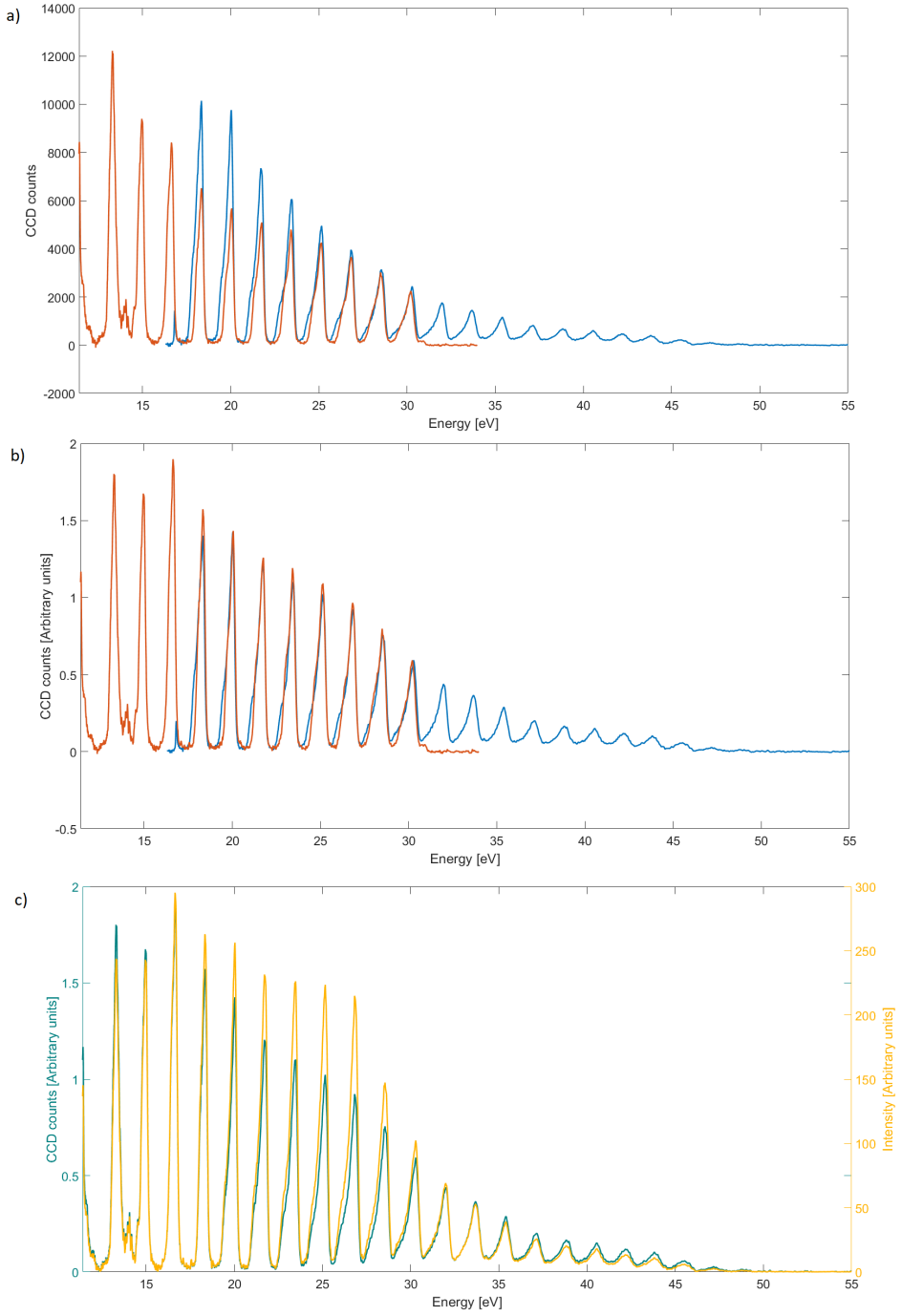

Figure 4.17: Calibration of the measurements taken in ethylene for a time $\tau = 8.9$ ps in its J-revival dynamics. a) Raw intensity data collected in the two frequency regions. b) Spectra calibrated for the pixel-dependent responsivity $A(X)$ of the detector. c) Comparison between the extended spectrum calibrated only for the pixel-dependent responsivity of the MCP (teal) and the one calibrated also for the spectral responsivity of the whole detection system (yellow). The spectra are normalized to the number of driving pulses.

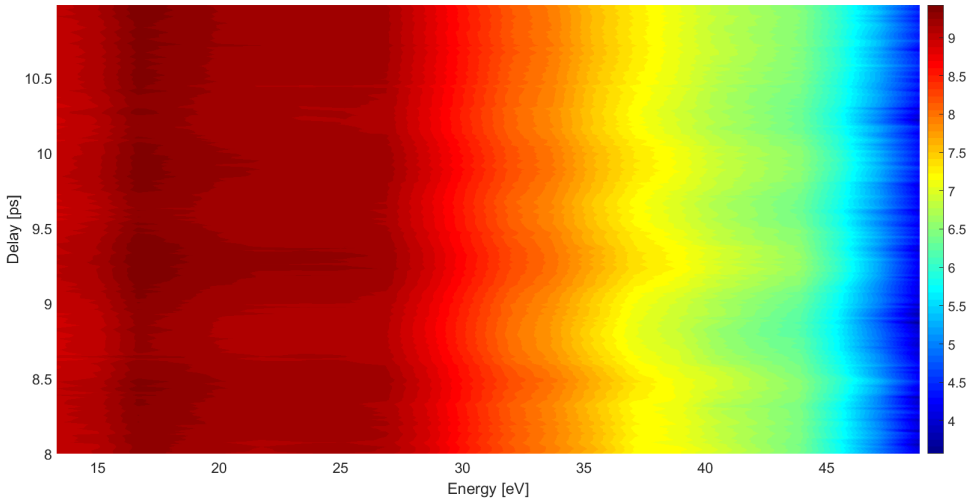

Figure 4.18: Intensity map of high harmonics generated around the first half J-revival of ethylene in the delay range $\tau \in [8 \text{ ps}, 11 \text{ ps}]$, with a driving wavelength of $\lambda_f = 1450$ nm normalized to the number of driving pulses. Logarithmic units have been used.

measured in the case of allene, it could be reasonable to assume that also in this case the limiting factor is the saturation of the generating medium. Moreover, another explanation could also be given by the fast decreasing of the one-photon ionization cross section of ethylene, which represents the recombination step of HHG. Indeed the experimental data show a drop of almost a factor 60 between 20 eV and 100 eV [131].

Regarding the influence of the revival dynamics on the harmonic emission only a slight modulation is present. However it is important to underline that, for all the reasons exposed before, it is quite difficult to obtain a high degree of alignment in asymmetric top molecules such as ethylene. Anyway, since its HOMO is a π_u orbital, it is possible to predict a maximum of the emission around antialignment and a minimum around alignment during the half J-revival, as an effect of the relative position of the orbital nodal axis with respect to the polarization of the driving field [77]. This allows to confront the delays of higher ($\tau \approx 8.45$ ps, 9.3 ps, 10 ps) and lower ($\tau \approx 8.85$ ps, 9.65 ps, 10.25 ps) signal with the behaviour of $\langle cos^2\theta \rangle$ given in Figure 4.15. A quantitative correspondence cannot be established due to the different experimental conditions, however it seems reasonable to assume the highest modulation in our experiment between $\tau \approx 8.85$ ps and $\tau \approx 9.3$ to be identifiable with the alignment around 8 ps in Figure 4.15.

Another interesting feature of the scan is the presence of what seems to be a fast intensity modulation at very high orders of harmonics (> 45 eV). One intriguing possibility could be that they are the fingerprint of some vibration in the molecule, which reflects on the harmonic yield as a periodic modulation of the nuclear auto-correlation function presented in Section 2.1.2. However, the attempts to perform a

Fourier analysis on the signal have not given any satisfying result. Moreover, the aligning pulse is hardly able to excite Raman vibrational modes due to its rather long temporal duration ($\Delta\tau \approx 100$ fs). Another possible cause of this modulation could be linked to the molecular rotations with respect to the angle χ during the J-type revival. Indeed due to the symmetry of the molecular orbital, a quenching is expected when $\chi = 0, \pi$, as the nodal plane along the molecular axis is in this case parallel to the driving field. However, the rotational periods of molecules are generally on the order of some ps, while the observed modulation seems to be in the fs time scale.

In order to analyse better this modulation we then performed a narrower scan in the range $\tau \in [8.2 \text{ ps}, 9.984 \text{ ps}]$ with a step of $\Delta\tau = 8$ fs, integrating each spectrum over 400 pulses. The results are showed in Figure 4.19. Differently from the previous scan, in this case we focused only on the high energy region of the spectrum and each harmonic peak was integrated in an interval ± 0.4 eV, as the signal was much more clean and symmetric.

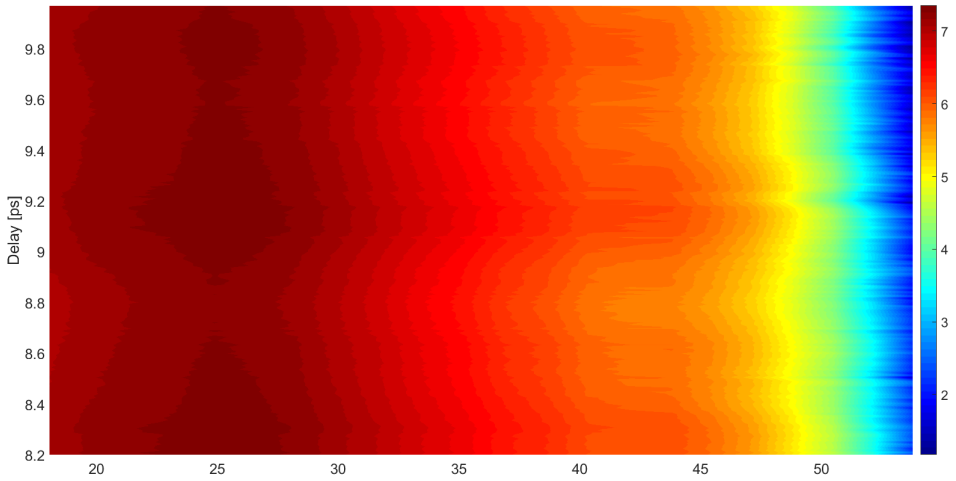

Figure 4.19: Intensity map of high harmonics generated around the first half J-revival of ethylene in the delay range $\tau \in [8.2 \text{ ps}, 9.984 \text{ ps}]$, with a driving wavelength of $\lambda_f = 1450$ nm normalized to the number of driving pulses. Logarithmic units have been used.

However, even if the temporal sampling in this acquisitions was higher with respect to the previous one, its Fourier analysis was still inconclusive. Further studies are therefore needed in order to understand better the origin of this effect.

Anyway, another interesting feature was underlined by this scan, which is a modulation of the harmonic position with respect to the temporal delay between the aligning and the generating pulse. We must underline the fact that this was actually visible also in the previous one, but it was not as clear. An analysis of the harmonic centroids was thus performed for understanding the physics behind this effect. The result for the 31^{th} harmonic of the driving field (27 eV) in comparison with its intensity modulation due to the half J-revival is presented in Figure 4.20.

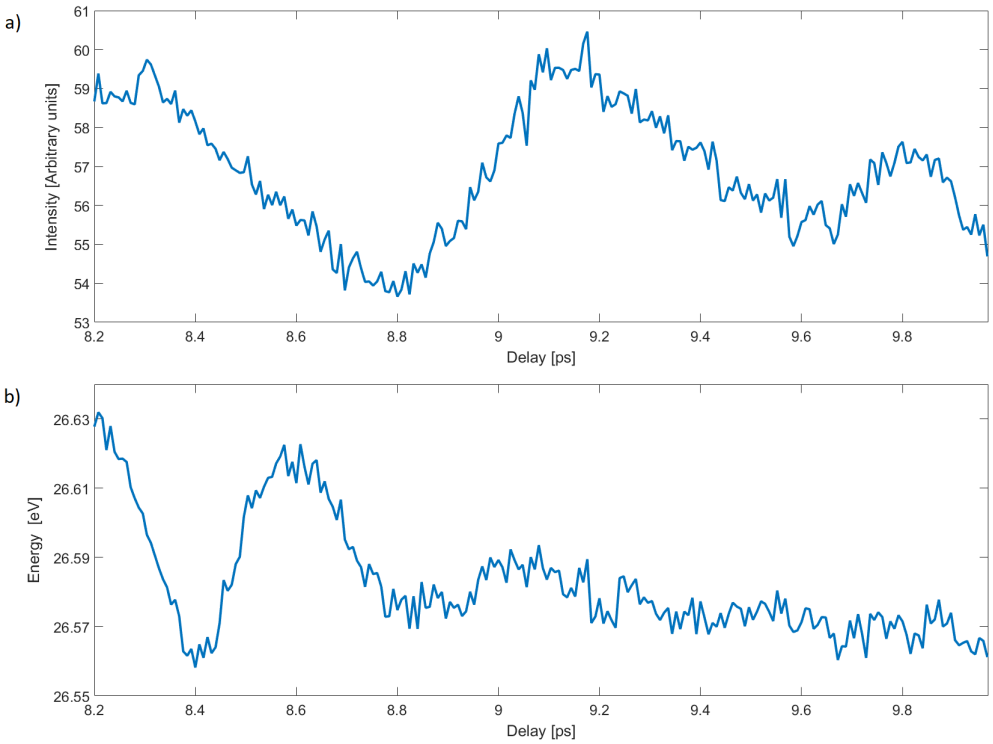

Figure 4.20: Analysis of the centroid shift for the 31$^{\text{th}}$ harmonic of $\lambda_f = 1450$ nm in ethylene. a) Intensity modulation of the harmonic due to the half J-revival. b) Modulation of the centroid position during the scan.

In literature similar effects are generally ascribed to the time-dependence of the gas refractive index following the rotational dynamics of the molecules. In principle, the refractive index of the ensemble can be written as:

$$n(\mathbf{r},t) = \sqrt{1 + \frac{N}{\varepsilon_0}(\alpha_a \langle \cos^2\theta \rangle + \alpha_b \langle \sin^2\theta \sin^2\chi \rangle + \alpha_c \langle \sin^2\theta \cos^2\chi \rangle)}$$

where the dependence on $\mathbf{r}$ has been included to account for the transverse profile of the aligning beam. During its propagation in a medium of length L the radiation will therefore experience a shift given by:

$$\Delta\omega = -\frac{2\pi}{\lambda} L \frac{\partial n}{\partial t}$$

with λ its wavelength in vacuum. However the treatment is not as trivial as it may seem. Indeed, during the half J-revival both the euler angles θ and χ are expected to change in time in a complex way. Moreover, both the driving and the harmonic fields may in principle experience such shift. To simplify the problem, as a first approximation, we may suppose that only the IR radiation is influenced by the refractive index change induced by the alignment dynamics. This assumption is supported by the fact that the amplitude of the measured frequency modulation is

an increasing quantity with respect to the harmonic order, although not linearly. In this way, as exposed in Section 1.3.1, the refractive index is very near unity and we may consider a Taylor expansion of the radical at the first order:

$$n(\mathbf{r},t) \approx 1 + \frac{N}{2\varepsilon_0}(\alpha_a \langle \cos^2\theta \rangle + \alpha_b \langle \sin^2\theta \sin^2\chi \rangle + \alpha_c \langle \sin^2\theta \cos^2\chi \rangle)$$

We further neglect the dependence on the transverse profile of the aligning beam and we rewrite the parenthesis exploiting simple trigonometric identities:

$$n(t) \approx 1 + \frac{N}{2\varepsilon_0}(\alpha_b + \Delta\alpha_{ab} \langle \cos^2\theta \rangle - \Delta\alpha_{cb} \langle \sin^2\theta \cos^2\chi \rangle)$$

where we have called $\Delta\alpha_{ij} = \alpha_i - \alpha_j$ following the notation of Section 2.2.2. From this equation it is therefore clear that the asymmetry of the molecule acts as a correction through the third term in the parenthesis.

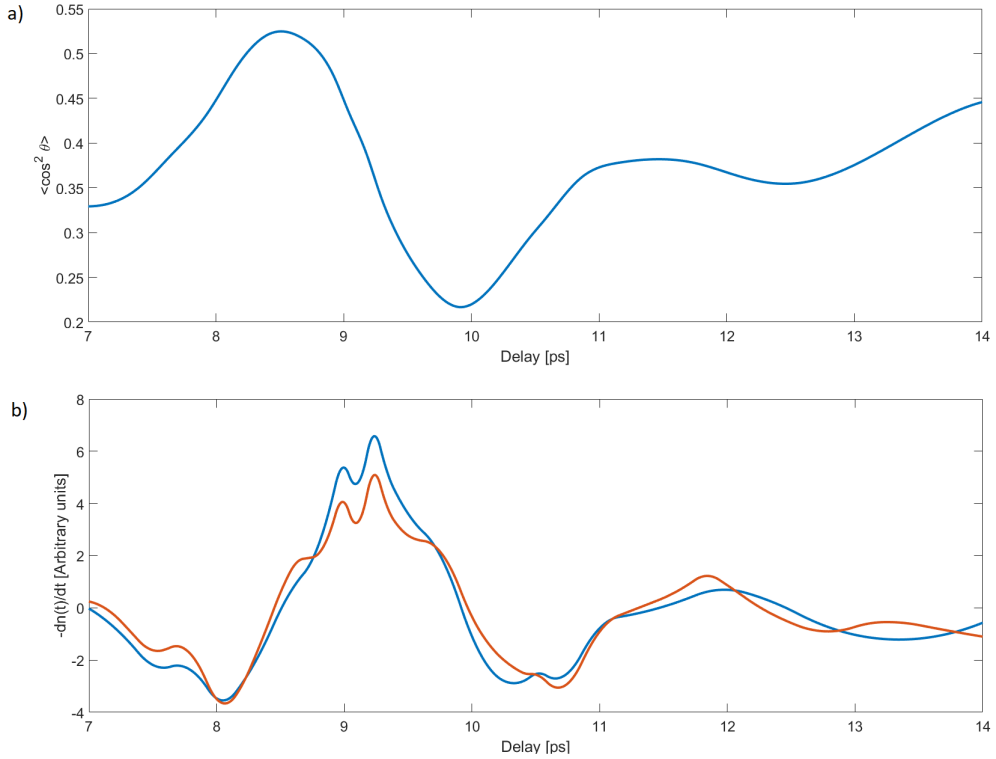

Figure 4.21: Refractive index change during the first half J-revival. a) Simulation of $\langle \cos^2\theta \rangle$ for an aligning pulse of peak intensity $I_0 = 3 \cdot 10^{13}$ W/cm^2 and a gas temperature of $T = 5$ K. Values taken directly from [128]. b) Computed value of $-dn(t)/dt$ both in the perfect prolate limit (blue line) and with the asymmetric correction (red line).

Since ethylene has a very low value of the Ray parameter $\kappa \approx -0.915$, usually it is assumed to be well approximated by the prolate limit $\Delta\alpha_{cb} \to 0$, for which the

derivative of the refractive index simplifies:

$$\frac{\mathrm{d}n}{\mathrm{d}t} \approx \frac{N}{2\varepsilon_0}\Delta\alpha_{ab}\frac{\mathrm{d}\left\langle\cos^2\theta\right\rangle}{\mathrm{d}t}$$

Using the alignment parameter provided for ethylene in [128], we then performed the computation of $-dn(t)/dt$, both in the prolate limit and considering also the asymmetric correction factor, in order to confront it with the experimental observation. The results are represented in Figure 4.21. The first thing that can be noticed is that the two curves are very similar. This confirms the fact that ethylene can be quite well approximated by the prolate limit in this context. However, the computation does not fit our experimental results, in which the modulation is confined only within the first rising edge of the alignment parameter. This means that, in order to fully describe such effect, it is probably not possible to rely only on the change in the refraction index induced by the alignment dynamics. Therefore, further analysis must be undertaken to include also other possible causes of frequency shifts, like non linear effects in the ionized medium.
Anyhow, the most important result found with this measurements is without any doubt the fact that 1D alignment of ethylene is possible with our setup, even if the signal needs to be optimized, and the clear identification of J-revival structures in the field-free evolution of the molecules.

4.2 HHG in femtosecond laser fabricated devices

In this section the results concerning the generation of high-order harmonics in channels fabricated through the FLICE technique will be presented. These devices were manufactured by the group of Proff. R. Osellame and R. M. Vázquez from CNR-IFN Milano using the setup presented in Section 3.3. The experimental work concerning the generation of the XUV radiation and the analysis of the measurements were instead performed in UDynI laboratory by the group of Proff. S. Stagira and C. Vozzi.

In particular, in Section 4.2.1 we will briefly present the characterization performed on the IR driving beam to set the experimental conditions explored in this work. Afterwards, in Section 4.2.2 we will show the measurements acquired employing a simple straight waveguide geometry, while in Section 4.2.3 the possibility to generate radiation in a modulated channel designed for achieving QPM of the harmonics will be discussed. The latter will also prove the feasibility to obtain in the future more complex devices, with the integration of multiple functionalities on a single monolithic chip thanks to the manufacturing flexibility offered by the FLM technique.

4.2.1 Driving beam characterization

The beam delivered on the low-energy line by the laser system of UDynI ($\tau \approx 25$ fs, $f_{\text{rep}} = 1$ kHz, $\mathcal{E} \approx 2$ mJ; see Section 3.2) is divided using a beam splitter and only a smaller portion with an energy content of $\mathcal{E} \approx 400$ µJ enters the interaction chamber. There, an iris followed by a lens with $f = 20$ cm allows to adapt within a certain range the beam waist in the focus, where the chip is placed. The value of the focal length is chosen to provide a diameter of the laser spot which is near the optimum value for the coupling to the fundamental EH_{11} mode of the microstructured channels.

In order to characterize the IR driving beam in the focal region we employed a beam profiler (Beamage 3.0 by Gentec-eo) after properly reducing its intensity with a series of neutral density filters. The $f = 20$ cm lens was also mounted on a translation stage (Micronix) for scanning a region of 4 mm around the focus. The results are resumed in Figure 4.22. The beam is rather astigmatic with the position $x \approx 0$ being the circle of least confusion, that from now on will be simply referred to as the focus of the beam. This aberration is probably due to the amplifying system itself and its precise origin should be investigated in following campaigns. Even if this is not an ideal condition, it anyway provides enough similar dimensions for the radii W_z and W_y near the focus. Indeed, their values, measured by the beam profiler for 30 minutes at a sampling frequency of 10 Hz triggered by the oscillator and integrated over 20 ms, are:

$$\langle W_z \rangle = 30.27\ \mu m \quad \sigma(W_z) = 1.59\ \mu m$$

$$\langle W_y \rangle = 28.95\ \mu m \quad \sigma(W_y) = 3.68\ \mu m$$

where $\langle x \rangle$ identifies the average of x and $\sigma\,(\mathrm{x})$ its root mean square value. The beam profiler allowed also to directly quantify the ellipticity ξ of the spot in the focus, which is defined as the ratio between its shorter and its longer diameter:

$$\langle \, \rangle = 0.91\% \quad \sigma\,(\,) = 8.54\%$$

with a minimum sampled value of $\approx 50\%$, attained however only once.

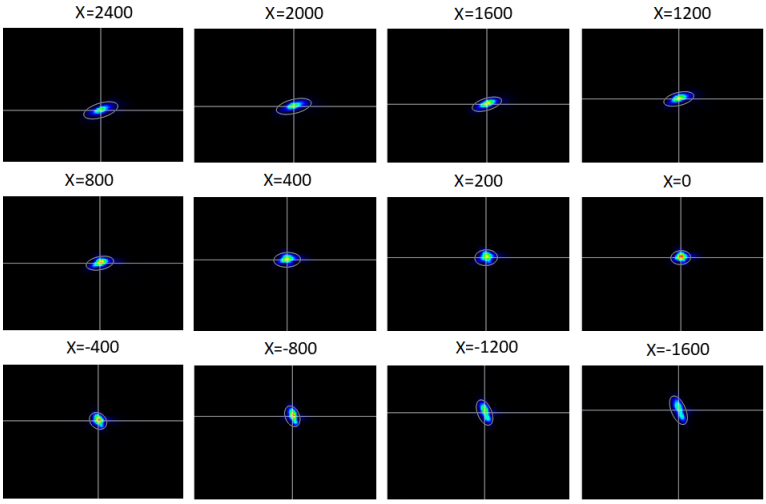

Figure 4.22: Profile of the IR driving beam around the focal position. Positive values of x are referred to positions after the focus.

Another important characterization that was performed is the one of the beam pointing stability, as it can highly influence the temporal evolution of the coupling to the channel. The result is presented in Figure 4.23, where the red dot is the average position of the beam centroid in the focal plane.
In particular the distribution of the centroid along the two transversal axis is almost Gaussian with root mean square values of:

$$\sigma(y) = 3.17\ \mu m \quad \sigma(z) = 2.9\ \mu m$$

and a maximum excursion of:

$$\Delta y = 12.8\ \mu m \quad \Delta z = 11.9\ \mu m$$

No temporal drift of the laser position was visible within the temporal range under investigation, but a dominant frequency component around 3 Hz is present in the the Fourier transform along both transversal directions (see Figure 4.24). This is a well know property of the driving laser, linked to the mechanical vibrations of the cryogenic chiller of the third amplification stage. This issue have been previously faced by placing some buffer pads to uncouple the cooling device from the optical table and in the present experimental conditions its influence is therefore minimized as much as possible.

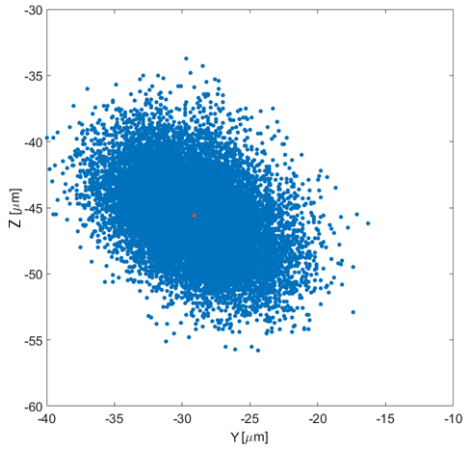

Figure 4.23: Position of the spot centroid in the focal plane. The red dot identifies the average over the measured temporal window.

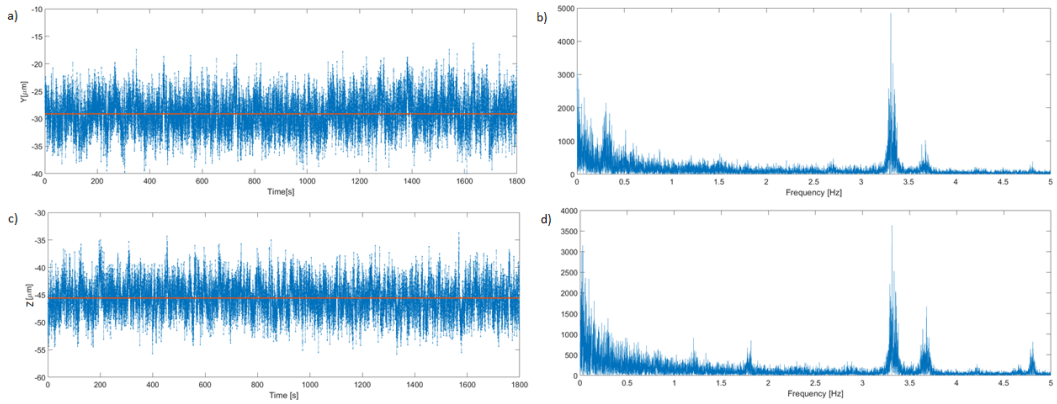

Figure 4.24: Measurement of the position of the beam centroid in the focal spot. a) and b) position along y with respect to time and its Fourier transform. c) and d) position along z with respect to time and its Fourier transform.

The same measurement allowed also to characterize the peak intensity of the pulses, which is found to be stable within the 2.5% RMS during the same temporal window. Moreover, the intensity of the beam is known from other measurements performed on the line to show some fluctuations with a frequency of 100 Hz in the Fourier domain. This is probably due to the laser system itself, even if its precise origin is currently unknown. However, since these fluctuations are not too much high and usually the acquisitions are done integrating the signal over rather long temporal windows, we expect this issue not to play an important role in the final results.

The last characterization performed on the beam was done in the frequency domain employing a spectrometer in the range $\lambda = 200 - 1100$ nm (AvaSpec-

2048XL by Avantes). These measurements were taken after the focus, firstly in air and then after putting the interaction chamber in vacuum. The results are resumed in Figure 4.25.

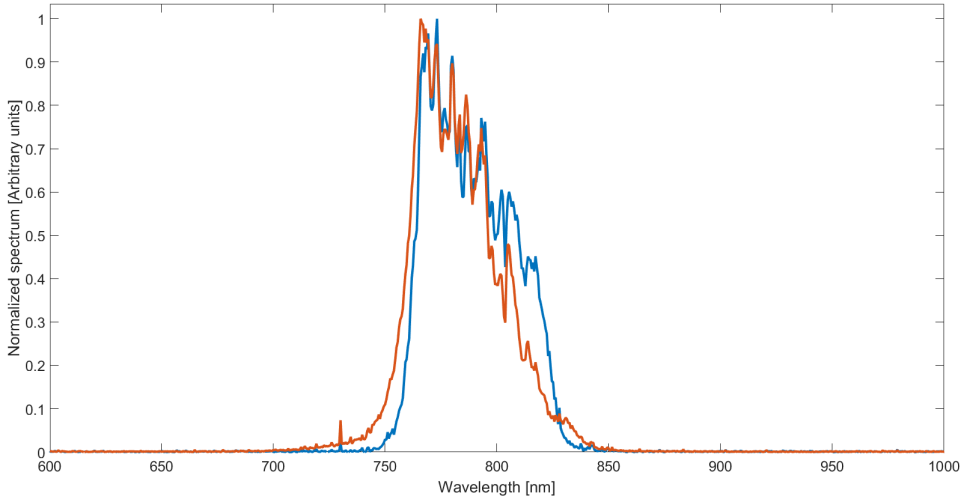

Figure 4.25: Spectrum after the focus in air (blue line) and in vacuum (red line).

When focused in air the laser undergoes filamentation for almost one centimetre around the focus and this gives some spectral broadening and modulation mainly due to self phase-modulation (SPM). However, as can be seen from the figure, this effect is rather limited. Moreover, measurements taken after the straight waveguide device showed a spectrum intermediate between these two conditions and with no evident dependence on the particular choice of the gas inserted in the channel. This is probably due both to the rather small interaction length and gas pressure used, which is always lower than one bar, and to the guiding mechanism itself, which reduces the effective intensity of the field with respect to the one of a Gaussian beam near the focus. For all these reasons, at least as a first approximation, we won't expect strong influences on the harmonic generation process from the spectral modulations of the driving laser due to lower order nonlinearities.

4.2.2 Straight waveguide device

The first device that was employed in these experiments is a simple linear channel with a length of $L = 6$ mm and a radius of $a \approx 65$ µm. Its fabrication was performed using the second harmonic of the Yb:KYW laser source presented in Section 3.3, with a power of $P \approx 300$ mW and a repetition rate of $f_{\text{rep}} \approx 1$ MHz, which allow to reach an inscription speed of $v \approx 0.2$ mm/s. The polarization of the source was maintained perpendicular with respect to the translational direction, in order to fabricate long nanoplanes, which help the diffusion of the acid during the etching process. The gas flow in the waveguide is ensured by six channels, separated by 1 mm each, that are linked to a reservoir where an external inlet can be inserted. Some

preliminary results regarding this configuration were discussed in previous works [132, 133]. In particular, the correct working of the device and an amplification of the signal with respect to the usual gas jet interaction geometry were demonstrated.

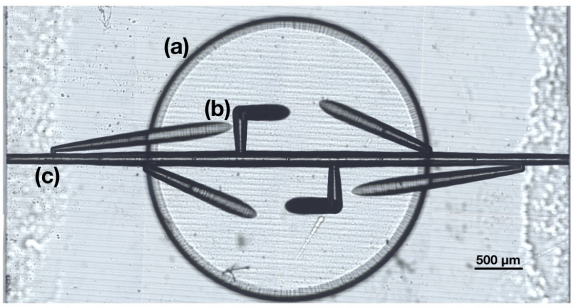

Figure 4.26: Photographic images of the linear channel from the top. a) Section of the gas reservoir. b) Gas entrance channel. c) Main waveguide.

Various experimental parameters were then analysed in order to better understand their influence on the harmonic generation and to optimize its output. Since the waveguide radius is fixed and both the iris aperture and the relative position of the channel with respect to the beam focus are optimized each time, the most important control knob in our case is the gas pressure. Indeed, for a fixed driving intensity, it defines the relative contribution of the phase mismatch linked to the medium dispersion with respect to the geometrical one. In particular, at low intensities the ionization of the medium may be neglected and for this reason the more dispersive is the gas the less will be the pressure needed to obtain a good phase matching. At higher intensities, instead, also the ionization potential of the considered atom will start to play an important role, as it ultimately defines the relative importance of the plasma and neutral terms. However, it is important to remember that this simple reasoning stands only as long as the medium pressure and the channel length are enough low to avoid the absorption of the XUV radiation, which is proportional to both of them.

The prediction of the optimum pressure for the harmonic generation in the channel is therefore not trivial from a theoretical point of view, even if it can be easily determined experimentally by means of a pressure scan. This was done for various noble gases obtaining a maximization of the integrated signal for $P > 300$ mbar in He and for $P \approx 50 \div 100$ mbar in Ne and Ar, depending on the particular experimental conditions. It is important to underline that what we refer to is always the backing pressure, which is measured at the entrance of the reservoir, while its exact value inside the channel may in principle be different and is generally not homogeneous both in space and time. Anyway, it is interesting to notice that this founding is in agreement with what we would expect by comparing the behaviour of the refractive indexes of these gases in the XUV region, as it is shown in Figure 4.27. Therefore, we may conclude that in our experimental conditions the

low-intensity regime is usually the predominant one. This is proved also by the computation of the ionization percentage of the media in the channel, which can be estimated by the ADK rate to be far below few percent, owing to the relatively short pulse duration. For these reasons, a first approximative description of the phase matching conditions inside the channel may consider only the neutral and geometrical terms, with the plasma contribution that acts only as a second order correction.

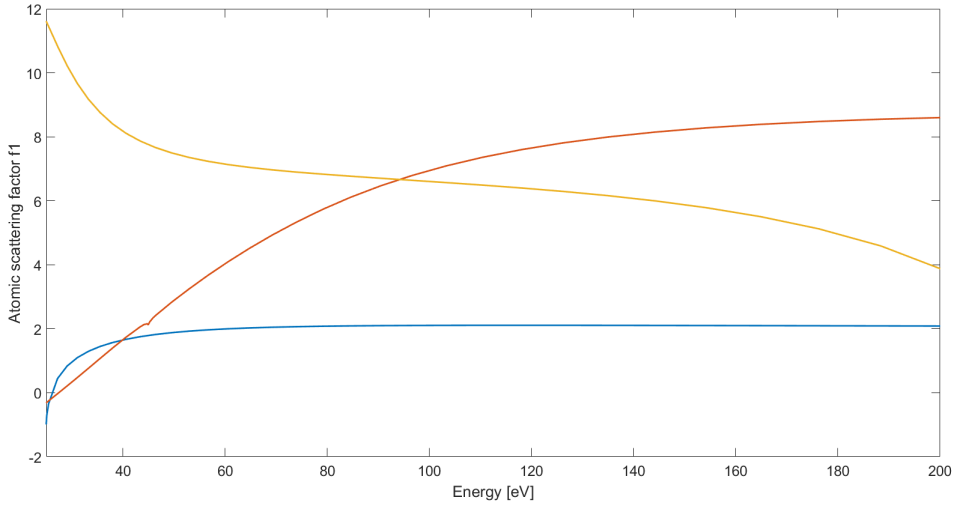

Figure 4.27: Dispersive term of the atomic scattering factor for the three analysed noble gases: helium (blue), neon (red) and argon (yellow).

However, the maximization of the integrated signal can give only little information about the generation process, since both absorption and phase matching reshape the harmonic spectrum as a function of the pressure. This can be understood with the fact that the optimal pressure actually varies with the harmonic order. As an example, in Figure 4.28 the spectra for $P = 300, 500$ and 700 mbar of helium are given. Each measurement was calibrated on the energy axis using the recurrence of the second order of the spectrometer and it was multiplied by the Jacobian dpixels/d$\mathcal{E}$ in order to maintain constant its integral value. As the backing pressure increases lower order harmonics are quenched with respect to the higher order ones. This is a feature that is visible in all the acquired pressure scans and it is in agreement with the fact that the XUV absorption of noble gases is a decreasing function of the photon energy. Therefore, as the pressure increases, the bandwidth over which harmonics are efficiently generated reduces and the spectrum becomes more peaked near the cutoff.

In order to better understand this issue, a rather simple model for harmonic generation in the channel can be implemented using Eq.(1.39) to evaluate the phase mismatch as a function of the harmonic order and then Eq.(1.27) to retrieve the signal at the exit of the waveguide. The computation doesn't account for the characteristic dipole moment of the considered atom but following [46] this quantity

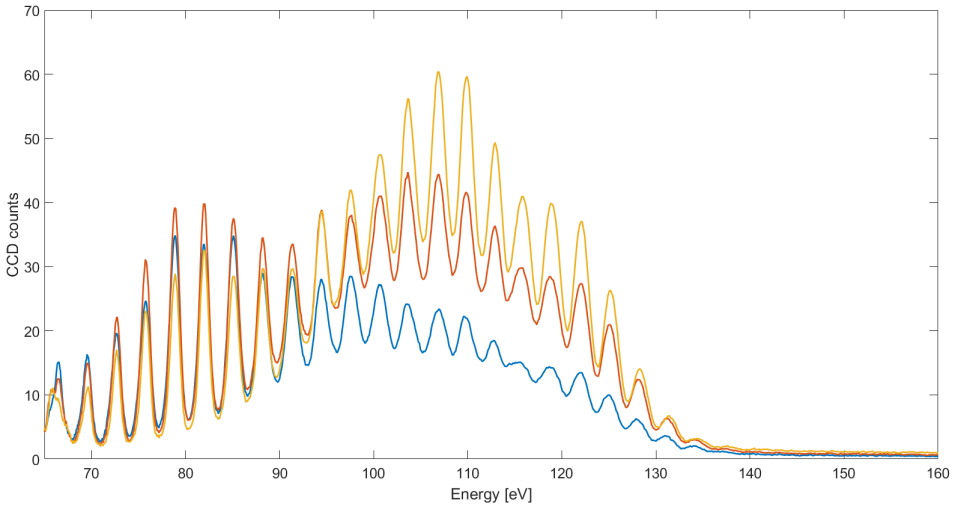

Figure 4.28: Harmonic spectra in helium for $P = 300$ mbar (blue), $P = 500mbar$ (red) and $P = 70$ mbar (yellow). Each curve is normalized with respect to the number of driving pulses and only the signal above $\mathcal{E} = 65$ eV is considered, in order to exclude the second order of the spectrometer.

is approximated only with a simple power law dependence on the driving field $|d| \propto |E|^p$, where $p = 5$ is chosen to better fit the experimental results. In addition, to account for the spatio-temporal dynamics of the phase mismatch in the channel, the model is developed in 2D considering the temporal and transversal coordinates, while the pressure and the field shape are assumed fixed along the longitudinal direction. The intensity of the driving field was instead retrieved from the semiclassical evaluation of the experimental HHG cutoff. Finally, Eq.(1.27)is also divided for the photon energy in order to obtain the photon irradiance, which can be more directly confronted with the CCD counts. Some result of this simple model in the case of helium are presented in Figure 4.29. Only a qualitative agreement can be established with the experimental results, as the absorption of the low-order harmonics increases with the gas pressure while the maximum of the spectrum is shifted from $\mathcal{E} \approx 80$ eV to $\mathcal{E} \approx 110$ eV. However, it is important to consider that in principle this computation provides only the emission at the exit of the channel, while the measured signal is influenced also by the efficiency and the responsivity of the whole detection system, which may further modify the spectrum. Nevertheless, a characterization of the spectrometer in UdynI is not available. Anyway, it is clear that more quantitative results for the harmonic spectra are not possible with this simple model, as it implies a lot of approximations.

One of the most important of them is the assumption that the XUV radiation propagates like a plane wave. Indeed, as it was treated in Section 1.2, we know that the emitted harmonics show always a phase term inherited from the electron excursion in the continuum. Considering a monochromatic and linearly polarized driving field, this phase can be expressed as [13]:

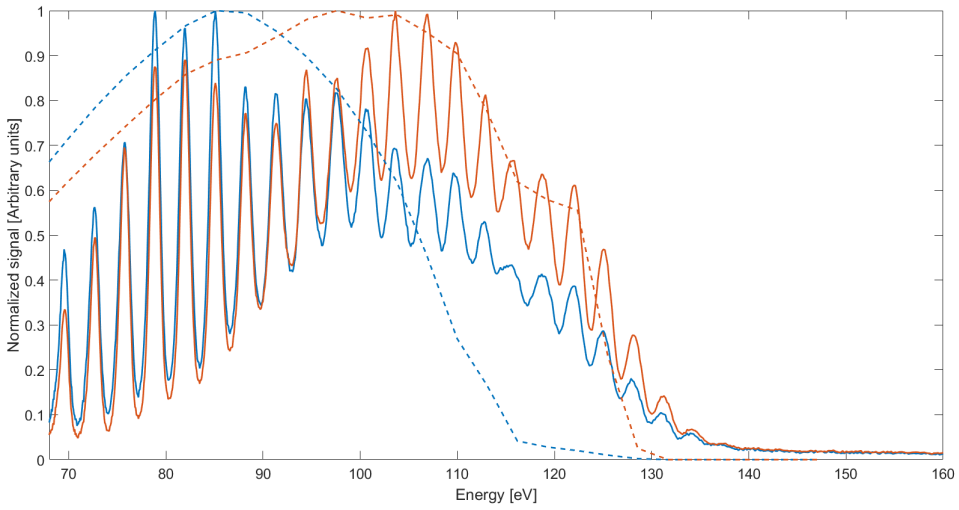

Figure 4.29: Harmonic spectra in helium for $P = 300$ mbar(blue) and $P = 500$ mbar (red). Simulations are represented with dashed lines. Each curve is normalized to its peak for comparing their shape and only the signal above $\mathcal{E} = 65$ eV is considered, as in Figure 4.28.

$$\phi_n(q, I) = q\omega_f t - \frac{1}{\hbar} S(\mathbf{p}, t, t')$$

$$S(\mathbf{p}, t, t') = I_p \tau + 2\frac{U_p K(t, \tau)}{\omega_f}$$

$$K(t, \tau) = \frac{\omega_f \tau}{2} - \left[\frac{1 - \cos(\omega_f \tau)}{\omega_f \tau} + \frac{C(\tau)}{2}\cos(2\omega_f t - \omega_f \tau)\right]$$

$$C(\tau) = -\frac{4}{\omega_f \tau}\sin^2\left(\frac{\omega_f \tau}{2} + \sin(\omega_f \tau)\right)$$

where $\tau = t - t'$ is the time spent by the electron in the continuum. In this approach the dipole phase is thus independent on the particular choice of generating medium and on the gas pressure, while depends heavily on the transversal profile of the driving field inside the waveguide. The computed phase fronts for the semiclassical short and long trajectories considering a perfect coupling to the fundamental EH_{11} mode of the channel are sketched in Figure 4.30. As can be easily noticed, long trajectories are always more divergent than short ones, like it is well known also in the case of the gas-jet interaction geometry. However, the two classes of trajectories display a different behaviour with respect to the harmonic order. Indeed, short trajectories are more divergent for higher orders while the opposite is true for long ones. For this reason, it is not trivial to understand how to improve the simple plane wave description for the XUV radiation as a more correct description should account not only for the exact distribution of the driving field in the channel but also for the selection of trajectories provided by the phase matching conditions. Moreover, as a

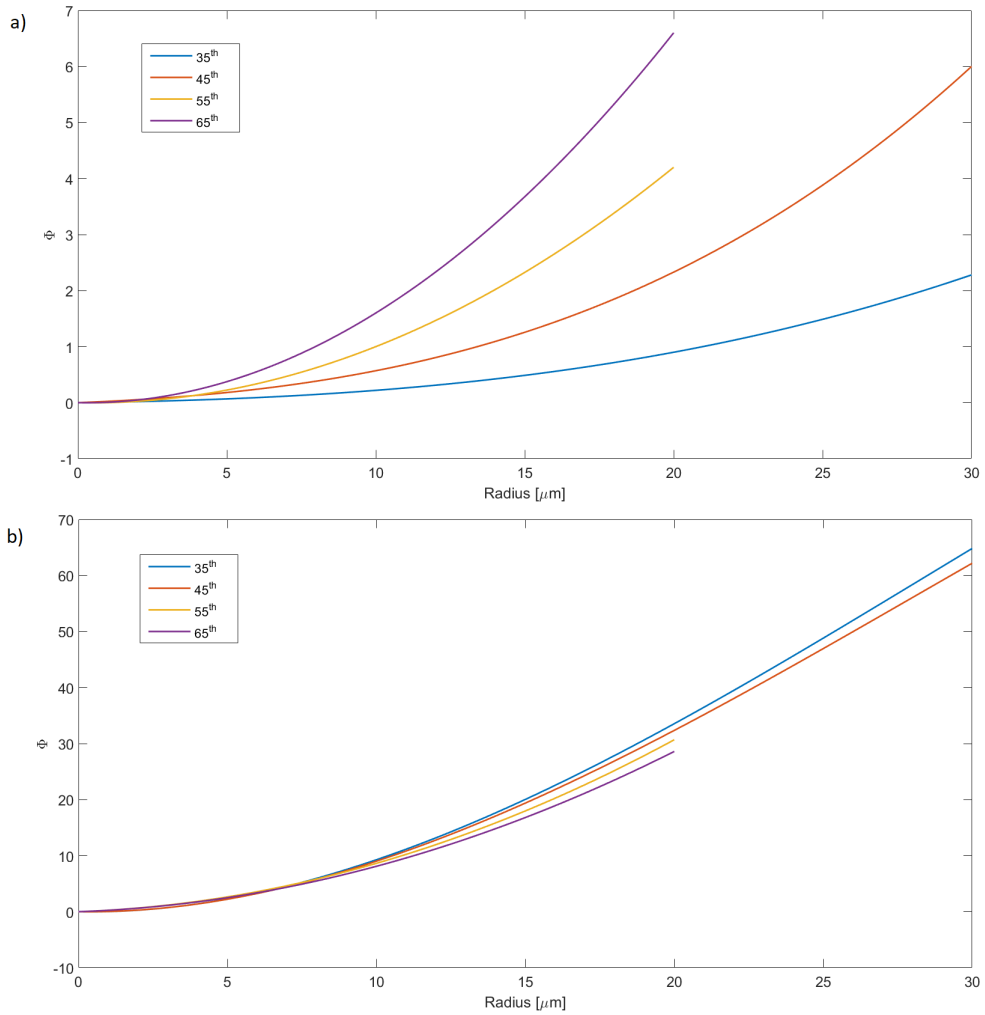

Figure 4.30: Phases of the generated harmonics in the channel as a function of its radius. The peak intensity of the EH_{11} field is set to $I_0 \approx 6 \cdot 10^{14} \mathrm{W/cm^2}$ from the evaluation of the experimental cutoff and only semiclassical trajectories are considered. a) Short trajectories and b) long trajectories.

matter of fact, the trajectories which due to absorption cannot propagate enough to encounter the boundaries of the channel may probably still be treated as plane waves.

The intrinsic limits of Eq.(1.27) are therefore mainly linked to the assumed homogeneity of the conditions in the longitudinal coordinate, both with respect to the gas density and the driving field. Indeed the shape of the IR field in the waveguide could be reshaped by the coupling to higher order modes. For instance, this may happen due to nonlinear effects taking place in the medium or to the energy losses caused by its ionization. Moreover, the gas pressure will be far from constant owing to its free expansion in vacuum. For improving the understanding of the generation process in the channel, the group previously established a collaboration with the group of Prof. V. Tosa (National Institute for R& D of Isotopic and Molecular Technologies Cluj-Napoca) regarding the simulation of the phase matching conditions and the propagation of the radiation in the waveguide and with the group of Prof. A. Frezzotti (Aerospace Department, Politecnico di Milano) regarding the study of the microfluidic dynamics in the channels. Further insight on these preliminary results will therefore be probably gained in the future.

As a last comment on these measurements, it is important to underline that, even if the amplification of the HHG signal with respect to the tight focusing geometry is the biggest advantage of the straight waveguide device, its exploitation in spectroscopic studies is not straightforward. Indeed, although a higher output allows in principle to enhance the signal-to-noise ratio and to identify also very small features of the spectrum, the single atom response, which is ultimately the quantity of interest, cannot be retrieved easily due to the reshaping induced both by the absorption and the phase matching conditions. Therefore the simulations provided by the mentioned collaborations could be extremely useful also in this perspective.

4.2.3 Modulated waveguide device

Exploiting the full potential of the FLM technique, a device constituted by a waveguide with a modulation step of $\Lambda \approx 200$ µm was fabricated in order for studying the possibility to accomplish QPM of the XUV radiation. The channel has the same length of the straight one, while the radius of its section varies between $a_{\max} \approx 65$ µm and $a_{\min} \approx 55$ µm. In correspondence of each narrowing a channel linked to the reservoir allows the gas to flow in the waveguide, while opposite to it another one facilitates its removal (see Figure 4.31). The experiments employing this new device have only recently started and therefore we will present here just few very preliminary results. In particular, we concentrated also in this case on the characterization of the emitted spectrum as a function of the generating medium and the gas backing pressure, while all other parameters were optimized before each acquisition. These results are resumed in Figure 4.32, where a comparison with the same pressure scans measured in the straight channel is made. The optimal value of the backing pressure for maximizing the emission seems to be always higher for the QPM device with respect to the straight waveguide. In particular, the signal in helium seemed to

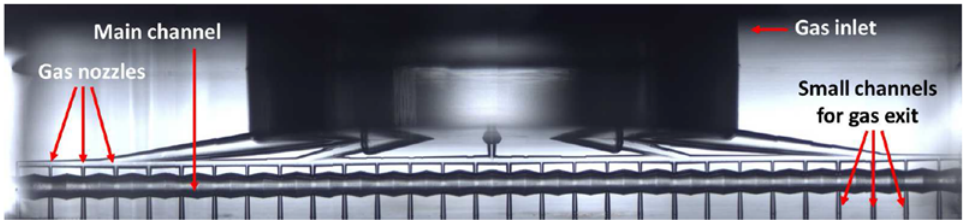

Figure 4.31: Photographic image of the modulated waveguide, directly taken from [133]. The principal channels where the gas flows are indicated.

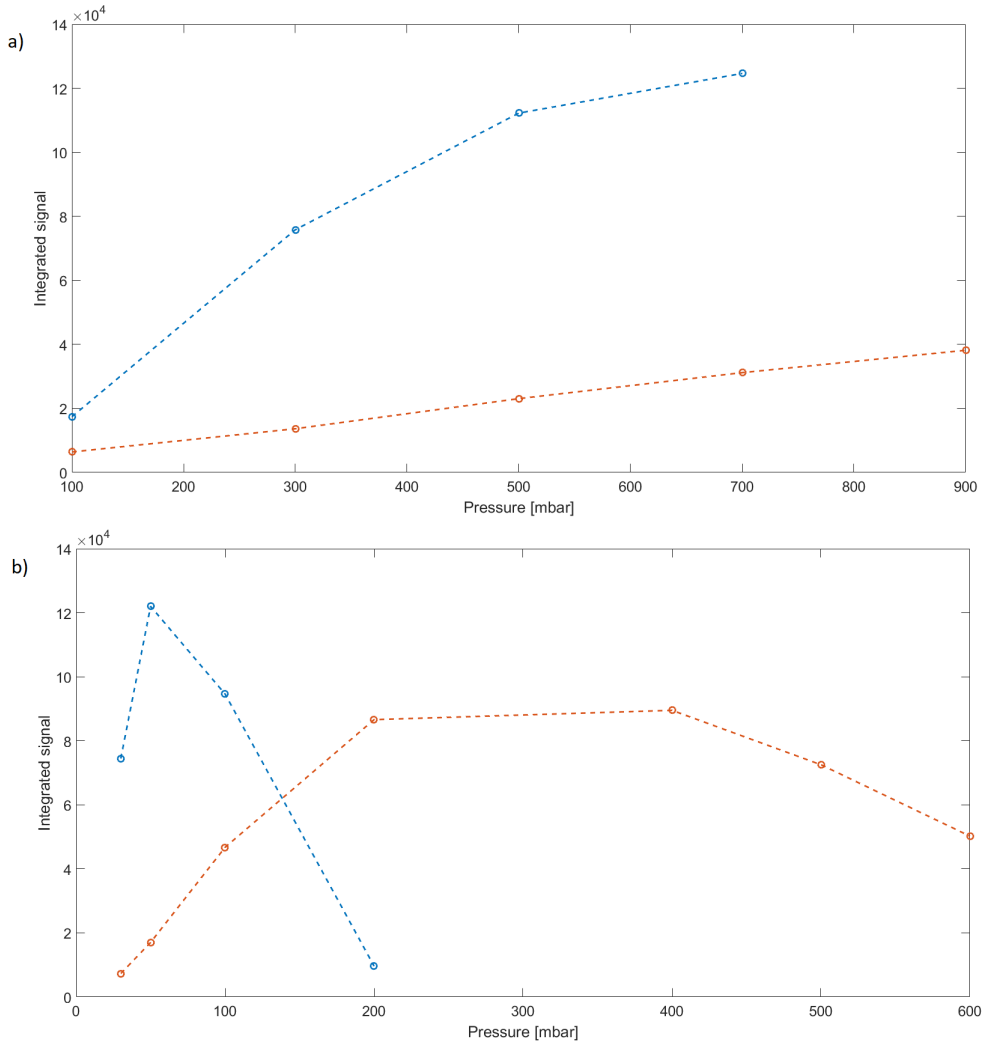

Figure 4.32: Integrated harmonic signal as a function of the channel backing pressure a) in helium and b) in neon. The blue curve represents the straight channel, while the red one represents the modulated waveguide. Each measurement is normalized to the number of driving pulses and only the signal above 60 eV is considered, in order to exclude the contribution of the second order of the spectrometer.

be constantly increasing and we couldn't reach its maximum due to the limitation of the pumping system for maintaining the vacuum inside the interaction chamber. Moreover the measurements in neon suggest that the emission could also be much less influenced by the pressure, as the sharp maximum at $P = 50$ mbar is substituted by a more regular plateau-like behaviour in the region $P = 200 \div 400$ mbar. It is also clear that generally the straight waveguide offers a higher integrated signal, even if for a narrower pressure window and in a shorter spectral bandwidth. Anyway we must underline that a direct comparison is not significant in the case of helium, as the energy range selected in the analysis to exclude the contribution of the second order of the spectrometer highly disadvantages the signal of the modulated channel.

More informations were then gained studying the evolution of the harmonic spectrum with pressure, instead of its integrated value. An example in the case of helium is given in Figure 4.33.

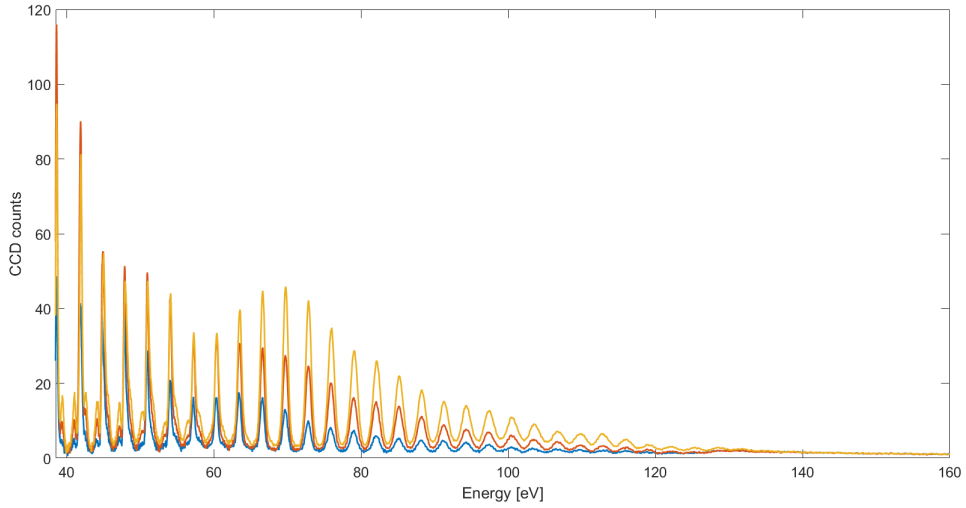

Figure 4.33: Harmonic spectrum as a function of the backing pressure in the modulated waveguide device in helium: $P = 300$mbar (blu), $P = 500$ mbar (red) and $P = 900$ mbar (yellow). Each measurement is normalized to the number of driving pulses.

The cutoff is generally comparable with the one obtained with the straight waveguide, differently from what would be expected if an efficient QPM of the higher harmonics were present. However, no quenching of lower-order harmonics is present as the backing pressure increases and only a few spectral reshaping is visible. Indeed, it seems like the absorption of the XUV radiation along the channel can be generally neglected for this device configuration. This could be caused by an higher confinement of the medium in the narrowings of the waveguide, as the exit channels allow the gas to flow outside more rapidly and efficiently with respect to the main waveguide. Thus, the effective length over which absorption can take place is reduced. If this were the case, this interaction geometry may be

thought of as an hybrid between the QPM schemes employing modulated channels and multiple sources which were presented in Section 1.3.4. Another hint in this direction could be provided also by the overall shape of the spectra, which generally resemble much more the ones measured with the gas jet geometry than the ones measured after the straight channel.

However this is just a preliminary hypothesis and only more precise microfluidic simulations can dismiss or confirm it. Anyway, if this were the case, the use of a modulated waveguide could be potentially useful in spectroscopic studies, allowing to overcome the limitations linked to the reshaping of the spectra in the straight channel.

Conclusions and perspectives

In this thesis two different approaches for increasing the amount of information that can be gained in high-harmonic spectroscopy experiments were analysed. The first relies on a motorized translation stage, designed by the group of Proff. S. Stagira and C. Vozzi, to move the detector along the focal curve of a spherical varied line spacing grating and to acquire the signal in different spectral windows. This is particularly useful when systems characterized by low ionization potentials are studied, as the information is concentrated at rather small photon energies. In the second case an extended interaction length is exploited in microstructured channels for reaching a more intense emission and a potentially higher cutoff. In this perspective the manufacturing flexibility offered by the FLM technique provides the possibility to fabricate very complex 3D structures and to potentially integrate more functionalities on the same device.

For the first one of such approaches a calibration procedure was developed to connect the different acquisitions. In this way the extended harmonic spectrum of the molecules under investigation can be obtained. This method was validated with the investigation of the XUV emission from systems of increasing complexity, starting from carbon dioxide, which is a linear and well studied molecule, and moving to allene and ethylene, that are respectively a symmetric and an asymmetric rotor. In these preliminary measurements it was possible to detect harmonics lying just above the ionization potential of the molecular HOMO. This represents the edge between the perturbative and strong field regime for the interaction between the molecule and the external field. The generation process in such region is not so well understood, thus giving the possibility to study interesting new physics in the future.

These measurements allowed also to explore the feasibility to obtain 1D alignment of complex molecules with the same experimental setup. This is crucial as the vast majority of molecular systems, in particular the ones of biological interest, are asymmetric rotors. The harmonic signal was found to show a clear modulation in all the acquisitions, confirming the correct alignment of the targets. In particular, in the case of allene both a recession of the cutoff and a feature similar to a two-center interference pattern were underlined. However further studies should be done in order to prove or dismiss this last hypothesis, although the low ionization potential of the molecule makes the achievement of a high-enough cutoff very difficult. In the case of ethylene, instead, its complex rotational dynamics was analysed and the fingerprint of J-revivals was observed in the acquisitions. Some modulation of the harmonic positions with respect to the temporal delay between the aligning and generating pulses was also observed. Similar effects in literature are generally

ascribed to the time dependence of the gas refractive index following the rotational dynamics of the molecules. However this picture is not able to explain our observation and therefore further studies will be needed to better investigate its origin.

In the second part of this experimental work, the generation of high-order harmonics in femtosecond laser fabricated devices was studied. Previous works already demonstrated the possibility to obtain a higher output employing a straight channel in place of the standard gas-jet geometry [132, 133]. A deeper study of the experimental conditions influencing the harmonic spectrum was undertaken, focusing in particular on the backing pressure of the gas. In the case of the linear waveguide this exhibits an optimal value for the integrated harmonic signal, which depends on the considered noble gas and is in agreement with the conditions of the low-ionization regime. Moreover the shape of the emission is ultimately determined by the interplay between the absorption of the medium and the phase matching conditions in the channel. For better understanding these effects a simple plane wave model was used, which however could get only few very qualitative features of the spectra. The reasons behind these discrepancies were analysed and the main issue was found in the assumed homogeneity of the conditions along the longitudinal dimension of the channel. More quantitative results will require numerical simulations for both the gas dynamics and the field propagation in the waveguide. For this reason the group has previously established external collaborations.

Finally, the generation of XUV radiation in modulated microchannels was studied. Due to time constraints only very preliminary results were obtained. Differently from what would be expected if quasi phase matching of the harmonics were present, no increment of the cutoff is visible. However, the optimal pressure is found to be higher with respect to the straight waveguide device for all gases and the effect of spectral reshaping due to absorption and phase matching seems to be generally negligible. The origin of such effects needs to be investigated more deeply in the future. Moreover, the harmonic generation in even more complex geometries will be explored, along with the possibility to perform spectroscopic studies in such waveguides. In particular, the signal amplification offered by the straight channel could provide a way to identify also very small spectral features, while the robustness to absorption and phase matching conditions of the modulated waveguide could allow to retrieve more easily the single atom response.

APPENDIX A

Continuum wave packet

To find the expression for the amplitude of the continuum wave packet we should substitute Eq.(1.11) inside the time dependent Schrödinger equation describing the system. The left-hand side thus reads:

$$i\hbar\frac{\partial}{\partial t}\left|\Psi\right\rangle = i\hbar e^{i\frac{I_p t}{\hbar}}\Big[\frac{\partial a(t)}{\partial t}\left|0\right\rangle + i\frac{I_p}{\hbar}a(t)\left|0\right\rangle + \int\frac{\partial b(\mathbf{k},t)}{\partial t}\left|\mathbf{k}\right\rangle d\mathbf{k} + i\frac{I_p}{\hbar}\int b(\mathbf{k},t)\left|\mathbf{k}\right\rangle d\mathbf{k}\Big]$$

while the right-hand side becomes:

$$\hat{H}\left|\Psi\right\rangle = e^{i\frac{I_p t}{\hbar}}\Big\{\Big(-\frac{\hbar^2}{2m_e}\nabla_r^2 + V_{\text{eff}}(r) + e\mathbf{E}_f\cdot\mathbf{r}\Big)\Big(a(t)\left|0\right\rangle + \int b(\mathbf{k},t)\left|\mathbf{k}\right\rangle d\mathbf{k}\Big)\Big\}$$

From the TDSE of the unperturbed system it is possible to simplify the terms:

$$i\hbar\frac{\partial}{\partial t}\left|0\right\rangle = -I_p\left|0\right\rangle = -\frac{\hbar^2}{2m_e}\nabla_r^2|0\rangle + V_{\text{eff}}(r)\left|0\right\rangle$$

Then for further reducing this equation, it is projected along one of the continuum wavefunctions $\langle\mathbf{k'}|$ and it is integrated in wave vector space. Indeed since the states representing plane waves are orthogonal among them, we have that:

$$\langle\mathbf{k'}|\mathbf{k}\rangle = \delta(\mathbf{k'}-\mathbf{k})$$

Moreover from the expression of the continuum states it is possible to demonstrate that:

$$\nabla_r^2\left|\mathbf{k}\right\rangle = -(\mathbf{k}\cdot\mathbf{k})\left|\mathbf{k}\right\rangle$$

$$-i\boldsymbol{\nabla}_k\left|\mathbf{k}\right\rangle = \mathbf{r}\left|\mathbf{k}\right\rangle$$

Therefore while projecting along $\langle\mathbf{k'}|$ we can also exploit these properties to simplify the following terms:

$$\langle\mathbf{k'}|\nabla_r^2\left|\mathbf{k}\right\rangle = -(\mathbf{k}\cdot\mathbf{k})\langle\mathbf{k'}|\mathbf{k}\rangle = -(\mathbf{k'}\cdot\mathbf{k'}) = -|\mathbf{k'}|^2$$

$$\int b(\mathbf{k},t)\langle\mathbf{k'}|\mathbf{r}\left|\mathbf{k}\right\rangle d\mathbf{k} = \int b(\mathbf{k},t)\langle\mathbf{k}|\mathbf{r}\left|\mathbf{k'}\right\rangle^* d\mathbf{k} = \int b(\mathbf{k},t)[-i\langle\mathbf{k}|\boldsymbol{\nabla}_{k'}\left|\mathbf{k'}\right\rangle]d\mathbf{k} =$$

$$= \boldsymbol{\nabla}_{k'}\int b(\mathbf{k},t)[-i\langle\mathbf{k}|\mathbf{k'}\rangle^*]d\mathbf{k} = i\boldsymbol{\nabla}_{k'}b(\mathrm{k'},t)$$

Finally, since it can be demonstrated that $a(t)$ is a term that varies slowly in time, we can further assume $\partial a(t)/\partial t \approx 0$. The TDSE is thus reduced to:

$$i\hbar\frac{\partial}{\partial t}b(\mathbf{k'},t) = \int b(\mathbf{k},t)\,\langle\mathbf{k'}|\,V_{\text{eff}}(r)\,|\mathbf{k}\rangle\,d\mathbf{k} + \Big[\frac{|\mathbf{k'}|^2\hbar^2}{2m_e} + I_p\Big]b(\mathbf{k'},t) + \\ + ea(t)\,\langle\mathbf{k'}|\,\mathbf{E}_f\cdot\mathbf{r}(t)\,|0\rangle + ie\mathbf{E}_f\cdot\boldsymbol{\nabla}_{k'}b(\mathbf{k'},t)$$

which defines an infinite set of differential equations for the $b(\mathbf{k'},t)$ terms coupled by the integral. To find a closed-form solution we can once again exploit the SFA, for which the contribution of the effective atomic potential $V_{\text{eff}}(r)$ on the continuum states can be neglected. Thus the integral can be setted to zero and the equations become uncoupled:

$$i\hbar\frac{\partial}{\partial t}b(\mathbf{k'},t) = \Big[\frac{|\mathbf{k'}|^2\hbar^2}{2m_e} + I_p\Big]b(\mathbf{k'},t) + ea(t)\,\langle\mathbf{k'}|\,\mathbf{E}_f\cdot\mathbf{r}(t)\,|0\rangle + ie\mathbf{E}_f\cdot\boldsymbol{\nabla}_{k'}b(\mathbf{k'},t)$$

We then do a formal substitution of the only variable present $\mathbf{k'}\to\mathbf{k}$ and define the dipole transition matrix element $\mathbf{d}(\mathbf{k}) = \langle\mathbf{k}|\,\mathbf{r}(t)\,|0\rangle$ to make the expression more readable:

$$\frac{\partial}{\partial t}b(\mathbf{k},t) = -\frac{i}{\hbar}\Big[\frac{|\mathbf{k}|^2\hbar^2}{2m_e} + I_p\Big]b(\mathbf{k},t) - \frac{ie}{\hbar}a(t)\mathbf{d}(\mathbf{k})\cdot\mathbf{E}_f + \frac{e}{\hbar}\mathbf{E}_f\cdot\boldsymbol{\nabla}_k b(\mathbf{k},t)$$

In this form all the coefficients in the equation are proportional to important physical quantities:

$$G = \frac{1}{\hbar}\Big[\frac{k^2\hbar^2}{2m_e} + I_p\Big]$$

$$U = \frac{e}{\hbar}a(t)\mathbf{d}(\mathbf{k})\cdot\mathbf{E}_f(t)$$

$$\mathbf{F} = -\frac{e}{\hbar}\mathbf{E}_f(t)$$

where the first one is the sum of the atomic ionization potential and the kinetic energy of the plane wave, the second is the energy of the dipole $\mathbf{d}(\mathbf{k})$ inside the laser pulse and the last one is the force experienced by the electron due to the external field. In order to solve such differential equation it is then usefull to perform a change of variable $t\to\zeta$ and $\mathbf{k}\to\mathbf{p}$. The idea is to choose a variable ζ in order to have $\mathbf{p}$ constant as $b(\mathbf{k},t)$ evolves in time. A good solution is to set [27]:

$$\frac{\mathrm{d}\mathbf{k}}{\mathrm{d}\zeta} = \mathbf{F} \qquad \frac{\mathrm{d}t}{\mathrm{d}\zeta} = 1$$

so that we obtain a simple differential equation:

$$\frac{\mathrm{d}}{\mathrm{d}\zeta}b(\mathbf{k}(\zeta),t(\zeta)) = -iGb\left(\mathbf{k}(\zeta),t(\zeta)\right) - iU$$

and then choose as change of variables:

$$\zeta = t$$

$$\mathbf{p} = \hbar\mathbf{k} + e\int \mathbf{E}_f(\zeta)d\zeta = \hbar\mathbf{k} - e\mathbf{A}_f(\zeta)$$

where $\mathbf{A}_f(\zeta)$ is the vector potential of the field. It is important to underline that with this choice $\mathbf{p}$ is the canonical momentum of the electron. The differential equation thus reads:

$$\frac{\mathrm{d}}{\mathrm{d}\zeta}b(\mathbf{p},\zeta) = -iGb\,(\mathbf{p},\zeta) - iU$$

whose general solution can be demonstrated to be

$$b(\mathbf{p},\zeta) = e^{-i\int d\zeta' G(\zeta')}\left[-i\int U e^{i\int d\zeta'' G(\zeta'')}d\zeta' + C\right]$$

The constant C is found by setting as boundary condition $b(\mathbf{p},-\infty) = 0$ since we consider the electron initially in the atomic ground state:

$$C = i\int U(\zeta')e^{i\int d\zeta'' G(\zeta'')}d\zeta'$$

Finally, substituting it in the expression for $b(\mathbf{p},\zeta)$, making all terms explicit and going back to the initial temporal variable $\zeta \to t$ we get our final result:

$$b(\mathbf{p},t) = -i\frac{e}{\hbar}\int_{-\infty}^{t} a(t')\mathbf{d}[\mathbf{p} + e\mathbf{A}_f(t')]\cdot\mathbf{E}_f(t')e^{-\frac{i}{\hbar}S(\mathbf{p},t,t')}dt'$$

where

$$S(\mathbf{p},t,t') = \int_{t'}^{t}(I_p + \frac{[\mathbf{p} + e\mathbf{A}_f(t'')]^2}{2m_e})dt''$$

is the quasi-classical action of the electron in the driving field from the ionization time t' to the recombination time t. The notation $\mathbf{x}^2 = \mathbf{x}\cdot\mathbf{x}$ is here used for the ease of the reader.

APPENDIX B

Hollow waveguide modes

In order to retrieve the modes of a cylindrical waveguide it is in principle necessary to determine both the electric and the magnetic field of the propagating light. In doing so we will follow the derivation of [44] and [45]. It is convenient to start from Maxwell curl equations for **E** and **H**:

$$\boldsymbol{\nabla} \times \mathbf{E} = -\mu_0 \frac{\partial}{\partial t}\mathbf{H} \qquad \boldsymbol{\nabla} \times \mathbf{H} = \epsilon_0 n^2 \frac{\partial}{\partial t}\mathbf{E}$$

where only the linear polarization of the medium has been considered, in accordance with the approximation already used for plane wave and tight focusing geometries. A simplification of this equations is expected when exploiting cylindrical coordinates (r, θ, x) due to the symmetry of the problem.

$$\boldsymbol{\nabla} \times \mathbf{E} = \Big(\frac{1}{r}\frac{\partial}{\partial \theta}E_x - \frac{\partial}{\partial x}E_\theta\Big)\mathbf{e}_r + \Big(\frac{\partial}{\partial x}E_r - \frac{\partial}{\partial r}E_x\Big)\mathbf{e}_\theta + \Big(\frac{1}{r}\frac{\partial}{\partial r}(rE_\theta) - \frac{\partial}{\partial \theta}E_r\Big)\mathbf{e}_x$$

The same expression is valid also for the magnetic field. Moreover, assuming that the medium is homogeneous and thus the refractive index depends only on the frequency of the field $n = n(\omega)$, it is possible to use a separated variable ansatz in the transverse and longitudinal direction for the electric and magnetic fields:

$$\mathbf{E}(r, \theta, x, \omega) = \mathbf{A}(r, \theta, \omega)e^{i(\omega t - \gamma(\omega)x)}$$

$$\mathbf{H}(r, \theta, x, \omega) = \mathbf{G}(r, \theta, \omega)e^{i(\omega t - \gamma(\omega)x)}$$

Substituting them in the Maxwell equations we can demonstrate that their solutions depend only on the x components of the two fields:

$$\frac{\partial^2}{\partial r^2}A_x + \frac{1}{r}\frac{\partial}{\partial r}A_x + \frac{1}{r^2}\frac{\partial}{\partial \theta}A_x + (k^2 n^2(\omega) - \gamma(\omega))A_x = 0$$

$$\frac{\partial^2}{\partial r^2}G_x + \frac{1}{r}\frac{\partial}{\partial r}G_x + \frac{1}{r^2}\frac{\partial}{\partial \theta}G_x + (k^2 n^2(\omega) - \gamma(\omega))G_x = 0$$

while the other two components can be found directly from these:

$$A_r = -\frac{i}{k^2 n(\omega)^2 - \gamma(\omega)^2}\Big(\gamma(\omega)\frac{\partial}{\partial r}A_x + \frac{\omega\mu_0}{r}\frac{\partial}{\partial \theta}G_x\Big)$$

$$A_\theta = -\frac{i}{k^2 n(\omega^2 - \gamma(\omega)^2}\Big(\frac{\gamma(\omega)}{r}\frac{\partial}{\partial \theta}A_x - \omega\mu_0\frac{\partial}{\partial r}G_x\Big)$$

$$G_r = -\frac{i}{k^2 n(\omega)^2 - \gamma(\omega)^2}\Big(\gamma(\omega)\frac{\partial}{\partial r}G_x - \frac{\omega\epsilon_0 n^2}{r}\frac{\partial}{\partial\theta}A_x\Big)$$

$$G_\theta = -\frac{i}{k^2 n(\omega)^2 - \gamma(\omega)^2}\Big(\frac{\gamma(\omega)}{r}\frac{\partial}{\partial\theta}G_x + \omega\epsilon_0 n^2\frac{\partial}{\partial r}A_x\Big)$$

Therefore in order to obtain the modes in the waveguide it is sufficient to consider the equations for the x components of the fields, which are uncoupled. For solving them it is possible to use another ansatz which further separate the variables in the radial and angular coordinates:

$$A_x = \mathcal{A}_x(r,\omega)\sin(s\theta+\phi)$$

$$G_x = \mathcal{G}_x(r,\omega)\cos(s\theta+\phi)$$

with s an integer number called mode parameter and ϕ a generic offset phase. In this way the so-called Bessel equations for the longitudinal components of the fields in the waveguide are found:

$$\frac{\partial^2}{\partial r^2}\mathcal{A}_x + \frac{1}{r}\frac{\partial}{\partial r}\mathcal{A}_x + \Big(k^2 n^2(\omega) - \gamma^2(\omega) - \frac{s^2}{r^2}\Big)\mathcal{A}_x = 0$$

$$\frac{\partial^2}{\partial r^2}\mathcal{G}_x + \frac{1}{r}\frac{\partial}{\partial r}\mathcal{G}_x + \Big(k^2 n^2(\omega) - \gamma^2(\omega) - \frac{s^2}{r^2}\Big)\mathcal{G}_x = 0$$

These are well known equations in mathematical physics, whose solutions can be written either as a sum of Bessel function of the first kind and Neumann functions or a sum of Hankel functions of first and second kind. Until now the assumption of a perfectly homogeneous medium was taken and the index of refraction was dependent only on the frequency of the field ω. However, considering an actual waveguide, two different solutions are present in the core and in the cladding, having respectively refraction indexes of n_i and n_e. Therefore we need to join them on the boundary $r = a$ and to set the physical condition of $\mathbf{E}, \mathbf{H} \to 0$ as $r \to \infty$. Doing so, the longitudinal field in the core is described by Bessel functions J_s only and in the cladding by Hankel function of first kind H_s^1 only. In particular we are interested in the first region, which describes the propagation of the fields, while in the second one only an almost exponential decaying is present.

Marcatili further classifies the solutions of these equations in three categories: the transverse electric (TE) modes, with no axial component of the electric field; the transverse magnetic (TM) modes, with no axial component of the magnetic field; the hybrid modes (EH), for which the axial components of both fields are different from zero (see Figure B.2). The first two are more straightforward to calculate, but have little interest in this treatment since they cannot describe the linearly polarized fields commonly used in high-order harmonic generation. For this reason we will concentrate only on EH modes.
In the core the solutions of the Bessel equations thus read:

$$\mathcal{A}_x^{int} \propto J_s\Big(\frac{u}{a}r\Big)\sin(s\theta+\phi)$$

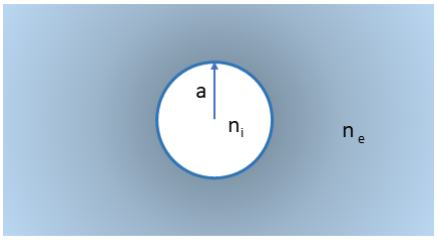

Figure B.1: Sketch of the considered geometry for the problem. The circular inner core or radius a has refractive index n_i while the cladding has refractive index n_e

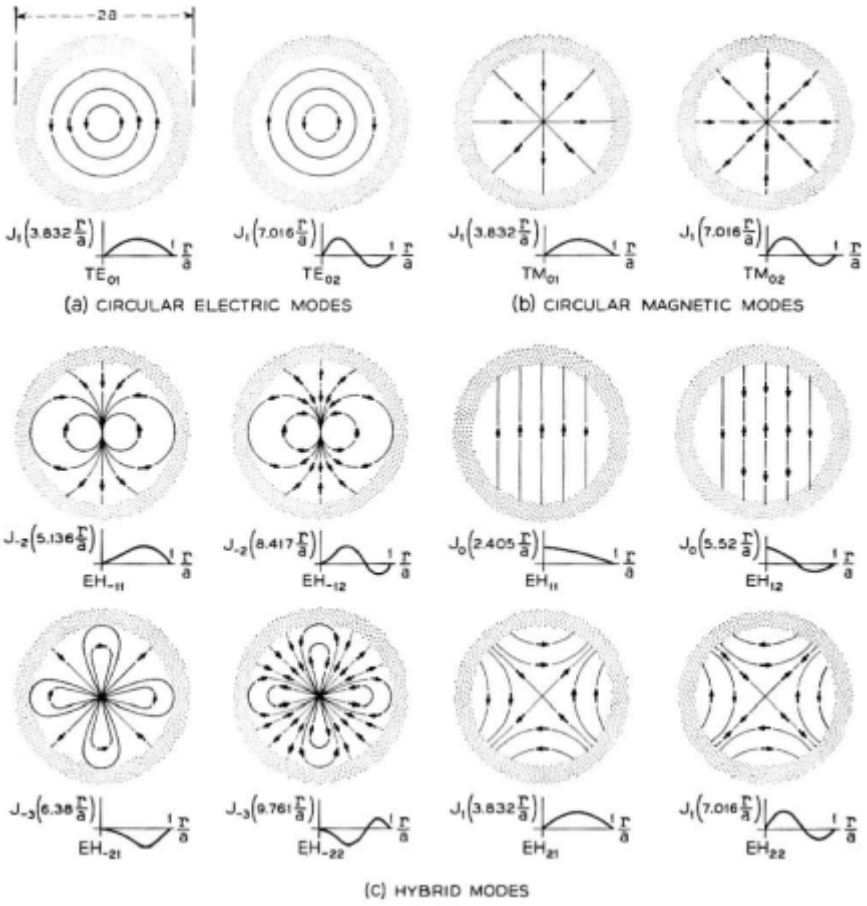

Figure B.2: Electric field lines of hollow dielectric waveguides: (a) TE, (b) TM and (c) EH modes. The figure was directly taken from [44]

$$\mathcal{G}_x^{int} \propto J_s\left(\frac{u}{a}r\right)\cos(s\theta+\phi)$$

with the field distribution that depends on the mode parameter s and the so-called radial wavenumber u/a, where u is a constant that can be obtained from the

boundary conditions. To retrieve it in the most general case one should solve a complex transcendental equation. However an approximate solution is possible if three assumptions are made: $a >> \lambda$, which is always true for the wavelengths usually employed in HHG experiments; the axial wave vector of the propagating field is similar to the one in the vacuum $\gamma \approx k$, which reduces the analysis to modes with low losses; $n_i \approx 1$, that is generally a good approximation for noble gases [1]. In such cases by setting:

$$u(k) \approx u_{sm}\Big(1 - i\frac{(n_e^2+1)}{\sqrt{n_e^2-1}}\frac{1}{ka}\Big)$$

where u_{sm} is the m^{th} root of the equation:

$$J_{s-1}(u_{sm}) = 0$$

we can express the complex propagation constant of the mode by considering the decomposition of the wave vector onto the radial and axial directions:

$$k^2 = \Big(\frac{u}{a}\Big)^2 + \gamma_{sm}^2$$

where u/a is the transversal component of the wave vector while γ_{sm} is the longitudinal one. Isolating the complex propagation constant and taking a Taylor expansion to the second order, a rather simple expression is finally retrieved:

$$\gamma_{sm} \approx k\Big[1 - \frac{1}{2}\Big(\frac{u_{sm}}{ka}\Big)^2\Big(1 - i\frac{(n_e^2+1)}{\sqrt{n_e^2-1}}\frac{1}{ka}\Big)\Big]$$

Therefore, once both γ_{sm} and $\mathcal{A}_x$ are known, the waveguides modes can be obtained directly from Maxwell equations. In particular if we focus on the solutions for the electric field in the core region we have:

$$A_x = -i\frac{u_{sm}}{ka}J_s\Big(\frac{u}{a}r\Big)\sin(s\theta+\phi)$$

$$A_r = \Big[J_{s-1}\Big(\frac{u}{a}r\Big) + i\frac{u_{sm}^2}{2ska}\sqrt{n_e^2-1}J_s'\Big(\frac{u}{a}r\Big)\Big]\cos(s\theta+\phi)$$

$$A_\theta = \Big[J_{s-1}\Big(\frac{u}{a}r\Big) + i\frac{u_{sm}}{2kr}\sqrt{n_e^2-1}J_s'\Big(\frac{u}{a}r\Big)\Big]\sin(s\theta+\phi)$$

These expression are very general but can be further simplified if only the behaviour far from the boundary is considered and the terms depending on λ/a are neglected in the propagation constant. In this case indeed only one of the terms in the sum is important and we can write:

$$A_x = J_s\Big(\frac{u_{sm}}{a}r\Big)\sin(s\theta+\phi)$$

$$A_r = J_{s-1}\Big(\frac{u_{sm}}{a}r\Big)\sin(s\theta+\phi)$$

[1] Of the three assumptions this is the weaker one, since in some cases the refractive index of the gas can be far from unity for some of the wavelengths involved in the HHG process. These results, however, can still describe the system to a certain degree of approximation.

$$A_\theta = J_{s-1}\Big(\frac{u_{sm}}{a}r\Big)\cos(s\theta+\phi)$$

If projected back onto the Cartesian coordinates, these can also be expressed as:

$$A_x = J_s\Big(\frac{u_{sm}}{a}r\Big)\sin(s\theta+\phi)$$

$$A_y = J_{s-1}\Big(\frac{u_{sm}}{a}r\Big)\cos((s-1)\theta+\phi)$$

$$A_z = J_{s-1}\Big(\frac{u_{sm}}{a}r\Big)\sin((s-1)\theta+\phi)$$

Each EH mode is thus identified by two integers numbers s and m, with the most general field inside the waveguide being a combination of all of them:

$$\mathbf{E}(r,\theta,x,t) = \sum_{\mathrm{s,m}} \mathbf{E}_{sm} = \sum_{\mathrm{s,m}} c_{sm}\mathbf{A}_{sm}(r,\theta,\omega)e^{i(\omega t-\gamma_{sm}x)}$$

$$\mathbf{H}(r,\theta,x,t) = \sum_{\mathrm{s,m}} \mathbf{H}_{sm} = \sum_{\mathrm{s,m}} d_{sm}\mathbf{G}_{sm}(r,\theta,\omega)e^{i(\omega t-\gamma_{sm}x)}$$

Since only linearly polarized fields should be considered for the purposes of this thesis, it is then possible to demonstrate that the only interesting EH modes are the ones having $s = 1$, with ϕ fixing the polarization direction [2].

However this is not sufficient to have a complete set of solutions. Indeed from one very general property of Bessel functions of the first kind we have that $J_{-s}(u) = (-1)^s J_s(u)$. Since the propagation constant γ_{sm} depends on the mode only through u_{sm}, it can thus be shown that $u_{-|s|,m} = u_{|s|+2,m}$. Therefore $\mathrm{EH}_{-|s|,m}$ and $\mathrm{EH}_{|s|+2,m}$ are degenerate and can be combined. In particular, if they are added with equal amplitude and phase the solution will show a linear polarization[3]. These so-called composite modes are not radial symmetric as the hybrid modes and suffer from the variation of the relative amplitude or phase between the two modes. Indeed any small variation of them causes such modes to loose their linear polarization. Anyway these can be excited when a linearly polarized wave with no radial symmetry is present at the entrance of the waveguide, for example due to a misalignment of the optical axis between the incoming field and the channel. Anyway in this thesis we will not consider the contribution of such composite modes, assuming always fields with a well defined radial symmetry.

[2] For $a >> \lambda$ the axial part of the EH_{1m} modes is indeed negligible with respect to their longitudinal part.

[3] The hybrid modes that can be combined does not need to be linearly polarized themselves. Within composite modes therefore all EH modes having $s \neq 1$ can in principle contribute to the field propagation.

APPENDIX C

Molecular structure

From a quantum mechanical point of view, to obtain all the information about a molecule one should solve its multi-body Schrödinger equation:

$$i\hbar\frac{\partial}{\partial t}\left|\Psi_{\mathrm{mol}}\right\rangle(\mathbf{r},\mathbf{R},t)=\hat{H}_{\mathrm{mol}}\left|\Psi_{\mathrm{mol}}\right\rangle(\mathbf{r},\mathbf{R},t)$$

$$\hat{H}_{\mathrm{mol}}=-\frac{\hbar^2}{2m_e}\sum_i\nabla_i^2-\frac{\hbar^2}{2}\sum_\alpha\frac{1}{M_\alpha}\nabla_\alpha^2+\sum_{i<j}\frac{e^2}{4\pi\epsilon_0\left|r_i-r_j\right|^2}+$$

$$+\sum_{\alpha<\beta}\frac{Z_\alpha Z_\beta e^2}{4\pi\epsilon_0\left|R_\alpha-R_\beta\right|^2}-\sum_{i,\alpha}\frac{Z_\alpha e^2}{4\pi\epsilon_0\left|R_\alpha-r_i\right|^2}$$

where r_i and R_α are respectively the coordinates of the electrons and the nuclei in the system, while M_α and Z_α are respectively the mass and the positive charge of the nucleus identified by α. This equation however cannot be solved analytically, even for the simplest molecules. In order to overcome this difficulty, it thus is necessary to assume the so-called *Born-Oppenheimer approximation* (BO), which allows to uncouple the electron and nuclear motions. Indeed, due to their high difference in mass, the electrons can respond almost instantaneously to a displacement of the nuclei and so one can solve the electronic problem considering the nuclei fixed in different arrangements. In this way a molecular potential energy curve is found, whose minimum will describe the equilibrium configuration of the molecule. We will not deal deeply with the mathematical formulation of this approximation, but we will assume that the molecular problem can be effectively treated with this approach. The system of uncoupled equations for the nuclear and the electronic problem thus reads:

$$\left|\Psi_{\mathrm{mol}}\right\rangle(\mathbf{r},\mathbf{R},t)=\left|\psi_{\mathrm{el}}\right\rangle(\mathbf{r},t)\left|\psi_{\mathrm{nuc}}\right\rangle(\mathbf{R},t) \tag{C.1}$$

$$\left(-\frac{\hbar^2}{2m_e}\sum_i\nabla_i^2+\sum_{i<j}\frac{e^2}{4\pi\epsilon_0\mid r_i-r_j\mid^2}-\sum_{i,\alpha}\frac{Z_\alpha e^2}{4\pi\epsilon_0\mid R_\alpha-r_i\mid^2}\right)\left|\psi_{\mathrm{el}}\right\rangle(\mathbf{r},t)=\mathcal{E}_{\mathrm{el}}(\mathbf{R})\left|\psi_{\mathrm{el}}\right\rangle(\mathbf{r},t) \tag{C.2}$$

$$\left(-\frac{\hbar^2}{2}\sum_\alpha\frac{1}{M_\alpha}\nabla_\alpha^2+\sum_{\alpha<\beta}\frac{Z_\alpha Z_\beta e^2}{4\pi\epsilon_0\mid R_\alpha-R_\beta\mid^2}+\mathcal{E}_{\mathrm{el}}(\mathbf{R})\right)\left|\psi_{\mathrm{nuc}}\right\rangle(\mathbf{R},t)=\mathcal{E}_{\mathrm{mol}}\left|\psi_{\mathrm{nuc}}\right\rangle(\mathbf{R},t) \tag{C.3}$$

In this framework Eq.(C.2) is solved treating the nuclear coordinates **R** as parameters to obtain the electronic contribution to the molecular energy $\mathcal{E}_{\text{el}}(\mathbf{R})$, which is the function whose minimum with respect to **R** defines the equilibrium configuration of the molecule. Once this is known it can be substituted in Eq.(C.3) to get the total molecular energy $\mathcal{E}_{\text{mol}}$. The eigenfunction of the molecule can finally be obtained by multiplying the found electronic and nuclear ones as in Eq.(C.1). In the following sections we will therefore treat the electronic and nuclear problems separately under BO approximation in order to obtain the full structure of the molecule. In the treatment we will mainly follow [61].

C.1 Molecular orbital theory

Generally the electronic eigenvalue problem of Eq.(C.2) is still too difficult to be solved even after the BO approximation. The most crude approach is then to further assume that the electronic wavefunction can be factored out in the individual contributions of each one of the N-electrons in the system:

$$|\psi_{\text{el}}\rangle(\mathbf{r},t) = |\psi_1\rangle(\mathbf{r}_1,t)\,|\psi_2\rangle(\mathbf{r}_2,t)\,|\psi_3\rangle(\mathbf{r}_3,t)...\,|\psi_N\rangle(\mathbf{r}_N,t)$$

where the $|\psi_i\rangle$ are called molecular orbitals and describe the delocalization of a single electron on the whole molecule. The interaction between electrons is thus neglected or treated in averaged terms, which is the most important approximation linked to this approach. The simplest way to define such single-electron wavefunctions is to write them as a linear superposition of the atomic orbitals $|\phi_n\rangle$ of the single atoms in the molecule (LCAO):

$$|\psi_i\rangle(\mathbf{r}_i) = \sum_{\text{n}} c_n\,|\phi_n\rangle \tag{C.4}$$

Indeed near each atom the Hamiltonian of the system is expected to be similar to the atomic one and so this choice of base is physically reasonable. In principle, however, an infinite basis set would be necessary to represent precisely the electron system and thus the use of this finite base will introduce some further approximation in the final wavefunction. Anyway, in this framework the molecular orbitals are described as a delocalization of charge in the molecule arising from the interference of the single atomic orbitals. Once the energy of each molecular orbital is found, the energy diagram of the molecule can be constructed. Each single electron can then be assigned to one of the molecular energy levels following the same Hund's Rules of multi-electron atoms in order to define its ground state. In particularly the occupied orbital with higher energy is usually called HOMO while the unocuppied orbital with lower energy is called LUMO. These define the energetic frontier of the electronic system of the molecules, where most of its chemistry takes place.

Following this approach the linear combination of N atomic orbitals give rise to N molecular orbitals. Some of them are called *bonding orbitals*, since their energy is lower than the one of the atomic orbitals from which they are constituted, while in the opposite case they are called *antibonding orbitals* (identified with the symbol *).

A given ensemble of atoms is therefore able to form a stable molecule only if the electronic configuration of the molecular orbitals attains altogether a lower energy with respect to the separated atomic orbitals. An important aspect to consider is that the LCAO energy levels of molecules are not symmetric since the repulsion between the nuclei tends to increase their value. In this way antibonding orbitals are more antibonding than bonding orbitals are bonding. When complex molecules are examined, the number of atomic orbitals that should be in principle considered in the linear combination starts then to become very high. Luckily, however, some empirical rules can be exploited to simplify the task. First of all it is possible to demonstrate that only atomic orbitals with similar energy and same symmetry with respect to the rotation along the molecular axis can be effectively combined to form a molecular orbital. Therefore, since the molecular orbitals of interest are usually the most energetic ones, which they are the ones linked to the chemical properties of the molecule, it is generally enough to consider the atomic orbitals of the outer shells. Closed-shells electrons, indeed, can be assumed to be effectively confined in the vicinity of the relative atom, giving thus a negligible contribution to the bonds.

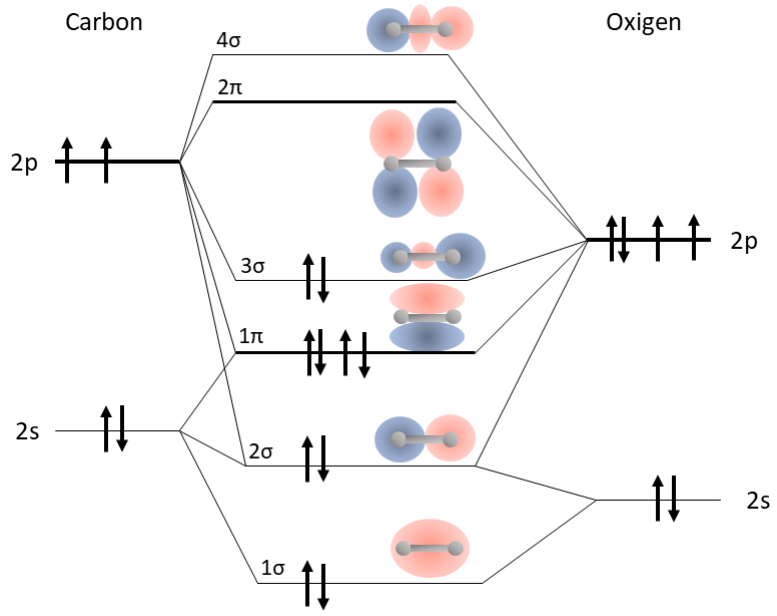

Figure C.1: Energy level diagram of carbon monoxide (CO) as computed from the LCAO theory. Electron spin is represented by the arrows while the spatial shape of the molecular orbital is sketched on the side of each level. The HOMO is in this case a 3σ orbital while the LUMO is a doubly degenerate 2π orbital.

The molecular orbitals can then be classified according to their symmetry properties. The first one is their parity, or inversion of coordinates with respect to center of the molecule. In particular a molecular orbital is defined as *gerade* (represen-

ted with the letter g) if its sign doesn't change under the parity operation while it is defined *ungerade* (represented with the letter u) if its sign changes under the inversion of coordinates. However, this classification is relevant only as long as the system posses a center of inversion and so it is generally not applicable to all molecules. Another important symmetry of the molecular orbitals is then the one with respect to the internuclear axis. Differently from atomic orbitals, molecular ones cannot be spherically symmetric and therefore l is not a good quantum number. However m, linked to the projection of the orbital angular momentum along the internuclear axis, is conserved and can be used to classify them: if $m = 0$ we talk about a σ-orbital, if $m = \pm 1$ we talk about a π-orbital and if $m = \pm 2$ we talk about a δ-orbital. Even if strictly speaking this classification is applicable only to diatomic orbitals, a similar designation based on group theory is extendible also to more complex cases, for which capitol greek letters are used (Σ if $m = 0$, Π if m=1 and Δ if $m = 2$).

It must be however stressed that LCAO theory implies a lot of approximations and it is therefore not able to give highly reliable quantitative results, even if it can qualitatively describe a lot of molecular properties. For more quantitative results it is thus necessary to rely on more complex theories. Two main approaches are generally possible: *ab initio* calculations, in which a model for the wavefunction is chosen based on previous knowledge about the system for computing the electronic energies; *semiempirical methods*, in which a simplified Hamiltonian is used, with some parameters derived from experimental data. One of the most used ab initio approaches is the so called Hartree-Fock self-consistent field method, in which the electron-electron repulsion is treated in averaged terms and the solution is found via an iterative procedure. Each electron is indeed considered to be moving in an effective potential given by the nuclei and the average field of the other electrons. Starting from trial single-electron wavefunctions, such potential is computed and then it is substituted in the BO equations (called in this frame Hartree-Fock equations) to obtain a new set of eigenstates. This is then iteratively repeated until a convergence criterion is satisfied. When reliable single-electron wavefunctions are known the total electronic eigenstate is then found using a Slater determinant to satisfy the antisymmetry character of fermions. These methods however are much more complex than LCAO theory and don't give a fast and physically intuitive picture of the electronic structure of molecules, even if they can deliver more precise results.

C.2 Molecular rotations

In the framework of BO approximation once the *potential energy surface* (PES) of each molecular orbital is known, the nuclear problem can be treated. In particular, a molecule composed of N nuclei posses 3N degrees of freedom in its dynamics. Among these 3N-6 are given by internal vibrations (3N-5 in the case of linear molecules), 3 are given by rotations (2 for linear molecules) and 3 are given by the translation in space of the molecular center of mass. The nuclear Hamiltonian can

thus be partitioned as:

$$\hat{H}_{\text{nuc}} = \hat{H}_{\text{vib}} + \hat{H}_{\text{rot}} + \hat{H}_{\text{trasl}}$$

For the purposes of this thesis the most interesting part of nuclear dynamics is the rotational one and therefore we will concentrate only on this one. In particular we will start considering the simplified picture of rigid rotor molecule in which the rotational and vibrational dynamics are completely uncoupled. The rotation of the molecule can thus be described by its angular momentum **J**, once the tensor of the moment of inertia I is known:

$$\mathbf{J} = I\boldsymbol{\omega}$$

From classical mechanics it is known that this equation can be highly simplified if such tensor is diagonalized onto the three principal axis **a**, **b** and **c** of the system (for convention the axis are defined such that $I_a < I_b < I_c$). Since there is no contribution from the potential energy, the rotational Hamiltonian reads:

$$\hat{H}_{\text{rot}} = \frac{\hat{J}_a^2}{2I_a} + \frac{\hat{J}_b^2}{2I_b} + \frac{\hat{J}_c^2}{2I_c}$$

Rigid rotor molecules can then be classified depending on the values of their moments of inertia along the three principal axis.

I. **Linear:** In this case only one moment of inertia is present, which is perpendicular to the molecular axis.

II. **Spherical top:** The three moments of inertia are all equal and different from zero. In this way, due to the high degree of symmetry, the molecule cannot exhibit any permanent electric dipole or any anisotropy of its polarizability.

III. **Symmetric top:** In this case two moments of inertia of the molecule are equal and different from the third, which lies along the principal symmetry axis of the system. It is then possible to distinguish between *oblate* molecules, for which I_c is the different one, and *prolate* molecules, for which I_a is the different one.

IV. **Asymmetric top:** This is the most complex case, for which all three moments of inertia are different from zero and different from one another.

The symmetry of the first three categories highly simplify the TDSE, which is instead very complex in the most general asymmetric rotor case. Therefore we will start focusing on a generic prolate molecule for which the rotational Hamiltonian can be simply written as:

$$\hat{H}_{\text{rot}} = \frac{\hat{J}_a^2}{2I_{\parallel}} + \frac{\hat{J}_b^2 + \hat{J}_c^2}{2I_{\perp}}$$

where for convenience we have defined $I_a = I_{\parallel}$ and $I_b = I_c = I_{\perp}$. To further reduce this expression it is possible to exploit the decomposition of the molecular angular momentum along the principal axis:

$$\hat{J}^2 = \hat{J}_a^2 + \hat{J}_b^2 + \hat{J}_c^2 \rightarrow \hat{H}_{\text{rot}} = \frac{\hat{J}^2}{2I_{\perp}} + \left(\frac{1}{2I_{\parallel}} - \frac{1}{2I_{\perp}}\right)\hat{J}_a^2$$

In this way the Hamiltonian becomes proportional to the modulus squared of the total molecular angular momentum and to its projection along the unique rotational axis **a**. Therefore the rotational energy levels of such molecule are easily obtained remembering the results for the angular momentum in quantum mechanics:

$$\mathcal{E}_{\text{rot}}(J,K) = \frac{J(J+1)\hbar^2}{2I_\perp} + \Big(\frac{1}{2I_\parallel} - \frac{1}{2I_\perp}\Big)K^2\hbar^2 \tag{C.5}$$

$$J = 0,1,2,3,... \qquad\qquad K = J, J-1, ..., -J$$

In a semiclassical vectorial picture, the quantum number K thus encodes the information about the molecular rotation along its principal symmetry axis. In particular if $|K| \approx J$ almost all of the angular momentum can be considered to be about this axis, while if $|K| \approx 0$ the angular momentum can be considered to be almost perpendicular to it. It is important to underline that the rotational energy depends quadratically on K and therefore it is not affected by the direction of such rotation. As a convention, the energy of Eq.(C.5) is then usually written in terms of the so-called *molecular rotational constants* A and B:

$$A = \frac{\hbar^2}{2I_\parallel} \qquad\qquad B = \frac{\hbar^2}{2I_\perp}$$

so that it takes the simpler form:

$$\mathcal{E}_{\text{rot}} = BJ(J+1) + (A-B)K^2 \tag{C.6}$$

We can then quite easily study also linear and spherical top molecules as special cases of symmetric tops. For a spherical rotor indeed all moments of inertia are equal and so $A = B$. This gives a rotational energy that is independent on the quantum number K and therefore each energy level becomes (2J+1)-fold degenerate:

$$\mathcal{E}_{\text{rot}} = BJ(J+1)$$

For linear rotors instead the angular momentum needs to be perpendicular to the intermolecular axis and therefore $I_\parallel = 0$. This gives an expression for the rotational energy that is mathematically equal to the previous one:

$$\mathcal{E}_{\text{rot}} = BJ(J+1)$$

However, the physical picture is very different. For a spherical top molecules indeed this result is due to the possibility to arbitrary choose the axis over which the total angular momentum is projected, giving thus a degeneracy of the energy levels with respect to K. In the case of linear molecules instead this result is due to the necessity to fix the rotational axis of the molecules and therefore $K \equiv 0$ for all its states and no degeneracy is present.

This energetic analysis is however in many ways too simplified. Indeed the treatment of molecules as rigid rotors is a very crude approximation since while the system rotates the bonds are stretched and this influences back the rotation. This so

called *centrifugal distortion* is more important for higher values of J and makes the molecular energy levels less well separated with respect to the perfectly rigid rotor case. As a first approximation this correction can be simply treated adding three terms in the energy equation:

$$\mathcal{E}_{\text{rot}} = BJ(J+1) - D_J J^2(J+1)^2 + (A-B)K^2 - D_k K^4 - D_{jk} J(J+1)K^2 \qquad \text{(C.7)}$$

where D_j,D_k and D_{jk} are called centrifugal distortion constants and are usually found empirically for each molecule of interest. Generally speaking they are higher for molecules having bonds with lower force constants.

Moreover the analysis presented so far has been developed in the molecular frame of reference, while usually in experiment the laboratory frame of reference is the relevant one. These two can be related through three angular coordinates, named Euler angles (θ, ϕ, χ).

$$\begin{pmatrix} b \\ c \\ a \end{pmatrix} = \begin{pmatrix} \cos\theta\cos\phi\cos\chi - \sin\phi\sin\chi & \cos\theta\sin\phi\cos\chi + \cos\phi\sin\chi & \sin\theta\cos\chi \\ -\cos\theta\cos\phi\sin\chi - \sin\phi\cos\chi & -\cos\theta\sin\phi\sin\chi + \cos\phi\cos\chi & \sin\theta\sin\chi \\ \sin\theta cos\phi & \sin\theta\sin\phi & cos\theta \end{pmatrix} \begin{pmatrix} x \\ y \\ z \end{pmatrix}$$

In this way the expression for the quantum operators of the angular momentum can be obtained in both frame of reference [62]. In particular, the most important result of such analysis is that both $\hat{J}_a$ and $\hat{J}_z$ commute with the rotational Hamiltonian of symmetric top systems. It is therefore possible to find a set of wavefunctions $|JKM\rangle$ that are simultaneous eigenfunctions of both of them, where the quantum number $M = -J, -J+1..., J$ is related to the projection of the total angular moment along the laboratory **z** axis and it is a conserved quantity. Physically this is due to the symmetry of the system with respect to the laboratory fixed axis. The exact expression of these wavefunctions is anyway complex to be computed since the different moments of inertia don't allow to write the Hamiltonian as a function of $\hat{J}^2$ only, apart from spherical top or linear molecules.

For asymmetric top systems the theory is instead more complex and the equations are generally not solvable analytically. This is mainly due to the fact that, being all the moments of inertia different one from the others, it is not possible to factor out the Hamiltonian in the sum of two terms, one dependent only on $\hat{J}^2$ and one dependent only on the projection of the angular moment along one rotational axis. However the $|JKM\rangle$ wavevectors of the symmetric rotor case are still a complete basis set for the system and so the wavefunctions of asymmetric top molecules can be represented as a linear combination of these. For fixed good quantum numbers J and M the asymmetric top wavefunction can thus be written as:

$$\Psi_{\text{J,M}} = \sum_{K=-J}^{J} c_K \, |JKM\rangle$$

where K is no more a good quantum number and it is used only as an index. This expression can then be exploited to diagonalize the correspondent Hamiltonian and to obtain the energy levels of an asymmetric top molecule. For convention

such levels are labelled as J_{K_{-1},K_1} where K_{-1} and K_1 are indexes that are linked respectively to the prolate and oblate limit. Indeed for a given J a number of possible energy levels J_{K_{-1},K_1} are present, bounded between the energy of the prolate molecule with quantum numbers (J, K_{-1}) and the one of the oblate molecule with quantum numbers (J, K_1). It is important to notice that in the case of prolate rotors the rotational energy is increasing with K_{-1}, while for oblate rotors it is decreasing with K_1. For each combination of such numbers a given molecule will then attain a particular energy as a function of the so called Ray's asymmetry parameter:

$$\kappa = \frac{2B - A - C}{A - C}$$

In the symmetric prolate limit this parameter is $\kappa = -1$, in the oblate limit $\kappa = 1$ while for a generic asymmetric molecule $-1 < \kappa < 1$. Each one of these molecular energy levels are then usually numbered using the so-called pseudo-magnetic number $\tau = K_{-1} - K_1 = -J, -J + 1, ..J$, which is a good quantum number for the system. In Figure C.3 some of the energy levels of asymmetric top molecules are given, using a linear approximation between the two symmetric rotor limits, while for more precise results numerical methods should be exploited. It is important to underline the fact that asymmetric rotors show much less regularity in the structure of the energy levels with respect to symmetric top molecules and much of their rich rotational dynamics derives from this.

$J_{K_aK_c}$	J_τ	$F(J_\tau)$
0_{00}	0_0	0
1_{10}	1_1	$A + B$
1_{11}	1_0	$A + C$
1_{01}	1_{-1}	$B + C$
2_{20}	2_2	$2A + 2B + 2C + 2[(B - C)^2 + (A - C)(A - B)]^{1/2}$
2_{21}	2_1	$4A + B + C$
2_{11}	2_0	$A + 4B + C$
2_{12}	2_{-1}	$A + B + 4C$
2_{02}	2_{-2}	$2A + 2B + 2C - 2[(B - C)^2 + (A - C)(A - B)]^{1/2}$
3_{30}	3_3	$5A + 5B + 2C + 2[4(A - B)^2 + (A - C)(B - C)]^{1/2}$
3_{31}	3_2	$5A + 2B + 5C + 2[4(A - C)^2 - (A - B)(B - C)]^{1/2}$
3_{21}	3_1	$2A + 5B + 5C + 2[4(B - C)^2 + (A - B)(A - C)]^{1/2}$
3_{22}	3_0	$4A + 4B + 4C$
3_{12}	3_{-1}	$5A + 5B + 2C - 2[4(A - B)^2 + (A - C)(B - C)]^{1/2}$
3_{13}	3_{-2}	$5A + 2B + 5C - 2[4(A - C)^2 - (A - B)(B - C)]^{1/2}$
3_{03}	3_{-3}	$2A + 5B + 5C - 2[4(B - C)^2 + (A - B)(A - C)]^{1/2}$

Figure C.2: Rotational energies of rigid asymmetric top molecules as a function on its moments of inertia. The energies as given in terms rotational wavevectors F with $\mathcal{E}_{rot} = \hbar c F$ while the rotational constants A, B and C are in this case expressed in cm^{-1} [62].

Bibliography

[1] T.H. Maiman, *Stimulated optical radiation in Ruby*, Nature 187 (1960).

[2] D. Strickland, G. Mourou, *Compression of amplified chirped optical pulses*, Optics Communications 56 (1985)

[3] A. McPherson, G. Gibson, H. Jara, U. Johann, T. S. Luk, I. A. McIntyre, K. Boyer, and C. K. Rhodes,*Studies of multiphoton production of vacuum-ultraviolet radiation in rare gases*, J. Opt. Soc. Am. B 4 (1987).

[4] J. L. Krause, K. J. Schafer, and K. C. Kulander, *High-Order Harmonic Generation from Atoms and Ions in the High Intensity Regime*, Physical Review Letters 68, 3535–3538 (1992).

[5] P.M. Paul, E.S. Toma, P. Breger, G. Mullot, F. Auge, P. Balcou, H.G. Muller and P. Agostini, *Observation of a train of attosecond pulses from high harmonic generation*, Science 292(2001).

[6] G. Sansone, E. Benedetti, F. Calegari, C. Vozzi, L. Avaldi, R. Flammini, L. Poletto, P. Villoresi, C. Altucci, R. Velotta, S. Stagira, S. De Silvestri, M. Nisoli, *Isolated single-cycle attosecond pulses*, Science 314 (5798), 443-446 (2006).

[7] F. Calegari, D. Ayuso, A. Trabattoni, L. Belshaw, S. De Camillis, S. Anumula, F. Frassetto, L. Poletto, A. Palacios, P. Decleva, J. B. Greenwood, F. Martín, and M. Nisoli, *Ultrafast electron dynamics in phenylalanine initiated by attosecond pulses*, Science 346, 6207, 336–339 (2014).

[8] E. Goulielmakis, Z.-H. Loh, A. Wirth, R. Santra, N. Rohringer, V. S. Yakovlev, S. Zherebtsov, T. Pfeifer, A. M. Azzeer, M. F. Kling, S. R. Leone, and F. Krausz, *Real-time observation of valence electron motion*, Nature 466, 7307, 739–743 (2010).

[9] A. Rundquist, C. Durfee, Z. Chang, C. Herne, S. Backus, M. Murnane and H. Kapteyn, *Phase-Matched Generation of Coherent Soft X-Rays*, Science 280, 1412-1415 (1998).

[10] T. Popmintchev, M.C. Chen, D. Popmintchev, P. Arpin, S. Brown, S. Ališauskas, G. Andriukaitis, T. Balčiunas, O.D. Mücke,A. Pugzlys, A. Baltuška, B. Shim, S.E. Schrauth, A. Gaeta, C. Hernández-García, L. Plaja, A. Becker, A. Jaron-Becker, M.M. Murnane, H.C. Kapteyn, *Bright Coherent Ultrahigh Harmonics in the keV X-ray Regime from Mid-Infrared Femtosecond Lasers*, Science 336, 6086, 1287-91 (2012).

[11] P. B. Corkum, *Plasma Perspective on Strong-Field Multiphoton Ionization*, Physical Review Letters 71, 1994–1997 (1993).

[12] K. C. Kulander, K. J. Schafer, J. L. Krause, and B. Piraux, *Proceedings of the Workshop, Super Intense Laser Atom Physics (SILAP) III*, Plenum Press, New York (1993).

[13] M. Lewenstein, P. Balcou, M. Y. Ivanov, A. L'Huillier, and P.B.Corkum, *Theory of high-harmonic generation by low-frequency laser fields*, Physical Review A 42, 2117–2133 (1994).

[14] V. S. Popov, *Tunnel and multiphoton ionization of atoms and ions in a strong laser field (Keldysh theory)*, Physics-Uspekhi (2004)

[15] L. V. Keldysh, *Ionization in the Field of a Strong ElectromagneticWave*, Journal of Experimental and Theoretical Physics 20, 1307–3538 (1965).

[16] M. W. Walser, C.H. Keitel, A. Scrinzi, T. Brabec, *High Harmonic Generation Beyond the Electric Dipole Approximation*, Physical Review Letters 85 (2000)

[17] H. R. Reiss, *Limits on Tunneling Theories of Strong-Field Ionization*, Physical Review Letters 101 (2008)

[18] L. D. Landau, E. M. Lifshitz, *Quantum Mechanics Non-Relativistic Theory: Volume 3*, (1981)

[19] A. M. Perelomov, V. S. Popov, M. V. Terent'ev, *Ionization of atoms in an alternating electrical field*, JETP 23 (1966)

[20] A. M. Perelomov, V. S. Popov, M. V. Terent'ev, *Ionization of atoms in an alternating electrical field II*, JETP 24 (1967).

[21] A. M. Perelomov, V. S. Popov, *Ionization of atoms in an alternating electrical field III*, JETP 25 (1967)

[22] F. A. Ilkov, J. E. Decker, S. L. Chin, *Ionization of atoms in the tunnelling regime with experimental evidence using Hg atoms*, J- Phys. B: At. Mol. Opt. Phys. 25 (1992)

[23] Z. Chang, *Fundamentals of attosecond optics*, CRC Press (2011)

[24] A.D. Shiner, C. Trallero-Herrero, N. Kajumba, H.C. Bandulet, D. Comtois, F. Légaré, M. Giguère, J.C. Kieffer, P.B. Corkum, D.M. Villeneuve, *Wavelength scaling of high harmonic generation efficiency*, Physical Review Letters 103 (2009)

[25] K. Zhao, Q. Zhang, M. Chini, Y. Wu, X. Wang, Z. Chang, *Tailoring a 67 attosecond pulse through advantageous phase-mismatch*, Optics Letters 37 (2012)

[26] S. Beaulieu, S. Camp, D. Descamps, A. Comby, V. Wanie, S. Petit, F. Légaré, K. J. Schafer, M. B. Gaarde, F. Catoire, Y. Mairesse, *Role of Excited States In High-order Harmonic Generation*, Physical Review Letters 117 (2016)

[27] D.Faccialà, *Attosecond multi-electron dynamics probed by high-order harmonic generation in bi-chromatic fields*, Scuola di Dottorato - XXIX Ciclo (2017)

[28] Y. Mairesse, A. de Bohan, L. J. Frasinski, H. Merdji, L. C. Dinu, P. Monchicourt, P. Breger, M. Kovačev, R. Taïeb, B. Carr1, H. G. Muller, P. Agostini, P. Salières, *Attosecond Synchronization of High-Harmonic Soft X-rays*, Science 302 (2003)

[29] M. Lewenstein, P. Salières, A. L'Huillier, *Phase of the atomic polarization in high-order harmonic generation*, Physical Review A 52 (1995)

[30] K. Varjú, Y. Mairesse, B. Carré, M.B. Gaarde, P. Johnsson, S. Kazamias, R. Lopez-Martens, J. Mauritsson, K.J. Schafer, Ph. Balcou, A. L'Huillier, P. Salières,*Frequency chirp of harmonic and attosecond pulses*, Journal of Modern Optics 52 (2005)

[31] A. L'Huillier, P. Balcou,*High-order harmonic generation in rare gases with a 1-ps 1053-nm laser*, Physical Review Letters 70 (1993)

[32] J. Zhou, J. Peatross, M.M. Murnane, H.C. Kapteyn, *Enhanced High-Harmonic Generation Using 25 fs Laser Pulses*, Phys. Rev. Lett. 76 (1996)

[33] Z. Chang, A. Rundquist, H. Wang, M. M. Murnane, H. C. Kapteyn, *Generation of Coherent Soft X Rays at 2.7 nm Using High Harmonics*, Physical Review Letters 79 (1997)

[34] A. L'Huillier, K. J. Schafer, K. C. Kulander, *Theoretical aspects of intense field harmonic generation*, J. Phys. B: At. Mol. Opt. Phys. 24 (1991)

[35] P. Balcou, P. Salières, A. L'Huillier, M. Lewenstein. *Generalized phasematching conditions for high harmonics: The role of field-gradient forces*, Physical Review A 55 (1997)

[36] P. Schwerdtfeger *Table of experimental and calculated static dipole polarizabilities*, CTCP, Massey University, Auckland (2015)

[37] B.L. Henke, E.M. Gullikson, J.C. Davis *X-ray interactions: photoabsorption, scattering, transmission, and reflection at E=50-30000 eV, Z=1-9*, Atomic Data and Nuclear Data Tables 54 (1993)

[38] E. R. Peck, D. J. Fisher, *Dispersion of argon*, J. Opt. Soc. Am. 54 (1964)

[39] F. F. Chen, *Introduction to Plasma Physics and Controlled Fusion*, Springer International Publishing (2016)

[40] E. Constant, D. Garzella, P. Breger, E. Mével, Ch. Dorrer, C. Le Blanc, F. Salin, P. Agostini, *Optimizing High Harmonic Generation in Absorbing Gases: Model and Experiment*, Physical Review Letters 82 (1999)

[41] S. Kazamias, S. Daboussi, O. Guilbaud, K. Cassou, D. Ros, B. Cros, G. Maynard, *Pressure-induced phase matching in high-order harmonic generation*, Physical Review A 83 (2011)

[42] P. Salières, A. L'Huillier, M. Lewenstein, *Coherence Control of High-Order Harmonics*, Physical Review A (1995)

[43] P. Ye, X. He, H. Teng, M. Zhan, S. Zhong,W. Zhang, L.Wang, Z.Wei, *Full Quantum Trajectories Resolved High-Order Harmonic Generation* Physical Review Letters 113 (2014)

[44] E. A. J. Marcatili, R. A. Schmeltzer, *Hollow metallic and dielectric waveguides for long distance optical transmission and lasers*, Bell System Technical Journal 43 (1964)

[45] Katsunari Okamoto, *Fundamentals of Optical Waveguides*, Elsevier (2000)

[46] E. T. F. Rogers, S. L. Stebbings, A. M. de Paula, C. A. Froud, M. Praeger, B. Mills, J. Grant-Jacob, W. S. Brocklesby, J. G. Frey, *Spatiotemporal phase-matching in capillary high-harmonic generation*, J. Opt. Soc. Am. B 29 (2008)

[47] T. Brabec, F. Krausz, *Intense few-cycle laser fields: Frontiers of nonlinear optics*, Rev. Mod. Phys. 72 (2000)

[48] E. A. Gibson, A. Paul, N. Wagner, R. Tobey, D. Gaudiosi, S. Backus, I. P. Christov, A. Aquila, E. M. Gullikson, D. T. Attwood, M. M. Murnane, H. C. Kapteyn, *Coherent Soft X-ray Generation in the Water Window with Quasi–Phase Matching*, Science 302 (2003)

[49] J. Seres, V. S. Yakovlev, E. Seres, C.H. Streli, P. Wobrauschek, C.H. Spielmann, F. Krausz, *Coherent superposition of laser-driven soft-X-ray harmonics from successive sources*, Nature Physics (2007)

[50] J. Peatross, S. Voronov, I. Prokopovich, *Selective zoning of high harmonic emission using counter-propagating light*, Optics Express 115 (1997)

[51] X. Zhang, A. L. Lytle, T. Popmintchev, X. Zhou, H. C. Kapteyn, M. M. Murnane, O. Cohen, *Quasi-phase-matching and quantum-pathcontrol of high-harmonic generation using counterpropagating light*, Nature (2007)

[52] R. M. Jenkins, R. W. J. Devereux, *Effect of field regeneration on the TEM_{00} transmission characteristics of a circular-section waveguide*, Applied Optics 31(1992)

[53] M. Zepf, B. Dromey, M. Landreman, P. Foster, S. M. Hooker, *Bright Quasi-Phase-Matched Soft-X-Ray Harmonic Radiation from Argon Ions*, Physical Review Letters 99 (2007)

[54] C. Jin, H. J. Wörner, V. Tosa, A.T. Le, J. B. Bertrand, R. R. Lucchese, P. B. Corkum, D. M. Villeneuve, C. D. Lin, *Separation of target structure and medium propagation effects in high-harmonic generation*, Journal of Physics B 44 (2011)

[55] H. Niikura, F. Légaré, R. Hasbani, A. Bandrauk, M. Y. Ivanov, D. Villeneuve, P. Corkum, *Sublaser-cycle electron pulses for probing molecular dynamics*, Nature 417(2002)

[56] J. Itatani, J. Levesque, D. Zeidler, H. Niikura, H. Pèpin, J. C. Corkum, D. M. Villeneuve *Tomographic imaging of molecular orbitals* Nature 432 (2004)

[57] C. Vozzi, M. Negro, F. Calegari, G. Sansone, M. Nisoli, S. D. Silvestri, S. Stagira, *Generalized molecular orbital tomography*, Nature Physics 7, (2011)

[58] S. Baker, J. S. Robinson, C. A. Haworth, H. Teng, R. A. Smith, C. C. Chirila, M. Lein, J. W. G. Tisch, J. P. Marangos, *Probing Proton Dynamics in Molecules on an Attosecond Time Scale*, Science 312 (2006)

[59] A. D. Shiner, B. E. Schmidt, C. Trallero-Herrero, H. J. Wörner, S. Patchkovskii, P. B. Corkum, J-C. Kieffer, F. Légaré, D. M. Villeneuve, *Probing collective multi-electron dynamics in xenon with high-harmonic spectroscopy*, Nature Physics 7 (2011)

[60] N. L. Wagner, A. Wüest, I. P. Christov, T. Popmintchev, X. Zhou, M. M. Murnane, H. C. Kapteyn, *Monitoring molecular dynamics using coherent electrons from high harmonic generation*, PNAS USA 103 (2006)

[61] P. W. Atkins, R. S. Friedman, *Molecular quantum mechanics*, Oxford University Press (2010)

[62] Marek Tulej, *Application of Spectroscopic Methods*, Lecture Notes (2008)

[63] J. P. Marangos, *Development of high harmonic generation spectroscopy of organic molecules and biomolecules*, J. Phys. B: At. Mol. Opt. Phys. 49 (2016)

[64] L. Cardellino, *Study of rotational dynamics in impulsively aligned molecules by high-order harmonic generation*, Master Thesis (2014)

[65] S. Haessler, J. Caillat, P. Salières, *PhD tutorial: Self-probing of molecules with high harmonic generation*, J. Phys. B: At. Mol. Opt. Phys. 44 (2011)

[66] X. M. Tong, Z. X. Zhao, C. D. Lin, *Theory of molecular tunneling ionization*, Physical Review A 66 (2002)

[67] S. F. Zhao, J. Xu, C. Jin, A. T. Le, C. D. Lin, *Effect of orbital symmetry on the orientation dependence of strong field tunnelling ionization of nonlinear polyatomic molecules*, J. Phys. B: At. Mol. Opt. Phys. 44 (2011)

[68] S. F. Zhao, X. X. Zhou, C. D. Lin, *Probing Orbital Symmetry of Molecules Via Alignment-Dependent Ionization Probability and High-Order Harmonic Generation by Intense Lasers*, Advances of Atoms and Molecules in Strong Laser Fields, World Scientific Publishing Co. Pte. Ltd. (2016)

[69] E. P. Wigner, *Group Theory and its Application to the Quantum Mechanics of Atomic Spectra*, Academic Press Inc (1959)

[70] Z. B. Walters, O. Smirnova, *Attosecond correlation dynamics during electron tunnelling from molecules*, J. Phys. B: At. Mol. Opt. Phys. 43 (2010)

[71] G. Jordan, A. Scrinzi, *Core-polarization effects in molecular high harmonic generation*, New Journal of Physics (2008)

[72] M. Lein, *Molecular imaging using recolliding electrons*, J. Phys. B: At. Mol. Opt. Phys. 40 (2007)

[73] O. Smirnova, S. Patchkovskiia, Y. Mairessea, N. Dudovicha, M. Y. Ivanova, *Strong-field control and spectroscopy of attosecond electron-hole dynamics in molecules*, PNAS 106 (2009)

[74] M. Lein, *Attosecond Probing of Vibrational Dynamics with High-Harmonic Generation*, Physical Review Letters 94 (2005)

[75] O. Smirnova, Y. Mairesse, S. Patchkovskii, N. Dudovich, D. Villeneuve, P. Corkum, M. Y. Ivanov, *High harmonic interferometry of multi-electron dynamics in molecules*, Nature 460 (2009)

[76] M. Lein, N. Hay, R. Velotta, J. P. Marangos, P. L. Knight, *Role of intramolecular phase in high harmonic generation*, Phys. Rev. Lett. 88 (2002)

[77] C. Vozzi, F. Calegari, E. Benedetti, J. P. Caumes, G. Sansone, S. Stagira, M. Nisoli, R. Torres, E. Heesel, N. Kajumba, J. P. Marangos, C. Altucci, R. Velotta *Controlling two-centre interference in molecular high harmonic generation*, Phys. Rev. Lett. 95 (2005)

[78] P. H. Bucksbaum, M. G. McFarland, J .P. Farrell, *High Harmonic Generation from Multiple Orbitals in N2* Science, 322 (2008)

[79] A. Rupenyan, P. M. Kraus, J. Schneider, H. J. Wörner, *High-harmonic spectroscopy of isoelectronic molecules:Wavelength scaling of electronic-structure and multielectron effects*, Physical Review A 87 (2013)

[80] D. Normand, L. A. Lompre, C. Cornaggia, *Laser-induced molecular alignment probed by a double-pulse experiment*, J. Phys. B 25 (1992)

[81] B. Friedrich, D. Herschbach, *Alignment and Trapping of Molecules in Intense Laser Fields*, Phys. Rev. Lett. 74 (1995)

[82] W. Kim, P. M. Felker, *Spectroscopy of pendular states in optical-field-aligned species*, The Journal of Chemical Physics 104 (1996)

[83] T. Seideman, *Revival Structure of Aligned Rotational Wave Packets*, Phys. Rev. Lett. 83 (1999)

[84] J. G. Underwood, B. J. Sussman, A. Stolow, *Field-Free Three Dimensional Molecular Axis Alignment*, Phys. Rev. Lett. 94 (2005)

[85] X. Ren, V. Makhija, V. Kumarappan, *Multipulse Three-Dimensional Alignment of Asymmetric Top Molecules*, Phys. Rev. Lett. 112 (2014)

[86] J. Ortigoso, M. Rodrguez, M. Gupta, B. Friedrich, *Time evolution of pendular states created by the interaction of molecular polarizability with a pulsed nonresonant laser field*, The Journal of Chemical Physics 110 (1999)

[87] P. R. Bunker, P. Jensen, *Molecular Symmetry and Spectroscopy*, Ontario: NRC Research Press, (1998)

[88] S. J. Weber, M. Oppermann, J. P. Marangos, *Role of Rotational Wave Packets in Strong Field Experiments*, Physical Review Letters 111 (2013)

[89] R. M. Lock, S. Ramakrishna, X. Zhou, H. C. Kapteyn, M. M. Murnane, T. Seideman, *Extracting Continuum Electron Dynamics from High Harmonic Emission from Molecules*, Physical Review Letters 108 (2012)

[90] E. Hamilton, T. Seideman, T. Ejdrup, M. D. Poulsen, C. Z. Bisgaard, S. S. Viftrup, H. Stapelfeldt, *Alignment of symmetric top molecules by short laser pulses*, Physical Review A 72 (2005)

[91] E. Péronne, M. D. Poulsen, C. Z. Bisgaard, H. Stapelfeldt, T. Seideman, *Nonadiabatic Alignment of Asymmetric Top Molecules: Field-Free Alignment of Iodobenzene*, Physical Review Letters 91 (2003)

[92] C. Vozzi, F. Calegari, E. Benedetti, S. Gasilov, G. Sansone, G. Cerullo, M. Nisoli, S. De Silvestri, S. Stagira, *Millijoule-level phase-stabilized few-optical-cycle infrared parametric source*, Opt. Lett. 32 (2007)

[93] C. Vozzi, C. Manzoni, F. Calegari, E. Benedetti, G. Sansone, G. Cerullo, M. Nisoli, S. De Silvestri, S. Stagira, *Characterization of a high-energy self-phase-stabilized near-infrared parametric source*, J. Opt. Soc. Am. B 25 (2008)

[94] B. Prade, M. Franco, A. Mysyrowicz, A.Couatron, H. Buersing, B. Eberle, M. Krenz, D. Seiffer, O. Vasseur, *Spatial mode cleaning by femtosecond filamentation in air*, Optics Letters 31 (2006)

[95] L. Poletto, G. Naletto, G. Tondello, *Grazing-incidence flat-field spectrometer for high-order harmonic diagnostics*, Optical Engineering 40 (2001)

[96] L. Poletto, G. Tondello, P. Villoresi, *High-order laser harmonics detection in the EUV and soft x-ray spectral regions*, Review of Scientific Instruments 72 (2001)

[97] R. Osellame, G. Cerullo, R. Ramponi, *Femtosecond laser micromachining: photonic and microfluidic devices in transparent materials*, Springer Science & Business Media (2012)

[98] K. Itoh, W. Watanabe, S. Nolte, C. B. Schaffer, *Ultrafast processes for bulk modification of transparent materials* MRS bulletin 31 (2006)

[99] J. W. Chan, T. Huser, S. Risbud, D. M. Krol, *Structural changes in fused silica after exposure to focused femtosecond laser pulses*, Optics letters 26 (2001)

[100] P. Dekker, M. Ams, G. D. Marshall, D. J. Little, M. J. Withford, *Annealing dynamics of waveguide bragg gratings: evidence of femtosecond laser induced colour centres*, Optics express 18 (2010)

[101] K. M. Davis, K. Miura, N. Sugimoto, K. Hirao, *Writing waveguides in glass with a femtosecond laser*, Optics letters 21 (1996)

[102] C. Hnatovsky, R. S. Taylor, E. Simova, P. P. Rajeev, D. M. Rayner, V. R. Bhardwaj, P. B. Corkum, *Fabrication of microchannels in glass using focused femtosecond laser radiation and selective chemical etching*, Applied Physics A 84 (2006)

[103] A. Marcinkevičius, S. Juodkazis, M. Watanabe, M. Miwa, S. Matsuo, H. Misawa, J. Nishii, *Femtosecond laser-assisted three-dimensional microfabrication in silica*, Optics Letters 26 (2001)

[104] S. Juodkazis, K. Nishimura, S. Tanaka, H. Misawa, E. G. Gamaly, B. Luther-Davies, L. Hallo, P. Nicolai, V. T. Tikhonchuk, *Laser-induced microexplosion confined in the bulk of a sapphire crystal: evidence of multimegabar pressures*, Physical review letters 96 (2006)

[105] K. Miura, J. Qiu, H. Inouye, T. Mitsuyu, K. Hirao, *Photowritten optical waveguides in various glasses with ultrashort pulse laser*, Applied Physics Letters 71 (1997)

[106] Y. Shimotsuma, P. G. Kazansky, J. Qiu, K. Hirao, *Self-organized nanogratings in glass irradiated by ultrashort light pulses*, Physical review letters 91 (2003)

[107] E. N. Glezer, M. Milosavljevic, L. Huang, R. J. Finlay, T. H. Her, J. P. Callan, E. Mazur, *Three-dimensional optical storage inside transparent materials*, Optics Letters 21 (1996)

[108] P. P. Rajeev, M. Gertsvolf, E. Simova, C. Hnatovsky, R. S. Taylor, V. R. Bhardwaj, D. M. Rayner, P. B. Corkum, *Memory in nonlinear ionization of transparent solids*, Physical review letters 97 (2006)

[109] V. R. Bhardwaj, E. Simova, P. P. Rajeev, C. Hnatovsky, R. S. Taylor, D. M. Rayner, P. B. Corkum, *Optically produced arrays of planar nanostructures inside fused silica*, Physical review letters 96 (2006)

[110] R. S. Taylor, C. Hnatovsky, E. Simova, D. M. Rayner, M. Mehandale, V. R. Bhardwaj, P. B. Corkum, *Ultra-high resolution index of refraction profiles of femtosecond laser modified silica structure*, Optics express 11 (2003)

[111] A. Marcinkevičius, V. Mizeikis, S. Juodkazis, S. Matsuo, H. Misawa, *Effect of refractive index-mismatch on laser microfabrication in silica glass*, Applied Physics A 76 (2003)

[112] C. Hnatovsky, R. S. Taylor, E. Simova, V. R. Bhardwaj, D. M. Rayner, P. B. Corkum, *High-resolution study of photoinduced modification in fused silica produced by a tightly focused femtosecond laser beam in the presence of aberrations*, Journal of applied physics 98 (2005)

[113] C. Hnatovsky, R. S. Taylor, E. Simova, P. P. Rajeev, D. M. Rayner, V. R. Bhardwaj, P. B. Corkum, *Fabrication of microchannels in glass using focused femtosecond laser radiation and selective chemical etching*,Applied Physics A 84 (2006)

[114] K. C. Vishnubhatla, N. Bellini, R. Ramponi, G. Cerullo, R. Osellame, *Shape control of microchannels fabricated in fused silica by femtosecond laser irradiation and chemical etching*, Optics express 17 (2009)

[115] N. Bellini, *Integrated optofluidic devices for biophotonic applications fabricated by femtosecond laser pulses*, Scuola di Dottorato - XXIV Ciclo (2011)

[116] L. Shah, A. Y. Arai, S. M. Eaton, P. R. Herman,*Waveguide writing in fused silica with a femtosecond fiber laser at 522 nm and 1 mhz repetition rate*, Optics Express 13 (2005)

[117] J. Itatani, J. Levesque, D. Zeidler, H. Niikura, H. Pépin, J. C. Kieffer, P. B. Corkum, D. M. Villeneuve, *Tomographic imaging of molecular orbitals*, Nature 432 (2004)

[118] M. Negro, *High order harmonic generation driven by a mid-infrared laser source: a tool for attosecond science and molecular spectroscopy*, Scuola di Dottorato - XXV Ciclo (2013)

[119] P. M. Paul, E. S. Toma, P. Breger, G. Mullot, F. Auge, P. Balcou, H. G. Muller, P. Agostini, *Observation of a train of attosecond pulses from high harmonic generation*, Science 292 (2001)

[120] L. D. Landau, E. M. Lifshitz, *Quantum Mechanics: Non-relativistic theory*, Pergamon Press, Oxford (1991)

[121] Y. Mairesse , J. Levesque , N. Dudovich , P. B. Corkum, D. M. Villeneuve, *High harmonic generation from aligned molecules–amplitude and polarization*, Journal of Modern Optics 55 (2008)

[122] A. T. Le, R. R. Lucchese, M. T. Lee, C. D. Lin, *Probing Molecular Frame Photoionization via Laser Generated High-Order Harmonics from Aligned Molecules*, Physical Review Letters 102 (2009)

[123] J. C. Baggesen, L. B. Madsen, *On the dipole, velocity and acceleration forms in high-order harmonic generation from a single atom or molecule*, Journal of Physics B: Atomic, Molecular and Optical Physics 44 (2011)

[124] C. Vozzi, R. Torres, M. Negro, L. Brugnera, T. Siegel, C. Altucci, R. Velotta, F. Frassetto, L. Poletto, P. Villoresi, S. De Silvestri, S. Stagira, J. P. Marangos, *High harmonic generation spectroscopy of hydrocarbons*, Applied Physics Letters 97 (2010)

[125] N. Kajumba, R. Torres, J. G. Underwood, J. S. Robinson, S. Baker, J. W. G. Tisch, R. de Nalda, W. A. Bryan, R. Velotta, C. Altucci, I. Procino, I. C. E. Turcu,

J. P. Marangos, *Measurement of electronic structure from high harmonic generation in non-adiabatically aligned polyatomic molecules*, New Journal of Physics 10 (2008)

[126] S. M. Hankin, D. M. Villeneuve, P. B. Corkum, D. M. Rayner, *Nonlinear Ionization of Organic Molecules in High Intensity Laser Fields*, Physical Review Letters (2000)

[127] R. Torres, T. Siegel, L. Brugnera, I. Procino, J. G. Underwood, C. Altucci, R. Velotta, E. Springate, C. Froud, I. C. E. Turcu, M. Y. Ivanov, O. Smirnova, J. P. Marangos, *Extension of high harmonic spectroscopy in molecules by a 1300 nm laser field*, Optics Express 18 (2010)

[128] A. Rouzée, S. Guérin, V. Boudon, B. Lavorel, O. Faucher, *Field-free one-dimensional alignment of ethylene molecule*, Physical Review A 73 (2006)

[129] T. Grohmann, M. Leibscher, *Nuclear spin selective alignment of ethylene and analogues*, The Journal of Chemical Physics 134 (2011)

[130] M. Varun, *Laser-induced rotational dynamics as a route to molecular frame measurements*, PhD thesis, Kansas State University (2014)

[131] G. Cooper, T. N. Olney, C. E. Brion, *Absolute UV and Soft X-ray photoabsorption of ethylene by high resolution dipole (e, e) spectroscopy*, Chemical Physics 194 (1995)

[132] C. Comparelli, *High-order harmonic generation in a chip fabricated through femtosecond laser irradiation followed by chemical etching techniques*, Master Thesis (2017)

[133] G. Ciriolo, *Development of ultrafast sources for applications to spectroscopy and strong-field physics*, Scuola di Dottorato - XXX Ciclo (2018)

Ringraziamenti

Desidero utilizzare questo piccolo spazio per rivolgere un enorme ringraziamento alle molte persone che mi sono state accanto in questi anni. Se ho potuto portare a termine questo percorso è anche, se non sopratutto, merito vostro.

Un primo grazie va al Prof. Salvatore Stagira e alla Prof.ssa Caterina Vozzi. La vostra pazienza, il vostro sostegno e i vostri consigli mi hanno permesso di compiere quest'ultimo passo e di svolgere un lavoro di cui posso dire di andare fiero. Grazie anche a Davide, Anna, Michele, Eugenio, Aditya, Prabhash e a tutto il gruppo in cui ho svolto l'attività sperimentale. Da ognuno di voi ho imprato molto.

Un grosso ringraziamento va poi a tutta la mia famiglia, anche a quelli di essa che non ci sono più. Il vostro ostinato affetto mi è sempre stato vicino e mi ha guidato in molti momenti. In particolare, un profondo grazie ai miei genitori e a mio fratello. Con i vostri sacrifici e il vostro esempio mi avete cresciuto e mi avete dato la possibilità di scegliere ciò che amo. Non potrò mai esprimervi abbastanza quanto tutto il vostro sostegno e tutta la vostra silenziosa sopportazione del mio pazzo umore siano stati fondamentali.

Un enorme grazie va anche alla mia seconda famiglia. Sia agli amici di sempre Andrea, Matteo B. e Matteo F. che a quelli che l'università mi ha regalato Simone, Silvia, Stefano, Nicolò, Martina e Illya; poichè avete reso con la vostra compagnia più leggero il peso di questi anni e avete creduto in me anche quando io stesso non avevo il coraggio di farlo. Ognuno di voi ha contributo a rendere possibile tutto ciò che ho realizzato.